Using Space Geodesy to Constrain Variations in Seismogenic Behavior on Subduction Megathrusts

Thesis by
Yunung Nina Lin

In Partial Fulfillment of the Requirements for the
degree of
Doctor of Philosophy

CALIFORNIA INSTITUTE OF TECHNOLOGY
Pasadena, California
2013
(Defended May 31, 2013)

ACKNOWLEDGEMENTS

I want to thank my two thesis advisors, Professor Mark Simons and Jean-Philippe Avouac, for the past six years of valuable advisement and support. Mark is so sharp in science and always sees through the core of any scientific topic. Jean-Philippe has a great mind and point of view about science that inspires me all the time. I learn from both of them in so many different aspects: the courses they offered during my first few years (*Tectonic Geodesy* from Mark and *Geology of Earthquakes* from Jean-Philippe), the moments that we sat down together and worked through the equations and codes, and the thoughts and ideas about science that they shared during official talks and casual conversations. Most important of all, as the saying "*Example is better than percept*" goes, they show me as the best examples what great scientists are, how they target scientific problems, and how they perceive the value of science. These are the fruits that I will walk away with and will accompany me through the rest of my career.

I also want to thank Professor Joann Stock, my academic advisor, for being my role model of a great scientist and a mother. The stories about how she took care of her babies and did great science at the same time always remind me that everything is possible, and that we ought not to set limits to ourselves. Her understanding of the difficulties that a female graduate student with babies may face, and the support and advices she offered, always give me courages to move on during my hard times.

My first year project advisor, Professor Kerry Sieh, now at Earth Observatory of Singapore, is another person that I owe gratitude to. He is a very close family friend (thanks for attending my wedding!) and a great scientist to work with. We had a lot of fun time together in Taiwan (2005), in Bandong, Indonesia (2006), in Singapore (2007) and in my first year at Caltech (2007-08).

My officemates are important stress relief to me. Nneka Williams (and her husband Geoff) and I exchanged various thoughts of life, of families and of many others things in N. Mudd 303. Our secret gossips always help each other relieve the stress from the high-intensity work. Laurie Kovalenko introduced me into the world of outreach, which I found equally interesting as scientific research. I would never know what I am capable of in terms of speaking to the public and intriguing the kids without her encouragement.

My labmates are the most important resources I go to whenever I encounter problems. Former members include Chris DeCaprio, Eric Hetland, Ravi Kanda, Sarah Minson, Anthony Sladen; current members include Piyush Agram, Zacharie Duputel, Junle Jiang, Romain Jolivet, Hilary Martens, Brent Minchew, Francisco Ortega, Bryan Riel and Jeff Thompson. Thank you so much for being supportive to me at all times.

There are many other people who really make my life at Caltech, mostly former and current members of the Tectonics Observatory. They are Thomas Ader, Willy Amadom (and his wife Susan), Sylvain Barbot, Alan Chapman (and his wife Kelly), Nadaya Cubas, John Galetzka, Janet Harvey, Jamshid Hassanzadeh, Yihe Huang, Steve Kidder (and his wife Robin), Young-Hee Kim, Aron Meltzner, Lingsen Meng, Belle Philibosian (and her husband Adam), Steve Skinner, Marion Thomas, Zhongwen Zhan, and Dongzhou Zhang. Thank Tectonics Observatory for gathering so many interesting people to make the research life exciting and after-work life colorful.

And my most sincere thanks to the administrative and supportive staff: Mike Black, Dian Buchness, Leticia Calderon, Lisa Christiansen, Scott Dungan, Marcia Hudson, Rosemary Miller, Donna Mireles, and Heather Steele. Without their help, my life would be a lot more miserable with the crazy logistics and computer stuff.

Other important family friends who supported me during these six years include Wei-Ting Chen and Eh Tan (both former Caltech graduate students), Fan-Chi Lin (current GPS post-doc) and his families, and Yue-Gau Chen (my master thesis advisor at National Taiwan University). Their companion makes the transition from Taiwanese culture to American culturer much easier.

Finally, I owe a million thanks to my mother, Hsiu-man Yang, who offered unconditional help to take care of my two boys, Jing (2 year 9 month) and Ying (11 month). Without her, it may take me another 1-2 year to finish. And Wangyu, my husband, another new PhD in this year of 2013. His love and support is the major reason that I move on with my PhD, and will continue to be the driving force for my career in the future.


MODELING IS A PIECE OF CAKE.
Pylith
GPS
Earth quake
Gm=d
Bayesian
Tide
InSAR
Glacier
SIMONS' THIRTEEN
05 31 13
www.simons13.com

ABSTRACT

The concept of seismogenic asperities and aseismic barriers has become a useful paradigm within which to understand the seismogenic behavior of major faults. Since asperities and barriers can be thought of as defining the potential rupture area of large megathrust earthquakes, it is thus important to identify their respective spatial extents, constrain their temporal longevity, and to develop a physical understanding for their behavior. Space geodesy is making critical contributions to the identification of slip asperities and barriers but progress in many geographical regions depends on improving the accuracy and precision of the basic measurements. This thesis begins with technical developments aimed at improving satellite radar interferometric measurements of ground deformation whereby we introduce an empirical correction algorithm for unwanted effects due to interferometric path delays that are due to spatially and temporally variable radar wave propagation speeds in the atmosphere. In chapter 2, I combine geodetic datasets with complementary spatio-temporal resolutions to improve our understanding of the spatial distribution of crustal deformation sources and their associated temporal evolution – here we use observations from Long Valley Caldera (California) as our test bed. In the third chapter I apply the tools developed in the first two chapters to analyze postseismic deformation associated with the 2010 Mw=8.8 Maule (Chile) earthquake. The result delimits patches where afterslip occurs, explores their relationship to coseismic rupture, quantifies frictional properties associated with inferred patches of afterslip, and discusses the relationship of asperities and barriers to long-term topography. The final chapter investigates interseismic deformation of the eastern Makran subduction zone by using satellite radar interferometry only, and demonstrates that with state-of-art techniques it is possible to quantify tectonic signals with small amplitude and long wavelength. Portions of the eastern Makran for which we estimate low fault coupling correspond to areas where

bathymetric features on the downgoing plate are presently subducting, whereas the region of the 1945 M=8.1 earthquake appears to be more highly coupled.

TABLE OF CONTENTS

LIST OF ILLUSTRATIONS

Number *Page*

LIST OF TABLES

Number *Page*

Introduction

Determining the spatial extent and temporal evolution of seismic ruptures, as well as the physical parameters controlling their extent and locations, has been a theme in earthquake physics over the past three decades. It is generally observed that large earthquakes consist of subevents, relatively compact patches with locally high slip, called 'asperities.' The term "seismic asperity" was first defined by *Kanamori* [1978] to describe "*geometrical asperities, heterogeneities of the frictional strength or a combination* (of both)" on the fault plane. A complementary concept is that of a "barrier," defined as the region that does not fail during the mainshock [*Das and Aki*, 1977; *Kanamori*, 1986]. The asperity and barrier models were originally two separate concepts used in the context of dynamic failure properties [*Lay et al.*, 1982]. However, these concepts are now frequently combined to describe spatial, mainly along-strike variations of seismic and aseismic regions on the subduction interface. The spatial distribution of asperities and barriers may potentially bound the rupture area and moment release for future large earthquakes; their temporal evolution may help define any relationship between a single seismic cycle and long-term geologic features. The underlying controls for this heterogeneity in style of fault slip are directly related to the fundamental physical properties of the subduction zone. Imaging the spatial distribution of seismic asperities and zones of aseismic creep is therefore essential to advance our understanding of the seismic behavior of faults and governing physics.

One model for the control on seismogenesis in subduction zones proposes that seismic decoupling occurs "*when the normal stress at the frictional interface is decreased by an amount sufficient to cross the friction stability transition*" [*Scholz and Campos*, 1995; 2012]. In this model, the degree of coupling is controlled by variations of normal stress on

the subduction interface. More explicitly, it states that shear tractions on the fault are mainly dependent on the effective normal stresses. *Scholz and Campos* [1995] use this model to predict the seismogenic behaviors across different subduction zones, although notable exceptions exist [*Scholz and Campos*, 2012].

Another model proposes a different hypothesis regarding the relationship between the state of stress on the megathrust and seismogenic behavior. This model suggests that "*spatial variations in frictional properties on the plate interface control trench-parallel variations in fore-arc topography, gravity, and seismogenic behavior*" [*Song and Simons*, 2003] and that "*forearc basins may be useful indicators of long-term seismic moment release*" [*Wells et al.*, 2003] (although in *Wells et al.* [2003] they attribute this relationship to subduction erosion). *Song and Simons* [2003] observed strong correlation of negative gravity and topography anomalies with seismogenic patches in large earthquakes, and related the distribution of seismic asperities within individual subduction zones to regions of increased shear traction. They argued that since negative gravity and topography anomalies are associated with decreased normal stress, the regions of shear traction increase are more likely due to increases in the effective coefficient of friction, although normal tractions may also modulate the shear tractions. This model is consistent with the inferred slip distribution of most large earthquakes; but again, exceptions also exist (e.g., the 2005 Mw 8.7 Nias in Sumatra and the 2011 Mw 9.0 Tohoku-oki in Japan).

Scholz and Campos [1995] focused on differentiating relatively coupled and uncoupled subduction zones on a global scale, whereas *Song and Simons* [2003] focused on intra-arc variations. However, *Scholz and Small* [1997] associated large subducted seamounts with increased seismic coupling and thus brought the normal-stress hypothesis from the global scale down to the smaller scale discussion of variations within a single subduction zone.

Thus, *Scholz and Campos* [1995] and *Song and Simons* [2003] may represent end-member models. Before delving into these models in detail, it is important to recognize ongoing controversies associated with the role of commonly found bathymetric features: subducting seamounts, subducting fracture zones, and fore-arc depressions.

Seamounts

Many studies infer a strong correlation between subducted seamounts and either seismic asperities (e.g., *Ichinose et al.*, [2007] for the 1964 Alaska earthquake) or barriers (e.g.. *Perfettini et al.* [2010] and *Chlieh et al.* [2011] for the role of the Nazca ridge), whereas many other studies reveal ambiguous or even opposite correlations. For example, recent large interplate earthquakes seem to nucleate near or on patches with high P wave velocities that are interpreted as subducted oceanic ridges, including the 2010 Mw=8.8 Maule earthquake along the south-central Chile megathrust [*Hicks et al.*, 2012], and the 2011 Mw=9.1 Tohoku-Oki earthquake along the Japan Trench [*Zhao et al.*, 2011]. A similar phenomenon has been observed for smaller earthquakes. Along the southern segment of the Japan Trench, repeating earthquakes of intermediate magnitudes (M ~ 7) were found to occur on the downdip side of a subducted seamount [*Mochizuki et al.*, 2008]. Opposite correlations were found even along the same subduction zone. The subducted paleo-Zenisu ridge along the Tokai segment of the Nankai Trough was correlated to the highly coupled patches obtained from geodetic studies [*Kodaira et al.*, 2003, 2004], but on the same megathrust to the south, the subducted seamount off Cape Muroto was considered as a barrier that deflected coseismic slip in the 1946 Ms=8.2 Nankaido earthquake [*Baba et al.*, 2002; *Kodaira et al.*, 2000, 2002].

Various attempts have been made to explain how seamount subduction influences plate coupling. Analogue models suggest that the dense fracture network generated by seamount subduction would favor fluid expulsion and induce a decrease in the fluid pressure and effective basal friction, possibly leading to lower coupling [*Dominguez et al.*, 2000]. This conclusion is further supported by the complexity of moment rate functions for events in areas of subducting seamounts in Costa Rica [*Wang and Bilek*, 2011].

Yang et al. [2012] numerically modeled a seamount as a strong patch of high effective normal stress within a rate-and-state friction subduction zone setting. Their result suggests that a seamount may act as a rupture barrier whose efficiency depends on both the increase of effective normal stress and the seamount-to-trench distance. Whenever the stress state becomes favorable, ruptures can also nucleate on the same seamount. This numerical model may explain many of the past controversies, although the model does not associate seamounts with any specific rate-and-state frictional properties, and therefore how these properties may influence the asperity and barrier effect of a seamount remains unknown.

Fracture Zones

The small number of studies investigating the role of subducting fracture zones suggest a strong correlation between these regions and low fault coupling. Examples include the Investigator fracture zone in Sumatran megathrust [*Chlieh et al.*, 2008; *Lange et al.*, 2010], the Mocha and Valdivia fracture zone in the South-Central Chile subduction zone [*Moreno et al.*, 2011], and the Nazca fracture zone in southern Peru [*Chlieh et al.*, 2011]. Systematic studies of the South American trench suggest a strong correlation between bathymetric

highs (mostly fracture zones with some ridges) on the downgoing plate and rupture extents of large earthquakes [*Carena* 2011; *Contreras-Reyes and Carrizo*, 2011], while the exact mechanism is still debated. Some consider that incoming fracture zones may enhance the flux of water into the subduction zone and may induce pore pressure changes or hydration and hence serpentinization of ultramafic rocks on the subducting plate [*Chlieh et al.*, 2008; *Contreras-Reyes et al.*, 2008], both leading to variations in the frictional behavior on the plate interface [*Escartin et al.*, 1997], while others propose that the bathymetric steps across the fracture zone constitute a major geometric control over the rupture extent, similar to the lateral ramps associated with crustal faults [*Carena* 2011].

Fore-arc Depressions

The correlation of gravity lows and topographic depression with seismic asperities is the basis of the *Song and Simons* [2003] model and is supported by many observations [*Wells et al.*, 2003]. This correlation is manifested in dynamic Coulomb wedge models [*Wang and Hu*, 2006] and by analogous sandbox models [*Rosenau and Oncken*, 2009]. Several studies also show correlations between the down-dip base of the strongly coupled seismogenic zone and the coastline position [*Ruff and Tichelaar*, 1996; *Loveless et al.*, 2010; *Sladen et al.*, 2010; *Béjar-Pizarro et al.*, 2013], suggesting a relationship between the frictional properties on the megathrust and the long-term evolution of the entire fore-arc. However, two obvious and troubling exceptions to the *Song and Simons* [2003] model, the 2005 Mw=8.7 Nias and 2011 Mw=9.0 Tohoku earthquakes, show rupture extents that correlate strongly with positive topography and gravity anomalies. Thus far there is no satisfactory explanation for these exceptions.

From a Geodetic Perspective

The ambiguous evidence associated with the *Scholz and Campos* [1995] and *Song and Simons* [2003] models indicates that the underlying physical process is more complicated than a simple dichotomy between the normal-stress dominant and frictional-property dominant interplate coupling. It is likely that the two models are end members over a wide spectrum, in which two or more major factors contribute to controlling the seismogenic process. Our ability to disentangle the multiple potential controls on seismogenic behavior of the megathrust relies intimately on our ability to reliably resolve the distribution of coseismic and aseismic fault slip on subduction megathrusts. As elucidated by several studies [e.g. *Wells et al.*, 2003; *Singh et al.*, 2011], some of the aforementioned disputes may result from the insufficient resolution of coseismic slip or interseismic coupling models and/or plate interface topography due to poor data quality, especially for earlier historic events.

Part of this thesis contributes to the discussion by improving the resolution of geodetic measurements. The first half of the thesis focuses on methodological developments. In chapter 1, I describe a new algorithm to correct for differential atmospheric delays in Interferometric Synthetic Aperture Radar (InSAR) observations of crustal deformation. This multi-scale approach allows a robust estimate of the topographically-correlated tropospheric delays when no other correction method is available. In chapter 2, I implement a joint inversion method by using ground-based geodetic measurements, continuous in time but sparse in space, and the satellite images, sparse in time but continuous in space. Joint inversion with these datasets of complementary spatiotemporal

resolution can provide detailed mapping of the source parameters and the associated temporal evolution. The inversion is carried out via a Principal Component Analysis based Inversion Method (PCAIM) [*Kositsky and Avouac*, 2010].

The second half of the thesis focuses on specific case studies. In chapter 3, I apply the techniques described in the first two chapters to infer the space-time evolution of postseismic deformation associated with the 2010 Mw=8.8 Maule earthquake, south-central Chile. Using a combination of InSAR and GPS-derived constraints, we are able to distinguish between patches of different frictional properties on the megathrust and to further quantify these properties. In chapter 4, I shift the focus to the eastern Makran subduction zone, a more challenging target from the perspective of present-day geodesy. For this region, I try to constrain the pattern of interseismic deformation using only InSAR observations. This target is challenging given a sub-optimal radar viewing geometry and extensive atmospheric path delays (related to the East Asian monsoon) which results in a low signal-to-noise ratio. I demonstrate that despite all these difficulties, with proper image correction and processing procedures, it is possible to isolate the signal due to interseismic deformation. Using these observations, I provide the first estimate of coupling patterns along this subduction zone along with first order estimates of cumulative moment deficits since the last event.

References of Introduction

Baba, T., Y. Tanioka, P. R. Cummins, and K. Uhira (2002), The slip distribution of the 1946 Nankai earthquake estimated from tsunami inversion using a new plate model, *Phys. Earth Planet. Inter.*, *132*(1-3), 59-73.

Béjar-Pizarro, M., A. Socquet, R. Armijo, D. Carrizo, J. Genrich, and M. Simons (2013), Andean structural control on interseismic coupling in the North Chile subduction zone, *Nat. Geosci.*, doi: 10.1038/ngeo1802.

Carena, S. (2011), Subducting-plate Topography and Nucleation of Great and Giant Earthquakes along the South American Trench, *Seismol. Res. Lett.*, *82*(5), 629-637, doi: 10.1785/gssrl.82.5.629.

Chlieh, M., J. P. Avouac, K. Sieh, D. H. Natawidjaja, and J. Galetzka (2008), Heterogeneous coupling of the Sumatran megathrust constrained by geodetic and paleogeodetic measurements, *J. Geophys. Res.*, *113*(B5), B05305, doi: 10.1029/2007jb004981.

Chlieh, M., H. Perfettini, H. Tavera, J.-P. Avouac, D. Remy, J.-M. Nocquet, F. Rolandone, F. Bondoux, G. Gabalda, and S. Bonvalot (2011), Interseismic coupling and seismic potential along the Central Andes subduction zone, *J. Geophys. Res.*, *116*(B12), B12405, doi: 10.1029/2010JB008166.

Contreras-Reyes, E., and D. Carrizo (2011), Control of high oceanic features and subduction channel on earthquake ruptures along the Chile-Peru subduction zone, *Phys. Earth Planet. Inter.*, *186*(1-2), 49-58.

Contreras-Reyes, E., I. Grevemeyer, E. R. Flueh, and C. Reichert (2008), Upper lithospheric structure of the subduction zone offshore of southern Arauco peninsula, Chile, at ~38°S, *J. Geophys. Res.*, *113*(B7), B07303, doi: 10.1029/2007JB005569.

Das, S., and K. Aki (1977), Fault plane with barriers - versatile earthquake model, *J. Geophys. Res.*, *82*(36), 5658-5670, doi: 10.1029/JB082i036p05658.

Dominguez, S., J. Malavieille, and S. E. Lallemand (2000), Deformation of accretionary wedges in response to seamount subduction: Insights from sandbox experiments, *Tectonics*, *19*(1), 182-196, doi: 10.1029/1999tc900055.

Escartin, J., G. Hirth, and B. Evans (1997), Nondilatant brittle deformation of serpentinites: Implications for Mohr-Coulomb theory and the strength of faults, *J. Geophys. Res.*, 102(B2), 2897-2913, doi: 10.1029/96jb02792.

Hicks, S. P., A. Rietbrock, C. A. Haberland, I. M. A. Ryder, M. Simons, and A. Tassara (2012), The 2010 Mw 8.8 Maule, Chile earthquake: Nucleation and rupture propagation controlled by a subducted topographic high, *Geophys. Res. Lett.*, *39*, doi: 10.1029/2012gl053184.

Ichinose, G., P. Somerville, H. K. Thio, R. Graves, and D. O'Connell (2007), Rupture process of the 1964 Prince William Sound, Alaska, earthquake from the combined inversion of seismic, tsunami, and geodetic data, *J. Geophys. Res.*, *112*(B7), doi: 10.1029/2006jb004728.

Kanamori, H. (1978), Use of seismic radiation to infer source parameters, USGS Open File Report 78-380, 283-318 pp.

Kodaira, S., N. Takahashi, A. Nakanishi, S. Miura, and Y. Kaneda (2000), Subducted seamount imaged in the rupture zone of the 1946 Nankaido earthquake, *Science*, *289*(5476), 104-106, doi: 10.1126/science.289.5476.104.

Kodaira, S., A. Nakanishi, J. O. Park, A. Ito, T. Tsuru, and Y. Kaneda (2003), Cyclic ridge subduction at an inter-plate locked zone off central Japan, *Geophys. Res. Lett.*, *30*(6), doi: 10.1029/2002gl016595.

Kodaira, S., T. Iidaka, A. Kato, J. O. Park, T. Iwasaki, and Y. Kaneda (2004), High pore fluid pressure may cause silent slip in the Nankai Trough, *Science*, *304*(5675), 1295-1298, doi: 10.1126/science.1096535.

Kodaira, S., et al. (2002), Structural factors controlling the rupture process of a megathrust earthquake at the Nankai trough seismogenic zone, *Geophys. J. Int.*, *149*(3), 815-835.

Kositsky, A., and J. P. Avouac (2010), Inverting geodetic time-series with a principal component analysis-based inverison method (PCAIM), *J. Geophys. Res.*, *115*, B03401, doi: 10.1029/2009JB006535.

Lange, D., F. Tilmann, A. Rietbrock, R. Collings, D. H. Natawidjaja, B. W. Suwargadi, P. Barton, T. Henstock, and T. Ryberg (2010), The fine structure of the subducted Investigator Fracture Zone in western Sumatra as seen by local seismicity, *Earth Planet. Sci. Lett.*, *298*(1-2), 47-56, doi: 10.1016/j.epsl.2010.07.020.

Lay, T., H. Kanamori, and L. Ruff (1982), The asperity model and the nature of large subduction zone earthquakes, *Earthquake Pred. Res.*, *1*(1), 3-71.

Loveless, J. P., M. E. Pritchard, and N. Kukowski (2010), Testing mechanisms of subduction zone segmentation and seismogenesis with slip distributions from recent Andean earthquakes, *Tectonophysics*, *495*(1–2), 15-33, doi: 10.1016/j.tecto.2009.05.008.

Mochizuki, K., T. Yamada, M. Shinohara, Y. Yamanaka, and T. Kanazawa (2008), Weak interplate coupling by seamounts and repeating M~7 earthquakes, *Science*, *321*(5893), 1194-1197, doi: 10.1126/science.1160250.

Moreno, M., et al. (2011), Heterogeneous plate locking in the South-central Chile subduction zone: Building up the next great earthquake, *Earth Planet. Sci. Lett.*, *305*(3-4), 413-424.

Perfettini, H., et al. (2010), Seismic and aseismic slip on the Central Peru megathrust, *Nature*, *465*(7294), 78-81, doi: 10.1038/nature09062.

Rosenau, M., and O. Oncken (2009), Fore-arc deformation controls frequency-size distribution of megathrust earthquakes in subduction zones, *J. Geophys. Res.*, *114*, doi: 10.1029/2009jb006359.

Ruff, L. J., and B. W. Tichelaar (1996), What controls the seismogenic plate interface in subduction zones?, in *Subduction Top to Bottom*, edited, pp. 105-111, AGU, Washington, DC.

Scholz, C. H., and J. Campos (1995), On the mechanism of seismic decoupling and back-arc spreading at subduction zones, *J. Geophys. Res.*, *100*(B11), 22103-22115, doi: 10.1029/95jb01869.

Scholz, C. H., and C. Small (1997), The effect of seamount subduction on seismic coupling, *Geology*, *25*(6), 487-490, doi: 10.1130/0091-7613(1997)025<0487:TEOSSO>2.3.CO;2.

Scholz, C. H., and J. Campos (2012), The seismic coupling of subduction zones revisited, *J. Geophys. Res.*, *117*, doi: 10.1029/2011jb009003.

Singh, S. C., et al. (2011), Aseismic zone and earthquake segmentation associated with a deep subducted seamount in Sumatra, *Nat. Geosci.*, *4*(5), 308-311, doi: 10.1038/ngeo1119.

Sladen, A., H. Tavera, M. Simons, J. P. Avouac, A. O. Konca, H. Perfettini, L. Audin, E. J. Fielding, F. Ortega, and R. Cavagnoud (2010), Source model of the 2007 M-w 8.0 Pisco, Peru earthquake: Implications for seismogenic behavior of subduction megathrusts, *J. Geophys. Res.*, *115*, B02405, doi: 10.1029/2009JB006429.

Song, T. R. A., and M. Simons (2003), Large trench-parallel gravity variations predict seismogenic behavior in subduction zones, *Science*, *301*(5633), 630-633, doi: 10.1126/science.1085557.

Wang, K., and Y. Hu (2006), Accretionary prisms in subduction earthquake cycles: The theory of dynamic Coulomb wedge, *J. Geophys. Res.*, *111*(B6), B06410, doi: 10.1029/2005jb004094.

Wang, K. L., and S. L. Bilek (2011), Do subducting seamounts generate or stop large earthquakes?, *Geology*, *39*(9), 819-822, doi: 10.1130/g31856.1.

Wells, R. E., R. J. Blakely, Y. Sugiyama, D. W. Scholl, and P. A. Dinterman (2003), Basin-centered asperities in great subduction zone earthquakes: A link between slip, subsidence, and subduction erosion?, *J. Geophys. Res.*, *108*(B10), 2507, doi: 10.1029/2002JB002072.

Yang, H. F., Y. J. Liu, and J. Lin (2012), Effects of subducted seamounts on megathrust earthquake nucleation and rupture propagation, *Geophys. Res. Lett.*, *39*, doi: 10.1029/2012gl053892.

Zhao, D. P., Z. C. Huang, N. Umino, A. Hasegawa, and H. Kanamori (2011), Structural heterogeneity in the megathrust zone and mechanism of the 2011 Tohoku-oki earthquake (Mw 9.0), *Geophys. Res. Lett.*, *38*, doi: 10.1029/2011gl048408.

Chapter 1

A MULTISCALE APPROACH TO ESTIMATING TOPOGRAPHICALLY CORRELATED PROPAGATION DELAYS IN RADAR INTERFEROGRAMS

Originally published in Lin, Y.-N. N., M. Simons, E. A. Hetland, P. Muse, and C. DiCaprio (2010), A multiscale approach to estimating topographically correlated propagation delays in radar interferograms, *Geochem. Geophys. Geosyst.*, 11(9), Q09002, doi: 10.1029/2010GC003228.

Abstract

When targeting small amplitude surface deformation, using repeat orbit Interferometric Synthetic Aperture Radar (InSAR) observations can be plagued by propagation delays, some of which correlate with topographic variations. These topographically-correlated delays result from temporal variations in vertical stratification of the troposphere. An approximate model assuming a linear relationship between topography and interferometric phase has been used to correct observations with success in a few studies. Here, we present a robust approach to estimating the transfer function, K, between topography and phase that is relatively insensitive to confounding processes (earthquake deformation, phase ramps from orbital errors, tidal loading, etc.). Our approach takes advantage of a multiscale perspective by using a band-pass decomposition of both topography and observed phase. This decomposition into several spatial scales allows us to

determine the bands wherein correlation between topography and phase is significant and stable. When possible, our approach also takes advantage of any inherent redundancy provided by multiple interferograms constructed with common scenes. We define a unique set of component time intervals for a given suite of interferometric pairs. We estimate an internally consistent transfer function for each component time interval, which can then be recombined to correct any arbitrary interferometric pair. We demonstrate our approach on a synthetic example and on data from two locations: Long Valley Caldera, California, which experienced prolonged periods of surface deformation from pressurization of a deep magma chamber, and one coseismic interferogram from the 2007 Mw 7.8 Tocopilla earthquake in northern Chile. In both examples, the corrected interferograms show improvements in regions of high relief, independent of whether or not we pre-correct the data for a source model. We believe that most of the remaining signals are predominately due to heterogeneous water vapor distribution that requires more sophisticated correction methods than those described here.

1.1 Introduction

Interferometric Synthetic Aperture Radar (InSAR) images are widely used in the analysis of tectonic deformation, magmatic activity, flow of glaciers, and other surface deformation processes (for reviews, see *Massonnet et al.* [1994], *Burgmann et al.* [2000], *Hanssen* [2001], *and Simons and Rosen* [2007]). These observations are frequently plagued by spatially heterogeneous propagation delays between the radar platform and the ground. Propagation delays have three major sources: wet delays, hydrostatic delays and ionosphere effects. For microwaves, the refractivity changes due to the dipole components

of water vapor, also known as "wet delays," contribute the most to the neutral atmospheric propagational delays [*Bevis et al.,* 1992]. Recent study also shows that hydrostatic delays, which depends on the pressure to temperature ratio, vary significantly at low elevation and cannot be neglected [*Doin et al.,* 2009]. Ionospheric effects result from spatio-temporal variations in ionospheric electron density. These effects are in general more obvious in the higher latitude and in the L-band SAR data than the C-band SAR, due to the dispersive nature of the atmospheric medium [*Gray et al.,* 2000]. Wet delays and hydrostatic delays may strongly obscure tectonic signals when the signal amplitude is small - as is frequently the case with interseismic deformation. For example, in two-pass interferometry, a 20% change in humidity may result in 10 cm of deformation error [*Zebker et al.,* 1997], thereby compromising the effectiveness for InSAR to detect mm-to-cm scale deformation. Wet delays and hydrostatic delays are non-dispersive and therefore the multi-wavelength approach generally used to correct for GPS ionospheric biases cannot be applied to tackle this problem [*Zebker et al.,* 1997].

One way to mitigate the tropospheric delay problem is to average N independent interferograms, since the neutral atmospheric signals are uncorrelated over timescales longer than 1 day [*Zebker et al.,* 1997*; Emardson et al.,* 2003]. This simple technique can reduce the variance of atmospheric errors by a factor of $\sqrt{N}$. The averaging method is practical and effective when trying to estimate secular rates from a large number of interferometric pairs. However, if time-dependent deformation is expected or only a few interferograms are available, the stacking approach is no longer useful. One way to mitigate the tropospheric delays in a time series is to apply filtering techniques, such as the temporal plus spatial filters suggested by *Berardino et al.* [2002]. The choice of filter in

this approach is subjective, leading to the concern of smoothing out signals over the same time scales as the noise.

Other studies propose more complicated but direct methods for estimating and removing the effects of wet delays. Proposed methods include use of GPS data [*Onn and Zebker,* 2006] and radiometric data to produce zenith path delay difference maps for InSAR atmospheric correction, for instance using either MODIS (MODerate-resolution Imaging Spectroradiometer) [*Li et al.,* 2005, 2006a], or MERIS (MEdium Resolution Image Spectrometer, for ENVISAT system only) [*Li et al.,* 2006b, 2006c]. Other approaches use weather models together with radiometric data to generate an instant water vapor map, such as MERIS with MM5 (Mesoscale Meteorological Model) [*Puysségur et al.,* 2007], or use a weather model only to predict atmospheric delays [*Foster et al.,* 2006]. These imagery-based or model-based approaches may provide estimates of water vapor distribution from independent data sources or models at the time the SAR image was acquired. However, imagery-based approaches have limited application for older SAR images. MODIS and MERIS were launched in 1999 and 2002, respectively. Radiometric systems require solar illumination, so they can not be used to correct for SAR images acquired at night. Some calibration statement is also necessary for the user to accommodate the radiometric data to different study areas. GPS-based approaches are limited by the density and existence of GPS stations in some remote areas. Moreover, the efficacy of modeling-based approaches are still debated, especially the extent to which they consistently reduce or add noise to interferometric observations.

The approach proposed in this study, compared to the aforementioned methods, is relatively simple and not limited by the availability of other independent data. Our

approach focuses on mitigating the effects of the time-variable vertically stratified component of the atmospheric delays, as described by *Hanssen* [2001]. Correction of the static component is relatively straightforward and efficient, and in some cases can be very effective. In a study of the Lake Mead area, Nevada, *Cavalié et al.* [2007] showed that static tropospheric delays can be estimated by analyzing the correlation between phase and topography. (To be more accurate, it is a correlation between phase change and topography, but for simplicity we use "phase" to refer to "phase change"). This method, however, does not always work well because in some cases phase does not seem linearly related to topography due to multiple tectonic/non-tectonic sources and confounding effects of delays due to turbulent atmospheric circulation.

Our study proposes an improved method that is less sensitive to all these confounding factors. We use a multiscale approach to estimate variations in topographically-correlated propagation delays. This approach is based on the same assumption made by earlier works of a linear relationship between phase and topography. We first test our approach in a synthetic example, and validate that in regions where there is no strong turbulent mixing, this approach can serve as the first order correction. We then demonstrate our method with examples from the Long Valley Caldera in California, and northern Chile.

1.2 A Multiscale Approach to Estimating Topographically Correlated Delays

1.2.1 Model

Correlation between range change and topography results from the variation of the refractivity of the atmosphere along the vertical due to changes in pressure (P),

temperature (T), humidity and water vapor content in the lowermost atmosphere between two SAR acquisitions [*Hanssen*, 2001]. For a vertically stratified troposphere model, if elevation changes across the scene, propagation delays vary at different elevation with a rate increasing with water vapor content and P/T ratio [*Doin et al.*, 2009]. In contrast to the effect of turbulent mixing, this vertical stratification is considered static over a given area throughout a certain period of time. As the concentration of water vapor generally decreases exponentially with elevation, the theoretical delay curve is an exponential function of elevation [*Delacourt et al.*, 1998]. In an interferogram subject to only static tropospheric delays, the signal is the difference between the delay curves for two individual SAR acquisitions. If we take a Taylor series expansion over the resultant exponential function, and ignore the second order and higher terms, we can derive a simple linear relation

$$\Delta\varphi = b + Kh \tag{1-1}$$

where b is a bias term and K is the transfer function between topography (h) and phase ($\Delta\varphi$) [*Cavalié et al.*, 2007]. This simple linear model works for most weather conditions, except for extraordinary cases such as inverted or non-monotonic tropospheric stratifications. The transfer function, K, is best determined by a global rather than a local linear regression, since the phase/elevation relationship may have local trade-offs with the deformation/elevation relationship [*Cavalié et al.*, 2007]. This transfer function is therefore considered as a scene-wide property rather than a value that changes heterogeneously across the scene. However, global correlations may result in large uncertainties in the transfer function, making it difficult to define the linear relationship, thus emphasizing the need for a robust method for determining K.

1.2.2 Estimation Approach

Our approach explicitly recognizes that various length scales, λ, should have different sensitivities to different sources of confounding noises. For example, very large λ (>100 km) may be more sensitive to other processes such as tidal loading [*DiCaprio and Simons*, 2008] or orbital error, whereas the smallest λ (≤2 km) may not be very sensitive to larger-scale tropospheric signals. Surface deformation resulting from tectonic, magmatic or glacial processes also has a rich scale-dependent spectrum. In the presence of all these confounding factors, given that K is assumed to be a global property, there should be a reasonable range of λ in which the value of K almost stays constant and is independent of λ. Therefore, we can take advantage of the multiscale perspective to robustly estimate a spatially constant K which is relatively insensitive to confounding processes.

To begin with, we decompose both topography and interferogram into different length scales (Figure 1.1). We generate band-passed images by applying a series of Gaussian filters with different spatial scales and taking the difference between two neighboring scales. We choose filter limits that scale with integer powers of two (in units of integer numbers of pixels). To properly represent the amount of information carried in each channel, we resample them according to the Shannon - Nyquist sampling theorem. We use the resampled point sets from selected band-pass channels to estimate K.

Band-pass (BP) components usually show clearer and more constant linear relationships between topography and phase than high-pass (HP) and low-pass components (LP). The high-pass and low-pass components are therefore excluded from the estimation of K. Next, we rewrite equation (1) as

$$\Delta\varphi(\lambda_i) = b_{igram} + K_{igram} h(\lambda_i) \tag{1-2}$$

where $h(\lambda_i)$ and $\Delta\varphi(\lambda_i)$ are the ith band-passed components of h and $\Delta\varphi$. b_{igram} and K_{igram} denote the bias term and transfer function of each interferogram. When multiple interferograms are available for the same region we must estimate a consistent set of values for K. We do so by defining a unique set of component time intervals, ΔT, for a suite of interferograms (Figure 1.2). Each ΔT has a corresponding $b_{\Delta T}$ and $K_{\Delta T}$, which represents the internally consistent b and K changes over this time interval. Next we construct the linear system

$$\begin{bmatrix} h_1(\lambda_1) & h_2(\lambda_2) & 0 & \cdots & 0 & 1 & 1 & 0 & \cdots & 0 \\ h_1(\lambda_2) & h_2(\lambda_2) & 0 & \cdots & 0 & 1 & 1 & 0 & \cdots & 0 \\ & & \vdots & & & & & \vdots & & \\ h_1(\lambda_n) & h_2(\lambda_n) & 0 & \cdots & 0 & 1 & 1 & 0 & \cdots & 0 \\ & & \vdots & & & & & \vdots & & \\ 0 & 0 & h_m(\lambda_n) & \cdots & h_m(\lambda_n) & 0 & 0 & 1 & \cdots & 1 \end{bmatrix} \begin{bmatrix} K_{\Delta T_1} \\ K_{\Delta T_2} \\ K_{\Delta T_3} \\ \vdots \\ K_{\Delta T_p} \\ b_{\Delta T_1} \\ b_{\Delta T_2} \\ b_{\Delta T_3} \\ \vdots \\ b_{\Delta T_p} \end{bmatrix} = \begin{bmatrix} \Delta\varphi_1(\lambda_1) \\ \Delta\varphi_1(\lambda_2) \\ \\ \Delta\varphi_1(\lambda_n) \\ \\ \Delta\varphi_m(\lambda_n) \end{bmatrix} \tag{1-3}$$

where $h_m(\lambda_n)$ represents the n selected decomposed bands of topography corresponding to m interferograms, and $\Delta\varphi_m(\lambda_n)$ represents the n selected decomposed bands of m interferograms, while $K_{\Delta T_p}$ and $b_{\Delta T_p}$ represent the transfer function and bias term for the pth ΔT. By solving this large system of equations, we can derive both the transfer function and bias term at the same time, making the whole system internally consistent.

We assume that there exist minor outliers in the data due to unwrapping errors or other measurement or processing defects. Under this assumption, an outlier-resistant L1-norm regression is a better choice than least-squares regression. In practice, we use a convex optimization algorithm (available online as Matlab package cvx) (M. Grant and S. Boyd, CVX: Matlab software for disciplined convex programming, 2009, available at http://stanford.edu/boyd/cvx) for L1 regression to derive the best solution of $K_{\Delta T}$ [*Boyd and Vandenberghe*, 2004]. Since there is no analytical equation to define model errors of L1-norm regression, we estimate the standard error of $K_{\Delta T}$ ($\sigma_{K_{\Delta T}}$) using a bootstrapping technique. Given that InSAR data are correlated in space, ideally we should include the full covariance matrix into our regressions. However, because we apply a multiscale decomposition by using a series of Gaussian filters, there is an issue of transforming the covariance matrix into each band-pass channel. The details are beyond the scope of this study, so we ignore data covariance in our regressions. The reader should keep in mind that the standard errors of *K* may be larger than what we present if the full covariance is considered. Finally, we form the time series of K_T by choosing an arbitrary origin (we use zero here) for the whole series and sequentially adding up all $K_{\Delta T}$. Once the time series of the transfer function K_T is formed, it is easy to determine the K_{igram} of an interferogram from any arbitrary pair of SAR scenes.

1.2.3 Synthetic Test

Our synthetic test is based on the inflation event between 1997 and 1998 in the Long Valley Caldera, California (Figure 1.3) [*Langbein*, 2003]. The components considered in the

synthetic interferogram include tectonic (magmatic inflation), static topographically-correlated delays, turbulent mixing and ramp signals. We construct the tectonic signals by using a point source of inflation in an elastic halfspace [*Mogi*, 1958]. We assume a source depth at 10.5 km, consistent with *Fialko et al.* [2001]. As for turbulent mixing signals, several pre-determined noise covariance functions have been proposed, such as a power law or an exponential decay [*Hanssen*, 2001; *Emardson et al.*, 2003; *Lohman and Simons*, 2005]. Here we chose the expression of *Lohman and Simons* [2005]

$$C_d^{ij} = e^{-L_{ij}/L_c} \tag{1-4}$$

$$n_c = vu^{1/2} n_n \tag{1-5}$$

where C_d^{ij} and L_{ij} are the covariance and distance between the *i*th and *j*th points, L_c is the scale distance, n_n is uncorrelated noise, and v and u are the matrices of eigenvectors and eigenvalues of C_d, respectively. We assume a ramp that varies bilinearly in space. The constructed ramp has a major gradient in the NW-SE direction, mimicking possible effects due to orbital error or horizontal water vapor gradients from north to south.

There are three major parameters that we vary to see how they influence the estimate of *K*. The first one is the standard deviation σ of non-correlated noise n_n. The value is set to be between 0 and 5 cm. The second parameter is the amplitude of the ramp. A small ramp has values between −0.5 to 0.5 cm, close to the amplitude of tectonic signals. A large ramp has amplitude 10 times the small ramp. The last parameter is the characteristic length scale, L_c, of turbulent signals. L_c is the distance over which the noise covariance decays by one fold.

Estimates from real observations suggest a scale distance usually between 5 and 30 km [*Lohman and Simons*, 2005]. We test values of 5 km, 15 km and 30 km.

Figure 1.4 shows one realization of our synthetic interferograms. We project all the components into the line-of-sight direction and combine them together. In total we generate 120 interferograms and retrieve K values from each of them by using our multiscale approach. We then compare our results with the K values derived from a full (not multiscale) interferogram-topography correlation, with either ramp retained or ramp removed (Figure 1.5). The results show that the multiscale approach gives a stable estimate of K values regardless of noise strength. For the cases where L_c = 5 km, K values slightly deviate to higher values from the true K as the noise σ increases, but are still within the error bars. In general, at greater noise levels, the multiscale approach tends to estimate transfer functions that are smaller than the real values. This tendency to under-estimate K means that the multiscale approach is a more conservative method, so that in most cases it will under-correct rather than overcorrect the topographically-correlated tropospheric signals.

We also considered the influence of phase ramps across the scene. K values estimated from the ramp-retained full-interferogram correlation method are generally, but not always, better than those estimated from the ramp-removed full interferogram correlation method. A sophisticated ramp removal approach may allow one to avoid some intertwining signals, such as using the region outside the tectonically influenced zone to estimate the ramp [*Cavalié et al.*, 2007]. In contrast to the full-interferogram approaches, the multiscale analysis is not sensitive to ramp magnitude and therefore no ramp removal is needed.

L_c also has some influence on the multiscale method. The K values retrieved using the multiscale approach seem to be more stable at larger L_c. To explain this phenomenon, we compare the decomposed turbulent signals of different L_c (Figure 1.6). At L_c = 5 km, turbulent signals have more evenly spread amplitudes in all decomposed bands. As L_c increases, turbulent signals become more concentrated in the long-wavelength channels. Therefore in general, at large L_c, estimation of K should be less influenced by turbulent mixing effects, but still depends on how the turbulent peaks and troughs randomly correlate to topography. In real cases, unfortunately, most turbulent signals are frequently related to topography. The user should hence keep in mind that the retrieved K is likely to be degraded from the "true" K, with the level of deviation depending on the characteristic length scale and amplitude (standard deviation) of turbulent signals.

To summarize the results from the synthetic test, we find that a multiscale approach provides a more robust way to estimate the transfer function, K. This approach is insensitive to phase ramps, and therefore can yield better estimates of K when orbital error or long-wavelength deformation signals are present. Of course, as just alluded to, there may be a slight deviation of K depending on the characteristic length scale and amplitude of turbulent signals.

1.3 Correcting Real Interferograms

We test the multiscale approach in two study areas. Our first example is the 1997–98 magmatic inflation episode in Long Valley Caldera, California. This example presents a relatively simple tectonic source, combined with complicated atmospheric turbulent

signals. We test the robustness of *K* by removing the magmatic inflation signals from the interferograms. We also use this example to emphasize the stability of our algorithm in the presence of large-amplitude turbulent noise. Our second example, the 2007 Tocopilla earthquake (northern Chile), has "rich" tectonic signals that cover a large area and wide range of wavelengths. We show how the *K* values may vary with scene sizes and comment on whether it is reasonable to correct a large-size interferogram with a unique value of *K*. Since this study focuses on estimating topographically-correlated tropospheric signals, we do not discuss in detail the geophysical aspects of the two study cases.

1.3.1 Long Valley Caldera

Long Valley Caldera has experienced two phases of volcanic unrest since 1989. The first phase started rapidly in 1989, and slowly decayed through the early 1990s. The second phase started slowly in mid-1997, climaxed in late 1997, and returned to quiescence by mid -1998. During the second phase, it first showed an exponential growth increase in mid-April, and an exponential growth decay in late November 1997, cumulating in ~10 cm of uplift [*Newman et al.*, 2001; *Hill et al.*, 2003; *Langbein*, 2003].

The only satellite that has acquisitions throughout the whole 1997–1998 Long Valley Caldera inflation episode is ERS. Unlike ENVISAT, ERS does not have any onboard device that measures water vapor content in real time. To remove troposphere-related delays, one may want to use GPS data instead to model the water vapor distribution in that area. Unfortunately most of the available permanent GPS stations were established in 2000. In

this case, our correction approach may serve as the best available tool to mitigate these static delays for older interferograms.

We analyzed 65 interferograms based on 24 ERS acquisitions between 1992 and 2006. We tried to minimize the number of interferograms according to several criteria: (1) the length of the perpendicular component of baseline ($B_{\perp}$) should be less than 300 m; (2) the date of acquisition should lie outside the winter season, according to snow precipitation records (Daily snow depth data of Rock Creek Lakes (RCK), California Data Exchange Center, Department of Water Resources, available at http://cdec.water.ca.gov/cgi-progs/staMeta?station_id=RCK); and (3) the difference in Doppler frequency between two acquisitions must be less than 900 Hz. The third criterion is particularly important, because the Doppler frequency starts to wander over a large range of values starting in 2001 [*Meadows et al.*, 2007].

We first carried out a multiscale decomposition of topography and interferograms with 720 m mean ground resolution. The length scales thus chosen, from low to high frequencies, are >44.5, 22.2–44.5, 11.1–22.2, 5.6–11.1, 2.8–5.6 and <2.8 km. As we assume that smaller length scales (l ≤ 2 km) may not be sensitive enough to larger-scale tropospheric signals, there is no need to use higher data ground resolution, which also saves computation time. Of course, once K is estimated, we can apply the correction to the full resolution interferogram. We then constructed and solved the linear system of equations (1-3). The time it takes to solve this linear system (65 interferograms) on an average PC is currently usually less than half an hour. We apply a bootstrapping technique [*Tichelaar and Ruff*, 1989] and derive the standard errors for $K_{\Delta T}$, with the average as 0.06 cm/km. Figure 1.7 shows the $K_{\Delta T}$ time series. Values of K_{igram} estimated from

$K_{\Delta T}$ are nearly identical to those estimated on an interferogram by interferogram basis, except for few outliers (Figure 1.8). After examining outlier interferograms individually, we found that these interferograms have larger areas with unwrapping errors. In this case our assumption that there are only minor unwrapping errors does not hold.

We tested the sensitivity of our multiscale approach to confounding tectonic signals. We modeled the 1997–1998 inflation episode by using a point inflation source [*Mogi*, 1958]. Source parameters are determined in the same way as in constructing synthetic interferograms. We assume that the source depth remains fixed during the whole inflation episode, with inflation volume as the only changing parameter. We then remove models from original interferograms, and carry out the multiscale decomposition and calculated the K_{igram} value again. The K_{igram} values thus derived are almost identical to the K_{igram} values derived before model removal (Figure 1.9). This real case test proves that the estimate of K by using the multiscale approach is robust. The full - interferogram correlation approach, by contrast, does not seem to be stable after the inflation model is removed from the interferogram.

This example also demonstrates significant influence of intermediate-wavelength turbulent disturbance, particularly near the center of the interferogram (Figure 1.9), where topography is not as high as the Sierra Nevada. This turbulent disturbance is prominent in multiple interferograms, probably due to the water vapor brought by the northerly or southerly prevailing winds along the Owens Valley [*Zhong et al.*, 2008]. The phase-topography plot for each band-pass channel of this interferogram shows large scatter (Figure 1.10b), similar to what we derive from synthetic test when turbulent noise (with

mid-to-large L_c) is high (Figure 1.10a). From what we have found through the synthetic test, our estimates of K are more likely to under-correct than over-correct the interferograms.

1.3.2 The 2007 Tocopilla Earthquake, Chile

The Mw 7.8 Tocopilla earthquake occurred on 14 November 2007 (15:41 UTC) in northern Chile. The epicenter is located 25 km south of the town of Tocopilla and 150 km north-northeast of the city of Antofagasta (Figure 1.11) [*Delouis et al.*, 2009]. The Global Centroid Moment Tensor (GCMT) catalog solution for the mainshock shows a centroid depth of 38 km and a focal mechanism of a low-angle nodal plane with reverse motion. The solution suggests that this event should be categorized as a subduction underthrusting earthquake occurring at the interface between the subducting Nazca plate and the overriding South American plate. The resultant tectonic signal therefore covers a large area (over 100 km × 500 km).

We obtained data from ENVISAT ASAR descending track 96 acquired on April 9, 2007 and December 10, 2007 (Figure 1.11). We assume that the interferogram made from these two SAR scenes is dominated by coseismic deformation signals. We use the aftershock distribution to construct the fault plane, and use a finite-fault inversion routine [*Ji et al.*, 2002a, 2002b] to invert for the slip on the fault plane with constraints from both the interferogram measurements. We then remove the modeled displacement field from the interferogram. We estimate K values with the model-retained and model removed interferograms, and find very close results: 0.43 ± 0.01 and 0.48 ± 0.01 cm/km (Figure

1.12). These two values do not fall into each other's 95% confidence interval, but this is likely due to the fact that we did not consider the full covariance matrix in our calculation, which is computationally expensive but gives larger and more reasonable values for standard errors [*Lohman and Simons*, 2005]. After correcting the topographically-correlated tropospheric signals by using these two *K* values, we clearly see that the phase gradient in the Andes (northern part of the interferogram) is reduced (Figures 1.12b and 1.12e). Compared with the multiscale correction result, the full-interferogram correlation removes even more of the gradient, but the derived *K* value is not stable, and in some regions there exists the possibility of over-correction (Figure 1.12f, near the northeastern corner of the interferogram). In the southernmost part of the interferogram near the Atacama Plateau, the phase increases after applying both corrections. It looks like on the original interferogram, there is positive phase-topography correlation, opposite to the trend in the Andes (Figure 1.12a). However, if we consider the phase change all the way from Antofagasta up to the Atacama Plateau, the phase decreases with elevation. Therefore, the *K* values derived from both methods are self consistent within the whole interferogram, and the correction result should be valid.

With an interferogram of such large scene size (120 × 590 km), we should consider the validity of using a single value for *K* to correct the whole interferogram. We test this idea by cropping the interferogram into various scene sizes and carrying out multiscale corrections individually. The resultant *K* values do not stay constant (Table 1.1). The values of *K* derived for the sub-scenes using the multiscale approach do not vary nearly as much as do the values estimated by using the standard approach. Furthermore, the average of the *K* values derived from each sub-scene is close to the *K* value derived from the full-

length interferogram by using the multiscale approach. Therefore for a given scene, the *K* value represents the average condition of the vertically stratified troposphere in that given area. Treatment of a system in which *K* varies slowly in space will be confounded by the effects of convective processes, and is thus not likely to be fruitful.

1.4 Discussion and Conclusions

In the synthetic test, we show that the multiscale approach is insensitive to phase ramps. One important implication of this result is that we can apply this correction before baseline re-estimation without confounding the orbital phase ramp with topographically-correlated tropospheric signals. When re-estimating baseline model parameters from the unwrapped phase and a DEM, large-scale differential atmospheric artifacts will be aliased into the baseline estimate [*Buckley et al.*, 2003]. *Li et al.* [2006a] showed that correcting the interferogram for atmospheric artifacts can effectively improve estimates of baseline parameters. When no satellite imagery-based or modeling-based correction method is available, incorporating a multiscale correction approach can reduce the long-wavelength topographically-correlated phase to a reasonable extent without over-estimating it, allowing more accurate baseline refinement.

We demonstrate the robustness of the estimation of *K* in two examples by using real observations. In our Long Valley Caldera example, the corrected interferograms still show strong delays near the caldera. This phenomenon is observed in multiple interferograms, probably due to the water vapor brought by the northerly or southerly prevailing winds in the Owens Valley. This dynamic signal has a strong amplitude (~3–5 cm) and intermediate

spatial wavelength (~20–40 km; Figure 1.10). Despite the existence of such prominent turbulent mixing signals, out synthetic test shows that the multiscale approach still can provide a robust and conservative estimate of *K*. In the Tocopilla example, the cropping test shows that *K* value can vary with scene size. The *K* value derived from the full-length interferogram by using the multiscale approach represents an average of the vertically stratified troposphere in the given area, and therefore is a more conservative estimate of the transfer function. In conclusion, our multiscale correction should be considered as a fast and handy tool when nothing else is available, but it is not a panacea that can cure all challenges posed by tropospheric delays.

References of Chapter I

Berardino, P., G. Fornaro, R. Lanari, and E. Sansosti (2002), A new algorithm for surface deformation monitoring based on small baseline differential SAR interferograms, *IEEE Trans. Geosci. Remote Sens.*, 40, 2375–2383.

Bevis, M., S. Businger, T. Herring, C. Rocken, R. Anthes, and R. Ware (1992), GPS meteorology: Remote sensing of atmospheric water vapour using the Global Positioning System, *J. Geophys. Res.*, 97, 15787–15801.

Boyd, B., and L. Vandenberghe (2004), *Convex Optimization*, Cambridge Univ. Press, Cambridge, U. K.

Buckley, S., P. Rosen, S. Hensley, and B. Tapley (2003), Land subsidence in Houston, Texas, measured by radar interferometry and constrained by extensometers, *J. Geophys. Res.*, 108(B11), 2542, doi:10.1029/2002JB001848.

Burgmann, R., P. Rosen, and E. Fielding (2000), Synthetic aperture radar interferometry to measure Earth's surface topography and its deformation, Annu. *Rev. Earth Planet. Sci.*, 28, 169–209.

Cavalié, O., M.-P. Doin, C. Lasserre, and P. Briole (2007), Ground motion measurement in the Lake Mead area, Nevada, by differential synthetic aperture radar interferometry time series analysis: Probing the lithosphere rheological structure, *J. Geophys. Res.*, 112, B03403, doi:10.1029/2006JB004344.

Delacourt, C., P. Briole, and J. Achache (1998), Tropospheric corrections of SAR interferograms with strong topography: Application to Etna, *Geophys. Res. Lett.*, 25, 2849–2852.

Delouis, B., M. Pardo, D. Legrand, and T. Monfret (2009), The Mw 7.7 Tocopilla earthquake of 14 November 2007 at the southern edge of the Northern Chile Seismic Gap: Rupture in the deep part of the coupled plate interface, *Bull. Seismol. Soc. Am.*, 99(1), 87–94, doi:10.1785/0120080192.

DiCaprio, C., and M. Simons (2008), The importance of ocean tidal load corrections for differential InSAR, *Geophys. Res. Lett.*, 35, L22309, doi:10.1029/2008GL035806.

Doin, M. P., C. Lasserre, G. Peltzer, O. Cavalie, and C. Doubre (2009), Corrections of stratified tropospheric delays in SAR interferometry: Validation with global atmospheric models, *J. Appl. Geophys.*, 69(1), 35–50, doi:10.1016/j.jappgeo.2009.03.010.

Emardson, T., M. Simons, and F. Webb (2003), Neutral atmospheric delay in interferometric synthetic aperture radar applications: Statistical description and mitigation, *J. Geophys. Res.*, 108(B5), 2231, doi:10.1029/2002JB001781.

Fialko, Y., M. Simons, and Y. Khazan (2001), Finite source modeling of magmatic unrest in Socorro, New Mexico, and Long Valley, California, *Geophys. J. Int.*, 146, 191–200.

Foster, J., B. Brooks, T. Cherubini, C. Shacat, S. Businger, and C. Werner (2006), Mitigating atmospheric noise for InSAR using a high resolution weather model, *Geophys. Res. Lett.*, 33, L16304, doi:10.1029/2006GL026781.

Gray, A. L., K. E. Mattar, and G. Sofko (2000), Influence of ionospheric electron density fluctuations on satellite radar interferometry, *Geophys. Res. Lett.*, 27(10), 1451–1454.

Hanssen, R. F. (2001), *Radar Interferometry, Data Interpretation and Error Analysis*, Springer, New York.

Hill, D., J. Langbein, and S. Prejean (2003), Relations between seismicity and deformation during unrest in Long Valley Caldera, California, from 1995 through 1999, *J. Volcanol. Geotherm. Res.*, 127, 175–193, doi:10.1016/S0377-0273 (03)00169-0.

Ji, C., D. Wald, and D. Helmberger (2002a), Source description of the 1999 Hector Mine, California, earthquake, part I: Wavelet domain inversion theory and resolution analysis, *Bull. Seismol. Soc. Am.*, 92(4), 1192–1207.

Ji, C., D. Wald, and D. Helmberger (2002b), Source description of the 1999 Hector Mine, California, earthquake, part II: Complexity of slip history, *Bull. Seismol. Soc. Am.*, 92(4), 1208–1226.

Langbein, J. (2003), Deformation of the Long Valley caldera, California: Inferences from measurements from 1988 to 2001, *J. Volcanol. Geotherm. Res.*, 127, 247–267, doi:10.1016/S0377-0273(03)00172-0.

Li, Z., J.-P. Muller, and P. Cross (2005), Interferometric synthetic aperture radar (InSAR) atmospheric correction: GPS, Moderate Resolution Imaging Spectroradiometer (MODIS), and InSAR integration, *J. Geophys. Res.*, 110, B03410, doi:10.1029/2004JB003446.

Li, Z., E. Fielding, P. Cross, and J.-P. Muller (2006a), Interferometric synthetic aperture radar atmospheric correction: GPS topography-dependent turbulence model, *J. Geophys. Res.*, 111, B02404, doi:10.1029/2005JB003711.

Li, Z., E. Fielding, P. Cross, and J.-P. Muller (2006b), Interferometric synthetic aperture radar atmospheric correction: Medium Resolution Imaging Spectrometer and Advanced Synthetic Aperture Radar integration, *Geophys. Res. Lett.*, 33, L06816, doi:10.1029/2005GL025299.

Li, Z., J.-P. Muller, P. Cross, P. Albert, J. Fischer, and R. Bennartz (2006c), Assessment of the potential of MERIS near - infrared water vapour products to correct ASAR interferometric measurements, *Int. J. Remote Sens.*, 27, 349–365, doi:10.1080/01431160500307342.

Lohman, R., and M. Simons (2005), Some thoughts on the use of InSAR data to constrain models of surface deformation: Rupture in the deep part of the coupled plate interface, *Bull. Seismol. Soc. Am.*, 99(1), 87–94, doi:10.1785/0120080192.

Massonnet, D., K. Feigl, M. Rossi, and F. Adragna (1994), Radar interferometric mapping of deformation in the year after the Landers earthquake, *Nature*, 369(6477), 227–230.

Meadows, P., B. Rosich, A. Pilgrim, and M. Tranfaglia (2007), ERS-2 SAR performance and product evolution, in *Proceedings of the Envisat Symposium 2007, Montreux, Switzerland*, Eur. Space Agency Spec. Publ., ESA SP-636, 23–27.

Mogi, K. (1958), Relations between the eruption of various volcanoes and the deformation of the ground surface around them, *Bull. Earthquake Res. Inst.*, 36, 99–143.

Newman, A., T. Dixon, G. Ofoegbu, and J. Dixon (2001), Geodetic and seismic constraints on recent activity at Long Valley Caldera, California: Evidence for viscoelastic rheology, *J. Volcanol. Geotherm. Res.*, 105, 183–206, doi:10.1016/S0377-0273(00)00255-9.

Onn, F., and H. A. Zebker (2006), Correction for interferometric synthetic aperture radar atmospheric phase artifacts using time series of zenith wet delay observations from a GPS network, *J. Geophys. Res.*, 111, B09102, doi:10.1029/2005JB004012.

Puysségur, B., R. Michel, and J. - P. Avouac (2007), Tropospheric phase delay in interferometric synthetic aperture radar estimated from meteorological model and multispectral imagery, *J. Geophys. Res.*, 112, B05419, doi:10.1029/2006JB004352.

Simons, M., and P. Rosen (2007), Interferometric synthetic aperture radar geodes, in *Treatise on Geophysics*, vol. 3, Geodesy, edited by G. Schubert, pp. 391–446, Elsevier, Amsterdam.

Tichelaar, B. W., and L. J. Ruff (1989), How good are our best models?, *Eos Trans. AGU*, 70, 593–605.

Zebker, H. A., P. Rosen, and S. Hensley (1997), Atmospheric effects in interferometric synthetic aperture radar surface deformation and topographic maps, *J. Geophys. Res.*, 102, 7547–7563.

Zhong, S., J. Li, C. D. Whiteman, X. Bian, and W. Yao (2008), Climatology of high wind events in the Owens Valley, California, *Mon. Weather Rev.*, 136(9), 3536–3552, doi:10.1175/2008MWR2348.1.

Table 1.1. Variation of *K* values with change of scene size in Tocopilla example

Scene Size[a]	Multiscale	Full-Interferogram
Full length	−0.48 ± 0.01	−1.15 ± 0.03
1/2 length (291–580 km)	−0.46 ± 0.02	−0.60 ± 0.14
1/2 length (0–290 km)	−0.50 ± 0.04	−2.34 ± 0.11
Average of two 1/2 scenes	−0.48 ± 0.04	−1.47 ± 0.18
1/4 length (436–580 km)	−0.35 ± 0.02	−1.07 ± 0.01
1/4 length (291–435 km)	−1.15 ± 0.02	−1.51 ± 0.05
1/4 length (146–290 km)	−0.11 ± 0.04	−19.83 ± 0.19
1/4 length (0–145 km)	−0.53 ± 0.02	−0.50 ± 0.01
Average of four 1/4 scenes	−0.52 ± 0.05	−5.73 ± 0.20

[a]Full length: 120 km × 580 km; 1/2 length: 120 km × 290 km; 1/4 length: 120km × 145 km.

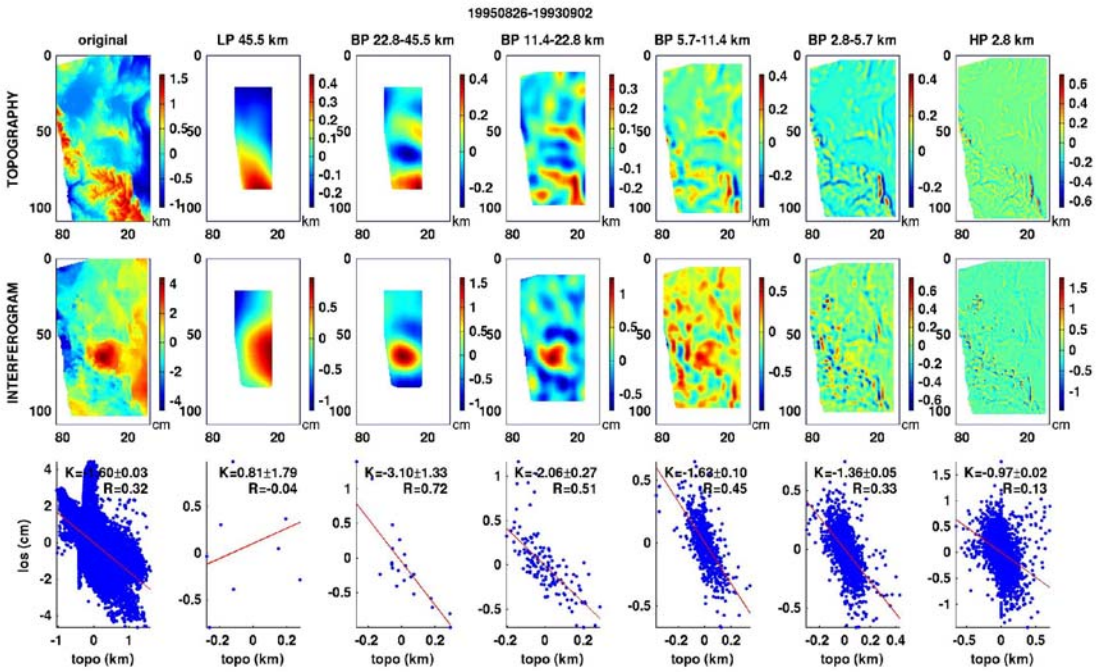

Figure 1.1. Original and decomposed (top) topography and (middle) interferograms. LP, BP and HP indicate low-pass, band-pass and high-pass respectively. The surrounding blank area in each channel results from omitting points along the scene boundaries to avoid edge effects when applying Gaussian filters. (bottom) The scatter plots of each decomposed band. The estimated value of K with uncertainties and correlation coefficient R for each channel are shown at the top right corners of the scatter plots. The final estimate of K is −1.53 cm/km in this example, close to what is derived from full-interferogram correlation (−1.60 cm/km). The interferograms are produced from ERS SAR images acquired on 1995/08/26 and 1993/09/02 (see Figure 1.3).

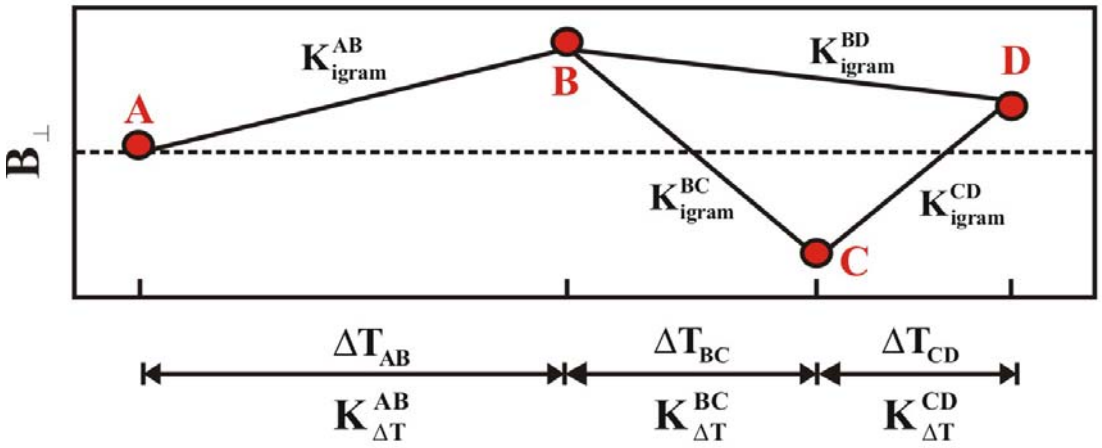

Figure 1.2. $B_\perp$ vs T plot. $K_{\Delta T}$ is formed by defining a unique set of component time intervals ΔT based on the acquisition dates.

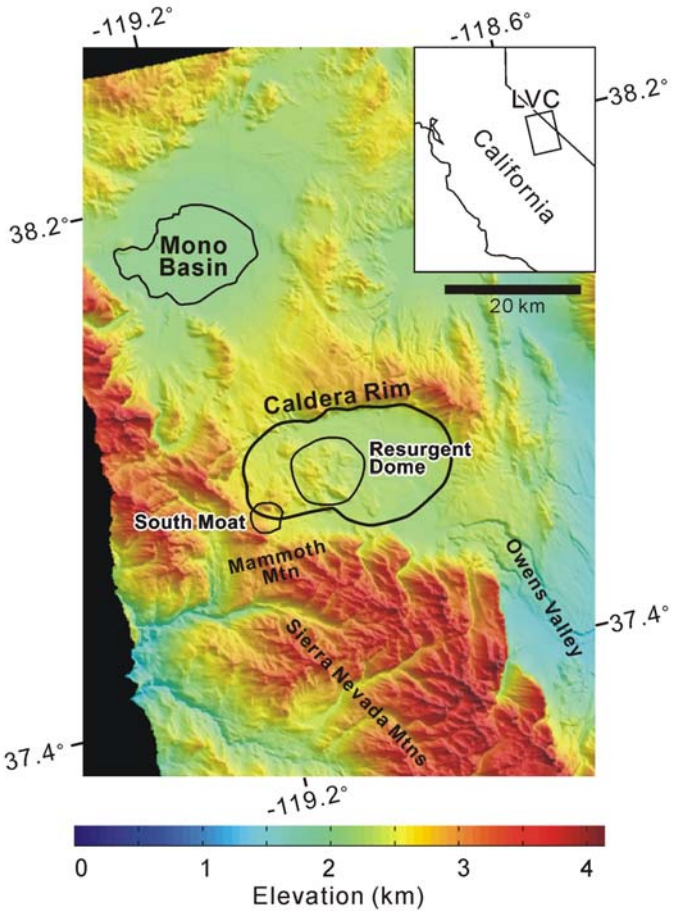

Figure 1.3. Reference map of Long Valley Caldera and the resurgent dome during the 1997–98 inflation episode. This map has the same extent as the data footprint of ERS track 485 used in this study.

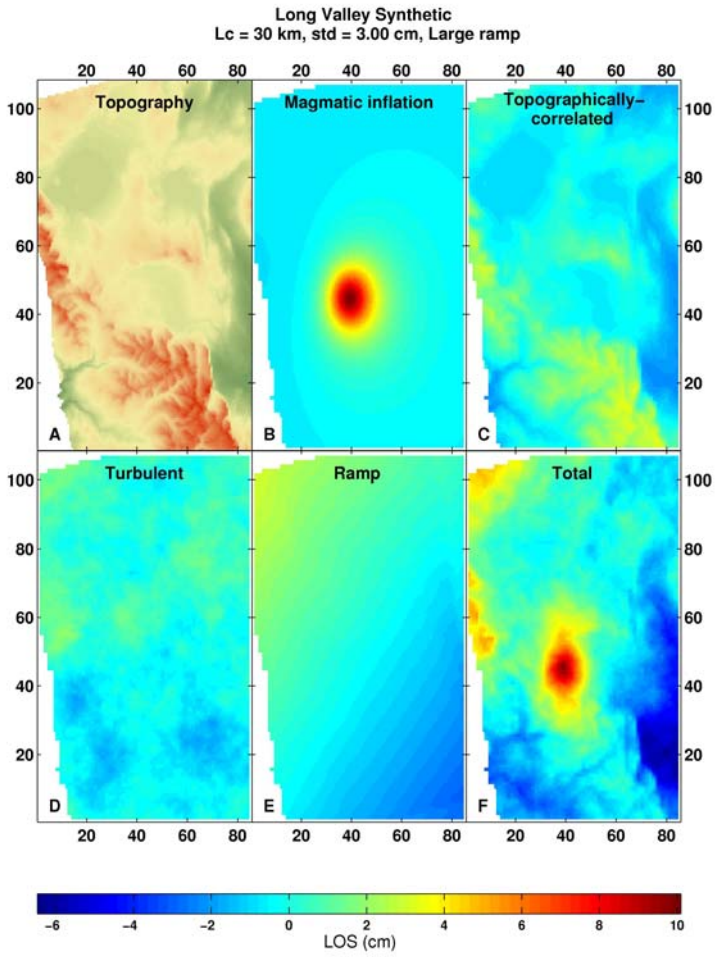

Figure 1.4. A schematic description of the construction of the synthetic interferometry. (a) The topography of Long Valley Caldera (location is the same as ERS track 485 in Figure 1.3), with maximum elevation (red color) up to ~4 km. We use the point source model of inflation [*Mogi*, 1958] to calculate the (b) line-of-sight surface displacement due to magmatic intrusion, and use topography to compute (c) topographically-correlated tropospheric delays. (d) Turbulent mixing signals and (e) small bilinear ramps are computed as described in the text. We project them to the line-of-sight direction and combine them to form the (f) final synthetic interferogram. In this example, σ for n_n is 3 cm, and noise scale distance L_c is 30 km.

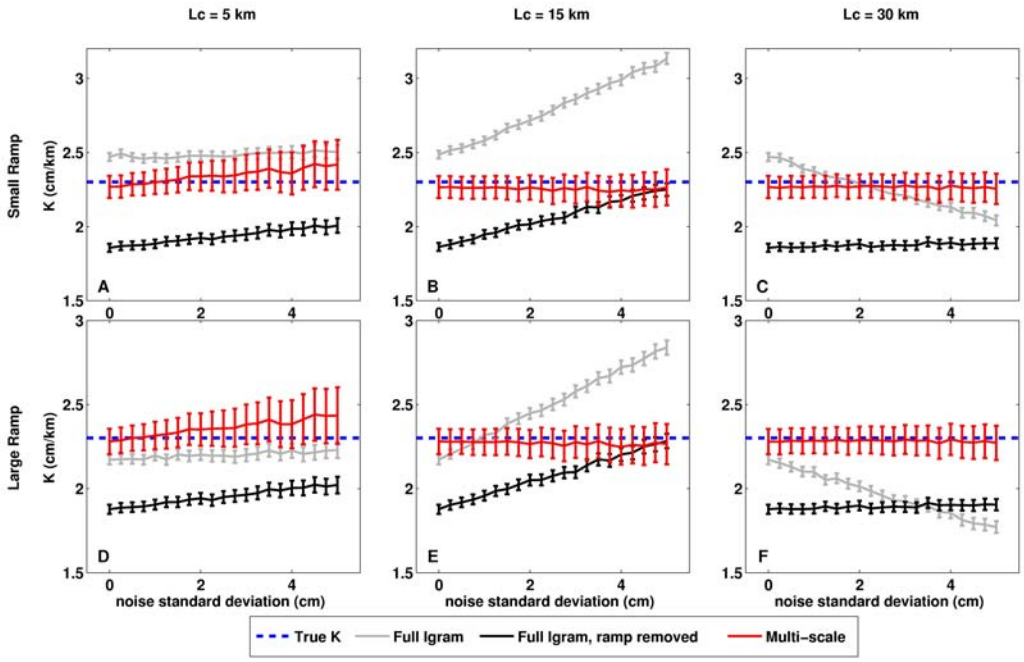

Figure 1.5. Comparison of *K* values calculated by using full interferogram correlation (gray lines), full interferogram correlation with ramp removed (black lines) and multiscale analysis (red lines). There are 20 realizations of synthetic interferograms in each plot, with different levels of noise standard deviation. The input *K* is 2.3 cm/km (blue dashed lines). Among the three methods, the multiscale approach gives *K* values that are most stable and closest to assigned *K*.

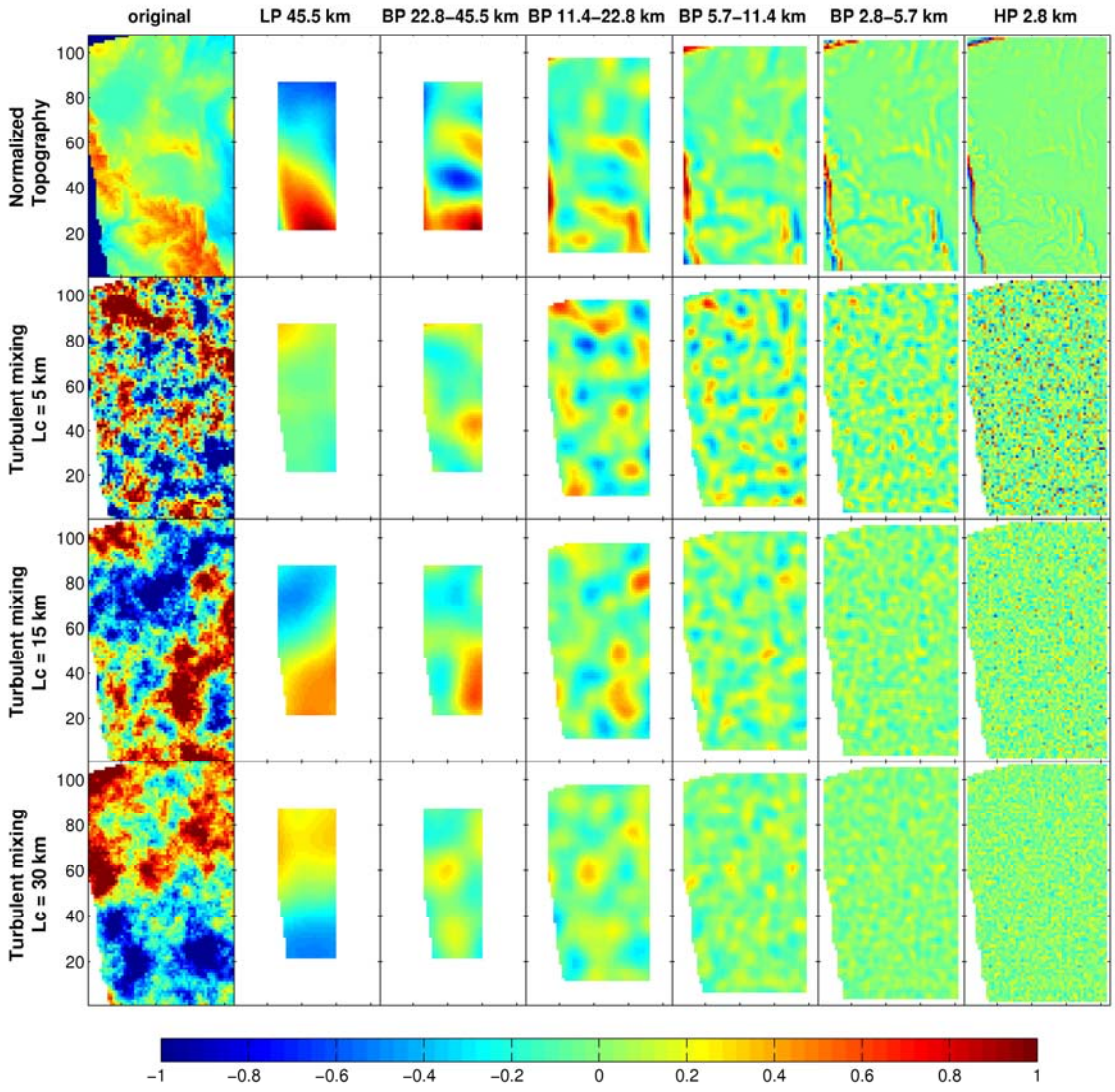

Figure 1.6. Comparison of decomposed turbulent signals with different scale distance L_c. Noise standard error is 2.5 cm in all cases. Notice that short-wavelength channels show higher amplitude at smaller L_c than at larger L_c.

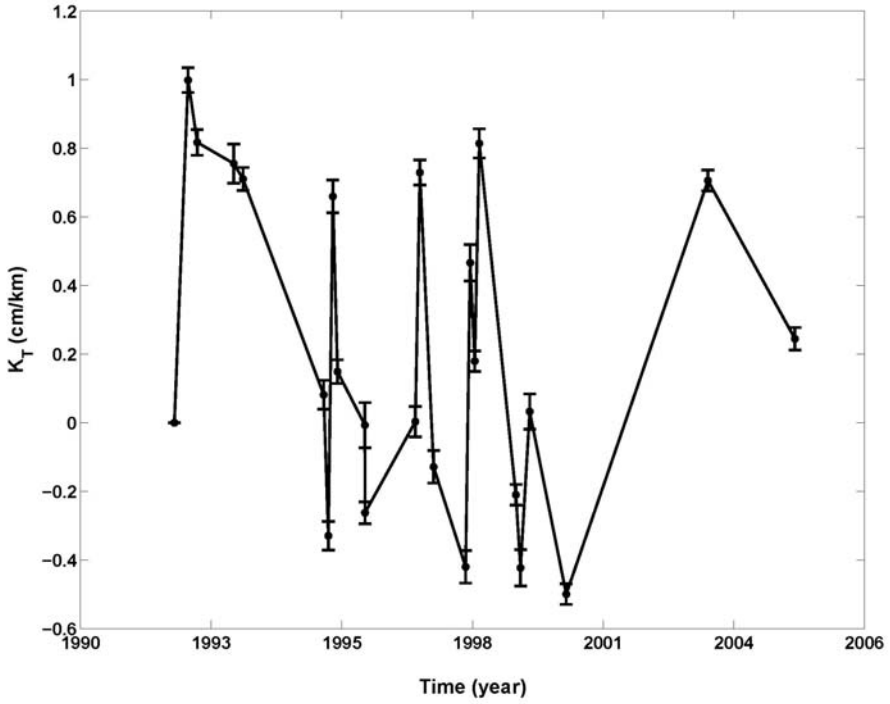

Figure 1.7. K_T time series derived from multiscale approach. We arbitrarily set the first value in this K_T time series as zero, and sequentially add up all $K_{\Delta T}$ values. The error bars here are shown with one standard error, derived by using a bootstrapping technique.

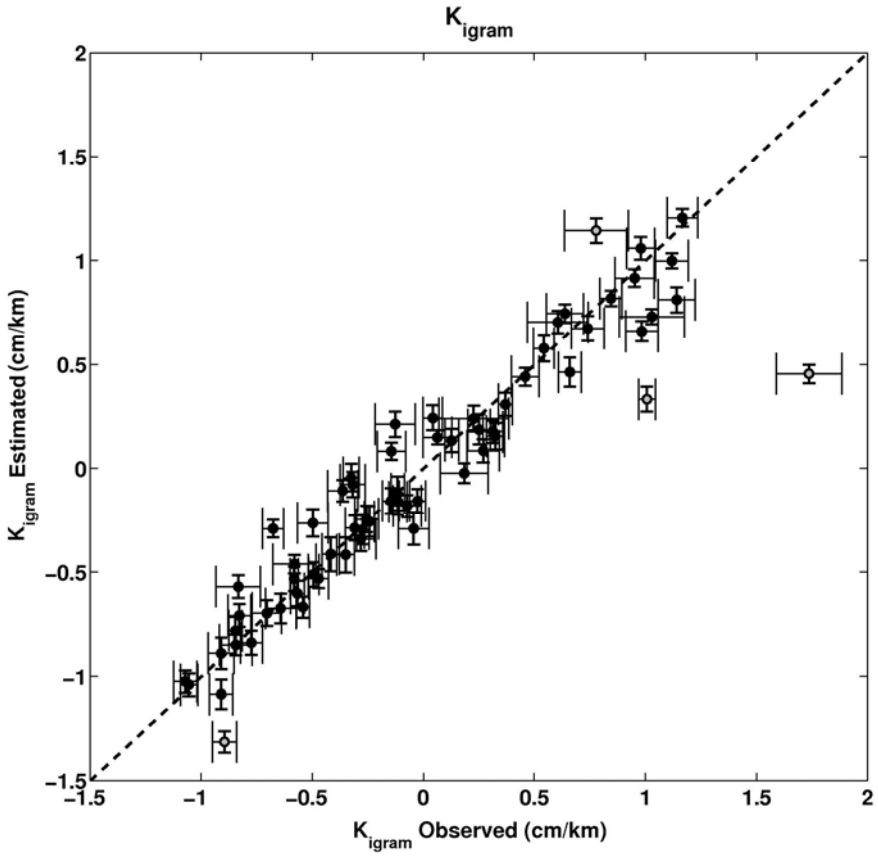

Figure 1.8. Comparison between observed K_{igram}, calculated directly from the phase-topography correlation of each interferogram as shown in equation (2), and estimated K_{igram}, derived from the K time series. Outliers are shown in grey circles. These outliers result from larger unwrapping errors in the interferograms.

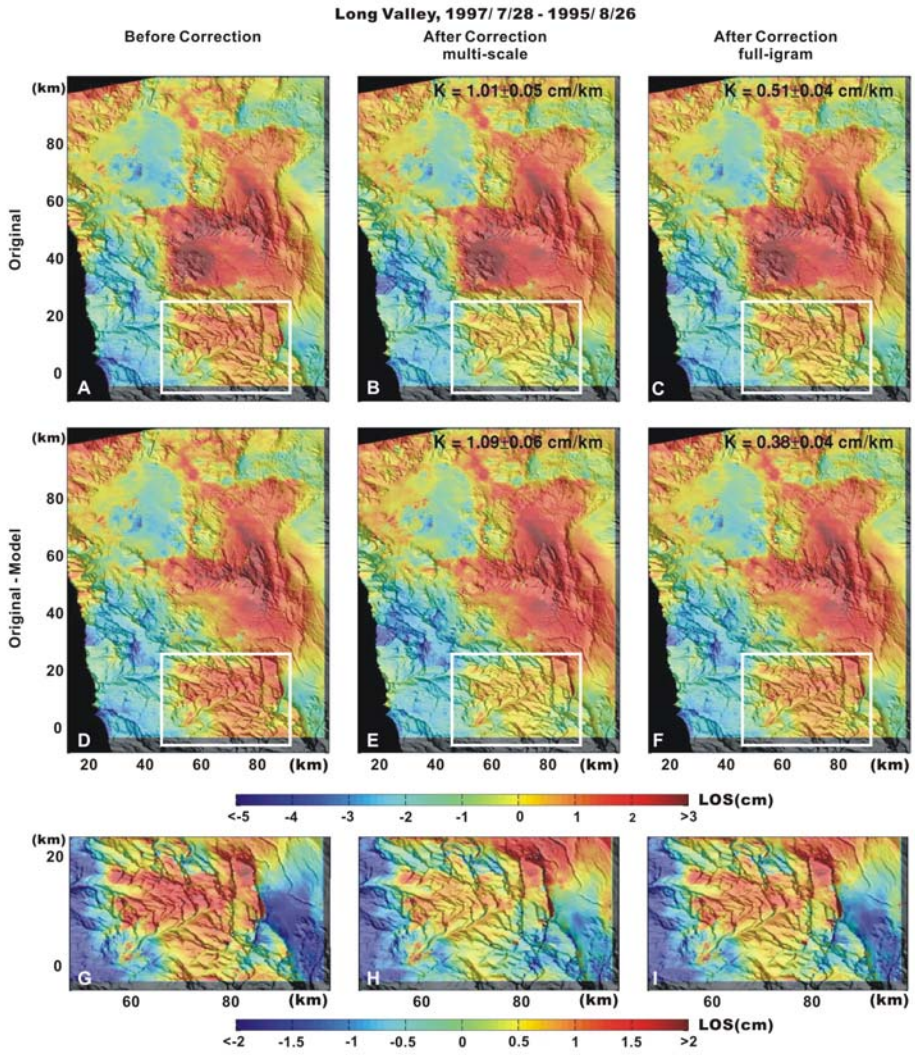

Figure 1.9. Comparison between the interferograms in the Long Valley Caldera example before and after correction by using the multiscale approach and full-interferogram correlation approach (ramp-retained). (a–c) The original interferograms before and after correction. (d–f) The interferograms with inflation model subtracted before and after correction. The delays around the Sierra Nevada Mountains area (white rectangle) are properly removed after applying the multiscale correction. (g–i) The enlarged plots of the area within the white rectangles in Figures 1.9a-c. The large blob of noise near the center of the interferogram does not correlate well with topography and may mostly result from heterogeneous water vapor distribution in Owens Valley.

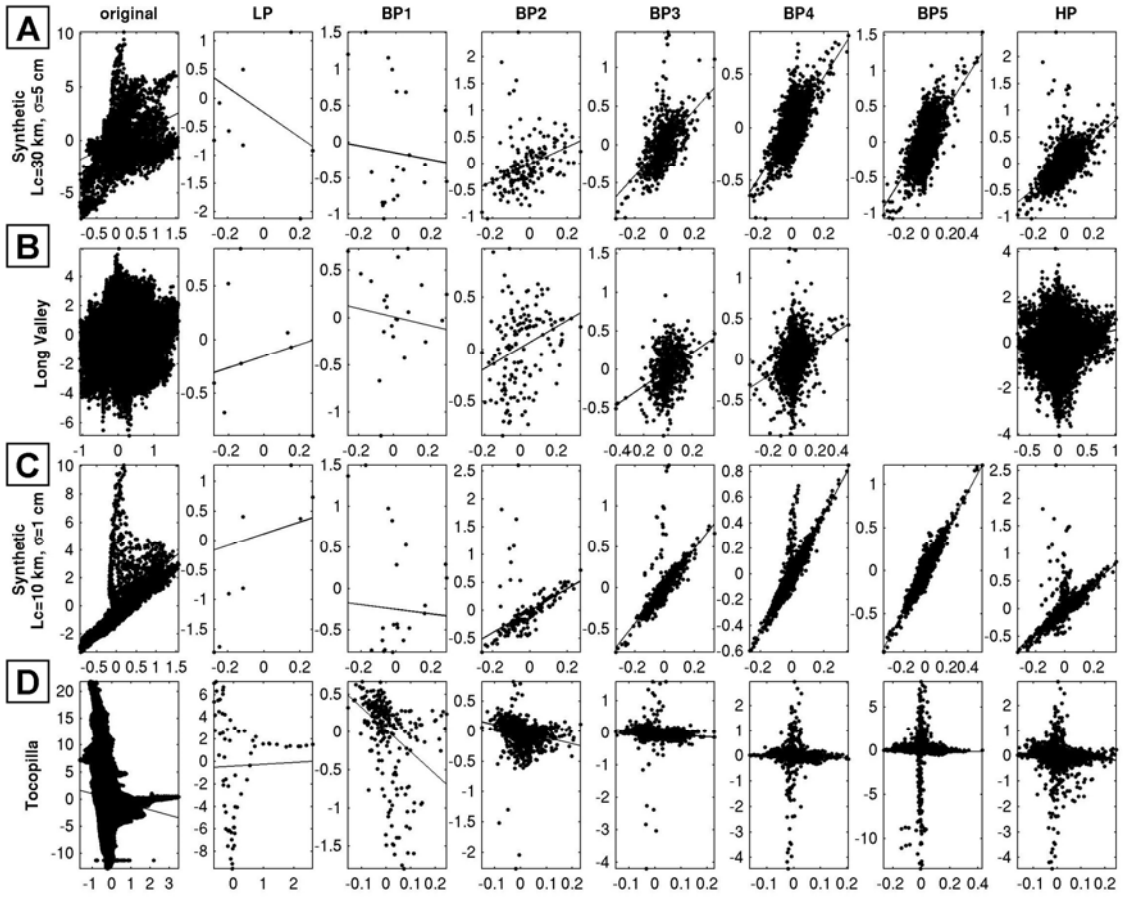

Figure 1.10. Scatter plots (phase vs. topography) between two real cases, Long Valley Caldera and Tocopilla, and two synthetic examples. This comparison verifies the high-amplitude and relatively low-amplitude turbulent signals in the Long Valley Caldera and Tocopilla interferograms, respectively. The high amplitude of turbulence in the Long Valley Caldera may suggest that the *K* derived from the multiscale approach may be smaller than "real" values, as shown by the synthetic test (Figure 1.5).

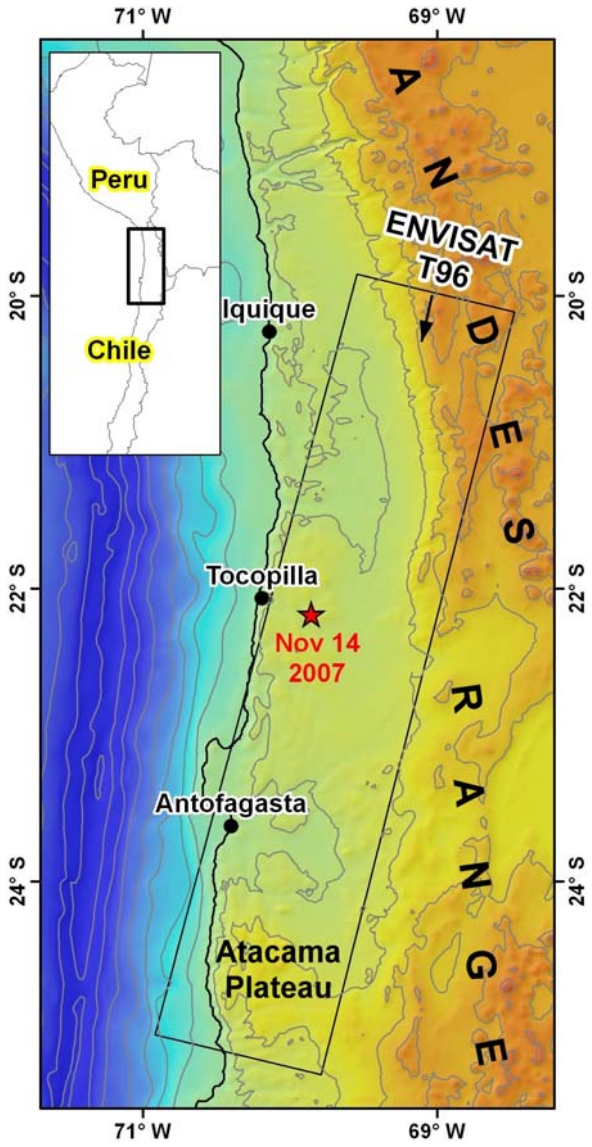

Figure 1.11. Reference map of the 2007 Tocopilla earthquake and the ENVISAT descending track 96. Contour interval is 1000 m.

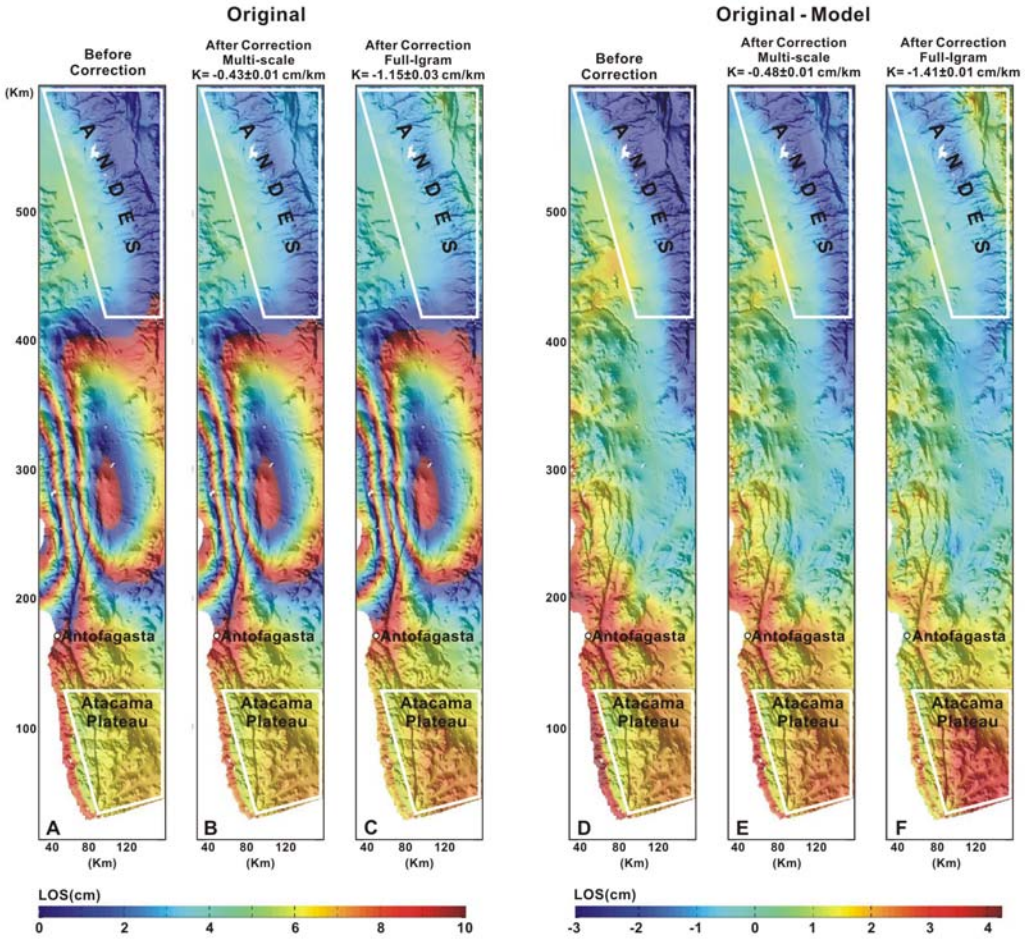

Figure 1.12. Comparison between the interferograms in the 2007 Tocopilla coseismic displacement example before and after correction by using the multiscale approach. (a–c) The original interferograms before and after correction, wrapped by every 10 - cm displacement. (d–f) The model - removed interferograms before and after correction. Notice that the phase gradient around the Andes (white polygons) is reduced after correction. The scatter plots of each bandpass channel are shown in Figure 1.10d. Those plots indicate relatively small influence of turbulent signals in the Tocopilla example. See text for more discussion about the comparison of the multiscale and full-interferogram correlation methods, and the explanation of the correction result in the Atacama Plateau region.

Chapter 2

PCAIM JOINT INVERSION OF INSAR AND GROUND-BASED GEODETIC TIME SERIES: APPLICATION TO MONITORING MAGMATIC INFLATION BENEATH THE LONG VALLEY CALDERA

Originally published in Lin, Y.-n. N., A. P. Kositsky, and J.-P. Avouac (2010), PCAIM joint inversion of InSAR and ground-based geodetic time series: Application to monitoring magmatic inflation beneath the Long Valley Caldera, *Geophys. Res. Lett.*, 37(23), L23301, doi: 10.1029/2010GL045769.

Abstract

This study demonstrates the interest of using a Principal Component Analysis-based Inversion Method (PCAIM) to analyze jointly InSAR and ground-based geodetic time series of crustal deformation. A major advantage of this approach is that the InSAR tropospheric biases are naturally filtered out provided they do not introduce correlated or high amplitude noise in the input times series. This approach yields source models which are well-constrained both in time and space due to the temporal resolution of the ground-based geodetic data and the spatial resolution of the InSAR data. The technique is computationally inexpensive allowing for the inversion of large datasets. To demonstrate

the performance of this approach, we apply it to the 1997–98 magmatic inflation event in the Long Valley Caldera, California.

2.1 Introduction

A number of ground-based geodetic techniques and remote sensing techniques are now available to monitor surface deformation induced by a variety of geophysical processes and are used to address a wide range of questions in various fields [e.g., *Blewitt*, 2007; *Simons and Rosen*, 2007]. Some ground-based geodetic techniques, such as Electronic Distance Meter (EDM) and Global Positioning System (GPS), allow high temporal resolution, with sampling rates typically between more than 1 measurement epoch per second and 1 measurement epoch every several days. These measurements are based on electromagnetic signals transmitted through the atmosphere between pairs of ground-based stations or between ground-based stations and satellites, and are therefore sensitive to atmospheric effects. Atmospheric effects are routinely estimated and corrected for in processing continuous GPS data [*Tregoning and Herring*, 2006; *Blewitt*, 2007] and EDM data [*Langbein et al.*, 1987]. Therefore, such post-corrected time series are relatively free of atmospheric bias.

While ground-based geodetic techniques provide dense time series of accurate positions at a limited number of points, remote sensing techniques, in particular Interferometric Synthetic Aperture Radar (InSAR), can provide dense spatial coverage, but at a limited number of epochs, given that the revisit period of most SAR systems is 10–50 days. Another issue is the sensitivity of InSAR to atmospheric disturbances, particularly

moisture variations in the troposphere. Various methods have been proposed to correct these effects [e.g., *Li et al.*, 2005, 2006; *Foster et al.*, 2006; *Onn and Zebker*, 2006; *Puysségur et al.*, 2007; *Doin et al.*, 2009; *Lin et al.*, 2010], but the potential of these techniques is limited by the availability of radiometric data, the density of GPS stations, or the accuracy of high-resolution weather models. Difficulties in correcting atmospheric influences, in addition to the generally long time span between interferometric pairs of images, strongly limit the possibility of using InSAR to monitor the temporal variation of surface deformation.

Because of the complementary resolution of InSAR and ground-based geodetic data, geophysical analyses can benefit from integrating both types of data into the same inversion [e.g., *Wei et al.*, 2010]. Here we explore the possibility of achieving this goal using the Principal Component Analysis-based Inversion Method (PCAIM) [*Kositsky and Avouac*, 2010]. PCAIM is a statistically-based approach to extract the signals with maximum spatiotemporal coherence and derive a best fitting source model with minimum computational cost. In the standard PCA approach the first principal component is the least squares approximation of the data matrix; the second principal mode is the best approximation of the residuals after subtracting the first principal component from the data matrix; and so forth [*Savage*, 1988]. PCAIM takes additional advantage of the fact that the components can be modeled separately and that the derived principal sources can be recombined to derive the best fitting time-varying source model. Because tectonics must affect both the ground-based geodetic and InSAR time series in a coherent way, while atmospheric delays ought not to do so, this technique utilizes ground-based geodetic data to help filter out InSAR tropospheric biases. The two datasets also complement each other

in terms of spatiotemporal sampling rates in the PCAIM output. In this study, we use the Long Valley Caldera example to test this joint inversion method. Long Valley Caldera experienced a large inflation episode between 1997 and 1998, resulting in ~10 cm of cumulative uplift [*Langbein*, 2003]. Hereafter we show how to derive a source model with high spatiotemporal resolution from the joint inversion of InSAR and ground-based geodetic data.

2. 2 Joint Inversion Using PCAIM

2.2.1 PCAIM Principles

Provided that the crust is considered as a linear elastic medium, surface displacements depend linearly on the source characteristics, typically parameterized as slip on a fault, opening of a dike or increase in pressure in a magmatic chamber [e.g., *Mogi*, 1958; *Okada*, 1985]. Source models can therefore be derived, through some standard linear inversion procedure. In principle, the time evolution of the source can be derived from inverting the displacement data available at each epoch. Such an approach is computationally expensive for a large dataset, and would not impose any coherent time evolution of the source since it would yield independent models at each epoch. PCAIM allows us to overcome these limitations. The displacement data are decomposed into a linear combination of principal components, each associated with its own spatial function, principal value and time function. *Kositsky and Avouac* [2010] have shown that if the dataset can be modeled as a time varying linear source model, the principal spatial functions can be modeled using the same formalism. After PCA (Principal Component Analysis) decomposition, each principal

spatial function is modeled individually and translated into a corresponding principal source model. The various principal source models are then recombined with their respective principal values and time functions to represent the estimate of the source model needed to fit the original dataset. PCAIM thus takes advantage of the linearity of the formulation and is cost effective because it generally requires inversion of only a handful of spatial components. For more details regarding the theoretical and technical aspects of this method, the reader can refer to *Kositsky and Avouac* [2010].

2.2.2 PCA Decomposition

We use a total of 65 interferograms formed from 24 ERS scenes acquired between 1992 and 2005, and two-color EDM records acquired every 1–15 days since January 1984 (Figure 2.1a). We applied a standard small baseline subset (SBAS) time series analysis [*Berardino et al.*, 2002] on the InSAR data, without any correction terms or additional filtering. The SBAS InSAR time series consist of 24 epochs on 7992 pixels (1-km spacing), with median time span of 70 days between epochs. The EDM time series consists of 185 epochs at 8 stations. These two datasets were combined into one large displacement data matrix, which is zero-padded in most entries due to the low temporal sampling rate of SAR imagery. Ordinary PCA cannot be applied to such sparse matrices. To get around this problem, we adopt a more sophisticated decomposition, a non-linear solver using the weighted low-rank approximation originally developed by *Srebro and Jaakkola* [2003] and adapted to geodetic applications by *Kositsky* [2010]. The method thus allows taking into account the formal uncertainties assigned to the data and is therefore more practical

than the standard PCA technique when the time series have missing data and/or varying uncertainties [*Kositsky and Avouac*, 2010].

Another adaptation is that each component is solved separately in order to preserve the continuity of time functions. This iterative decomposition strategy retains the signal continuity of each component (Appendix A). The resultant principal components are close to but not exactly orthogonal. Nevertheless, orthogonality is not geophysically necessary, whereas temporal continuity is. To maintain the continuity of time functions, we think it is an acceptable tradeoff with the cost of orthogonality. Figures 2.1b and 2.1c show the spatial functions, multiplied by the principal values associated with each component, and the normalized time functions.

Figure 2.2a shows how the fit between the original time series and the reconstructed time series improves as the number of components used in the reconstruction increases. Here, we consider separately the reduced Chi-square χ_r^2 of the residuals to the EDM and to the InSAR data for the 1 to *k*-th component, defined as,

$$\chi^2_{r,\mathrm{TYPE}} = \frac{1}{N-P}\sum_{i=1}^{k}\left[\frac{X^{\mathrm{obs}}_{\mathrm{TYPE,i}} - X^{\mathrm{pca}}_{\mathrm{TYPE,i}}}{\sigma^{\mathrm{obs}}_{\mathrm{TYPE,i}}}\right]^2 \qquad (2\text{-}1)$$

where *N* and *P* refers to the total number of observations and parameters respectively, *X* refers to one element in the data matrix, TYPE refers either to InSAR or EDM, and σ is the formal 1-sigma uncertainties assigned to the data. For the EDM data we used the original uncertainties from *Langbein* [2003]. For the InSAR data we used a standard estimate of 5 mm, ignoring the off-diagonal elements of the variance-covariance uncertainty matrix. Figure 2.2a shows that with only the 1st component, the InSAR data can be reconstructed

within the 5 mm estimated uncertainty. Under the same χ_r^2 criterion, it takes more than 10 components to fit the EDM data within their original uncertainties. It is thus difficult to determine the overall number of significant components because of the sensitivity of χ_r^2 to the observational/assigned uncertainty. In this situation, an *F*-test serves as a more robust approach. This statistical test estimates the probability that a particular component is significant based on the relative reduction of variance (χ_r^2 in fact) as this component is added. The test result indicates that 3 components are significant at the 95% confidence level to reconstruct the EDM data (Table 2.1). More components are needed for InSAR because higher order components account for the atmospheric noises that prevail in all interferograms.

2.2.3 Results of the Joint Inversion

We chose a source model consisting of a grid of point volume-sources in an elastic half space [*Masterlark and Lu*, 2004], and compute the Green's functions accordingly. The gridded source has dimensions of 110 km by 125 km by 20 km, with distribution of 5 km spacing in X and Y direction and 2 km spacing in Z direction. We applied regularization via imposing a penalty to roughness of the source model, and carried out cross-validation to determine the optimal value for the smoothing parameter. The χ_r^2 of the residuals between the observed time series and the predictions from the gridded source model shows decreasing trends as the number of components increases (Figure 2.2b), but still gives no clue regarding the cut-off component. We therefore applied the *F*-test again (Table 2.1), and found that the first 2 components are significant at the 95% confidence level with

regard to the fit to the original EDM data. More than 4 components are needed for the InSAR data because including higher-order components into the model improves the fit to the prevailing noises in the data. Since the EDM dataset is less influenced by atmospheric noise and hence its F-test will be less biased, we chose to use only 2 components to generate our final model. The first 2 principal volumes are then recombined with their time functions to generate the time-varying source model that best fits jointly the InSAR and EDM data, without being significantly biased by the tropospheric noise in the InSAR data (Figure 2.3).

The EDM time series are generally well-reproduced by the model obtained from the inversion of the first 2 components, except for the station MINER and TILLA (Figure 2.3a). These two stations lie along the southern flank of the caldera (Figure 2.1a). According to *Langbein* [2003], the southern flank is subject to the influence of the South Moat Fault, a right-lateral strike-slip fault dipping 70 degrees to the NE. MINER and TILLA should have recorded the deformation associated with the displacement on this fault, and so does the InSAR imagery as the pattern is visible in the spatial function of the 2nd component (Figure 2.1b). For the purpose of demonstration, we did not include this fault so that it is easier to keep track of the roles InSAR and EDM data play in one single source model, but one can certainly include multiple types of sources in PCAIM.

2. 3 Discussion and Conclusion

Our source model suggests inflation of a magma chamber close to a sphere centered at around 7–8 km, similar to the 7.5 km centroid depth estimated by *Langbein* [2003]. The

net increase of volume over the period of time analyzed here is estimated to be 0.02 km^3, a value slightly smaller than the (~0.03 km^3) estimate of *Langbein* [2003]. It should be noticed that the gridded point inflation source model is a purely kinematic description of the magmatic source; as such it does not necessarily satisfy the traction-free boundary condition of the prolate spheroid model of *Yang et al.* [1988]. In fact, PCAIM only requires the surface displacement to be a linear function of the source model parameters, and the source model itself to be linear so that it conforms to the principles of additivity and scaling. In this sense there is no theoretical difficulty using the prolate spheroid model [*Yang et al.*, 1988] and including the South Moat Fault in a PCAIM joint inversion.

Our study demonstrates that PCAIM is an effective tool to separate tectonic signals and noises into different components when EDM and InSAR data are analyzed jointly. Most tectonic signals are in the first component and some are in the second component, while the third and higher components are dominated by tropospheric effects or tectonic sources too weak to have induced significantly correlated and high-amplitude signals in the whole dataset analyzed here (Figure 2.1). We discuss in Appendix A the results obtained from the decomposition of the InSAR-only or the EDM-only data. They show that joint analysis of the EDM and InSAR indeed helps extract from the 1st and 2nd components the fraction of the InSAR signals that are not coherent with EDM data. The joint inversion allows better spatial constraints and less-biased temporal evolution history to the source model.

Low-amplitude transient signals may be mixed with short-timescale tropospheric noises into higher order components. The EDM data from station MINER and TILLA show indeed a short-lived transient that is very likely tectonic signal. This transient was captured into the InSAR dominant spatial function but unfortunately mixed with tremendous

tropospheric noises. This is a limitation of PCAIM: when high-amplitude noise exists, corresponding corrections (if available) must be carried out, otherwise small-amplitude signals at a small number of measurement locations will blend with noise in higher order components.

The final remark about PCAIM is its low computational cost: it takes only ~2–3 hours to invert the whole dataset used in this study on a standard Linux machine (2.4 GHz CPU). The PCAIM code and sample dataset is available from the Tectonics Observatory Web page (http://www.tectonics.caltech.edu/resources/pcaim/).

References of Chapter II

Berardino, P., G. Fornaro, R. Lanari, and E. Sansosti (2002), A new algorithm for surface deformation monitoring based on small baseline differential SAR interferograms, *IEEE Trans. Geosci. Remote Sens.*, 40, 2375–2383.

Blewitt, G. (2007), GPS and space-based geodetic methods, in *Treatise on Geophysics*, vol. 3, Geodesy, edited by G. Schubert, pp. 351–390, Elsevier, Amsterdam.

Doin, M. P., C. Lasserre, G. Peltzer, O. Cavalie, and C. Doubre (2009), Corrections of stratified tropospheric delays in SAR interferometry: Validation with global atmospheric models, *J. Appl. Geophys.*, 69, 35–50, doi:10.1016/j.jappgeo.2009.03.010.

Foster, J., B. Brooks, T. Cherubini, C. Shacat, S. Businger, and C. L. Werner (2006), Mitigating atmospheric noise for InSAR using a high resolution weather model, *Geophys. Res. Lett.*, 33, L16304, doi:10.1029/2006GL026781.

Kositsky, A. (2010), *PCAIM user's manual*, Calif. Inst. of Technol., Pasadena. (Available at http://www.tectonics.caltech.edu/resources/pcaim/)

Kositsky, A. P., and J.-P. Avouac (2010), Inverting geodetic time series with a principal component analysis - based inversion method, *J. Geophys. Res.*, 115, B03401, doi:10.1029/2009JB006535.

Langbein, J. (2003), Deformation of the Long Valley Caldera, California: Inferences from measurements from 1988 to 2001, *J. Volcanol. Geotherm. Res.*, 127, 247–267, doi:10.1016/S0377-0273(03)00172-0.

Langbein, J., M. Linker, and D. Tupper (1987), Analysis of two - color geodimeter measurements of deformation within the Long Valley Caldera: June 1983 to October 1985, *J. Geophys. Res.*, 92(B9), 9423–9442.

Li, Z., J.-P. Muller, P. Cross, and E. J. Fielding (2005), Interferometric synthetic aperture radar (InSAR) atmospheric correction: GPS, Moderate Resolution Imaging Spectroradiometer (MODIS), and InSAR integration, *J. Geophys. Res.*, 110, B03410, doi:10.1029/2004JB003446.

Li, Z., J.-P. Muller, P. Cross, P. Albert, J. Fischer, and R. Bennartz (2006), Assessment of the potential of MERIS near - infrared water vapour products to correct ASAR interferometric measurements, *Int. J. Remote Sens.*, 27, 349–365, doi:10.1080/01431160500307342.

Lin, Y. N., M. Simons, E. A. Hetland, P. Muse, and C. DiCaprio (2010), A multiscale approach to estimating topographically correlated propagation delays in radar interferograms, *Geochem. Geophys. Geosyst.*, 11, Q09002, doi:10.1029/2010GC003228.

Masterlark, T., and Z. Lu (2004), Transient volcano deformation sources imaged with interferometric synthetic aperture radar: Application to Seguam Island, Alaska, *J. Geophys. Res.*, 109, B01401, doi:10.1029/2003JB002568.

Mogi, K. (1958), Relations between the eruption of various volcanoes and the deformation of the ground surface around them, *Bull. Earthquake Res.*, Inst. Univ. Tokyo, 36, 99–143.

Okada, Y. (1985), Surface deformation due to shear and tensile faults in a half-space, *Bull. Seismol. Soc. Am.*, 75(4), 1135–1154.

Onn, F., and H. A. Zebker (2006), Correction for interferometric synthetic aperture radar atmospheric phase artifacts using time series of zenith wet delay observations from a GPS network, *J. Geophys. Res.*, 111, B09102, doi:10.1029/2005JB004012.

Puysségur, B., R. Michel, and J.-P. Avouac (2007), Tropospheric phase delay in interferometric synthetic aperture radar estimated from meteorological model and multispectral imagery, *J. Geophys. Res.*, 112, B05419, doi:10.1029/2006JB004352.

Savage, J. C. (1988), Principal component analysis of geodetically measured deformation in Long Valley Caldera, eastern California, 1983–1987, *J. Geophys. Res.*, 93(B11), 13,297–13,305.

Simons, M., and P. Rosen (2007), Interferometric synthetic aperture radar geodes, in *Treatise on Geophysics*, vol. 3, Geodesy, edited by G. Schubert, pp. 391–446, Elsevier, Amsterdam.

Srebro, N., and T. Jaakkola (2003), Weighted low-rank approximations, in *Proceedings of the Twentieth International Conference on Machine Learning*, pp. 720–727, AAAI Press, Menlo Park, Calif.

Tregoning, P., and T. A. Herring (2006), Impact of a priori zenith hydrostatic delay errors on GPS estimates of station heights and zenith total delays, *Geophys. Res. Lett.*, 33, L23303, doi:10.1029/2006GL027706.

Wei, M., D. Sandwell, and B. Smith-Konter (2010), Optimal combination of InSAR and GPS for measuring interseismic crustal deformation, *Adv. Space Res.*, 46(2), 236–249, doi:10.1016/j.asr.2010.03.013.

Yang, X.-M., P. M. Davis, and J. H. Dieterich (1988), Deformation from inflation of a dipping finite prolate spheroid in an elastic half-space as a model for volcanic stressing, *J. Geophys. Res.*, 93(B5), 4249–4257.

Table 2.1 *F*-test determination of the number of significant components needed for the InSAR and the EDM data based on our iterative decomposition and gridded source inversion

	Decomposition		Model Inversion	
	InSAR	EDM	InSAR	EDM
$P(F \geq F_{1,2})$	~0**	~0**	~0**	~0**
$P(F \geq F_{2,3})$	~0**	5.2e-3**	~0**	0.06
$P(F \geq F_{3,4})$	~0**	0.85	~0**	0.81
$P(F \geq F_{4,5})$	~0**	2		
$P(F \geq F_{5,6})$	~0**	2		
$P(F \geq F_{6,7})$	~0**	2		

*$F_{i,i+1}$ refers to the test between using the first i and the first $i+1$ components. When probability $P(F \geq F_{i,i+1})$ is smaller than 0.05, we consider this test as statistically significant, which allows us to make the claim that the incorporation of the $(i+1)$th component does improve the fit significantly at the 95% confidence level (the probability that the improvement would be due to pure chance is less than 5%).

**significant; ~0 indicates probability less than 10-323

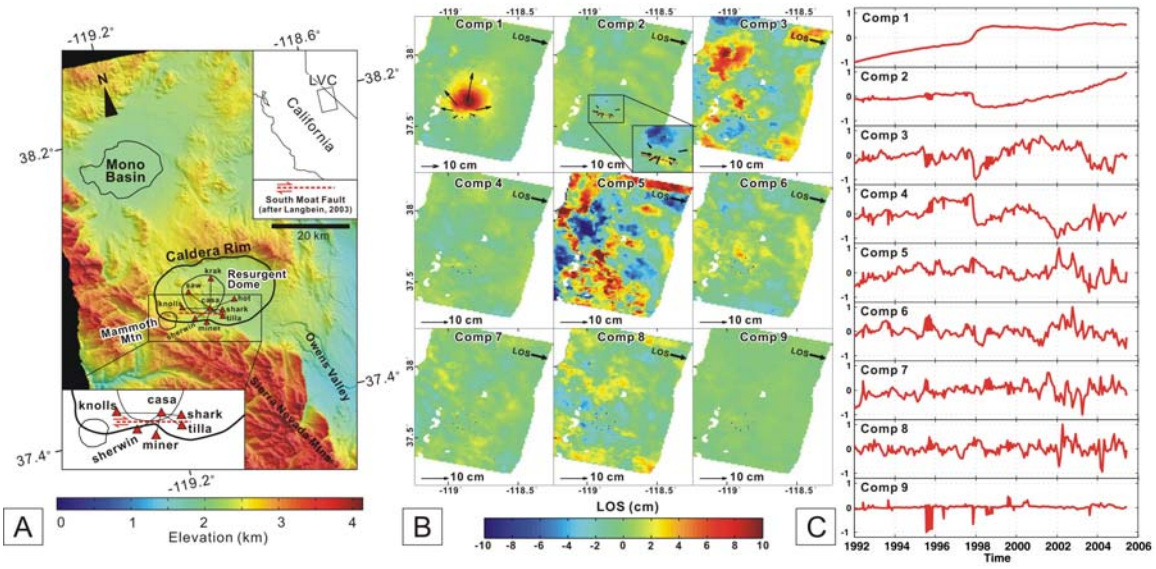

Figure 2.1. (a) Reference map of Long Valley Caldera and the resurgent dome during the 1997–98 inflation episode. This map has the same extent as the data footprint of ERS track 485 used in this study. Lower left inset shows the inferred location of the South Moat Fault [*Langbein*, 2003]. (b-c) The results from PCA decomposition. (b) The spatial functions of the displacement field, multiplied with the principal values associated with each component. Arrows in each component represent the principal slip functions (relative to CASA) associated with each EDM station. Notice that the inset in the 2nd component is on a different color scale for visualization purpose. (c) The corresponding time functions. The first two components show primarily tectonic signals although the spatial function associated with the 2nd component also shows signs of tropospheric effects.

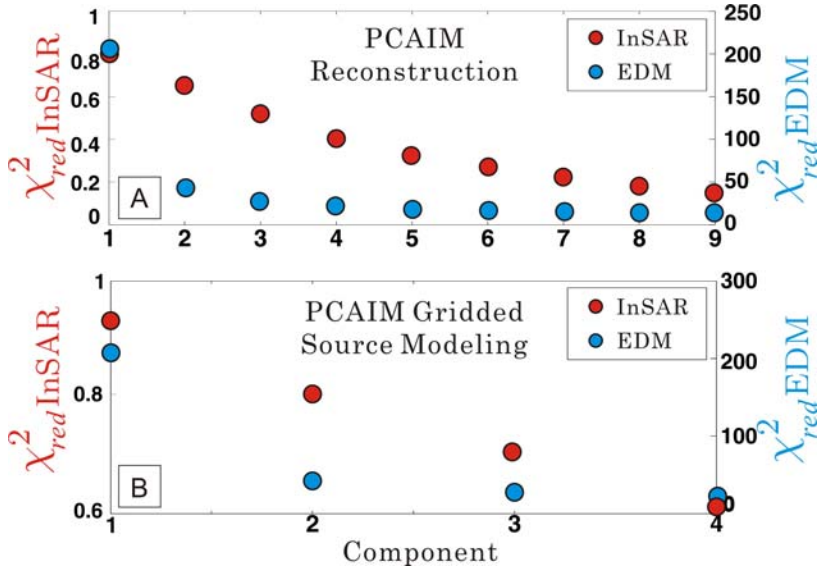

Figure 2.2. Graphs showing the changes of χ_r^2 of the residuals (a) between the observed and reconstructed time series and (b) between the observed and modeled times series as the number of components increases. χ_r^2 is computed considering either the InSAR or the EDM data separately according to equation (1). The closer χ_r^2 is to one, the closer the estimated errors are to the observational/assigned uncertainties, and hence the result is considered to be more reasonable.

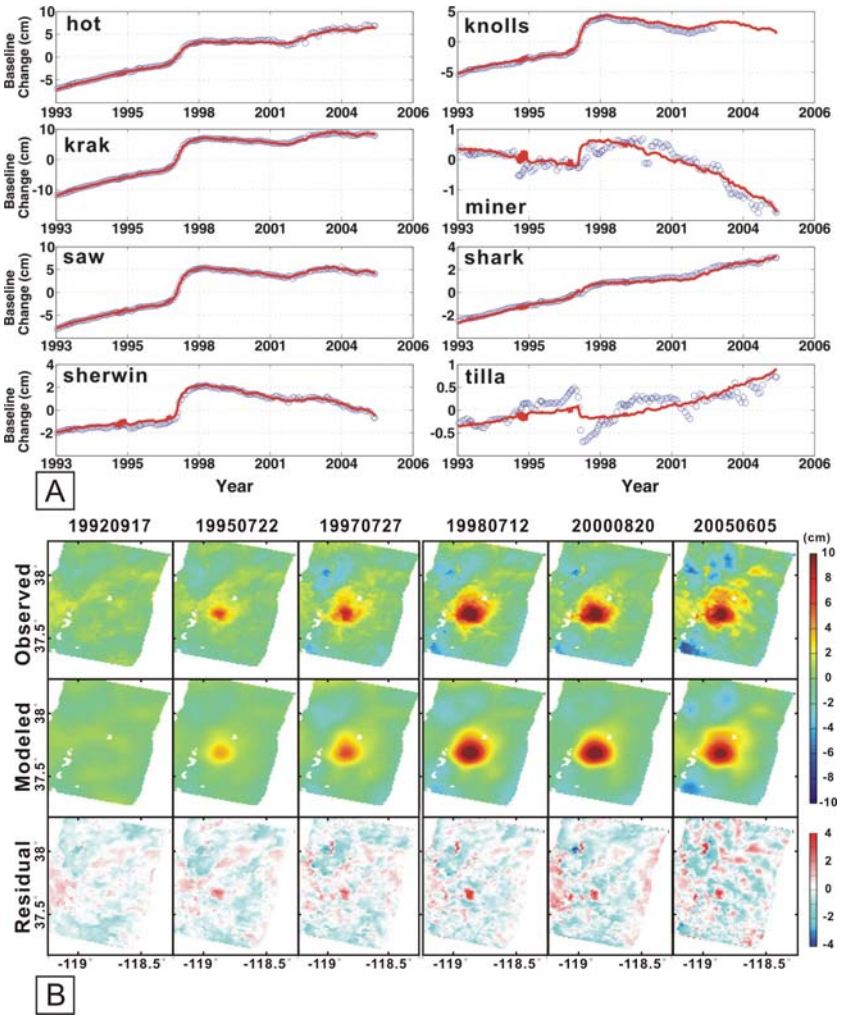

Figure 2.3. (a) Comparison between the observed and modeled EDM time series. The misfits are small at most stations but larger at station MINER and TILLA, probably due to the proximity of these stations to the South Moat fault, which is not taken into account in our modeling. Note the amplitude of the geodetic signals at these two stations is also way smaller than at all the other stations. (b) Upper plot shows the observed InSAR time series of cumulative deformation and the model predictions computed from the inversion of the first 2 components. All time steps are relative to the first date of the SBAS time series (19920604). Only selected time snapshots are shown in this plot. Lower plot shows the residual. Some noises in the 2nd component are captured when doing inversion, but in general there is no significant tectonic signal left in the residual plots. These plots show that the first 2 components are sufficient to account for most of the tectonic signals in the datasets.

Chapter 3

COSEISMIC AND POSTSEISMIC SLIP ASSOCIATED WITH THE 2010 MAULE EARTHQUAKE, CHILE: CHARACTERIZING THE ARAUCO PENINSULA BARRIER EFFECT

Originally published in Lin, Y.N., A. Sladen, F. Ortega-Culaciati, M. Simons, J.-P. Avouac, E. Fielding, B. Brooks, M. Bevis, J. Genrich, A. Rietbrock, C. Vigny, R. Smalley, and A. Socquet (2013) Coseismic and postseismic slip associated with the 2010 Maule earthquake, Chile: characterizing the Arauco Peninsula barrier effect, *J. Geophys. Res.*, doi: 10.1002/jgrb.50207. The modeling and analysis of coseismic slip in this study is carried out by Anthony Sladen.

Abstract

Observations of coseismic and postseismic deformation associated with the 2010 Mw=8.8 Maule earthquake in south-central Chile provide constraints on the spatial heterogeneities of frictional properties on a major subduction megathrust and how they have influenced the seismic rupture and postseismic effects. We find that the bulk of coseismic slip occurs within a single elongated patch approximately 460-km long and 100-km wide between the depths of 15 and 40 km. We infer three major patches of afterslip: one extends northwards along strike as well as down-dip of the major coseismic patch between 40 and 60 km depth; the other two bound the northern and southern ends of the coseismic patch. The southern

patch offshore of the Arauco Peninsula is the only place showing resolvable afterslip shallower than 20-km depth. Estimated slip potency associated with postseismic slip in the 1.3 years following the earthquake amounts to 20-30% of that generated coseismically. Our estimates of the megathrust frictional properties show that the Arauco Peninsula area has positive but relatively low $(a-b)\sigma_n$ values (0.01~0.22 MPa), that would have allowed dynamic rupture propagation into this rate-strengthening area as well as afterslip. Given the only modestly rate-strengthening megathrust friction in this region, the barrier effect may be attributed to its relatively large size of the rate-strengthening patch. Co- and post-seismic uplift of the Arauco Peninsula exceeds interseismic subsidence since the time of the last major earthquake in 1835, suggesting that co- and post-seismic deformation has resulted in some permanent strain in the forearc.

3.1 Introduction

Large megathrust earthquakes frequently trigger aseismic frictional afterslip on the megathrust in regions that are complimentary to those that slipped coseismically [e.g., *Miyazaki et al.*, 2004; *Ozawa et al.*, 2004; *Baba et al.*, 2006; *Hsu et al.*, 2006; *Pritchard and Simons*, 2006; *Perfettini et al.*, 2010; *Vigny et al.*, 2011; *Ozawa et al.*, 2012]. The amplitude of afterslip is generally estimated to range from tens of centimeters to several meters (partially dependent on the size of the mainshock, the time span of the observations, and the approach used to infer afterslip), and the location can range from near the trench to as deep as 100 km. Aftershocks tend to cluster along the boundary between the coseismic and postseismic slip zones [e.g., *Hsu et al.*, 2006; *Agurto et al.*, 2012; *Ozawa et al.*, 2012]. The observed spatial and temporal correlation between

afterslip and aftershocks, and the small contribution of the latter to the total postseismic energy release, suggest that aftershocks are at least partly triggered by afterslip [*Perfettini and Avouac*, 2004; *Hsu et al.*, 2006; *Pritchard and Simons*, 2006; *Perfettini et al.*, 2010]. All these observations suggest that megathrust frictional properties are heterogeneous, allowing interfingering and interplay of seismic and aseismic slip from the trench all the way down to 100 km. However, it is generally difficult to really assess true differences in fault properties due to heterogeneity in models resolution.

In this study, we estimate the distribution of coseismic and postseismic slip to assess the spatial variability of frictional properties on the south-central Chilean megathrust. As inferred from the strong correlation between coseismic slip patches and large-amplitude gravity anomalies in the region of a majority of (but not all) recent large earthquakes [S*ong and Simons*, 2003], the along-strike variations in frictional behavior appear to persist over multiple earthquake cycles [*Song and Simons*, 2003; *Wells et al.*, 2003; *Loveless et al.*, 2010]. Several long-lived geologic features are also correlated with differences in slip behavior on the megathrust. For example, the most prominent patch of aseismic fault slip after the Pisco earthquake in central Peru coincides with the subducting Nazca ridge, which seems to have repeatedly acted as a barrier to seismic rupture propagation in the past [*Perfettini et al.*, 2010]. The region of peak afterslip after the Antofagasta earthquake lies immediately beneath the Mejillones Peninsula, a proposed segment boundary during multiple seismic events, whose Quaternary deformation history is consistent with postseismic uplift [*Pritchard and Simons*, 2006; *Béjar-Pizarro et al.*, 2010; *Victor et al.*, 2011]. Along the Sumatran megathrust, the segment boundary beneath the Batu Islands also correlates with the subduction of the Investigator Fracture Zone [*Chlieh et al.*, 2008].

South-central Chile is an ideal natural laboratory to study the different stages of the seismic cycle and the role of purported seismic barriers because of the information available on past seismic ruptures, strain accumulation in the interseismic period and the seismological and geodetic constraints on the recent Maule earthquake [*Ruegg et al.*, 2002; *Moreno et al.*, 2008; *Ruegg et al.*, 2009; *Moreno et al.*, 2010; *Delouis et al.*, 2010; *Lay et al.*, 2010; *Vigny et al.*, 2011; *Lorito et al.*, 2011]. The Arauco Peninsula is of particular interest because it coincides with the boundary between the Mw=8.8 2010 Maule and the Mw=9.5 1960 Valdivia earthquakes (Figure 3.1a), and in particular may be the location of the 1960 Valdivia earthquake's Mw=8.1 foreshock that was located very close to Concepción [*Cifuentes*, 1989]. Thus, the region of the megathrust below the Arauco Peninsula area has acted as a seismic barrier over at least a few hundred years [*Barrientos and Ward*, 1990; *Moreno et al.*, 2009; *Delouis et al.*, 2010; *Lay et al.*, 2010]. *Melnick et al.* [2009] showed that the peninsula is a zone of rapidly accumulating geological deformation and further proposed that the Arauco acts as a permanent barrier to propagating seismic ruptures on the million-year time scale. They suggest that the Arauco barrier results from the juxtaposition of heterogeneous metamorphic rocks with homogeneous intrusive rocks (Figure 3.1b), causing a compositional and hence mechanical discontinuity in the crust all the way down to the plate interface. A possible alternative is that the Arauco Peninsula would overlie a section of the megathrust that is dominantly aseismic. Zones of aseismic creep have been proposed to act as permanent barriers based on numerical simulations [*Kaneko et al.*, 2010] and observations [e.g. *Chlieh et al.*, 2008; *Konca et al.*, 2008]. To explore this issue, we infer the distribution of coseismic and postseismic slip associated with the 2010 Maule earthquake and estimate the frictional properties along the megathrust.

To assess the uncertainties and resolution in different slip models, we first derive our own coseismic slip model by using an expanded set of available GPS, InSAR, teleseismic and tsunami data. We then derive a postseismic slip model relying on GPS and InSAR observations. We integrate these slip models with the distribution of aftershocks to further illuminate the seismic/aseismic behavior of the megathrust. Finally, we discuss the implications of these slip patterns in terms of associated potency or equivalent moment and implications for the frictional behavior of the megathrust.

3. 2 The 2010 Maule Earthquake and its Seismotectonic Settings

Prior to 2010, the Concepción–Constitución region experienced three large historical megathrust earthquakes in 1730, 1751, and 1835 (Figure 3.1b) [*Campos et al.*, 2002; *Lomnitz*, 2004]. Among these large historic events, the 1730 M 8.5~9 Great Valparaiso earthquake generated a sizable tsunami [*Lomnitz*, 2004]. The 1751 M=8.5 Concepción earthquake generated an even larger and more destructive tsunami. The last large earthquake, with an estimated magnitude of 8.5, has been described by Charles Darwin during the voyage of the HMS Beagle in 1835 [*Darwin*, 1851]. He and captain FitzRoy reported numerous geological phenomena that accompanied the earthquake, including coseismic coastal uplift/subsidence, postseismic deformation, tsunami waves of intermediate amplitude, and volcanic activity. Later in 1928, a smaller event, the M=7.9 Talca earthquake devastated the towns of Talca and Constitución and produced a local tsunami height of only 1.5 m [*Beck et al.,* 1998]. During the 1960 Valdivia earthquake, the Mw=8.1 foreshock ruptured only the southernmost part of this segment [*Cifuentes*, 1989]. Thus, for the majority of the Concepción–Constitución segment, there had been no major

subduction earthquakes since 1835 [*Beck et al.*, 1998; *Campos et al.*, 2002]. The potential for a Mw 8-8.5 earthquake in this region, based on the seismic gap hypothesis, was recognized before the 2010 event [*Ruegg et al.*, 2009], although *Lorito et al.* [2011] argued that the overall slip distribution of the 2010 event is inconsistent with that expected from the seismic gap hypothesis [*Campos et al.*, 2002; *Ruegg et al.*, 2002; *Moreno et al.*, 2008; *Ruegg et al.*, 2009; *Madariaga et al.*, 2010; *Moreno et al.*, 2010].

The 1960 M 9.5 South Chile earthquake occurred to the south of the Concepción–Constitución segment in a region referred to as the Valdivia segment [*Cifuentes*, 1989; *Barrientos and Ward*, 1990] (Figure 3.1a). This earthquake was preceded historically by earthquakes in 1575, 1737 and 1837 [*Lomnitz*, 2004]. The 1575 and 1837 earthquakes produced only small tsunamis at the Río Maullín estuary in the center of the 1960 rupture and they are now believed to be considerably smaller than the 1960 event [*Lomnitz*, 2004; *Cisternas et al.*, 2005] (Figure 3.1a). Between this segment and the Concepción–Constitución segment lies the Arauco Peninsula, a major anomaly along the Pacific margin of South America in terms of coastline morphology and trench-to-coast distance (Figure 3.1a).

The 2010 Maule earthquake nucleated northwest of Concepción [*Delouis et al.*, 2010; *Lay et al.*, 2010], with an epicenter located at 36.41°S and 73.18°W as determined using high-rate GPS records [*Vigny et al.*, 2011]. The rupture appears to have propagated bilaterally through two major asperities and caused severe damage to the city of Constitución, Santiago, Talca, and various others (Figure 3.1b) [*Astroza et al.*, 2010]. The hinge line between surface uplift and subsidence generally lies along the coastline. The only exception is the Arauco Peninsula, where the hinge line cuts through the east of the peninsula and where coastal uplift of up to 240±20 cm was observed [*Vargas et al.*, 2011].

This observation alone points to the peculiar nature of the Arauco Peninsula. Tsunami waves affected the coastal regions between the cities of Valparaíso and Valdivia, with a peak runup of 29 meters on a coastal bluff at Constitución. In most places runup heights are less than 10 meters [*Fritz et al.*, 2011].

Currently there are at least 6 different published coseismic slip models (see supplementary materials of *Vigny et al.* [2011]; also see *Moreno et al.*, [2012]). Major differences between these models include: (1) the updip extent of the primary slip zone (defined by 5-m slip contour) which may extend to the trench (modeling with teleseismic data only, e.g. *Lay et al.* [2010]), stop at 5-10 km (modeling with geodetic data only, e.g. *Tong et al.*, [2010]; *Vigny et al.*, [2011]; *Moreno et al.*, [2012]), or even stop 10-20 km down-dip from the trench (e.g. *Delouis et al.*, [2010]; *Lorito et al.*, [2011]); (2) the center of the southern slip patch may be to the north of the Arauco Peninsula [*Delouis et al.*, 2010; *Lay et al.*, 2010], right under the peninsula [*Tong et al.*, 2010; *Lorito et al.*, 2011; *Moreno et al.*, 2012] or to the west of the peninsula [*Vigny et al.*, 2011]. These published models of fault slip adopt different forms of regularization and boundary conditions and also consider different data sets, thereby making it difficult to compare models. In this study, we develop our own coseismic slip model. By doing so, we can better understand the resolution limit, the contribution and consistency of different datasets, the impact of regularization terms, and the extent to which we can use these models to extract reliable information on fault zone behavior. More importantly, we insure that our co- and post-seismic models are affected by the same potential bias introduced by the inversion procedure and the simplifications made to compute the Green's functions.

3. 3 Data

We combined GPS data from multiple networks, resulting in a total of 127 3-component continuous records. We use a conventional least squares approach to separate postseismic deformation from other signals, including secular rates, coseismic jumps (e.g., the Maule main shock, Pichilemu aftershock as well as other events) and seasonal variations (Figure 3.2). For the short time series whose records start after the Maule earthquake, we determined their horizontal secular rates and seasonal variations by using velocities from the long time series and from published literature (Figure 3.2A) [*Moreno et al.*, 2008; *Ruegg et al.*, 2009]. We did not carry out the same corrections on the vertical components due to the large uncertainties in their secular rates (Figure 3.2B) [*Ruegg et al.*, 2009], but chose to use only the long time series in our postseismic model. In the end, 79 3-component coseismic displacements are determined with 27 of them, mostly far-field stations, augmenting the dataset described in *Vigny et al.* [2011]; 66 cGPS stations are used in the postseismic model, among which 22 vertical records were considered usable.

By inspecting the cumulative postseismic displacements (Figure 3.2E & F) we found the peak horizontal displacement near the coast as expected; however the peak vertical displacement occurs near the Andes. This pattern is different from any analytical prediction of a thrust fault system in an elastic half-space or layered half-space (Figure 3.2C & D). The peculiarity in the postseismic data therefore indicates such models will have difficulty in fitting all the postseismic data with simple models of slip restricted to the megathrust.

Besides GPS time series, the Japanese L-band Advanced Land Observation Satellite (ALOS) provided continuous monitoring along this region after the earthquake for almost one year

(Figure 3.3). Among the data ALOS acquired, wide-swath descending track 422 forms the most continuous image of the coseismic and early postseismic deformation field (Figure 3.3 & 3.4). In addition to this wide-swath track, ascending tracks 111 through 119 provide continuous spatial coverage over different time spans all the way through the end of 2010. We refer the reader to Appendix B for more details regarding the GPS data processing, corrections applied to coseismic and postseismic InSAR images and the issues associated with data sampling.

3. 4 Coseismic Slip Model

To solve for the distribution of coseismic slip of the Maule earthquake, we perform a joint inversion of all the static data previously described (i.e. InSAR and GPS) as well as teleseismic body waves (Figure 3.5; also see Appendix B) using the method of *Ji et al.* [2002]. Consistent with previous models, our preferred coseismic slip model indicates that rupture was bilateral and extended over 500 km (Figure 3.5C). The slip model defines a relatively continuous band of significant slip extending ~100-km down dip that parallels but extends only slightly below the coastline (Figure 3.6). The distribution of slip is dominated by a region of high slip north of the epicenter (centered around latitude S35°) with a maximum slip of 16 m, close to the 15-m peak slip from *Vigny et al.* [2011]. In the southern part of the rupture, near the Arauco peninsula, the slip distribution is more irregular with slip amplitudes not exceeding 8 m.

The coseismic model allows us to reproduce the main characteristics of the different datasets (Figure 3.4, 3.5 & 3.6). There are several residual fringes in some of the InSAR tracks. However, given the orientation of those residual fringes, we suspect unmodeled

propagation delays due to ionospheric perturbations or non-optimal orbital ramp corrections. In the case of the GPS data, all vectors are fit extremely well with the exception of the vertical component of the profile extending eastwards from Constitución around latitude S35.3°. In essence, the region of observed coseismic subsidence is narrower (i.e., with a more limited eastward extent) than what our model produces (Figure 3.6). Extending the down-dip limit of our fault geometry allows improvement in the fit to the vertical displacements by allowing localized slip patches beneath the problematic stations near the Andes. Given the correlation of these deep slip patches with the sparse location of the GPS stations, we are not sure if they are reliable or if they reflect, for instance, an over-simplification in the model fault geometry and elastic model. We note that *Moreno et al.* [2012] adopted a finite-element model that takes more subtleties in the fault geometry into account, but their results also show the same residuals in the GPS vertical components near the Andes. We return to this point later in the discussion section.

To limit the potential trade-off between rupture time and rupture duration, which is enhanced by the bilateral rupture [e.g. *Lay et al.*, 2010], as well as to limit the non-uniqueness of the solution, we impose a narrow prior range of 2.5-3.0 km.s-1 for the rupture velocity [*Delouis et al.*, 2010; *Vigny et al.*, 2011] and allow each patch to rupture only once for a maximum of 14s. Despite these strong prior constraints on the solution, we obtain a slip distribution similar to the geodetic-only inversion (Figure B3) with a reasonable fit of the complex teleseismic P-wave train (Figure 3.5).

Coseismic slip in our preferred model stops about 15 km from the trench at the latitude of maximum slip (Figure 3.5). This behavior is similar to the models of *Delouis et al.* [2010] and *Lorito et al.* [2011], who also included multiple data types in their inversions. This slip extent agrees well with the 90% coupling patch determined by the interseismic GPS

measurements during the past decade [*Métois et al.*, 2012], although the resolution of the near-trench portion of the megathrust is significantly reduced. Coseismic slip on the shallowest part of the megathrust is difficult to constrain from on-land geodetic data alone because of the decreases in resolution with distance from the observations (illustrated by a checkerboard test in Figure B4). In addition to this well-established limitation, resolution is also affected by model errors, that is, the use of approximate Green's functions, not taking into account complex fault geometry (e.g. splay-faults), the effect of topography and of gradients in material properties (e.g. *Hsu et al.* [2011]). To illustrate just one of these effects, we estimated a solution adopting a homogeneous elastic half-space instead of a 1D layered half-space. The result (Figure B8) shows a slip distribution very similar to our preferred model but with slip extending closer to the trench. This simple test illustrates that the extent of shallow slip may be fairly sensitive to the assumed velocity structure. This conclusion is also supported by the checkerboard and sensitivity tests performed on the coseismic and postseismic models (Figure B4, B6 and B7) .

On the other hand, tsunami data recorded in the open ocean is sensitive to the outer extent of the megathrust rupture and can be used to constrain the rupture of large subduction earthquakes [e.g. *Satake*, 1993; *Piatanesi* and *Lorito*, 2007; *Sladen and Hébert*, 2008; *Sladen et al.*, 2010; *Lorito et al.*, 2011; *Simons et al.*, 2011]. The tsunami simulation for our slip model, using the tsunami model described in *Heinrich et al.*, [1998] and *Hébert et al.* [2001], provides good predictions of the tsunami waveforms at nearby tide gauges (with the exception of the Ancud and Corral tide gages located deep inside complex bays) and open-ocean buoys, but arrives too early at most stations south of the main tsunami energy beam (Figure 3.7). Back-projection of the tsunami (Figure B9) indicates that only buoy 51406 is directly sensitive to the slip distribution up-dip of the main slip patch (see

Appendix B). Even considering the effects of rupture propagation, the tsunami simulation of our preferred slip model arrives 4 min too early at that 51406 station(Figure 3.7), suggesting that it is unlikely that the slip extended even closer to the trench. This argument is consistent with the study of *Lorito et al.* [2011] who included the tsunami records in their inversion of the slip distribution. However, this result mainly relies on one distant station and we cannot exclude the possibility that dispersion effects not taken into account in the shallow-water approximation could have biased the timing of that tsunami record.

The along-strike extent of our preferred slip model, as defined by areas with slip in excess of 5 m, is about 460 km. The northern edge of the slip model (at latitude 34°S) is remarkably sharp, a characteristic also visible in the source time function which abruptly stops after 100 s. This sharp rupture termination may have promoted the static triggering of the Pichilemu aftershock sequence [*Farias et al.*, 2011; *Vigny et al.*, 2011]. The southern slip patch is centered under the Arauco Peninsula, extending slightly northwestwards. This pattern agrees with several published results in general [*Tong et al.*, 2010; *Lorito et al.*, 2011; *Moreno et al.*, 2012]. The total seismic moment of our slip model is 2.25e+21 N.m, equivalent to Mw 8.8, a value close to that estimated by GCMT (1.86e+21 N.m).

3. 5 Postseismic Slip Mode

There are a few differences in the construction of the coseismic and postseismic slip models. To derive the time-dependent finite source kinematic models, we use the Principle Component Analysis-based Inversion Method (PCAIM) [*Kositsky and Avouac*, 2010; *Lin et al.*, 2010]. We build a larger fault plane since postseismic slip may take place at greater

depth. The fault plane for the postseismic model assumes a curved shape to fit the geometry imaged by various techniques (seismicity, tomography and so on). In addition, we apply the sensitivity-modulated regularization scheme from the work of *Ortega-Culaciati et al.* [2013] to take care of the model resolution at different depths. The details of these changes are described in Appendix B.

The RMS residual is 0.9 cm for the horizontal GPS observations and 1.1 cm for vertical components. These values reflect both measurement and prediction error. We find systematic residuals for the GPS observations near the Andes, including SJAV, CURI, MAUL and ELA2 in the north and UDEC, ANTC, LAJA, LMNS and ESQA in the south (Figure 3.8). The E-W components of the time series of these stations display a slower westward increase during the initial postseismic period when compared with other stations, but a faster trend after the first 200 days. The misfit to these stations suggests a modeling inadequacy in our layered elastic half-space afterslip model. We discuss these misfits further in section 6.4.

In Figure 3.9 we compare three postseismic slip models, constrained by GPS horizontal components only, GPS horizontal plus vertical components, and 3-component GPS plus InSAR datasets, respectively. Strike-slip motion in these models is minor, so we can treat the slip as primarily dip-slip motion. The comparison of the patterns between the first two models (Figure 3.9A & 3.9B) reveals nuances, particularly the connectivity, in the afterslip patch down-dip of the coseismic slip region. This elongated zone, designated as A, extends from almost 40 km to 60 km at depth, with maximum slip of ~1.8 m over the first 488 days after the mainshock. This creeping zone generally agrees with the results from *Vigny et al.* [2011] but is more spatially focused, due to a combination of the augmented GPS and

InSAR data and the differing forms of regularization employed. This elongated afterslip zone also coincides with the down-dip slip deficit zone proposed by *Moreno et al.* [2012].

Incorporating the InSAR dataset (Figure 9C) allows us to resolve a shallow afterslip patch offshore of the Arauco Peninsula and a deep slip patch that is separated from the main slip patch. The offshore region of slip, designated as B, is the only region with slip shallower than 20 km. Slip on this patch is constrained primarily by InSAR observations, as we only have one near-coast GPS station between latitudes 38° and 40° S. This lack of GPS data is why this region of afterslip was not captured in the early model from of *Vigny et al.* [2011]. A third slip patch that is not as shallow as patch B is located to the northern edge of the coseismic slip patch. This patch, designated as C, is between 20-40 km at depth. Its spatial extent agrees well with the results from *Vigny et al.* [2011]. Patch B and C together bound the southern and northern edge of the whole coseismic slip patch and agree with the Arauco and San Antonio intersegment area that define the Maule segment in *Métois et al.* [2012].

The deep slip patch, designated as D, extends to 120-160 km at depth. This region of slip is spatially distinct from patch A and B located further up-dip. The slip on this patch is also primarily constrained by InSAR, since the residuals for the GPS observations in this region are large. It is therefore likely that our model maps some uncorrected noise in InSAR data (atmospheric noises in particular since this patch is close to the Andes) or other geophysical processes in the InSAR data onto the subduction interface. Given these issues, we do not interpret the slip in this patch further.

Except for patch B, we do not see significant afterslip updip of the regions that slipped coseismically, i.e. from the trench to 20 km at depth. This result agrees with the nearly

zero interseismic slip deficit in the up-dip portion of the megathrust [*Moreno et al.*, 2012]. Although the resolution of interseismic and postseismic slip is particularly poor there, it is possible that the shallowest portion of the megathrust might creep interseismically. However, *Agurto et al.* [2012] show that some M>4 earthquakes and associated seismically-related afterslip occurred postseismically between March 2010 and March 2012 along the updip edge of the coseismic slip patch south of 35.3°S (also see Appendix B). Given the trench-coast distance and the onshore distribution of GPS stations, it is possible that the extent and magnitude of shallow afterslip is beyond the resolution of this study. Our slip potency test (Appendix B) shows that some amount of shallow afterslip cannot be excluded, although the associated slip potency does not exceed ~10% of the total coseismic slip potency.

3. 6 Discussion

3.6.1 Postseismic Moment Release

Acknowledging that geodetic data primarily constrain the potency associated with fault slip and not seismic moment, we estimate that the moment released by postseismic slip in 1.3 years is 3.6~5.1 1021 N.m (Mw=8.34~8.44), equivalent to 20~30% of the coseismic moment. This ratio is similar to that of earthquakes of similar magnitude, such as the 2001 Mw=8.4 Arequipa earthquake in southern Peru (20-40% in 1 year) [*Ruegg et al.*, 2001; *Melbourne et al.*, 2002] and the 2005 Mw=8.7 Nias earthquake (>25% in 9 month) [*Hsu et al.*, 2006]. The relative magnitude of postseismic to coseismic moment seems to scale with the magnitude of the mainshock (Figure 3.10A). Smaller earthquakes tend to produce relatively less afterslip, such as the 1995 Mw=8.1 Antofagasta earthquake (<20%

in 1 year) [*Melbourne et al.*, 2002; *Chlieh et al.*, 2004; *Pritchard and Simons*, 2006] and 2007 Mw=8.0 Pisco earthquake (7-28% in 1.1 years) [*Perfettini et al.*, 2010], whereas larger earthquakes tend to have larger values, such as the 2004 Mw=9.1 Sumatra earthquake (30% in the first month and 38% in 3 months) [e.g., *Chlieh et al.*, 2007] and the 2011 Mw=9.0 Tohoku earthquake (18% in 7 months [*Ozawa et al.*, 2012] and ~25% in 1 year [*Geospatial Information Authority of Japan*, 2012]) .

Pritchard and Simons [2006] also pointed out the amount of sediment subducted may also help modulate the postseismic behavior. As shown in Figure 3.10B, the relative magnitude of postseismic to coseismic moment increases with sediment thickness, although the correlation is less prominent due to the large variations in trench sediment thickness and the uncertainties in its estimation. We may even attribute the correlation back to the idea that thick trench sediments smooth out the slab topography and encourage large earthquakes [*Ruff*, 1989]. Such relationship seems to hold in many earthquakes, the most well-known of which is the 1.5-km thick trench sediments in southern Chile and the Mw=9.5 1960 Valdivia earthquake [*Scherwath et al.*, 2009; *Contreras-Reyes et al.*, 2010]. It is therefore difficult to tell which factor, the sediment thickness or the coseismic stress drop, contributes more to the afterslip behavior along the subduction interface.

In both correlation plots, outliers exist. Smaller earthquakes can still be followed by afterslip having a large potency, such as the 1989-1994 Sanriku-oki earthquake sequences in Japan (ranging from Mw=6.9 to Mw=7.7) [*Heki and Tamura*, 1997; *Kawasaki et al.*, 2001]. Because the moment release rate is so large (100% in 5~50 days) these postseismic events were further defined as “ultra-slow earthquakes” and may likely result from very unique source properties on the subduction interface [*Kawasaki et al.*, 1995]. Other

examples include the large afterslip of the 2005-2008 Mw~7 earthquakes along the Japan Trench megathrust, whose postseismic moment release exceeded that of the corresponding coseismic events [*Suito et al.*, 2011]. Because the number of earthquakes is small and obvious exceptions exist, more case studies are required to elucidate the possible correlation between the coseismic and postseismic moment release.

3.6.2 Spatial Friction Variations and the Earthquake Barrier

The cumulative moment due to all aftershocks with Mw>3 reported in the National Earthquake Information Center (NEIC) catalogue over the same period of time amounts to only 5.58e+1019 N.m, indicating that about 99% of the observed postseismic deformation was aseismic, a value even larger than that of the 2005 Nias earthquake (93%, *Hsu et al.* [2006]). *Agurto et al.* [2012] found that in the case of Maule aftershocks, the concentration of larger aftershocks (M=4~6) at the boundary between coseismic and postseismic patches illuminates the region with the highest concentration of stress right after the mainshock, as well as the boundary of the regions of greatest aseismic afterslip. This region is also the loci of a majority of coseismic high-frequency radiators [*Lay et al.*, 2010]. Their spatial distribution depicts the region of frictional heterogeneities within the brittle-ductile transition zone, i.e. small discrete brittle asperities dotted amidst ductile creeping zone [*Ito et al.*, 2007; *Simons et al.*, 2011; *Meng et al.*, 2011]. However, this creeping zone is further bounded by a second band of aftershocks at the down-dip margin [*Rietbrock et al.*, 2012], with lobes of afterslip patches sandwiched in between the upper and lower aftershock clusters (Figure 3.9D), mimicking the complex mosaic of phenomena revealed by the study of the 1995 Antofagasta earthquake in northern Chile and its

corresponding afterslip and aftershocks [*Pritchard and Simons*, 2006]. These deeper aftershocks may result from slip on small stick-slip patches triggered by afterslip. Their locations suggest a non-monotonic change from a stick-slip regime to a creeping regime with increasing depth.

To explore the frictional properties of the fault patches that produced aseismic afterslip, we compute afterslip with a simple theoretical model. We calculate slip predicted from a one-dimensional rate-strengthening frictional sliding model, assuming that frictional stress increases linearly with the logarithm of the sliding velocity, as observed in laboratory experiments [*Marone*, 1998]. Based on this model and later analytical derivations [*Perfettini and Avouac*, 2004; *Perfettini et al.*, 2010], postseismic slip $U(t)$ evolves as

$$U(t) = V_{pl}\, t_r\, log[1+(V^+/ V_{pl}\, t_r)\, t] \quad (1)$$

where t is time, V_{pl} is the plate convergence velocity, t_r is the relaxation time, V^+ can be viewed as the instantaneous creeping velocity during the postseismic period, and the ratio V^+/ V_{pl} represents the postseismic creep rate normalized by the long-term plate convergence velocity.

For the elongated region of slip down-dip of the coseismic slip patch (patch A in Figure 3.9), the shallow afterslip offshore of the Arauco Peninsula (patch B), and the afterslip that bounds the coseismic slip patch to the north near San Antonio (patch C), we find a very stable value of tr of approximately 3.3-4.6 yrs and V^+/ V_{pl} of 70-130 (Figure 3.11). We further convert V_{pl} and t_r to parameters more closely related to material properties, following the formulation described by *Perfettini and Avouac* [2004]. Using a value of coseismic Coulomb stress change of 3 MPa for the elongated down-dip region, 0.5-1 MPa around the offshore Arauco Peninsula, and 2.5-3 MPa for the northern afterslip patch

[*Lorito et al.*, 2011], we find $(a-b)\sigma_n$ = 0.08-0.62 MPa for patch A, 0.01-0.22 MPa for patch B, and 0.04-0.65 MPa for patch C, where σ_n denotes effective normal stress, and *a-b* is the frictional parameter (see *Hsu et al.* [2006] for the steps of obtaining these ranges of $(a-b)\sigma_n$ values).

a-b describes how the coefficient of friction varies as a function of the logarithm of sliding velocity, with positive values corresponding to velocity strengthening and negative values to velocity weakening. The smaller estimated $(a-b)\sigma_n$ value for the offshore Arauco Peninsula and the intermediate value for the northern afterslip patch near San Antonio may result from smaller a-b values than surrounding regions, suggesting strong variations in effective megathrust fault properties in the Arauco and San Antonio intersegment areas. Alternatively, locally high pore pressure and therefore small effective normal stress may play an important role in changing the slip behavior in this region. However, *Cubas et al.* [2013] use the critical taper theory to infer a value of 0.375-0.6 for the Hubbert-Rubey parameter in these two areas (the ratio of pore pressure versus the lithostatic pressure, with 0.4 for hydrostatic, *Hubbert and Rubey* [1959]), suggesting that the pore pressures is not extraordinarily high in this region. Therefore, it is likely that local frictional heterogeneity (smaller positive *a-b* values) is responsible for the postseismic creep in the intersegment areas. Numerical modeling of rate-and-state frictional sliding on a shear-loaded planar fault also suggests that when a-b is smaller, postseismic sliding propagates far from the coseismic slip region over short time intervals [*Kato*, 2007].

Compared to intermediate $(a-b)\sigma_n$ values in the San Antonio intersegment area, the nearly neutral inferred value near Arauco might help explain some specific aspects of this area. It has been suggested, based on dynamic modeling of slip on a fault with heterogeneous rate-

and-state friction patches, that the barrier effect of a rate-strengthening patch scales with the product of $(a-b)\sigma_n$ and the size of the patch [*Kaneko et al.*, 2010]. It might be argued that because of a relatively small value of $(a-b)\sigma_n$ in the Arauco Peninsula area (0.01-0.22 MPa), dynamic ruptures can propagate into the area but do not rupture through it because of its relatively large size. This effect might explain why we observed both some co-seismic slip and aseismic afterslip beneath the Arauco Peninsula area. This inference would also be consistent with seismic slip of ~5 m beneath the Arauco Peninsula during the 1960 Valdivia earthquake [*Moreno et al.*, 2009], although the spatial resolution of the models is very low due to the limited availability of relevant observations. The Arauco Peninsula area would owe its character as a barrier to the size of the modestly rate-strengthening zone. The along-trench length of the Arauco Peninsula barrier is ~100 km, much longer than the Batu Islands barrier in Sumatra [*Chlieh et al.*, 2008] and the Mejillones Peninsula barrier in northern Chile [*Pritchard and Simons*, 2006; *Béjar-Pizarro et al.*, 2010; *Victor et al.*, 2011] which may also be examples of rate-strengthening barriers on subduction megathrusts. The findings from the Arauco Peninsula barrier are consistent with the idea that both the $(a-b)\sigma_n$ value and the barrier size determine the barrier effect of a velocity strengthening patch [*Kaneko et al.*, 2010].

3.6.3 Arauco Peninsula Uplift

We now consider the timing of the deformation of the peninsula in the context of the seismic cycle. If we assume that the whole medium is purely elastic, all elastic strain that accumulates during the interseismic period should be released in earthquakes. In this case, there is no permanent strain and no formation of the peninsula. Clearly, inelastic

deformation must have occurred or be occurring to account for the uplift of the Arauco Peninsula. *Melnick et al.* [2009] suggest that there are two styles of long-term deformation on the peninsula: anticlinal bending (Figure 3.12b), with the anticline axis going through the center of the peninsula in a WNW-ESE orientation, and back tilting, with the marine terraces tilting toward the east (Figure 3.12e). We now compare these deformation styles to the geodetic data and modeled results we obtained during the past two decades. Because of the lack of in-situ measurements within the swath along the profile a-a', we use only the modeled uplift to derive the total uplift between 1835 and 2010 (Figure 3.12c). Using the elapsed time of 175 years, the equivalent interseismic uplift rate is nearly equivalent to the measured subsidence rate (Figure 3.12d). The nearly neutral balance seems to indicate that all the elastic strain has been released during the two large earthquakes and no permanent strain has accumulated within the last seismic cycle. However, based on the estimates from *Melnick et al.* [2009], the long-term uplift rate ranges from 1.8 mm/yr near the anticline axis to 0.3 mm/yr near the bottom of the anticline flank. The difference is so small (1.5 mm/yr) that it resides within the errors of model predictions and the GPS observations. In this case, we probably would not be able to isolate coseismic or interseismic non-elastic deformation of the anticline on the Arauco Peninsula.

Along profile b-b', the uplift pattern from model predictions agrees in general with field observations (Figure 3.12f), and the cumulative coseismic deformation since 1835 mimics the back-tilting of the peninsula. The equivalent uplift rate during the past 175 years is slightly larger than the interseismic subsidence as we get close to the trench, resulting in backtilt-like deformation (Figure 3.12g). A straightforward interpretation is that the backtilting of the peninsula may form during the coseismic and early postseismic periods,

although it is not clear whether the anticlinal folding should also happen at the same time. This permanent non-elastic deformation could be either associated with the elastic cycle on the megathrust, or resulting from the slip on crustal splay faults in the frontal accretionary prism (Figure 3.1B; *Contreras-Reyes et al.* [2010]; *Melnick et al.* [2012]). As the chance of rupture propagation into this area increases due to low inferred $(a-b)\sigma_n$ values, so does the triggered slip on the crustal splay faults, and the accumulation of non-elastic deformation. This idea of coseismic and postseismic uplift of the Arauco Peninsula is different from the observations around the Mejillones Peninsula in northern Chile [*Ortlieb et al.*, 1996; *Pritchard and Simons*, 2006; *Loveless et al.*, 2010] and the Paracas Peninsula in Peru [*Sladen et al.*, 2010], whose patterns of coseismic vertical movement are different from that of the long-term deformation. The behavior of these peninsulas is considered to be dominated by postseismic and interseismic uplift [*Sladen et al.*, 2010; *Victor et al.*, 2011]. An alternative interpretation is that the backtilting of the Arauco Peninsula results from a deficit of interseismic subsidence, which in turn is the net effect of elastic subsidence and non-elastic uplift in the interseismic period. The coeval strain accumulation of opposite signs is a more complicated interpretation, and therefore field evidence is needed to support this view.

3.6.4 Limitations

We summarize here all the discrepancies between observations and predictions, together with the anomalies in our model. First, our favored coseismic slip model fails to predict the short-wavelength signals in the GPS vertical component (Figure 3.6), which can be fit only when allowing deep slip patches beneath the Andes [*Vigny et al.*, 2011]. Second,

there is a systematic misfit in postseismic horizontal displacements for GPS stations around the Andes (Figure 3.8). These stations demonstrate different deformation behaviors from the three major afterslip patches (Figure 3.11). These results suggest that the mid to far field sampling of the deformation field associated with the Maule earthquake will require more realistic models than elastic or layered elastic half-space.

The above-mentioned discrepancies and model anomalies can be potentially explained by one or more of the following: (1) over-simplification of the elastic model, (2) elastic deformation along other uppercrustal structures, and (3) deformation due to other mechanisms, such as viscoelastic deformation. We address these issues separately below.

As demonstrated earlier, adopting a homogeneous elastic half space or a 1D layered elastic half space can modulate the inferred patterns of fault slip (Figure B8). *Hsu et al.* [2011] have pointed out the important role played by 3D elastic structure in fault slip inversions. Based on heat flow observations and numerical models, *Völker et al.* [2011] estimated that the geothermal gradient varies greatly over a distance of 400-km, from 10℃/km near the coast, to 5.5℃/km near the Central Valley, and to 22.5℃/km below the Andes. Given the temperature and compositional dependence of elastic moduli, we may expect considerable 3D variations in elastic structure. Future models of this region using 3D elastic Green's functions may help us understand the discrepancies – although our relatively poor a priori understanding of 3D elastic structure may make such an effort pointless.

We are also concerned with the potential role played by upper-crustal structure(s) during and after the earthquake. This explanation for the misfits proximal to the Andes may be as viable as that of variations in 3D elastic structure, although elastic deformation associated with the earthquake cycle at the plate boundary will not result in the permanent

deformation that built the Andes. Slip on a shallow crustal fault, or a down-dip extension of such a fault, will create permanent surface deformation of a smaller spatial wavelength similar to the depth of the dislocation tip, a pattern that we see in the coseismic vertical displacement field. Given the locations of the GPS stations with large misfits across the Andes (Figure 3.8), the Neogene Deformation Front, the west-vergent thrust faults that bounds the west flank of the Andes (between 32° and 38°S, Figure 3.1B & 3.1C) and their associated décollement may be potential candidates for such an aseismically slipping upper crustal structure (Figure 3.1C; *Armijo et al.* [2010]). The Quaternary deformation pattern along this fault system has long been a subject of debate. There appears to be little indication of Quaternary contraction except along a small section of Southern Central Andes (36°-38°S) [*Folguera and Ramos*, 2009]. *Folguera et al.* [2007, 2008] even argue that an extensional state of stress in the Andean Cordillera and foothills is producing a regional collapse. On the other hand, *Cobbold and Rossello* [2003], *Galland et al.* [2007], *Guzmán et al.* [2007] and *Messager et al.* [2010] postulate that the stress regime remains mainly compressive. If this shallow crustal fault hypothesis holds, its associated surface deformation will still be intertwined with deformation from the interaction on the plate boundary, making it nontrivial to separate the relative contribution from each structure. A denser and more optimally designed GPS network may be needed to specifically target these upper plate structures. We recognize that considerably more study is needed in order to characterize the role, if any, of hypothesized upper crustal structures, how they are driven by the plate boundary, and how they contribute to the non-elastic deformation that creates the Andes.

It is also possible that viscoelastic deformation may account for a non-negligible part of the observed postseismic deformation [e.g. *Pollitz et al.*, 1998, 2006]. Nevertheless, since

viscoelastic deformation is triggered by coseismic stress change and acts mainly during the postseismic period, this process alone will not reconcile the discrepancies between the observed short-wavelength and modeled long-wavelength coseismic vertical deformation. It is likely that the combination of two or more of the aforementioned processes is necessary to explain all the coseismic and postseismic data for the Maule earthquake.

These discrepancies between our models and the data have significant implications. The Maule earthquake produced measureable deformation in the overriding plate out to a distance of over 1000 km. The standard co- and post-seismic modeling of such events using layered elastic half-space produces results that explain observations in western Chile well. Our models are less successful in explaining observations in central and eastern Chile and all of Argentina. Such observations, which are not available when the overriding plate consists of a relatively narrow island chain (such as Sumatra and Japan), will potentially provide the data needed to differentiate between competing models for postseismic behavior.

3. 7 Conclusion

To summarize, our joint inversion model shows a coseismic slip pattern similar to the previous ones derived from joint inversion of seismic, geodetic and tsunami data [*Delouis et al.*, 2010; *Lorito et al.*, 2011]. The shallowest 15-20 km of the megathrust shows neither significant coseismic slip nor resolvable postseismic slip, suggesting that the slip on this portion of the megathrust is dominantly due to interseismic creep (between 1835 and 2010). Slip on the megathrust at depth between 15-20 and 50 km is probably mostly seismic. An exception is near the Arauco Peninsula, where aseismic afterslip extends to as

shallow as 10 km near trench. We derive a nearly neutral *a-b* value for this shallow afterslip patch, consistent with the inferred propagation of seismic rupture into this region, whereas the large width of this segment boundary would be the main reason for its barrier effect. This conditionally stable characteristic may also be related to the coseismic uplift of the Arauco Peninsula, as seismic ruptures may propagate more easily into this barrier and trigger the slip on upper-crust structures. Postseismic energy release follows a general trend in which the amount of postseismic slip scales with the coseismic moment release. Our result also shows marked data misfit near the Andes, indicating that other geophysical processes may be involved in the postseismic deformation over the region.

References of Chapter III

Agurto, H., A. Rietbrock, I. Ryder, and M. Miller (2012), Seismic-afterslip characterization of the 2010 MW 8.8 Maule, Chile, earthquake based on moment tensor inversion, *Geophys. Res. Lett.*, 39, L20303, doi: doi:10.1029/2012GL053434.

Armijo, R., R. Rauld, R. Thiele, G. Vargas, J. Campos, R. Lacassin, and E. Kausel (2010), The West Andean Thrust, the San Ramon Fault, and the seismic hazard for Santiago, Chile, *Tectonics*, 29, TC2007, doi: 10.1029/2008TC002427, 2010.

Astroza, M., F. Cabezas, M. O. Moroni, L. Massone, S. Ruiz, E. Parra, F. Cordero, and A. Mottadelli (2010), *Intensidades sismicas en el area de danõs del terremoto del 27 de Febrero de 2010*, Departamento de Ingeniería Civil, Facultad de Ciencias Físicas y Matemáticas, Universidad de Chile.

Baba, T., K. Hirata, T. Hori, and H. Sakaguchi (2006), Offshore geodetic data conducive to the estimation of the afterslip distribution following the 2003 Tokachi-oki earthquake, *Earth Planet. Sci. Lett.*, 241, 281-292, doi: 10.1016/j.epsl.2005.10.019.

Barrientos, S. E., and S. N. Ward (1990), The 1960 Chile earthquake: inversion for slip distribution from surface deformation, *Geophys. J. Int.*, 103(3), 589-598.

Beck, S., S. Barrientos, E. Kausel, and M. Reyes (1998), Source characteristics of historic earthquakes along the central Chile subduction zone, *J. S. Am. Earth Sci.*, 11(2), 115-129.

Béjar-Pizarro, M., et al. (2010), Asperities and barriers on the seismogenic zone in North Chile: state-of-the-art after the 2007 Mw 7.7 Tocopilla earthquake inferred by GPS and InSAR data, *Geophys. J. Int.*, 183(1), 390-406, doi: 10.1111/j.1365-246X.2010.04748.x.

Burgmann, R., M. G. Kogan, V. E. Levin, C. H. Scholz, R. W. King, and G. M. Steblov (2001), Rapid aseismic moment release following the 5 December, 1997 Kronotsky, Kamchatka, earthquake, *Geophys. Res. Lett.*, 28(7), 1331-1334, doi: 10.1029/2000gl012350.

Cahill, T., and B. L. Isacks (1992), Seismicity and Shape of the Subducted Nazca Plate, *J. Geophys. Res.*, 97(B12), 17503-17529, doi: 10.1029/92jb00493.

Campos, J., D. Hatzfeld, R. Madariaga, G. Lopez, E. Kausel, A. Zollo, G. Iannacone, R. Fromm, S. Barrientos, and H. Lyon-Caen (2002), A seismological study of the 1835 seismic gap in south-central Chile, *Phys. Earth Planet. In.*, 132(1-3), 177-195, doi: 10.1016/S0031-9201(02)00051-1.

Chlieh, M., J. B. De Chabalier, J. C. Ruegg, R. Armijo, R. Dmowska, J. Campos, and K. L. Feigl (2004), Crustal deformation and fault slip during the seismic cycle in the North Chile subduction zone, from GPS and InSAR observations, *Geophys. J. Int.*, 158(2), 695-711, doi: 10.1111/j.1365-246X.2004.02326.x.

Chlieh, M., et al. (2007), Coseismic slip and afterslip of the great M(w) 9.15 Sumatra-Andaman earthquake of 2004, *B. Seismol. Soc. Am.*, 97(1), S152-S173, doi: 10.1785/0120050631.

Chlieh, M., J. P. Avouac, K. Sieh, D. H. Natawidjaja, and J. Galetzka (2008), Heterogeneous coupling of the Sumatran megathrust constrained by geodetic and paleogeodetic measurements, *J. Geophys. Res.*, 113(B5), B05305, doi: 10.1029/2007jb004981.

Cifuentes, I. L. (1989), The 1960 Chilean Earthquakes, *J. Geophys. Res.*, 94(B1), 665-680.

Cisternas, M., et al. (2005), Predecessors of the giant 1960 Chile earthquake, *Nature*, 437(7057), 404-407, doi: 10.1038/nature03943.

Cobbold, P. R., and E. A. Rossello (2003), Aptian to recent compressional deformation, foothills of the Neuquen Basin, Argentina, *Mar. Pet. Geol.*, 20(5), 429-443, doi: 10.1016/S0264-8172(03)00077-1.

Contreras-Reyes, E., E. R. Flueh, and I. Grevemeyer (2010), Tectonic control on sediment accretion and subduction off south central Chile: Implications for coseismic rupture processes of the 1960 and 2010 megathrust earthquakes, *Tectonics*, 29(6), TC6018, doi: 10.1029/2010TC002734.

Cubas, N., J.P. Avouac, N. Lapusta, P. Souloumiac, and Y. Leroy (2013), Megathrust frictional properties of the 2010 Mw 8.8 Maule earthquake area in relation to forearc morphology, mechanical stability, and earthquake rupture dynamics, in preparation.

Darwin, C. (1851), *Geological observations on coral reefs, volcanic islands, and on South America -- being the geology of the voyage of the Beagle, under the command of Captain Fitzroy, R.N., during the years 1832 to 1836*, 768 pp., Smith, Elder, and Co.

Delouis, B., J.-M. Nocquet, and M. Vallee (2010), Slip distribution of the February 27, 2010 Mw=8.8 Maule Earthquake, central Chile, from static and high-rate GPS, InSAR, and broadband teleseismic data, *Geophys. Res. Lett.*, 37, L17305, doi: 10.1029/2010GL043899.

Divins, D. L. (2003), *Total sediment thickness of the world's oceans & marginal seas*, edited by N. N. G. D. Center, Boulder, CO.

Farias, M., G. Vargas, A. Tassara, S. Carretier, S. Baize, D. Melnick, and K. Bataille (2010), Land-level changes produced by the Mw 8.8 2010 Chilean earthquake, *Science*, 329(5994), 916, doi: 10.1126/science.1192094.

Folguera, A., and V. A. Ramos (2009), Collision of the Mocha fracture zone and a < 4 Ma old wave of orogenic uplift in the Andes (36°-38°S), *Lithosphere*, 1(6), 364-369, doi: 10.1130/L66.1.

Folguera, A., V. A. Ramos, R. L. Hermanns, and J. Naranjo (2004), Neotectonics in the foothills of the southernmost central Andes (37°-38°S): Evidence of strike-slip displacement along the Antinir-Copahue fault zone, *Tectonics*, 23(5), TC5008, doi: 10.1029/2003TC001533.

Folguera, A., A. Introcaso, M. Giménez, F. Ruiz, P. Martinez, C. Tunstall, E. García Morabito, and V. A. Ramos (2007), Crustal attenuation in the Southern Andean retroarc (38°-39°30'S) determined from tectonic and gravimetric studies: The Lonco-Luán asthenospheric anomaly, *Tectonophysics*, 439, 129-147, doi: 10.1016/j.tecto.2007.04.001.

Folguera, A., G. Bottesi, T. Zapata, and V. A. Ramos (2008), Crustal collapse in the Andean backarc since 2 Ma: Tromen volcanic plateau, Southern Central Andes (36°40'-37°30'), *Tectonophysics*, 459, 140-160, doi: 10.1016/j.tecto.2007.12.013.

Fritz, H., et al. (2011), Field survey of the 27 February 2010 Chile tsunami, *Pure Appl. Geophys.*, 168(11), 1989-2010, doi: 10.1007/s00024-011-0283-5.

Galland, O., E. Hallot, P. R. Cobbold, G. Ruffet, and J. de Bremond d'Ars (2007), Volcanism in a compressional Andean setting: A structural and geochronological study of Tromen volcano (Neuquén province, Argentina), *Tectonics*, 26(4), TC4010, doi: 10.1029/2006TC002011.

Geospatial Information Authority of Japan (2012), Postseismic slip distribution model inferred from GEONET data, Japan.

Gordeev, E. I., A. A. Gusev, V. E. Levin, V. F. Bakhtiarov, V. M. Pavlov, V. N. Chebrov, and M. Kasahara (2001), Preliminary analysis of deformation at the Eurasia-Pacific-North America plate junction from GPS data, *Geophys. J. Int.*, 147(1), 189-198, doi: 10.1046/j.0956-540x.2001.01515.x.

Guzmán, C., E. Cristallini, and G. Bottesi (2007), Contemporary stress orientations in the Andean retroarc between 34°S and 39°S from borehole breakout analysis, *Tectonics*, 26(3), TC3016, doi: 10.1029/2006TC001958.

Haberland, C., A. Rietbrock, D. Lange, K. Bataille, and T. Dahm (2009), Structure of the seismogenic zone of the southcentral Chilean margin revealed by local earthquake traveltime tomography, *J. Geophys. Res.*, 114, B01317, doi: 10.1029/2008JB005802.

Hashimoto, M., N. Choosakul, M. Hashizume, S. Takemoto, H. Takiguchi, Y. Fukuda, and K. Frjimori (2006), Crustal deformations associated with the great Sumatra-Andaman earthquake deduced from continuous GPS observation, *Earth Planets Space*, 58(2), 127-139.

Hébert, H., P. Heinrich, S. François, and A. Piatanesi (2001), Far-field simulation of tsunami propagation in the Pacific Ocean: impact on the Marquesas Islands (French Polynesia), *J. Geophys. Res.*, 106(C5), 9161-9177, doi: 10.1029/2000JC000552.

Heinrich, P., F. Schindele, S. Guibourg, and F. P. Ihmlé (1998), Modeling of the February 1996 Peruvian tsunami, *Geophys. Res. Lett.*, 25(14), 2687-2690.

Heki, K., and Y. Tamura (1997), Short term afterslip in the 1994 Sanriku-Haruka-Oki earthquake, *Geophys. Res. Lett.*, 24(24), 3285-3288, doi: 10.1029/97gl03316.

Heki, K., S. Miyazaki, and H. Tsuji (1997), Silent fault slip following an interplate thrust earthquake at the Japan Trench, *Nature*, 386(6625), 595-598, doi: 10.1038/386595a0.

Hsu, Y.-J., M. Simons, C. Williams, and E. Casarotti (2011), Three-dimensional FEM derived elastic Green's functions for the coseismic deformation of the 2005 Mw 8.7 Nias-Simeulue, Sumatra earthquake, *Geochem. Geophys. Geosyst.*, 12(7), Q07013, doi: 10.1029/2011GC003553.

Hsu, Y.-J., M. Simons, J.-P. Avouac, J. Galetzka, K. Sieh, M. Chlieh, D. Natawidjaja, L. Prawirodirdjo, and Y. Bock (2006), Frictional afterslip following the 2005 Nias-Simeulue earthquake, Sumatra, *Science*, 312(5782), 1921-1926, doi: 10.1126/science.1126960.

Hubbert, M. K., and W. W. Rubey (1959), Role of fluid pressure in mechanics of overthrust faulting. I. Mechanics of fluid-filled porous solids and its application to overthrust faulting, *Geol. Soc. Am. Bull.*, 70(2), 115-166.

Hutton, W., C. DeMets, O. Sanchez, G. Suarez, and J. Stock (2001), Slip kinematics and dynamics during and after the 1995 October 9 M-w=8.0 Colima-Jalisco earthquake, Mexico, from GPS geodetic constraints, *Geophys. J. Int.*, 146(3), 637-658, doi: 10.1046/j.1365-246X.2001.00472.x.

Ito, Y., K. Obara, K. Shiomi, S. Sekine, and H. Hirose (2007), Slow earthquakes coincident with episodic tremors and slow slip events, *Science*, 315(5811), 503-506, doi: 10.1126/science.1134454.

Ji, C., D. J. Wald, and D. V. Helmberger (2002), Source description of the 1999 Hector Mine, California, earthquake, part I: Wavelet domain inversion theory and resolution analysis, *B. Seismol. Soc. Am.*, 92(4), 1192-1207, doi: 10.1785/0120000916.

Kaneko, Y., J.-P. Avouac, and N. Lapusta (2010), Towards inferring earthquake patterns from geodetic observations of interseismic coupling, *Nat. Geosci.*, 3(5), 363-369, doi: 10.1038/NGEO843.

Kato, N. (2007), Expansion of aftershock areas caused by propagating post-seismic sliding, *Geophys. J. Int.*, 168(2), 797-808, doi: 10.1111/j.1365-246X.2006.03255.x.

Kawasaki, I., Y. Asai, Y. Tamura, T. Sagiya, N. Mikami, Y. Okada, M. Sakata, and M. Kasahara (1995), The 1992 Sanriku-oki, Japan, ultra-slow earthquake, *J. Phys. Earth*, 43(2), 105-116.

Kawasaki, I., Y. Asai, and Y. Tamura (2001), Space-time distribution of interplate moment release including slow earthquakes and the seismo-geodetic coupling in the Sanriku-oki region along the Japan trench, *Tectonophysics*, 330(3-4), 267-283, doi: 10.1016/S0040-1951(00)00245-6.

Kendrick, E., M. Bevis, R. Smalley, B. Brooks, R. B. Vargas, E. Lauriia, and L. P. S. Fortes (2003), The Nazca South America Euler vector and its rate of change, *J. S. Am. Earth Sci.*, 16(2), 125-131, doi: 10.1016/S0895-9811(03)00028-2.

Konca, A. O., et al. (2008), Partial rupture of a locked patch of the Sumatra megathrust during the 2007 earthquake sequence, *Nature*, 456(7222), 631-635, doi: 10.1038/nature07572.

Kositsky, A., and J. P. Avouac (2010), Inverting geodetic time-series with a principal component analysis-based inverison method (PCAIM), *J. Geophys. Res.*, 115, B03401, doi: 10.1029/2009JB006535.

Lay, T., C. J. Ammon, H. Kanamori, K. D. Koper, O. Sufri, and A. R. Hutko (2010), Teleseismic inversion for rupture process of the 27 February 2010 Chile (M-w 8.8) earthquake, *Geophys. Res. Lett.*, 37, L13301, doi: 10.1029/2010GL043379.

Lin, Y.-n. N., A. P. Kositsky, and J.-P. Avouac (2010), PCAIM joint inversion of InSAR and ground-based geodetic time series: Application to monitoring magmatic inflation beneath the Long Valley Caldera, *Geophys. Res. Lett.*, 37(23), L23301, doi: 10.1029/2010GL045769.

Lomnitz, C. (2004), Major earthquakes of Chile: A historical survey, 1535-1960, *Seismol. Res. Lett.*, 75(3), 368-378.

Lorito, S., F. Romano, S. Atzori, X. Tong, A. Avallone, J. McCloskey, M. Cocco, E. Boschi, and A. Piatanesi (2011), Limited overlap between the seismic gap and coseismic slip of the great 2010 Chile earthquake, *Nat. Geosci.*, 4(3), 173-177, doi: 10.1038/NGEO1073.

Loveless, J. P., M. E. Pritchard, and N. Kukowski (2010), Testing mechanisms of subduction zone segmentation and seismogenesis with slip distributions from recent Andean earthquakes, *Tectonophysics*, 495(1–2), 15-33, doi: 10.1016/j.tecto.2009.05.008.

Madariaga, R., M. Metois, C. Vigny, and J. Campos (2010), Central Chile finally breaks, *Science*, 328(5975), 181-182, doi: 10.1126/science.1189197.

Marone, C. (1998), Laboratory-derived frictional laws and their application to seismic faulting, *Annu. Rev. Earth Planet. Sci.*, 26(1), 643-696, doi: 10.1146/annurev.earth.26.1.643.

Melbourne, T. I., F. H. Webb, J. M. Stock, and C. Reigber (2002), Rapid postseismic transients in subduction zones from continuous GPS, *J. Geophys. Res.*, 107(B10), 2241, doi: 10.1029/2001JB000555.

Melnick, D., B. Bookhagen, M. R. Strecker, and H. P. Echtler (2009), Segmentation of megathrust rupture zones from fore-arc deformation patterns over hundreds to millions of years, Arauco peninsula, Chile, *J. Geophys. Res.*, 114, B01407, doi: 10.1029/2008JB005788.

Melnick, D., M. Moreno, M. Motagh, M. Cisternas, and R. L. Wesson (2012), Splay fault slip during the Mw 8.8 2010 Maule Chile earthquake, *Geology*, doi: 10.1130/G32712.1.

Meng, L., A. Inbal, and J.-P. Ampuero (2011), A window into the complexity of the dynamic rupture of the 2011 Mw 9 Tohoku-Oki earthquake, *Geophys. Res. Lett.*, 38, L00G07, doi: 10.1029/2011GL048118.

Messager, G., B. Niviìre, J. Martinod, P. Lacan, and J. P. Xavier (2010), Geomorphic evidence for Plio-Quaternary compression in the Andean foothills of the southern Neuquén Basin, Argentina, *Tectonics*, 29(4), TC4003, doi: 10.1029/2009TC002609.

Métois, M., A. Socquet, and C. Vigny (2012), Interseismic coupling, segmentation and mechanical behavior of the central Chile subduction zone, *J. Geophys. Res.*, 117(B3), B03406, doi: 10.1029/2011jb008736.

Miyazaki, S., P. Segall, J. Fukuda, and T. Kato (2004), Space time distribution of afterslip following the 2003 Tokachi-oki earthquake: Implications for variations in fault zone frictional properties, *Geophys. Res. Lett.*, 31(6), L06623, doi: 10.1029/2003GL019410,.

Moreno, M. S., J. Klotz, D. Melnick, H. Echtler, and K. Bataille (2008), Active faulting and heterogeneous deformation across a megathrust segment boundary from GPS data, south central Chile (36-39°S), *Geochem. Geophys. Geosyst.*, 9, Q12024, doi: 10.1029/2008GC002198.

Moreno, M. S., J. Bolte, J. Klotz, and D. Melnick (2009), Impact of megathrust geometry on inversion of coseismic slip from geodetic data: Application to the 1960 Chile earthquake, *Geophys. Res. Lett.*, 36(16), L16310, doi: 10.1029/2009GL039276.

Moreno, M., M. Rosenau, and O. Oncken (2010), 2010 Maule earthquake slip correlates with pre-seismic locking of Andean subduction zone, *Nature*, 467(7312), 198-202, doi: 10.1038/nature09349.

Moreno, M., et al. (2012), Toward understanding tectonic control on the Mw 8.8 2010 Maule Chile earthquake, *Earth Planet. Sci. Lett.*, 321-322(0), 152-165, doi: 10.1016/j.epsl.2012.01.006.

Nishimura, T., et al. (2000), Distribution of seismic coupling on the subducting plate boundary in northeastern Japan inferred from GPS observations, *Tectonophysics*, 323(3-4), 217-238, doi: 10.1016/s0040-1951(00)00108-6.

Ortega-Culaciati, F. et al., (2013), Post-seismic deformation of the great 11 March 2011 Tohoku-Oki (Mw 9.0) earthquake, in preparation.

Ortlieb, L., S. Barrientos, and N. Guzman (1996), Coseismic coastal uplift and coralline algae record in Northern Chile: The 1995 Antofagasta earthquake case, *Quaternary Science Reviews*, 15(8–9), 949-960, doi: http://dx.doi.org/10.1016/S0277-3791(96)00056-X.

Ozawa, S., M. Kaidzu, M. Murakami, T. Imakiire, and Y. Hatanaka (2004), Coseismic and postseismic crustal deformation after the Mw 8 Tokachi-oki earthquake in Japan, *Earth Planets Space*, 56(7), 675-680.

Ozawa, S., T. Nishimura, H. Munekane, H. Suito, T. Kobayashi, M. Tobita, and T. Imakiire (2012), Preceding, coseismic, and postseismic slips of the 2011 Tohoku earthquake, Japan, *J. Geophys. Res.*, 117(B7), B07404, doi: 10.1029/2011JB009120.

Perfettini, H., and J. P. Avouac (2004), Postseismic relaxation driven by brittle creep: A possible mechanism to reconcile geodetic measurements and the decay rate of aftershocks, application to the Chi-Chi earthquake, Taiwan, *J. Geophys. Res.*, 109(B2), B02304, doi: 10.1029/2003JB002488.

Perfettini, H., et al. (2010), Seismic and aseismic slip on the Central Peru megathrust, *Nature*, 465(7294), 78-81, doi: 10.1038/nature09062.

Piatanesi, A., and S. Lorito (2007), Rupture process of the 2004 Sumatra-Andaman earthquake from tsunami waveform inversion, *B. Seismol. Soc. Am.*, 97(1), S223-S231, doi: 10.1785/0120050627.

Plafker, G., and J. C. Savage (1970), Mechanism of the Chilean Earthquakes of May 21 and 22, 1960, *Geol. Soc. Am. Bull.*, 81(4), 1001-1030.

Plank, T., and C. H. Langmuir (1998), The chemical composition of subducting sediment and its consequences for the crust and mantle, *Chemical Geology*, 145(3-4), 325-394.

Pollitz, F. F., R. Burgmann, and P. Segall (1998), Joint estimation of afterslip rate and postseismic relaxation following the 1989 Loma Prieta earthquake, *J. Geophys. Res.*, 103(B11), 26975-26992, doi: 10.1029/98jb01554.

Pollitz, F. F., R. Bürgmann, and P. Banerjee (2006), Post-seismic relaxation following the great 2004 Sumatra-Andaman earthquake on a compressible self-gravitating Earth, *Geophys. J. Int.*, 167(1), 397-420, doi: 10.1111/j.1365-246X.2006.03018.x.

Pritchard, M. E., and M. Simons (2006), An aseismic slip pulse in northern Chile and along-strike variations in seismogenic behavior, *J. Geophys. Res.*, 111(B8), B08405, doi: 10.1029/2006JB004258.

Pritchard, M. E., E. O. Norabuena, C. Ji, R. Boroschek, D. Comte, M. Simons, T. H. Dixon, and P. A. Rosen (2007), Geodetic, teleseismic, and strong motion constraints on slip from recent southern Peru subduction zone earthquakes, *J. Geophys. Res.*, 112(B3), n/a-n/a, doi: 10.1029/2006jb004294.

Rietbrock, A., C. Haberland, K. Bataille, T. Dahm, and O. Oncken (2005), Studying the seismogenic coupling zone with a passive seismic array, *Eos Trans. AGU*, 86, 293-300, doi: 10.1029/2005EO320001.

Rietbrock, A., I. Ryder, G. Hayes, C. Haberland, D. Comte, S. Roecker, and H. Lyon-Caen (2012), Aftershock seismicity of the 2010 Maule Mw=8.8, Chile, earthquake: Correlation between co-seismic slip models and aftershock distribution?, *Geophys. Res. Lett.*, 39(8), L08310, doi: 10.1029/2012GL051308.

Ruegg, J. C., M. Olcay, and D. Lazo (2001), Co-, post- and pre(?)-seismic displacements associated with the Mw 8.4 Southern Peru Earthquake of 23 June 2001 from continuous GPS measurements, *Seismol. Res. Lett.*, 72(6), 673-678, doi: 10.1785/gssrl.72.6.673.

Ruegg, J. C., J. Campos, R. Madariaga, E. Kausel, J. B. de Chabalier, R. Armijo, D. Dimitrov, I. Georgiev, and S. Barrientos (2002), Interseismic strain accumulation in south central Chile from GPS measurements, 1996-1999, *Geophys. Res. Lett.*, 29(11), 1517, doi: 10.1029/2001GL013438.

Ruegg, J. C., A. Rudloff, C. Vigny, R. Madariaga, J. B. de Chabalier, J. Campos, E. Kausel, S. Barrientos, and D. Dimitrov (2009), Interseismic strain accumulation measured by GPS in

the seismic gap between Constitución and Concepción in Chile, *Phys. Earth Planet. Inter.*, 175(1-2), 78-85, doi: 10.1016/j.pepi.2008.02.015.

Ruff, L. J. (1989), Do trench sediments affect great earthquake occurrence in subduction zones?, *Pure Appl. Geophys.*, 129(1-2), 263-282, doi: 10.1007/bf00874629.

Satake, K. (1993), Depth distribution of coseismic slip along the Nankai Trough, Japan, from joint inversion of geodetic and tsunami data, *J. Geophys. Res.*, 98(B3), 4553-4565, doi: 10.1029/92jb01553.

Scherwath, M., E. Contreras-Reyes, E. R. Flueh, I. Grevemeyer, A. Krabbenhoeft, C. Papenberg, C. J. Petersen, and R. W. Weinrebe (2009), Deep lithospheric structures along the southern central Chile margin from wide-angle P-wave modelling, *Geophys. J. Int.*, 179(1), 579-600, doi: 10.1111/j.1365-246X.2009.04298.x.

Simons, M., et al. (2011), The 2011 magnitude 9.0 Tohoku-Oki earthquake: Mosaicking the megathrust from seconds to centuries, *Science*, 332(6036), 1421-1425, doi: 10.1126/science.1206731.

Sladen, A., and H. Hébert (2008), On the use of satellite altimetry to infer the earthquake rupture characteristics: application to the 2004 Sumatra event, *Geophys. J. Int.*, 172(2), 707-714, doi: 10.1111/j.1365-246X.2007.03669.x.

Sladen, A., H. Tavera, M. Simons, J. P. Avouac, A. O. Konca, H. Perfettini, L. Audin, E. J. Fielding, F. Ortega, and R. Cavagnoud (2010), Source model of the 2007 M-w 8.0 Pisco, Peru earthquake: Implications for seismogenic behavior of subduction megathrusts, *J. Geophys. Res.*, 115, B02405, doi: 10.1029/2009JB006429.

Song, T. R. A., and M. Simons (2003), Large trench-parallel gravity variations predict seismogenic behavior in subduction zones, *Science*, 301(5633), 630-633, doi: 10.1126/science.1085557.

Subarya, C., M. Chlieh, L. Prawirodirdjo, J. P. Avouac, Y. Bock, K. Sieh, A. J. Meltzner, D. H. Natawidjaja, and R. McCaffrey (2006), Plate-boundary deformation associated with the great Sumatra-Andaman earthquake, *Nature*, 440(7080), 46-51, doi: 10.1038/nature04522.

Suito, H., T. Nishimura, M. Tobita, T. Imakiire, and S. Ozawa (2011), Interplate fault slip along the Japan Trench before the occurrence of the 2011 off the Pacific coast of Tohoku Earthquake as inferred from GPS data, *Earth Planets Space*, 63(7), 615-619, doi: 10.5047/eps.2011.06.053.

Tong, X., et al. (2010), The 2010 Maule, Chile earthquake: Downdip rupture limit revealed by space geodesy, *Geophys. Res. Lett.*, 37(24), L24311, doi: 10.1029/2010GL045805.

Vargas, G., M. Farias, S. Carretier, A. Tassara, S. Baize, and D. Melnick (2011), Coastal uplift and tsunami effects associated to the 2010 M(w)8.8 Maule earthquake in Central Chile, *Andean Geology*, 38(1), 219-238.

Victor, P., M. Sobiesiak, J. Glodny, S. N. Nielsen, and O. Oncken (2011), Long-term persistence of subduction earthquake segment boundaries: Evidence from Mejillones

Peninsula, northern Chile, *J. Geophys. Res.*, 116(B2), B02402, doi: 10.1029/2010JB007771.

Vigny, C., et al. (2011), The 2010 Mw 8.8 Maule megathrust earthquake of central Chile, monitored by GPS, *Science*, 332(6036), 1417-1421, doi: 10.1126/science.1204132.

Volker, D., I. Grevemeyer, M. Stipp, K. Wang, and J. He (2011), Thermal control of the seismogenic zone of southern central Chile, *J. Geophys. Res.*, 116(B10), B10305, doi: 10.1029/2011JB008247.

von Huene, R., and D. W. Scholl (1991), Observations at convergent margins concerning sediment subduction, subduction erosion, and the growth of continental crust, *Rev. Geophys.*, 29(3), 279-316.

Wells, R. E., R. J. Blakely, Y. Sugiyama, D. W. Scholl, and P. A. Dinterman (2003), Basin-centered asperities in great subduction zone earthquakes: A link between slip, subsidence, and subduction erosion?, *J. Geophys. Res.*, 108(B10), 2507, doi: 10.1029/2002JB002072.

Yagi, Y., M. Kikuchi, and T. Nishimura (2003), Co-seismic slip, post-seismic slip, and largest aftershock associated with the 1994 Sanriku-haruka-oki, Japan, earthquake, *Geophys. Res. Lett.*, 30(22), 2177, doi: 10.1029/2003gl018189.

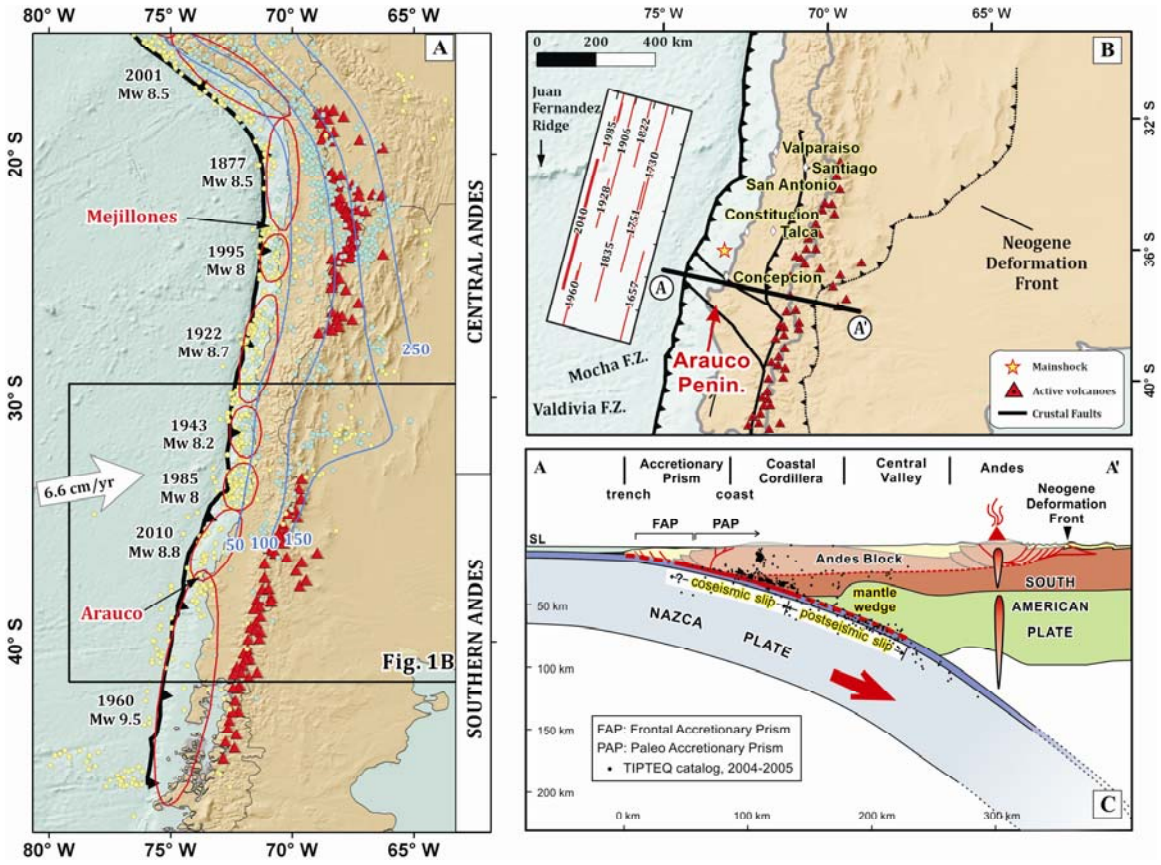

Figure 3.1. (A) Regional tectonic map showing slab isodepth contours (blue lines) [*Cahill and Isacks*, 1992], M>=4 earthquakes from NEIC catalog between 1976 and 2011 (yellow circles for depths less than 50 km, and blue circles for depths greater than 50 km), active volcanoes (red triangles), and the approximate extent of large megathrust earthquakes during the past hundred years (red ellipses) adapted from *Campos et al.* [2002]. The large white vector represents the direction of Nazca Plate with respect to stable South America [*Kendrick et al.*, 2003]. (B) Simplified seismo-tectonic map of the study area. Major Quaternary faults are adapted after *Melnick et al.* [2009] (black lines). The Neogene Deformation Front is adapted from *Folguera et al.* [2004]. The west-vergent thrust fault that bounds the west of the Andes between 32° and 38°S is adapted from *Melnick et al.* [2009]. (C) Schematic cross-section along line A-A' (Figure 3.1B), adapted from *Folguera and Ramos* [2009]. The upper bound of the coseismic slip coincides with the boundary between the frontal accretionary prism (FAP) and the paleo-accretionary prism (PAP) [*Contreras-Reyes et al.*, 2010], whereas the contact between the coseismic and postseismic patch is from this study. The thick solid red line and dashed red line on top of

the slab represent the approximate coseismic and post- plus interseismic slip section of the subduction interface. The thin red and grey lines within the overriding plate are active and inactive structures in the retroarc, adapted from *Folguera and Ramos* [2009]. The red dashed line underneath the Andean Block represents the regional décollement. Background seismicity is from the TIPTEQ catalog, recorded between November 2004 and October 2005 [*Rietbrock et al.*, 2005; *Haberland et al.*, 2009].

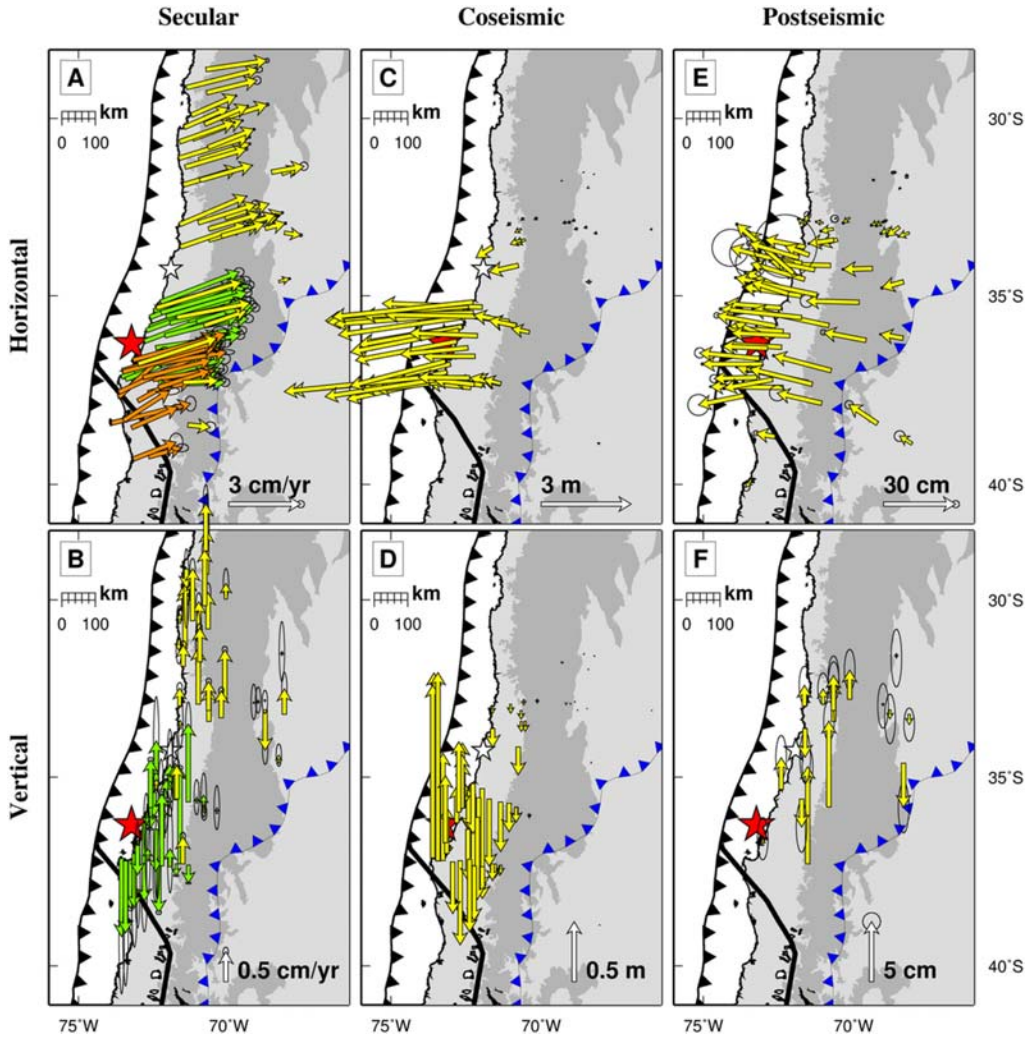

Figure 3.2. Horizontal and vertical secular interseismic velocities (left), coseismic displacement (middle) and postseismic displacement, determined from GPS data spanning the period between the 1st and 488th day after the mainshock (right). Note that for the postseismic displacement, when actual data time span for a given record does not cover this whole period, we have extrapolated it to represent the deformation between the 1st and 488th day using PCAIM,. Yellow vectors are derived from this study; green vectors and orange vectors in (A) and (B) are from are from *Ruegg et al.* [2009] and *Moreno et al.* [2008], respectively. The blue barbed line corresponds to the Neogene Deformation Front. The red and white stars represent the epicenter of the mainshock and the Pichilemu earthquake, respectively. The dark grey region is bounded by the 1000-m contour line, approximately the boundary of the Andes.

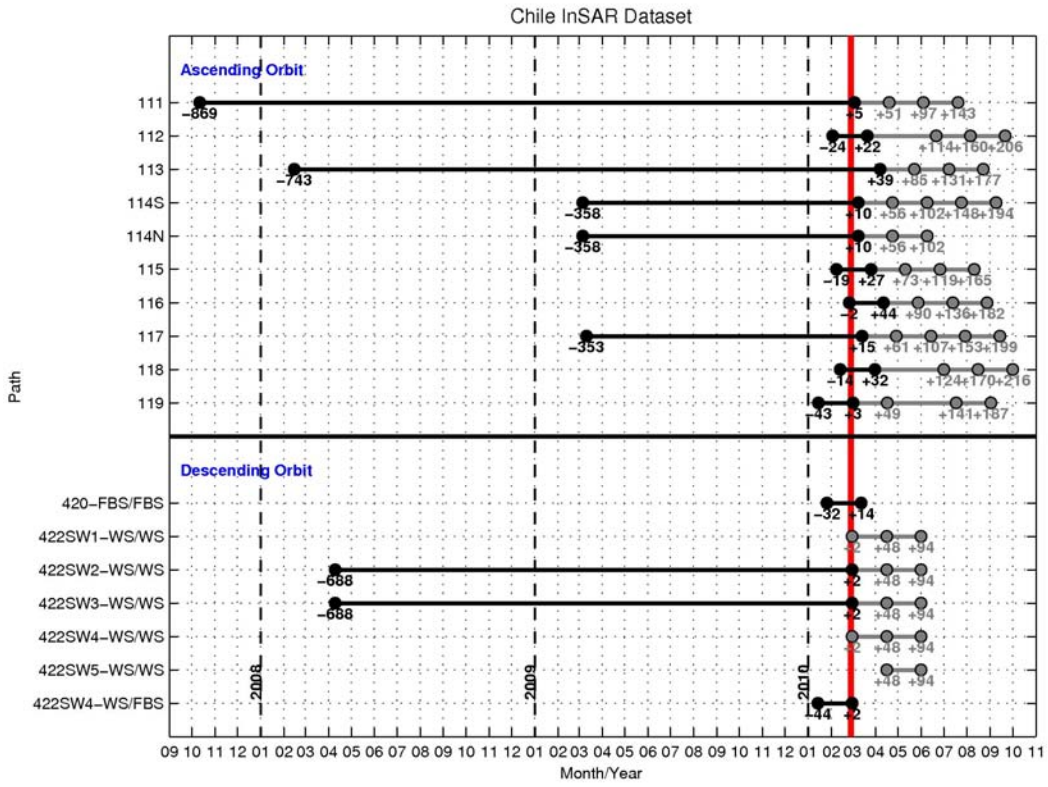

Figure 3.3. ALOS PALSAR acquisitions used in this study. FBS stands for fine mode single polarization mode while WS stands for wide swath data. Black lines indicate coseismic pairs and gray lines indicate postseismic pairs. Numbers under each acquisition dot represent the number of days before or after the earthquake.

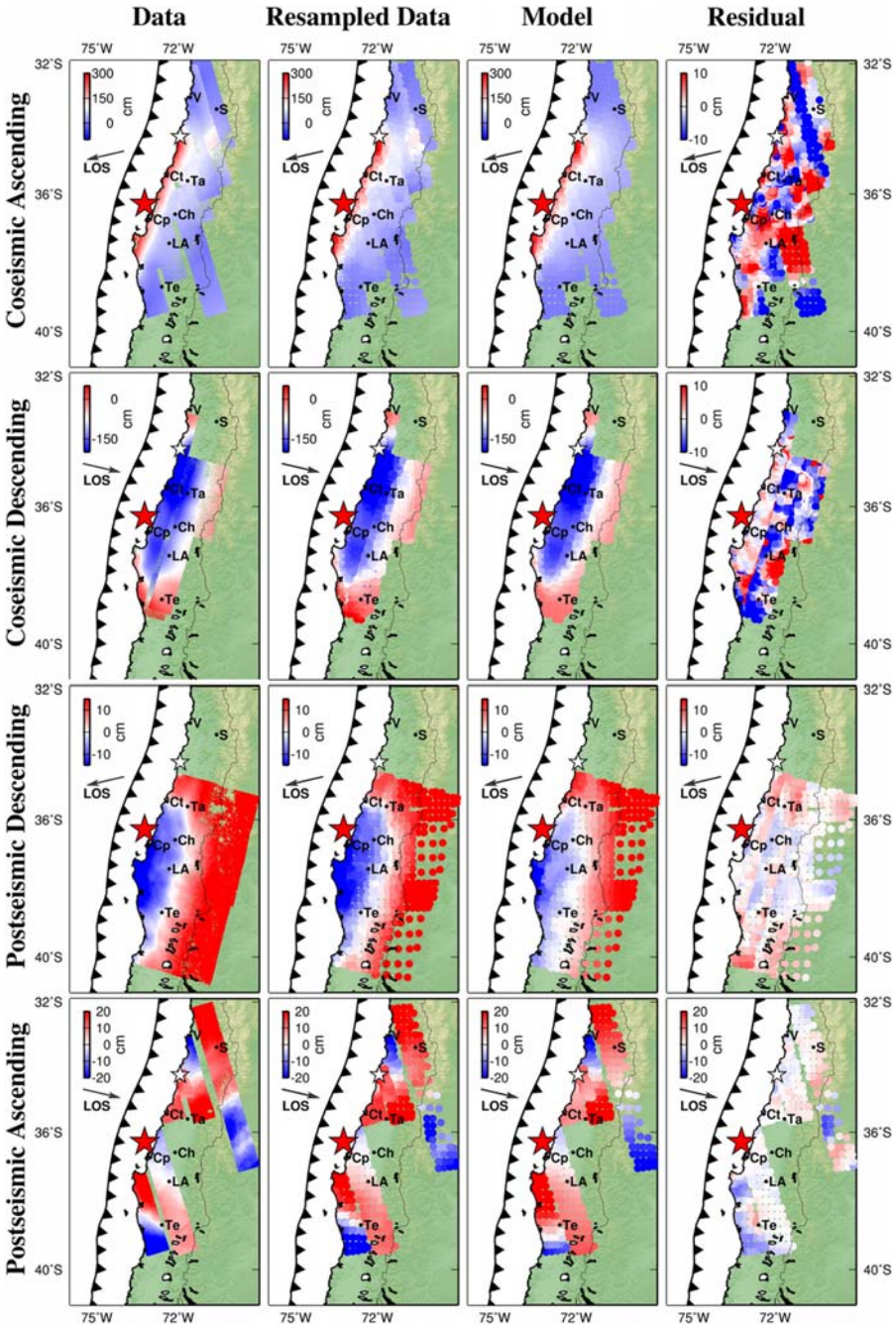

Figure 3.4. The original, resampled, modeled InSAR data, and the model residuals for both the coseismic and postseismic tracks. Red and white stars are for the Maule and Pichilemu earthquakes, respectively. Notice that for the postseismic ascending images, different tracks cover different time spans (Figure 3.3) and therefore they cannot form a continuous map as the postseismic descending tracks.

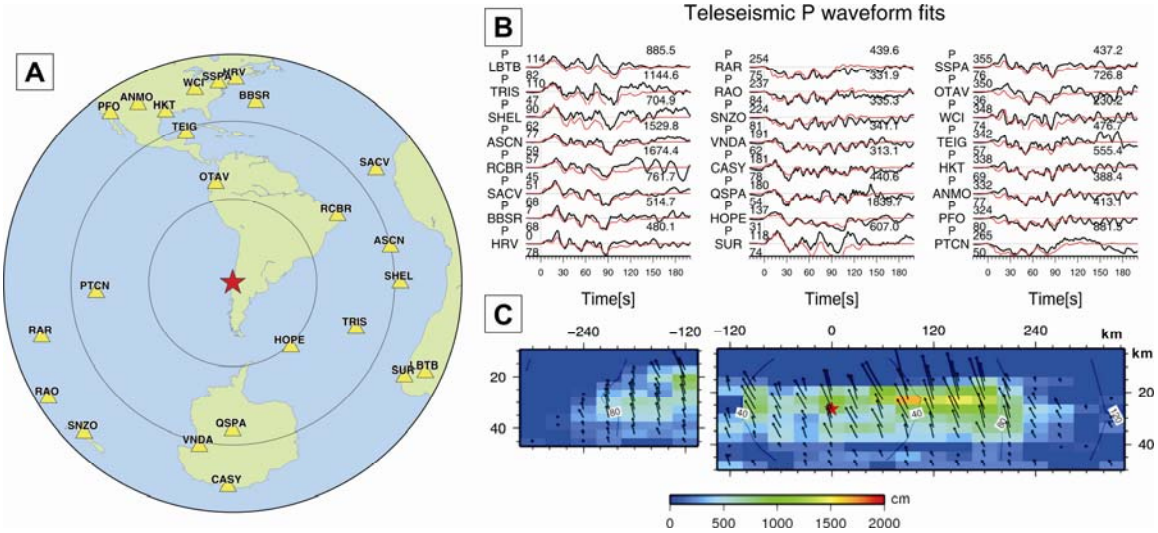

Figure 3.5. (A) The global distribution of seismic stations used in the coseismic model. Circles are every 30° of azimuthal distance. (B) Comparison of the observed (black) and modeled seismic waveforms (red) of the kinematic finite fault model. (C) The slip magnitude (colors), rake (arrows) and rupture propagation time in seconds (isochrones) for that same kinematic model.

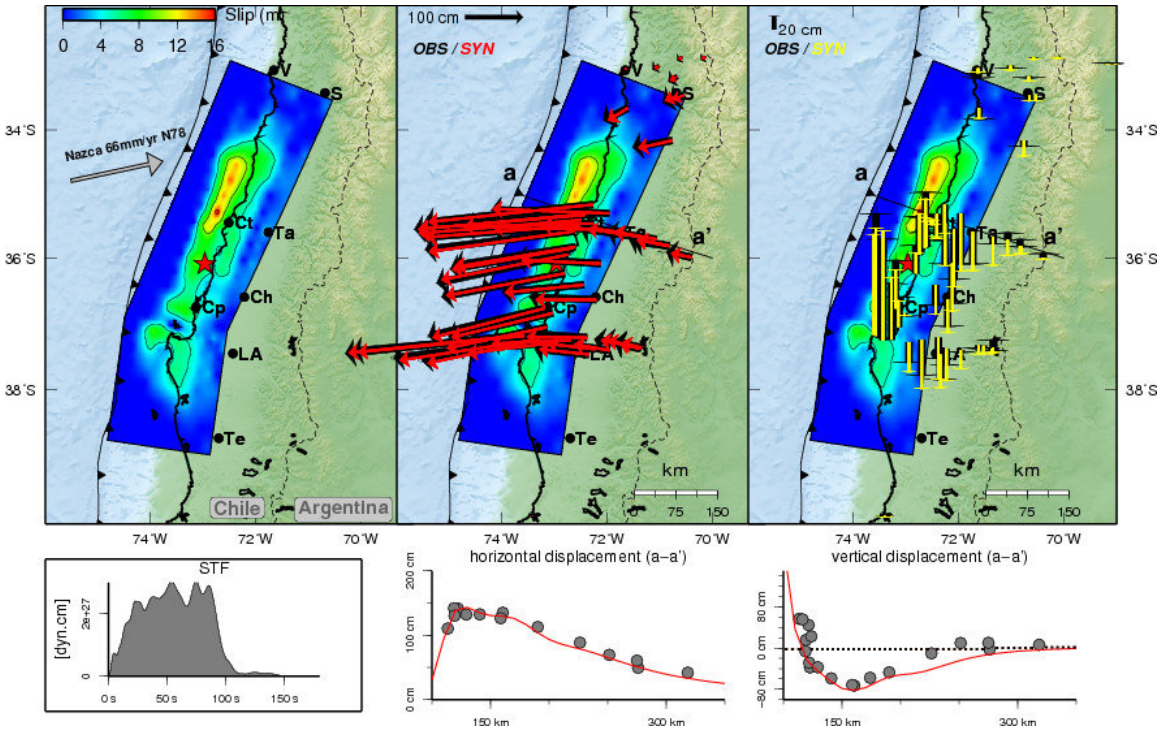

Figure 3.6. (Left) Coseismic slip with 5-m contour intervals from the best-fit model with the source time function of the solution plotted below. (Center and Right) Black vectors indicate the observed GPS data; red and yellow vectors indicate modeled results in the horizontal and vertical components, respectively. The profile (aa') shows the predicted (red line) and observed (grey solid dots) surface displacements at the latitude of the main asperity, around latitude 36°S. Notice that for the vertical components (right), the slip model predicts a displacement field of longer wavelength than the observed data. See text for a discussion of this discrepancy. STF: Source time function. Ch: Chillán; Ct: Constitución; Cp: Concepción; LA: Los Angeles; Ta: Talca; Te: Temuco; S: Santiago; V: Valparaiso.

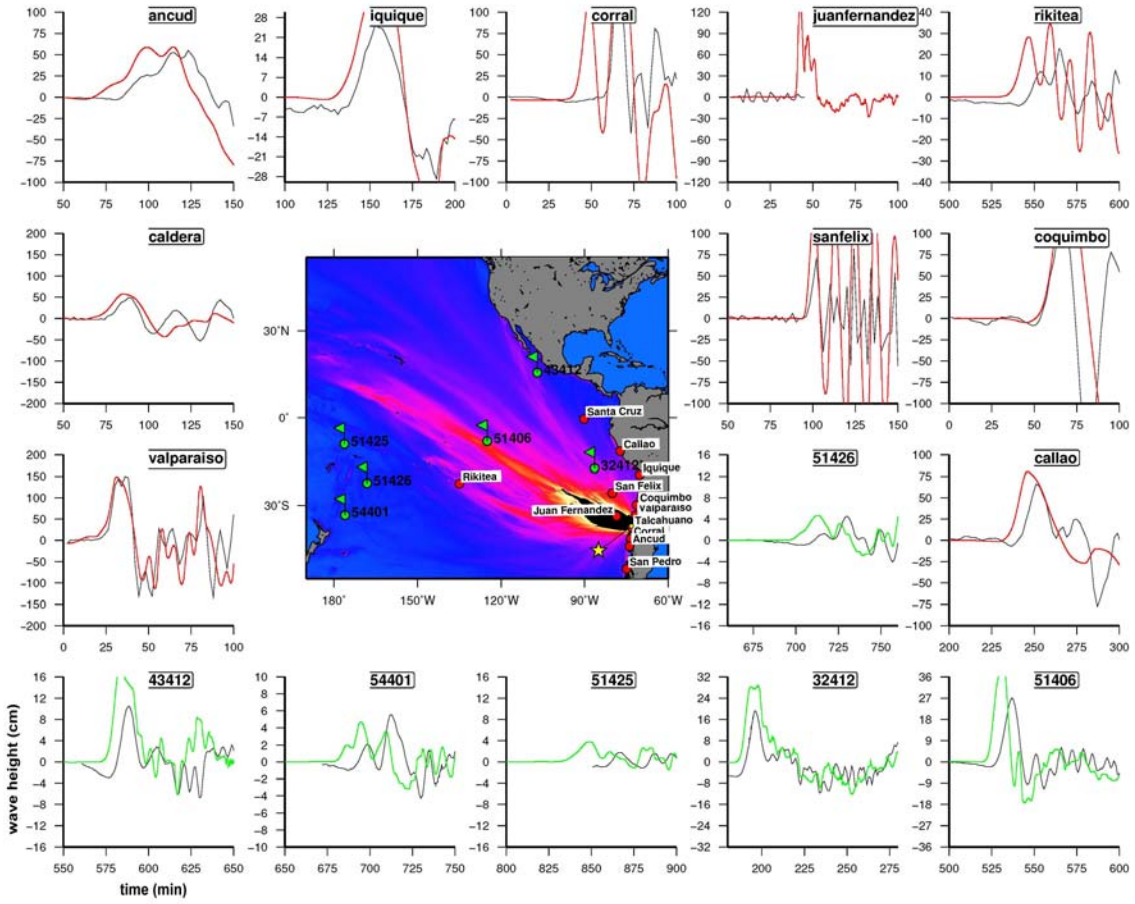

Figure 3.7. Tsunameter records as predicted by our preferred kinematic source model – this data was not used in the construction of the model. Black lines are observations; red and green lines are the modeled waves for tide gauges and deep-sea bottom pressure gauges, respectively. The map in the middle shows the predicted maximum open ocean wave heights. No time shift has been applied to the records.

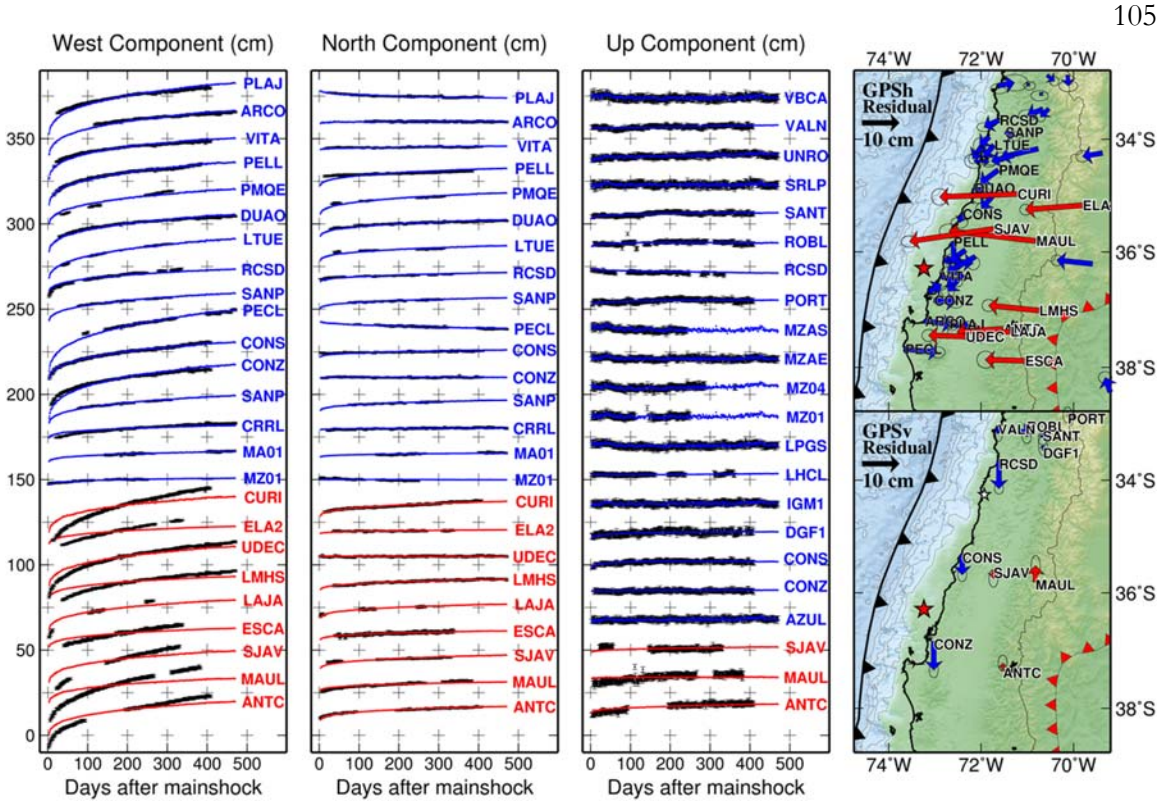

Figure 3.8. Time series of selected GPS stations. Blue lines and stations represent predicted time series that agree well with the data (black dots), whereas red lines and stations represent model prediction displaying large discrepancies with the data. The map views at the right panel show the residual vectors between the observed and modeled GPS components. The red stations are distributed along the Andes, indicating that the large systematic residuals are likely due to a common source.

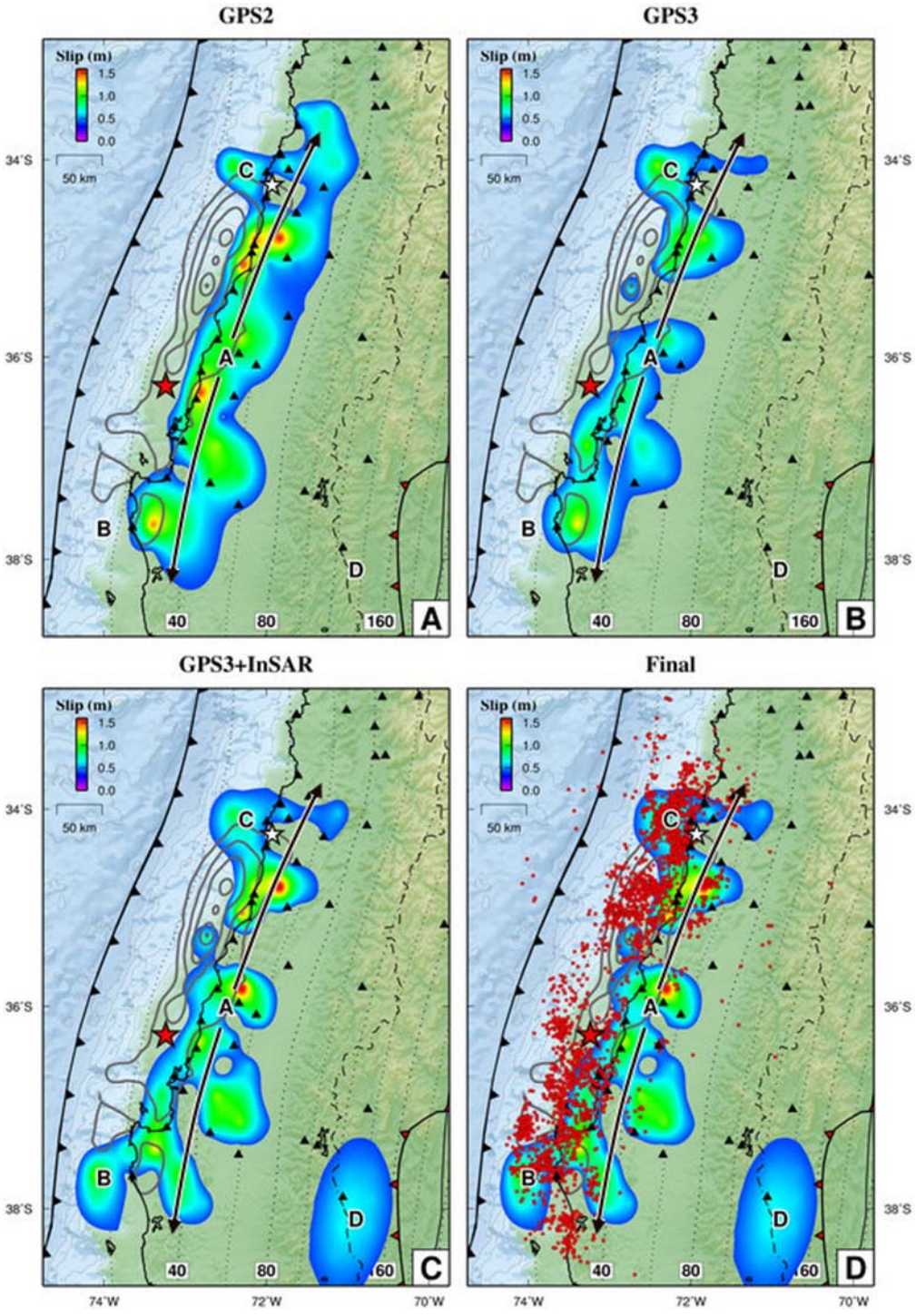

Figure 3.9. Comparison of the postseismic slip model between the 1st and 488th day constrained by (A) horizontal GPS observations only, (B) all three components of GPS observations, and (C) three component GPS observations plus InSAR data. Thick white

contours for the afterslip are of 0.5-m intervals, and the coseismic slip model is of 2.5-m contour intervals (gray lines). The final model in (D) is the same as (C) without the afterslip contours. Red circles are aftershocks [*Rietbrock et al.*, 2012]. Black triangles represent the location of GPS stations. A is the afterslip downdip of the coseismic slip patch, with the black arrows indicating the along-strike extent. B and C correspond to two regions of afterslip that bound the southern and northern end of the coseismic slip patch. D is a deep slip patch that may reflect some tropospheric errors in the Andes.

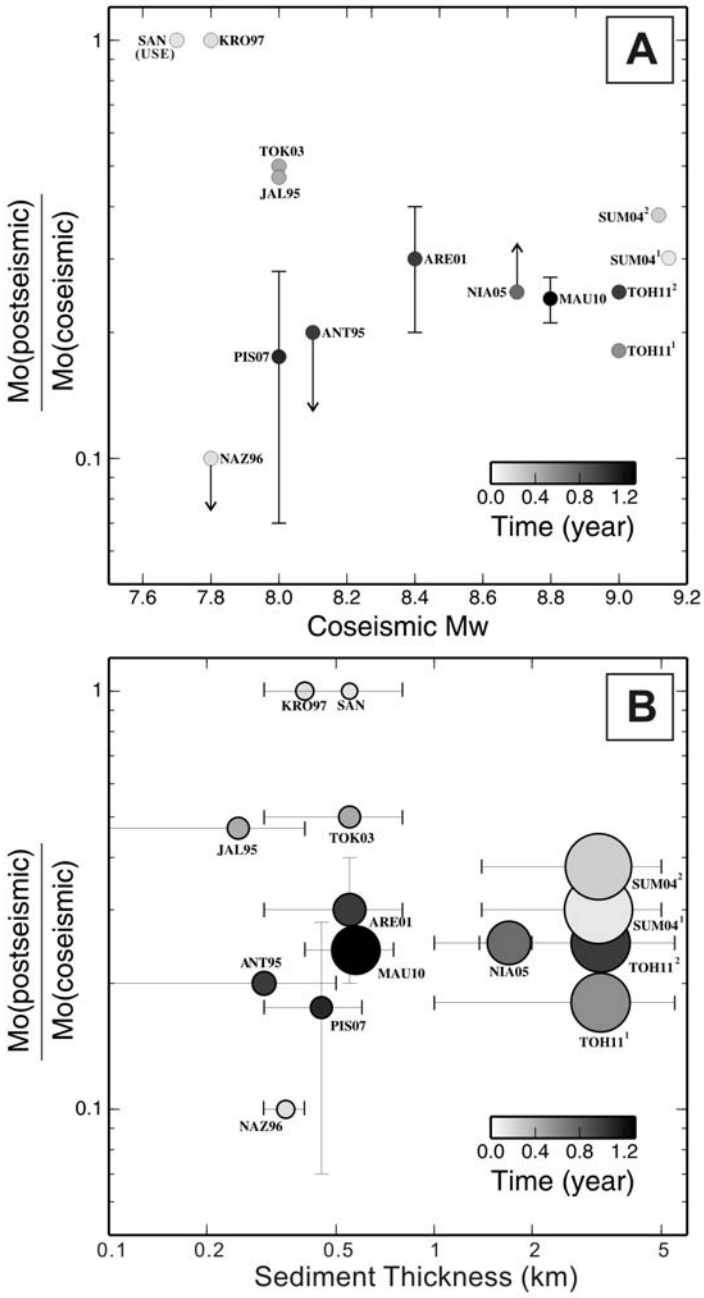

Figure 3.10. (A) Plot of the estimated postseismic-coseismic ratio as a function of coseismic moment for selected megathrust earthquakes. The ordinate is in log scale to reflect the relationship between Mo and Mw. The color scale of each dot represents the amount of time after the mainshock considered in each postseismic study. The code next to each circle is the first three letters of the event name and it occurrence year: ANT95,

1995 Antofagasta, Chile [*Melbourne et al.*, 2002; *Chlieh et al.*, 2004; *Pritchard and Simons*, 2006]; ARE01, 2001 Arequipa, Peru [*Ruegg et al.*, 2001; *Melbourne et al.*, 2002]; JAL95, 1995 Jalisco, Mexico [*Hutton et al.*, 2002; *Melbourne et al.*, 2002;]; KRO97, 1997 Kronotsky, Kamchatka [*Burgmann et al.*, 2001; *Gordeev et al.*, 2001]; MAU10, 2010 Maule, Chile (this study); NAZ96, 1996 Nazca, Peru [*Pritchard et al.*, 2007]; NIA05, 2005 Nias, Indonesia [*Hsu et al.*, 2006]; PIS07, 2007 Pisco, Peru [*Perfettini et al.*, 2010]; TOH11, 2011 Tohoku, Japan [*Ozawa et al.*, 2012; *Geospatial Information Authority of Japan*, 2012]; TOK03, 2003 Tokachi-oki, Japan [*Miyazaki et al.*, 2004; *Ozawa et al.*, 2004; *Baba et al.*, 2006]; SAN, 1989-1994 Sanriku-oki, Japan [*Kawasaki et al.*, 1995; *Heki et al.*, 1997; *Heki and Tamura*, 1997; *Nishimura et al.*, 2000; *Kawasaki et al.*, 2001; *Melbourne et al.*, 2002; *Yagi et al.*, 2003]; SUM04, 2004 Sumatra, Indonesia [*Hashimoto et al.*, 2006; *Subarya et al.*, 2006; *Chlieh et al.*, 2007]. Arrows instead of error bars indicate the circles as the upper bound or lower bound of the values. "USE" under the letters SAN (Sanriku-Oki events) represents "ultra-slow earthquake." (B) Plot of the estimated postseismic-coseismic ratio as a function trench sediment thickness. The size of the circles scales with the mainshock magnitude. Colors of the circles and name codes follow (A). The sediment thickness estimates are from multiple sources: *von Huene and Scholl* [1991], *Plank and Langmuir* [1998], and *Divins* [2003].

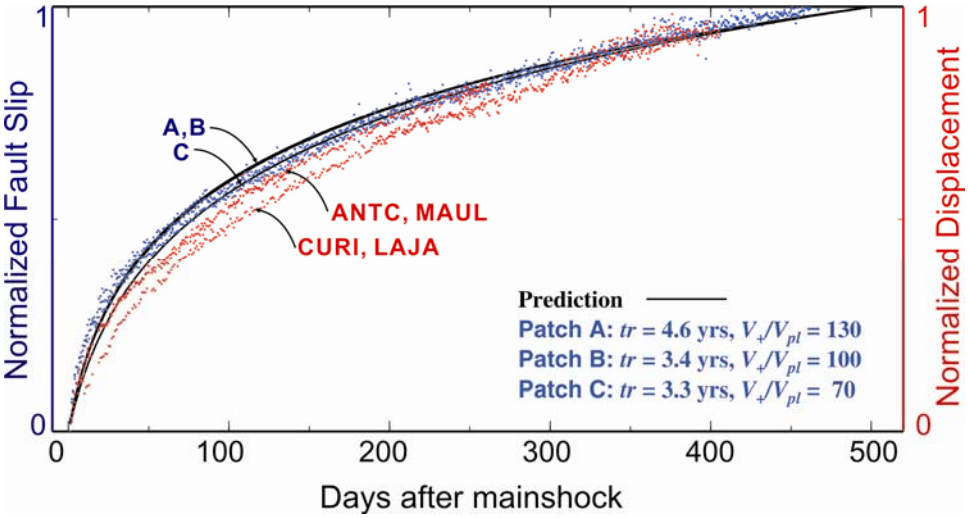

Figure 3.11. Normalized time-dependent fault slip over different postseismic slip patches from our model result (blue dots; see Figure 3.9D for locations). The normalized westward displacements over selected GPS stations are also shown for comparison (red dots; see Figure 3.8 for locations). Solid lines are the model predictions [*Perfettini et al.*, 2010].

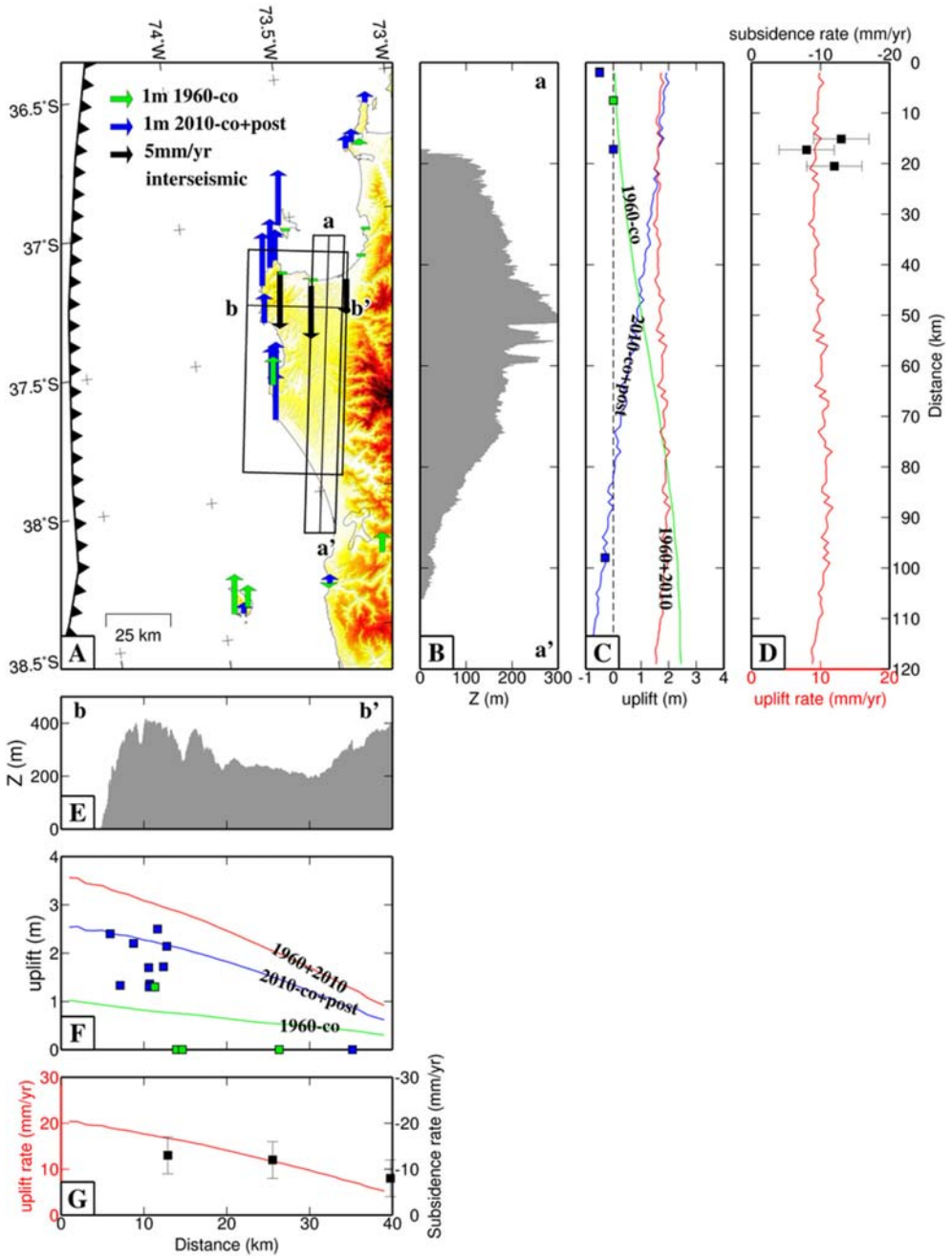

Figure 3.12. Topography, deformation and uplift/subsidence rate of the Arauco Peninsula along E-W and N-S directions. (A) Map of the Arauco Peninsula. a-a' and b-b' indicate locations of the profiles, with the bounding boxes showing the area of topography being projected onto the profiles. Green vectors and blue vectors are the in-situ measurements of coseismic and early postseismic vertical displacement from the 1960 Valdivia earthquake [*Plafker and Savage*,1970] and the 2010 Maule earthquake [*Vargas et al.*,

2011]. Black vectors are the vertical velocities from campaign-mode GPS between 1996 and 2002 [*Ruegg et al.*, 2009]. (B) Projected topography along the swath a-a'. Vertical exaggeration: 90X. The anticlinal deformation with a WNW-SES trending axis is discussed by *Melnick et al.* [2009]. (C) Coseismic uplift due to the 1960 Valdivia earthquake (green line, *Moreno et al.* [2009]), and the coseismic plus postseismic uplift of the 2010 Maule earthquake (blue line, this study) projected along profile a-a', and the total uplift (red line). Squares are the projected in-situ measurements with the same color codes as (A). Dashed black line indicates the location of the neutral line. (D) The equivalent uplift rate (red line), derived by dividing the total uplift in (C) by the period between 2010 and 1835, assuming the year of 1835 is the onset of another seismic cycle. Black squares are the projected GPS vertical velocities. (E) Projected topography along the swath b-b', showing clear back-tilting of the peninsula. Vertical exaggeration: 25X. (F) Uplift curves along the b-b' profile, with the same color codes as (C). (G) The equivalent uplift rate and GPS vertical velocities projected along profile b-b'.

Chapter 4

INTERSEISMIC PLATE COUPLING IN THE EASTERN MAKRAN SUBDUCTION ZONE

Paper in preparation: Lin, Y. N., M. Simons, R. Jolivet, P. Agram, H. Martens, and Z. Li (in prep.) Interseismic plate coupling in the eastern Makran Subduction Zone.

Abstract

The seismogenic potential of the eastern Makran subduction zone has long been an enigma due to lack of geodetic observations. We present the first interseismic coupling model in this region based on satellite radar interferometry measurements made from four parallel tracks of ENVISAT images covering the entire eastern Makran. Because the satellite line-of-sight direction is not optimal for detecting the presumably northward interseismic ground displacement, the expected tectonic signal is both long-wavelength and low amplitude in character. Using a MERIS-ECMWF atmospheric phase screen correction, together with ocean tidal load corrections, and by selecting a small subset of well-corrected images for time-series analysis, we are able to retrieve LOS velocities of 1-2 mm/yr at 300-km length scales. We develop 2D back-slip models along different projected LOS velocity profiles and find spatial variations of coupling, with higher coupling in the central part, and lower coupling on the two ends of the eastern Makran subduction zone. The region of low coupling may be associated with the subduction of the Little

Murray Ridge and the Sonne fault. Minimum cumulative moment deficits for regions corresponding to the 1851, 1945 and 1765 earthquakes are equivelant to earthquakes with magnitudes of 7.7, 7.9 and 7.6, respectively.

4. 1 Introduction

The Makran subduction zone extends from western Pakistan to eastern Iran, forming the boundary between the subducting Arabian plate and the overriding Eurasian plate, with the eastern corner of the Arabian plate further dissected into the Ormara microplate (Figure 1a). For many years this subduction zone attracts far less attention than most other seismogenic subduction zones. Geophysical research in this region has been primarily focused on the 400-km wide accretionary prism, which has the thickest accreted sediment section (~7.5 km) of any accretionary margin [*Smith et al.*, 2012]. Associated studies include the evolution of structural styles, critical taper and wedge mechanics, and hydrocarbon potentials [e.g., *Fowler et al.*, 1985; *Fruehn et al.*, 1997; *Kopp et al.*, 2000; *Kukowski et al.*, 2001; *Schluter et al.*, 2002; *Grando et al.*, 2007; *Spiess et al.*, 2007; *Mokhtari et al.*, 2008; *Ding et al.*, 2010; *Smith et al.*, 2012]. In contrast, there has been relatively little analysis of the seismogenic potential of this subduction zone. *Byrne et al.* [1992] provided a detailed analysis of the largest instrumentally recorded megathrust event in the region, the 1945 Mw 8.1 Balochistan earthquake, as well as an estimate of seismic potentials with constraints from other smaller events described by several earlier studies [*Nowroosi* 1972; *Jacob and Quittmeyer*, 1979; *Dziewonski et al.*, 1983; *Chandra* 1984; *Jackson and McKenzie*, 1984; *Quittmeyer and Kafka*, 1984; *Laane and Chen*, 1989]. Subsequent studies have been limited by the generally low rate of seismicity [*Engdahl et*

al., 2006; *Alinaghi et al.*, 2007; *Rani et al.*, 2011; *El-Hussain et al.*, 2012]. Several large (Mw 7-8) events have occurred [*Laane and Chen*, 1989; *Martin and Kakar*, 2012], including one on April 16, 2013 (Figure 4.1), but these are mainly at intermediate depth with normal faulting mechanisms, and therefore they do not reveal information about the megathrust.

Geodetic measurements can help distinguish regions of the plate boundary megathrust that are coupled from those that appear to be creeping. In the western (Iranian) Makran, sparsely spaced GPS measurements have been used to infer weak coupling [*McClusky et al.*, 2000; *McClusky et al.*, 2003; *Nilforoushan et al.*, 2003; *Vernant et al.*, 2004; *Bayer et al.*, 2006; *Reilinger et al.*, 2006; *Masson et al.*, 2007]. However in the eastern (Pakistani) Makran, region that encompasses the 1945 earthquake, there is no such GPS data available. This region lies in a remote area of western Pakistan, which due to political and safety concerns is difficult to visit. To our knowledge, over the past two decades, only one GPS station has been installed in eastern Makran (Figure 4.1a) [*Bilham et al.*, 2009], insufficient for inferring the extent of plate coupling in the region.

Fortunately, since 1992 this region has been routinely imaged by the ERS-1, ERS-2 and ENVISAT synthetic aperture radar (SAR) satellites - all three launched by the European Space Agency. With the accumulation of more than two decades of data, a time-series analysis of these images should allow us to resolve interseismic deformation in this region. As the SAR data cover a wide area (Figure 4.1b), we should then be able to derive the interseismic coupling pattern and thus the first-order estimates on the potential for future large megathrust earthquakes.

However, before using the large volume of available SAR data, we need to quantify our ability to detect the expected long-wavelength and small-amplitude signal associated with the plate coupling in a subduction zone environment. Such measurements are particularly challenging given that noise from other non-tectonic sources can be much larger than the signal itself [e.g. *Grandin et al.*, 2012; *Béjar-Pizarro et al.*, 2013]. Here we explore the limit of interferometric synthetic aperture radar (InSAR) to measure such deformation without aid of GPS or any other ground-based geodetic data. We show that with the current generation of techniques for estimating or modeling out non-tectonic signals in InSAR images, together with recently developmed time-series analysis tools, we can resolve the interseismic line-of-sight (LOS) velocities with approximately 1-2 mm/yr sensitivities. With the obtained LOS velocity fields, we estimate the slip deficit rate along the eastern Makran subduction zone. Using these rates, we make first-order estimates of the seismic potential along this subduction megathrust.

4. 2 Tectonic Setting of the Eastern Makran Subduction Zone

The Makran subduction zone is nearly 1000 km long, bounded by the sinistral Ornach Nal fault to the east and the dextral Minab-Zendan fault to the west (Figure 4.1b). *Byrne et al.* [1992] first separated the Makran subduction zone into eastern and western parts, divided roughly along the Sistan Suture and its southward extension. Geologic features that are offset across this boundary include: the Quaternary calc-alkaline volcanoes, topographic depressions (Mashkel and Jaz Murian) [*Byrne et al., 1992*], and the northern boundary of the accretionary prism (Figure 4.1b). All these features are systematically offset 70-80 km northwards in eastern Makran than those in the west. Similar offset phenomenon occurs

for the intermediate-depth normal faulting events (Figure 4.1a). Large historic earthquakes occurred mostly in eastern Makran, whereas west Makran has only one historic earthquake (the 1843 event) which was later re-interpreted as an event of moderate magnitude that happened in the Gulf of Hormuz based on reviewing historic literature [*Musson*, 2009] (Figure 4.1b).

Estimates of plate convergence rate also differ between eastern and western Makran. Along the Makran subduction zone, the Arabia Plate is subducting underneath the Eurasia Plate at rates that increase eastwards. Estimates of the plate convergence rate suggest a 3-7 mm/yr higher rate in eastern Makran than that inferred for western Makran (Figure 4.2) [*Gripp and Gordon*, 1990; *Argus and Gordon*, 1991; *DeMets et al.*, 1994; *McClusky et al.*, 2000; *Drewes* 1998; *Drewes and Angermann*, 2001; *Gripp and Gordon*, 2002; *Sella et al.*, 2002; *Kreemer et al.*, 2003; *McClusky et al.*, 2003; *Prawirodirdjo and Bock*, 2004; *Vernant et al.*, 2004; *Reilinger et al.*, 2006; *Drewes* 2009; *DeMets et al.*, 2010; *Argus et al.*, 2010]. Values obtained using space geodesy are generally 5-15 mm/yr smaller than geologic estimates (Figure 4.2), and thus underlie a discussion regarding a potential recent slowdown in convergence between the Arabia and Eurasia plate [*DeMets et al.*, 2010]. The scarcity of GPS stations along this plate boundary, plus the recognition of the Ormara microplate (not taken into consideration in all plate models), makes confusing attempts to quantify relative motion across the eastern Makran plate boundary. Just to further complicate matters, the slip directions projected from rakes of thrust events on the eastern Makran megathrust (from GCMT catalog [*Dziewonski et al.*, 1981; *Ekstrom et al.*, 2012] and from the catalog of *Byrne et al.* [1992]; see Figure 4.1a for event locations), indicate an average seismic slip direction that is almost due north, whereas the slip direction of the 1945 earthquake is N23°W [*Byrne et al.*, 1992], although the latter could be poorly

constrained because the solution is based on body waveform inversion of only two teleseismic stations. These directions are significantly different from the N12°E~N18°E convergence azimuth predicted by plate models. Here, we do not try to further constrain estimates of the convergence vector since all of our InSAR observations have approximately the same line-of-sight (LOS) imaging geometry and provide little ability to resolve this issue.

Although the onshore part of eastern Makran is difficult to visit, the offshore part has been the subject of many studies. Seismic surveys in eastern Makran show that structural patterns, such as zonations of active faults and styles of imbrications, are fairly homogeneous in the trench-parallel direction, with little evidence for large-scale segmentation [*Smith et al.*, 2012]. However, there is a significant decrease in the depth of the décollement from west (near Pasni) to east (near Ormara) presumably related to changes in basement topography associated with the impingement of the Little Murray Ridge (Figure 4.1). Both trench sediment thickness and subduction channel thickness to the east of Ormara are 60% of the values to the west of Pasni [*Smith et al.*, 2012]. Therefore, we may expect differences in the coupling patterns from west to east, despite no obvious signs of segmentation in surface structures.

The only GPS measurement in eastern Makran has a velocity of 21±3 mm/yr at N200°E relative to the Indian plate [*Bilham et al.*, 2009]. After transforming the vector to the stable Eurasia reference frame, the velocity becomes 17.7±3 mm/yr at N6°W based on the MORVEL 56-plate velocity estimates [*DeMets et al.*, 2010] (Figure 4.1a), whereas all other plate models give even more westerly vectors. Despite the azimuth difference between the GPS velocity and the plate convergence direction (N12°E~N18°E), the northward movement at an intermediate rate (as compared to the ~30 mm/yr plate convergence rate

from space geodesy models) at Ormara indicates a certain level of coupling on the megathrust. A tombolo at Ormara experienced 2 m of uplift during the 1945 earthquake [*Ambraseys and Melville*, 1982]. It is therefore reasonable to assume interseismic subsidence in Ormara, an elastic response opposite to the coseismic [Thatcher and Rundle, 1979; Savage, 1983]. Uplift of late-Holocene marine deposits near Ormara suggests that inelastic deformation exists in the forearc [*Page et al.*, 1979], but the extent to which this deformation occurs interseismically or coseismically is still unclear [*Victor et al.*, 2011; *Lin et al.*, 2013].

4. 3 Data Processing

We concentrate on four descending orbital tracks of ENVISAT ASAR (Advanced Synthetic Aperture Radar) images, T220, T449, T177, and T406 that cover the entire eastern Makran from 2003 to 2011 (Figure 4.1b). There is insufficient data from ascending tracks to allow for useful analysis. We do not extend the study period to times before 2002 using the same tracks from the ERS satellites because, as shown in later sections, we find that the use of the MERIS (Medium Resolution Imaging Spectrometer) images acquired concurrently with the ASAR images is crucial to the correction for tropospheric delays in radio signal propagation. We produce InSAR images by using the repeat-orbit interferometry package (ROI_PAC) [*Rosen et al., 2004*]. To control computational costs, we choose a subset of image pairs using a Delaunay triangulation in baseline vs time space (we recognize that this is a non-unique approach). There are in total 126 epochs and 264 InSAR images for all four tracks (Figure 4.3; see also Figure C1-C4 for post-correction inteferograms). This large ensemble of images gives a preliminary idea about data quality,

as well as the epochs for which atmospheric disturbances are well predicted by our correction methods (to be further discussed later). We then pick the epochs corresponding to interferograms that appear to be well corrected using our atmospheric correction models. Depending on the quality of correction associated with each epoch and the perpendicular baselines, the number of interferograms in this second stack varies from track to track, but in general there are fewer images in the second stacks, except for T177. In the end, there are 173 InSAR images constructed from 67 epochs in this smaller ensemble (Figure 4.3; see Figure C5-C8 for post-corrected interferograms).

We consider two major corrections to each interferogram: an atmospheric phase screen (APS) correction and an ocean tidal loads (OTL) correction. We describe in detail each of the correction procedures in the following sections.

4.3.1 Atmospheric Phase Screen (APS) Correction

Application of Atmospheric Phase Screen (APS) correction is essential to infer small-amplitude tectonic signals [*Grandin et al.*, 2012; *Hammond et al.*, 2012; *Li et al.*, 2012; *Béjar-Pizarro et al.*, 2013]. In eastern Makran, the dynamic range of atmospheric signals reaches 20 cm, particularly in summer months when the Indian monsoon prevails (Figure 4.4). Even though it is usually assumed that neutral atmospheric signals are uncorrelated over timescales longer than 1-day [*Zebker et al.*, 1997; *Emardson et al.*, 2003], we found that in Makran it is not always the case. The E-W trending Makran Coastal Range (Figure 4.1b) and the prevailing wind direction (mainly from the south) usually result in repeating APS patterns over different dates. A good APS correction is essential to resolving any underlying tectonic signals.

APS corrections generally consist of an ionospheric correction and a tropospheric correction. Here, we focus on the tropospheric correction since the influence of the ionosphere is usually relatively minor in the C-band interferometry. Several methods have been proposed to correct for the effect of spatially and temporally varying radar wave propagation speeds in the troposphere. These methods can be categorized into three groups: 1) corrections with concurrent observations, including GPS wet delays [*Webley et al.*, 2002; *Li et al.*, 2003; *Onn and Zebker*, 2006], MODIS (Moderate Resolution Imaging Spectroradiometer) [*Li et al.*, 2005, 2006a], and MERIS [*Li et al.*, 2006b, 2012]; 2) numerical weather model corrections, such as MM5 (mesoscale meteorological model) [*Foster et al.*, 2006; *Puysségur et al.*, 2007; *Foster et al.*, 2013], or Global Atmospheric Models [*Doin et al.*, 2009; *Jolivet et al.*, 2011; *Pinel et al.*, 2011]; 3) empirical corrections, mostly for the topographically-correlated phase delays [*Cavalié et al.*, 2007; *Lin et al.*, 2010].

In this study, we use MERIS to correct ENVISAT ASAR interferograms, but we also make use of information provided by numerical weather models. Here we use the freely and openly available tool PyAPS (http://earthdef.caltech.edu/) to incorporate the information from ERA-Interim, provided by the European Center for Medium-Range Weather Forecast (hereafter ECMWF model), as shown in the work of *Jolivet et al.* [2011]. We follow the procedures in *Li et al.* [2012] to compute the precipitable water vapor from MERIS data, but instead of using a constant conversion factor of 6.2 between the MERIS precipitable water vapor and the zenith wet delay, we compute the conversion factor as a function of time and space by using the partial pressure of water vapor and temperature information from the nearest prediction time in the ECMWF model [*Jolivet et al.*, in prep]. In most cases, wet delays from ECMWF model mimic those from MERIS (Figure 4.4), and

therefore the conversion factor obtained from ECMWF model should reflect the spatially and temporally variable atmospheric status. We find that the average reduction of variance from corrections with constant conversion factors to those with variable conversion factors is not very large (i.e., 1.5%), with the maximum difference of 12% (~1.5 cm noise level). Overall, the MERIS-ECMWF hybrid correction reduces the data variance by 50-80%.

An example of the correction results is shown in Figure 4.5. Here we compare results from ECMWF and MERIS-ECMWF hybrid corrections. Both methods significantly reduce the dynamic range of the interferograms, but the MERIS correction produces a cleaner image than the ECMWF correction, even when an empirical bilinear ramp is not removed from the original image. However, use of MERIS-derived corrections has its own limitations. In particular, there will be spatial gaps in the corrections, corresponding to regions with clouds; furthermore, some MERIS data fail to predict the right APS pattern or even increase the noise in a given interferogram due to inadequacies in the cloud mask; additionally, at some epochs, no MERIS data was acquired. ECMWF APS corrections are model-derived and thus always continuous in space and available for all epochs. Here, we compare the use of both approaches.

Given the amplitude of the expected deformation signal in the satellite LOS direction, correction for path delays will be essential. In this vein, we note that the GPS measurement at Ormara (Figure 4.1a) shows that horizontal displacement occurs primarily in the N-S direction, whereas our LOS observations are mostly sensitive to E-W and vertical displacements (Figure 4.1b). We expect sub-cm/yr velocities in the LOS direction, as compared with propagation delays that may cause noise with 20-cm characteristic amplitude on any given image. However, since MERIS-based corrections

have many limitations (e.g., lack of acquisitions, a poor cloud mask, failure in interpolating holes, etc.), we examined each corrected image individually and removed pairs that were clearly poorly corrected. While this cleaning step is somewhat subjective, we established the following guidelines for removing interferometric pairs:

1. Signals are locally correlated with topography.

2. Hummocky signals of strong amplitudes with length scales of approximately 10 to 30 km are likely due to water vapor/clouds.

3. For regions masked out by the MERIS cloud mask, it is likely that regions immediately abutting masked out areas may also be influenced by strong water vapor or clouds and be left due to inexact masking.

One may also hope to mitigate uncorrected noise via time-series analysis. As we show later, we find that even in the context of time series analysis, focusing on the cleanest image pairs is still very important.

4.3.2 Ocean Tidal Loads (OTL) Correction

The Earth is continually being loaded and unloaded by the periodic redistribution of ocean mass at the surface, which causes elastic deformation of the solid Earth [e.g., *Farrell* 1972; *Pugh* 1987; *Agnew* 1997]. The amplitude of Earth's response to the loading can exceed several centimeters in coastal regions, well within the sensitivity level of modern geodetic tools such as InSAR. Although removing the OTL signal from radar interferograms is not yet part of routine analysis procedures, *DiCaprio & Simons* [2008] highlighted the

importance of an OTL correction to tectonic geodesy surveys, noting that OTL displacement gradients can surpass 3 cm per 100 km in some regions. Since tectonic processes often occur over similar or larger length scales, an OTL correction may be important to produce the cleanest time series.

Here we model the OTL deformation signal at the location of the Makran subduction zone using the SPOTL software package [*Agnew* 2012]. The SPOTL subroutine `nloadf` computes the amplitude and phase of surface displacements for a given tidal constituent at a particular observation site by convolution of an ocean tidal model with elastic Greens functions that represent Earth's response to a point load at the surface [*Agnew* 1997]. Since InSAR acquisitions cover a large spatial swath, we discretize each interferogram into a regular grid of geographic points (e.g., 0.05° spacing). We then use nloadf to determine the amplitude and phase of displacements in three components (north, east, and vertical) at each grid point for the M2, S2, N2, O1, P1, Q1, S1, K1, M4, MF, and MM tidal constituents using the FES2004 global ocean model [Lyard et al. 2006] and the Greens functions derived from the Preliminary Reference Earth Model (PREM) [*Dziewonski and Anderson*, 1981]. Our Greens functions assume a reference frame centered at the center of mass of the solid Earth, but since we are concerned with relative displacements across an interferogram, we are not particularly sensitive to choice of reference frame.

In the eastern Makran subduction region, the predicted vertical displacements due to OTL vary by up to 4 cm across the length of a single interferogram for several of the epochs in our study period. This translates to an OTL displacement gradient greater than 1 cm per 100 km, large enough to interfere with the long-term tectonic signals. The examples shown in Figure 4.4 and 4.5 have relatively small predicted OTL signals, and therefore the

correction effect is not obvious. When the OTL response is up to 4 cm across the length of the swath, the OTL correction influences the estimate of any bilinear ramps (Figure 4.6).

4. 4 Time Series Analysis

We construct time series using two different methods: NSBAS (New Small-Baseline Subset) [*Lopez-Quiroz et al.*, 2009; *Doin et al.*, 2011; *Jolivet et al.*, 2012] and MInTS (Multi-scale InSAR Time Series) [*Hetland et al.*, 2012]. Both tools have been integrated into the Generic InSAR Analysis Toolbox (GIAnT) [*Agram et al.*, 2013], openly and freely available at http://earthdef.caltech.edu/.

We choose a first order polynomial formula, $\Phi=C+vt$, as our time function, where Φ is phase, C is a constant shift, v is the LOS secular velocity and t is time. Before inverting for the model parameters, bilinear ramps are removed in a network sense so that the ramp parameters are internally consistent within the whole time series [*Agram et al.*, 2013]. In NSBAS, the inversion is done on a pixel-by-pixel base. To assure the stability of the inversion results in NSBAS, we mask out the region where missing values exceed 10% of the total number of measurements. In MInTS, data are transformed into the wavelet domain so that the spatial covariance is accounted for. Temporal parameters are inferred in the wavelet domain and then inverse transformed into the space-time domain. We estimate model uncertainties using a Jackknifing technique.

We derive the secular LOS velocities for both the large ensemble of radar interferograms without culling and a smaller ensemble that has been subjectively determined to be as clean as possible. For the larger ensemble, inferred LOS velocities are very noisy (Figure 4.7). Short-wavelength patterns inconsistent across different tracks overwhelm any underlying long-wavelength tectonic signals. The velocity uncertainties are also large,

reflecting the impact of uncorrected noise. The smaller ensemble yields considerably cleaner estimates of LOS velocities with long-wavelength signals continuous across different tracks (Figure 4.8). This comparison illustrates the importance of pre-selection of well-corrected interferograms when studying tectonic signals of long wavelength and low SNR. At present, we do not have an automatic algorithm to preselect images.

NSBAS and MInTS produce identical estimates of the LOS velocities, but their uncertainties (1σ) are quite different, with the values from MInTS generally an order of magnitude smaller than those from NSBAS (notice the change of color scales in Figure 4.7 & 4.8). This difference may arise from the way these two methods treat the missing points. In MInTS, interferogram holes are interpolated before being transformed into the wavelet domain, and a weight matrix *W*, distinct for each scale and each location, keeps track of the extent each wavelet is associated with measured versus interpolated phase [*Hetland et al.*, 2012]. The inversion, with the weight matrix involved, is carried out in the wavelet domain, which by design effectively takes into account distance-dependent data covariance [*Emardson et al.*, 2003; *Lohman and Simons*, 2005]. Instead of the real loss of data points, MInTS allows information to propagate into no-data region via data covariances, while reducing the weight of interpolated wavelets by *W*. These approaches lead to a more stable parameter estimate, and hence smaller uncertainties.

4. 5 Interseismic Coupling Models

The purpose of this study is to understand the first-order coupling patterns on the eastern Makran megathrust. We consider a 2D rather than a 3D model for two reasons. First, as mentioned earlier, since the single LOS direction is not optimal for detecting the

interseismic deformation in eastern Makran, a 3-D model introduces many more unconstrained degrees of freedom. Second, short-wavelength features in the LOS velocities (Figure 4.8) can be easily mapped as spatial variation in coupling in a 3D model despite their uncertain (tectonic or atmospheric) sources. We choose to project each velocity map into profiles to concentrate on long-wavelength tectonic signals that vary in the direction normal to the trench. We consider a few independent projected profiles to gain some insights about possible lateral variations in coupling.

We adopt the megathrust geometry from the work of *Byrne et al.* [1992] (Figure 4.1c), and discretize the fault into segments with a down-dip width of 15 km. These fault segments are pseudo-3D models, which means each fault patch has the same length as the eastern Makran subduction zone, and their strike agrees with the general trend of the trench (~262°). This discretization gives 25 depth segments in total, with increasing z increments at depth due to steepening dip angles. The top of the fault is assigned to be 10 km below sea level, corresponding to the 3 km deep sea floor plus the 7-km thick ocean-bottom sediments at the deformation front [*Kopp et al.*, 2000]. We calculate Green's functions assuming a homogeneous elastic half-space [*Okada*, 1985].

We follow the back-slip approach [*Savage*, 1983] to obtain our interseismic coupling model. We derive the slip deficit rate (equivalent to the annual rate of back-slip but in the sense of deficit in reverse slip) on the megathrust, assuming all the LOS displacements are elastic. We then divide the annual slip deficit by the plate convergence rate to obtain the coupling ratio. As elluded to before, a discrepancy exists between geologic and geodetic plate convergence speed and azimuth (Figure 4.2). Considering the hypothesis of recent slowdown in convergence between the Arabia and Eurasia plate [*DeMets et al.*, 2010], we adopt the 30 mm/yr convergence rate from modern geodetic measurements, agreeing with

the time frame of the InSAR measurements. We assume several different convergent azimuths, including N10°E from geodetic plate models, due north from the average rake of the background seismicity, and N8°W, parallel to the GPS measurement at ORMA and the down-dip direction given the general trend of the trench (Figure 4.1a).

Our inversion minimizes the objective function $\Phi(\lambda) = ||C(Gm-d)||_2 + \lambda||Dm||_2$ where *C* has diagonals as the reciprocal of LOS velocity variances, *G* is the design matrix, *m* is the slip on each fault segment, *d* is the projected LOS velocity profile, *D* is the Laplacian operator, and λ is the weighting over the regularization term. We conduct separate inversions for each track of data. We compute multiple solutions for each track with a fixed set of parameters, and the tradeoffs between goodness of fit and model roughness show clear corners in the L-curve plots (Figure 4.9). To compare coupling models across different tracks, we set a common cut-off RMS residual to be 0.2 mm/yr, approximately the average level of MInTS uncertainties for all four tracks. Thus, instead of showing one single realization of a coupling model, we select several models over a spectrum of model smoothness.

In the results for the N10°E convergence azimuth (Figure 4.10-1), the coupling pattern is very sensitive to the selection of λ. The smoother the model, the smaller the coupled region and amount of coupling. This sensitivity comes from the orthogonality of the direction of plate convergence and the LOS vector, such that model predicted LOS displacements are dominated by vertical motions and are insensitive to different predictions of horizontal displacements. This instability does not necessarily mean the N10°E convergence azimuth is inherently wrong, but rather that the InSAR LOS velocities do not allow any definite result for this convergence direction. Having said that, if we

compare the amplitude of measured and predicted ORMA horizontal components, and ignore the difference in azimuth, the result suggests ~0.75 peak coupling near the shallow part of the proposed locked patch along T177 (Figure 4.10-1). In terms of vertical displacements, all models in this study predict subsidence at Ormara, broadly consistent with coseismic uplift there [*Ambraseys and Melville*, 1982].

We now consider models with plate convergence directions straight north and N8°W. The orthogonality between the LOS direction and the convergence azimuth decreases, as does the sensitivity to regularization (Figure 4.10-2 & 4.10-3). The ORMA horizontal component is well predicted by these two models, suggesting a highly coupled patch at 10-20 km depth along T177. The track to the west, T449, also suggests intermediate to high coupling in the same depth range. T220, the one closest to the Iran-Pakistan border, is slightly more sensitive to regularization and convergence angles, and therefore it is less conclusive whether or not average coupling exceeds 0.5 (Figure 4.10-2 & 4.10-3). T406 at the eastern end has the least coherent long-wavelength velocity field and the largest uncertainties (Figure 4.8). In the 2D profile, the projected velocities are also more scattered than the other three profiles (Figure 4.10). With the same set of λ values and same fault geometry, it is difficult to fit the profile well (Figure 4.9 & 4.10). The large uncertainties may suggest contamination of residual APS noises, possibly due to the increase in turbulence, rain and clouds associated with the rising mountain belt [*Rasul et al.*, 2005]. Based on the higher noise level and less coherent tectonic signals, our results are inconclusive for this track. However, to avoid mapping APS noises onto the megathrust as annual slip deficits, we choose the smoothest model among those selected to estimate the moment deficit (as detailed in the next section).

To summarize, by testing different plate convergence azimuths and different levels of smoothness constraints, we infer intermediate to high coupling at seismogenic depths for the central part of the eastern Makran subduction zone. This coupling model matches the horizontal GPS measurement at Ormara, and the predicted subsidence agrees with the elastic rebound theory given the observed coseismic uplift at the same location. To the west near the Iran-Pakistani border, there is possibility of low-to-intermediate coupling. To the east, the inversion result is unstable due to large uncertainties. To avoid over-fitting, we choose the smoothest model as the basis for our later discussions and this means low coupling on the megathrust.

4. 6 Discussion

Subduction of the Sonne fault and the Little Murray Ridge may be the underlying cause of low interseismic coupling values at the two ends of the eastern Makran subduction zone. The Sonne fault is considered to be a new plate boundary fault that initiated ca. 2 Ma [*Kukowski et al.*, 2000]. Similar to fracture zones, this strike-slip fault may enhance the flux of chemically bound water into the subduction zone [*Contreras-Reyes et al.*, 2008] and also influence the thermal regime inducing variations in the stick-slip-like frictional behavior on the interface. Similar examples include the subduction of the Investigator Fracture Zone and the low coupling region on the Sumatran megathrust near the equator [*Chlieh et al.*, 2008], and the subduction of different fracture zones and the low-coupling areas in the southern Chile megathrust [*Moreno et al.*, 2011]. As for the Little Murray Ridge, its subduction underneath the accretionary prism leads to significant decrease of sediment thickness and décollement depth [*Smith et al.*, 2012], which may change the

frictional properties on the plate interface. A possible analogous region is where the Nazca ridge subducts underneath the Andes in southern Peru. This region appears to be aseismically creeping [*Chlieh et al.*, 2011] and has been interpreted to have rate-strengthening properties on the megathrust as evidenced in studies of afterslip associated with the 2007 Mw 8.0 Pisco earthquake [*Perfettini et al.*, 2010].

Compared with the two ends of the eastern Makran subduction zone, the central part appears to be more highly coupled, as shown by the models derived with observations from orbital tracks 449 and 177. This central segment approximates the lateral rupture extent of the 1945 earthquake [*Byrne et al.*, 1992] (Figure 4.1b), although in our model the partially coupled region may extend down to 30 km at depth, deeper than the inferred depth extent of the 1945 event (Figure 4.10). Between 20-30 km depth the megathrust may be partially creeping, as indicated by the inferred low coupling values, and it may also be the region where postseismic slip occurs, as shown by the postseismic studies of several large subduction earthquakes [e.g., *Hsu et al.*, 2006; *Pritchard and Simons*, 2006; *Miyazaki and Larson*, 2008; *Ozawa et al.*, 2012; *Lin et al.*, 2013; *Ortega-Culaciati et al.*, 2013].

Based on the smoothest coupling models at different convergence azimuths, we estimate the cumulative moment deficit for the three regions associated with the 1851, 1945-47 and 1765 earthquakes, respectively (as proposed by *Byrne et al.* [1992]) (Figure 4.1 & 4.11). The moment deficit for the 1851 patch is 4.96e+20~1.01e+21 Nm, equivalent to Mw 7.7-7.9. The moment deficit for the 1945-47 patch is 5.59e+20~1.49e+21 Nm based on results from T449, and 1.03e+20~2.53e+21 Nm based on T177, equivalent to Mw 7.8-8.1 and Mw 7.9-8.2 respectively. The moment deficit for the 1765 patch is the smallest, 3.08e+20~4.42e+20 Nm, equivalent to Mw 7.6-7.7. These estimates are based on the

restrictive assumptions that the projected LOS velocity profiles represent the average interseismic deformation pattern over the designated influence area and that this pattern remains stable through time.

Our interpretation of the observed deformation field in terms of plate coupling and accumulating seismogenic potential assumes no long-term permanent strain accumulation. However, *Haghipour et al.* [2012] showed that uplift of Quaternary fluvial terraces in west Makran shows clear folding patterns, of 5-15 km wavelengths and at rates of 0.8-1.2 mm/year. If such permanent deformation is ongoing in eastern Makran, there could be some short-wavelength signals associated with the folding or faulting in the upper-crust, which may in turn explain some of the short-wavelength patterns in map view (Figure 4.8) and the short scale oscillations in the projected profiles (Figure 4.10). Currently, these oscillations are modeled by variation of coupling at depth, but it is also possible that some, if not all, of the oscillations are due to non-elastic deformation in thrust sheets [*Litchfield and Berryman*, 2006; *Matsu'ura et al.*, 2008; *Matsu'ura and Kase*, 2010]. To the extent that this process is active, the coupling models and cumulative moment deficits that we infer here should be considered as upper bounds. Deployment of a regional GPS network and/or InSAR observations over a longer period of time with shorter repeat time and at multiple LOS directions will help provide more accurate estimates.

4.7 Conclusions

We explore different approaches to isolating small amplitude, long wavelength tectonic deformation in noisy interferograms. In particular, we explore a hybrid MERIS-ECMWF atmospheric phase screen correction and the impact of ocean tidal load corrections. These

corrections reduce the data variance by 50-80%. The use of consistent time-series analysis methods (e.g., NSBAS and MInTS) even for estimating secular velocity fields allows us to estimate continuous LOS velocities over four parallel InSAR tracks. To further improve the signal-to-noise ratio, we project each LOS velocity field into trench perpendicular profiles that show clear long-wavelength deformation patterns. The success in retrieval of low-amplitude and long-wavelength tectonic signals indicates that appropriate data processing scheme and time-series analysis tools are critical for InSAR application on interseismic deformation in subduction zones.

Using these LOS velocity estimates, we obtain the first interseismic coupling models for the eastern Makran subduction zone. The models suggest that the central segment may be more extensively coupled than the eastern and western ends of this segment. These apparently less coupled region, coincide with the subduction of Little Murray Ridge and the Sonne fault. At face value, the apparent coupling models imply a cumulative moment deficit, since the most recent events, to be equivalent to a Mw 7.7-7.9 on the 1851 subsegment, a Mw 7.8-8.2 on the 1945-47 subsegment and a Mw 7.6-7.7 on the 1765 subsegment. Due to observational limitation, strong spatiotemporal variations in coupling and permanent non-elastic component of the deformation field are not considered in this model. More data over a longer time span, at multiple LOS directions, with shorter repeat time, and accompanied with path delay corrections based on concurrent observations will greatly improve the reliability of estimates in plate coupling.

References of Chapter 4

Agnew, D. C. (1997), NLOADF: A program for computing ocean-tide loading, *J. Geophys. Res.*, *102*(B3), 5109-5110, doi: 10.1029/96jb03458.

Agnew, D. C. (2012), SPOTL: some programs for ocean-tide loading, Scripps Institution of Oceanography.

Agram, P. S., R. Jolivet, B. Riel, Y. N. Lin, M. Simons, E. Hetland, M. P. Doin, and C. Lasserre (2013), New Radar Interferometric Time Series Analysis Toolbox Released, *Eos Trans. AGU*, *94*(7), 69-70, doi: 10.1002/2013e0070001.

Alinaghi, A., I. Koulakov, and H. Thybo (2007), Seismic tomographic imaging of P- and S-waves velocity perturbations in the upper mantle beneath Iran, *Geophys. J. Int.*, *169*(3), 1089-1102, doi: 10.1111/j.1365-246X.2007.03317.x.

Ambraseys, N. N., and C. P. Melville (1982), *A history of Persian earthquakes*, Cambridge University Press, New York.

Argus, D. F., and R. G. Gordon (1991), No-net-rotation model of current plate velocities in incorporating plate motion model NUVEL-1, *Geophys. Res. Lett.*, *18*(11), 2039-2042, doi: 10.1029/91gl01532.

Argus, D. F., R. G. Gordon, M. B. Heflin, C. Ma, R. J. Eanes, P. Willis, W. R. Peltier, and S. E. Owen (2010), The angular velocities of the plates and the velocity of Earth's centre from space geodesy, *Geophys. J. Int.*, *180*(3), 913-960, doi: 10.1111/j.1365-246X.2009.04463.x.

Bayer, R., J. Chery, M. Tatar, P. Vernant, M. Abbassi, F. Masson, E. Nilforoushan, E. Doerflinger, V. Regard, and O. Bellier (2006), Active deformation in Zagros-Makran transition zone inferred from GPS measurements, *Geophys. J. Int.*, *165*(1), 373-381, doi: 10.1111/j.1365-246X.2006.02879.x.

Béjar-Pizarro, M., A. Socquet, R. Armijo, D. Carrizo, J. Genrich, and M. Simons (2013), Andean structural control on interseismic coupling in the North Chile subduction zone, *Nat. Geosci.*, doi: 10.1038/ngeo1802.

Bilham, R., S. Lodi, R. Bendick, and P. Molnar (2009), Aseismic slip on the Makran coast?, 3-10 pp, UNAVCO.

Briggs, R. W., et al. (2006), Deformation and slip along the Sunda Megathrust in the great 2005 Nias-Simeulue earthquake, *Science*, *311*(5769), 1897-1901.

Byrne, D. E., L. R. Sykes and D. M. Davis (1992), Great thrust earthquakes and aseismic slip along the plate boundary of the Makran subduction zone, *J. Geophys. Res.*, *97*, 449-478.

Cavalié, O., M. P. Doin, C. Lasserre, and P. Briole (2007), Ground motion measurement in the Lake Mead area, Nevada, by differential synthetic aperture radar interferometry time series analysis: Probing the lithosphere rheological structure, *J. Geophys. Res.*, *112*, B03403.

Chandra, U. (1984), Focal mechanism solutions for earthquakes in Iran, *Phys. Earth Planet. Inter.*, *34*(1-2), 9-16, doi: 10.1016/0031-9201(84)90080-3.

Chlieh, M., J. P. Avouac, K. Sieh, D. H. Natawidjaja, and J. Galetzka (2008), Heterogeneous coupling of the Sumatran megathrust constrained by geodetic and paleogeodetic measurements, *J. Geophys. Res.*, *113*(B5), B05305, doi: 10.1029/2007jb004981.

Chlieh, M., H. Perfettini, H. Tavera, J.-P. Avouac, D. Remy, J.-M. Nocquet, F. Rolandone, F. Bondoux, G. Gabalda, and S. Bonvalot (2011), Interseismic coupling and seismic potential along the Central Andes subduction zone, *J. Geophys. Res.*, *116*(B12), B12405, doi: 10.1029/2010JB008166.

Contreras-Reyes, E., and D. Carrizo (2011), Control of high oceanic features and subduction channel on earthquake ruptures along the Chile-Peru subduction zone, *Phys. Earth Planet. Inter.*, *186*(1-2), 49-58.

Contreras-Reyes, E., I. Grevemeyer, E. R. Flueh, and C. Reichert (2008), Upper lithospheric structure of the subduction zone offshore of southern Arauco peninsula, Chile, at ~38°S, *J. Geophys. Res.*, *113*(B7), B07303, doi: 10.1029/2007JB005569.

DeMets, C., R. G. Gordon, and D. F. Argus (2010), Geologically current plate motions, *Geophys. J. Int.*, *181*(1), 1-80, doi: 10.1111/j.1365-246X.2009.04491.x.

DeMets, C., R. G. Gordon, D. F. Argus, and S. Stein (1994), Effect of recent revisions to the geomagnetic reversal time scale on estimates of current plate motions, *Geophys. Res. Lett.*, *21*(20), 2191-2194.

DiCaprio, C., and M. Simons (2008), The importance of ocean tidal load corrections for differential InSAR, *Geophys. Res. Lett.*, *35*, L22309.

Ding, F., V. Spiess, N. Fekete, B. Murton, M. Bruening, and G. Bohrmann (2010), Interaction between accretionary thrust faulting and slope sedimentation at the frontal Makran accretionary prism and its implications for hydrocarbon fluid seepage, *J. Geophys. Res.*, *115*, doi: 10.1029/2008jb006246.

Doin, M. P., C. Lasserre, G. Peltzer, O. Cavalie, and C. Doubre (2009), Corrections of stratified tropospheric delays in SAR interferometry: Validation with global atmospheric models, *J. Appl. Geophys.*, *69*(1, Sp. Iss. SI), 35-50.

Doin, M. P., S. Guillaso, R. Jolivet, C. Lasserre, F. Lodge, G. Ducret, and R. Grandin (2011), Presentation of the small baseline NSBAS processing chain on a case example: The etna deformation monitoring from 2003 to 2010 using ENVISAT data, *Eur. Space Agency Spec. Publ.*, *ESA SP-697*, 1-7.

Drewes, H. (1998), Combination of VLBI, SLR, and GPS determined station velocities for actual plate kinematic and crustal deformation models, in *Geodynamics*, edited by M. Feissel, Springer.

Drewes, H. (2009), The actual plate kinematic and crustal deformation model APKIM2005 as basis for a non-rotating ITRF, in *Geodetic Reference Frames*, edited by H. Drewes, pp. 95-99, Springer.

Drewes, H., and D. Angermann (2001), The actual plate kinematic and crustal deformation model 2000 (APKIM2000) as a Geodetic Reference System, in *AIG 2001 Scientific Assembly*, edited, Budapest.

Dziewonski, A. M., and D. L. Anderson (1981), Preliminary reference earth model, *Phys. Earth Planet. Inter.*, *25*(4), 297-356, doi: 10.1016/0031-9201(81)90046-7.

Dziewonski, A. M., T. A. Chou, and J. H. Woodhouse (1981), Determination of earthquake source parameters from waveform data for studies of global and regional seismicity, *J. Geophys. Res.*, *86*(NB4), 2825-2852, doi: 10.1029/JB086iB04p02825.

Dziewonski, A. M., A. Friedman, D. Giardini, and J. H. Woodhouse (1983), Global seismicity of 1982 - centroid-moment tensor solutions for 308 earthquakes, *Phys. Earth Planet. Inter.*, *33*(2), 76-90, doi: 10.1016/0031-9201(83)90141-3.

Ekstrom, G., M. Nettles, and A. M. Dziewonski (2012), The global CMT project 2004-2010: Centroid-moment tensors for 13,017 earthquakes, *Phys. Earth Planet. Inter.*, *200*, 1-9, doi: 10.1016/j.pepi.2012.04.002.

El-Hussain, I., A. Deif, K. Al-Jabri, N. Toksoz, S. El-Hady, S. Al-Hashmi, K. Al-Toubi, Y. Al-Shijbi, M. Al-Saifi, and S. Kuleli (2012), Probabilistic seismic hazard maps for the sultanate of Oman, *Nat. Hazards*, *64*(1), 173-210, doi: 10.1007/s11069-012-0232-3.

Emardson, T. R., M. Simons, and F. H. Webb (2003), Neutral atmospheric delay in interferometric synthetic aperture radar applications: Statistical description and mitigation, *J. Geophys. Res.*, *108*, B5, 2231.

Engdahl, E. R., J. A. Jackson, S. C. Myers, E. A. Bergman, and K. Priestley (2006), Relocation and assessment of seismicity in the Iran region, *Geophys. J. Int.*, *167*(2), 761-778, doi: 10.1111/j.1365-246X.2006.03127.x.

Farrell, W. E. (1972), Deformation of earth by surface loads, *Rev. Geophys.*, *10*(3), 761-&, doi: 10.1029/RG010i003p00761.

Foster, J., B. Brooks, T. Cherubini, C. Shacat, S. Businger, and C. Werner (2006), Mitigating atmospheric noise for InSAR using a high resolution weather model, *Geophys. Res. Lett.*, *33*, L16304.

Foster, J., J. Kealy, T. Cherubini, S. Businger, Z. Lu, and M. Murphy (2013), The utility of atmospheric analyses for the mitigation of artifacts in InSAR, *J. Geophys. Res.*, 118(2), 748-758, doi: 10.1002/jgrb.50093.

Fowler, S. R., R. S. White, and K. E. Louden (1985), Sediment dewatering in the Makran accretionary prism, *Earth Planet. Sci. Lett.*, *75*(4), 427-438, doi: 10.1016/0012-821x(85)90186-4.

Fruehn, J., R. S. White, and T. A. Minshull (1997), Internal deformation and compaction of the Makran accretionary wedge, *Terra Nova*, *9*(3), 101-104, doi: 10.1046/j.1365-3121.1997.d01-13.x.

Grandin, R., M.-P. Doin, L. Bollinger, B. Pinel-Puysségur, G. Ducret, R. Jolivet, and S. N. Sapkota (2012), Long-term growth of the Himalaya inferred from interseismic InSAR measurement, *Geology*, *40*(12), 1059-1062, doi: 10.1130/g33154.1.

Grando, G., and K. McClay (2007), Morphotectonics domains and structural styles in the Makran accretionary prism, offshore Iran, *Sediment. Geol.*, *196*(1-4), 157-179, doi: 10.1016/j.sedgeo.2006.05.030.

Gripp, A. E., and R. G. Gordon (1990), Current plate velocities relative to the hotspots in incorporating the NUVEL-1 global plate motion model, *Geophys. Res. Lett.*, *17*(8), 1109-1112, doi: 10.1029/GL017i008p01109.

Gripp, A. E., and R. G. Gordon (2002), Young tracks of hotspots and current plate velocities, *Geophys. J. Int.*, *150*(2), 321-361, doi: 10.1046/j.1365-246X.2002.01627.x.

Haghipour, N., J. P. Burg, F. Kober, G. Zeilinger, S. Ivy-Ochs, P. W. Kubik, and M. Faridi (2012), Rate of crustal shortening and non-Coulomb behaviour of an active accretionary wedge: The folded fluvial terraces in Makran (SE, Iran), *Earth Planet. Sci. Lett.*, *355*, 187-198, doi: 10.1016/j.epsl.2012.09.001.

Hammond, W. C., G. Blewitt, Z. H. Li, H. P. Plag, and C. Kreemer (2012), Contemporary uplift of the Sierra Nevada, western United States, from GPS and InSAR measurements, *Geology*, *40*(7), 667-670, doi: 10.1130/g32968.1.

Hetland, E. A., M. P, M. Simons, Y. N. Lin, P. S. Agram, and C. J. DiCaprio (2012), Multiscale InSAR Time Series (MInTS) analysis of surface deformation, *J. Geophys. Res.*, *117*(B2), B02404.

Hsu, Y.-J., M. Simons, J.-P. Avouac, J. Galetzka, K. Sieh, M. Chlieh, D. Natawidjaja, L. Prawirodirdjo, and Y. Bock (2006), Frictional afterslip following the 2005 Nias-Simeulue earthquake, Sumatra, *Science*, *312*(5782), 1921-1926, doi: 10.1126/science.1126960.

Jackson, J., and D. McKenzie (1984), Active tectonics of the Alpine Himalayan belt between western Turkey and Pakistan, *Geophys. J. Roy. Astr. S.*, *77*(1), 185-+, doi: 10.1111/j.1365-246X.1984.tb01931.x.

Jacob, K. H., and R. L. Quirtmeyer (1979), The Makran region of Pakistan and Iran: trench-arcs ystemw ith activep late subduction, in *Geodynamics of Pakistan*, edited by A. Farah and K. A. de Jong, pp. 305-317, Geological Survey of Pakistan, Quetta.

Jolivet, R., R. Grandin, C. Lasserre, M. P. Doin, and G. Peltzer (2011), Systematic InSAR tropospheric phase delay corrections from global meteorological reanalysis data, *Geophys. Res. Lett.*, *38*(17), L17311.

Jolivet, R., C. Lasserre, M. P. Doin, S. Guillaso, G. Peltzer, R. Dailu, J. Sun, Z. K. Shen, and X. Xu (2012), Shallow creep on the Haiyuan Fault (Gansu, China) revealed by SAR Interferometry, *J. Geophys. Res.*, *117*(B6), B06401, doi: 10.1029/2011jb008732.

Kopp, C., J. Fruehn, E. R. Flueh, C. Reichert, N. Kukowski, J. Bialas, and D. Klaeschen (2000), Structure of the Makran subduction zone from wide-angle and reflection seismic data, *Tectonophysics*, *329*(1-4), 171-191, doi: 10.1016/s0040-1951(00)00195-5.

Kreemer, C., W. E. Holt, and A. J. Haines (2003), An integrated global model of present-day plate motions and plate boundary deformation, *Geophys. J. Int.*, *154*(1), 8-34, doi: 10.1046/j.1365-246X.2003.01917.x.

Kukowski, N., T. Schillhorn, E. R. Flueh, and K. Huhn (2000), Newly identified strike-slip plate boundary in the northeastern Arabian Sea, *Geology*, *28*(4), 355-358, doi: 10.1130/0091-7613(2000)28<355:nispbi>2.0.co;2.

Kukowski, N., T. Schillhorn, K. Huhn, U. von Rad, S. Husen, and E. R. Flueh (2001), Morphotectonics and mechanics of the central Makran accretionary wedge off Pakistan, *Mar. Geol.*, *173*(1-4), 1-19, doi: 10.1016/s0025-3227(00)00167-5.

Laane, J. L., and W. P. Chen (1989), The Makran earthquake of 1983 April 18 - a possible analog to the Puget Sound earthquake of 1965, *Geophys. J. Int.*, *98*(1), 1-9, doi: 10.1111/j.1365-246X.1989.tb05509.x.

Li, Z., J.-P. Muller, and P. Cross (2003), Comparison of precipitable water vapor derived from radiosonde, GPS, and Moderate-Resolution Imaging Spectroradiometer measurements, *J. Geophys. Res.*, *108*(D20), 4651, doi: 10.1029/2003jd003372.

Li, Z., J. P. Muller, and P. Cross (2005), Interferometric synthetic aperture radar (InSAR) atmospheric correction: GPS, Moderate Resolution Imaging Spectroradiometer (MODIS), and InSAR integration, *J. Geophys. Res.*, *110*, B03410.

Li, Z., E. J. Fielding, P. Cross, and J. P. Muller (2006), Interferometric synthetic aperture radar atmospheric correction: GPS topography-dependent turbulence model, *J. Geophys. Res.*, *111*, B02404.

Li, Z., J. P. Muller, P. Cross, P. Albert, J. Fischer, and R. Bennartz (2006), Assessment of the potential of MERIS near-infrared water vapour products to correct ASAR interferometric measurements, *Int. J. Remote Sens.*, *27*, 349-365.

Li, Z. W., W. B. Xu, G. C. Feng, J. Hu, C. C. Wang, X. L. Ding, and J. J. Zhu (2012), Correcting atmospheric effects on InSAR with MERIS water vapour data and elevation-dependent interpolation model, *Geophys. J. Int.*, *189*(2), 898-910, doi: 10.1111/j.1365-246X.2012.05432.x.

Lin, Y.-N. N., M. Simons, E. A. Hetland, P. Muse, and C. DiCaprio (2010), A multiscale approach to estimating topographically correlated propagation delays in radar interferograms, *Geochem. Geophys. Geosyst.*, *11*(9), Q09002, doi: 10.1029/2010GC003228.

Lin, Y. N., et al. (2013), Coseismic and postseismic slip associated with the 2010 Maule earthquake, Chile: characterizing the Arauco Peninsula barrier effect, *J. Geophys. Res.*

Lohman, R. B., and M. Simons (2005), Some thoughts on the use of InSAR data to constrain models of surface deformation: Noise structure and data downsampling, *Geochem. Geophys. Geosyst.*, *6*, Q01007, doi: 10.1029/2004GC000841.

Lopez-Quiroz, P., M.-P. Doin, F. Tupin, P. Briole, and J.-M. Nicolas (2009), Time series analysis of Mexico City subsidence constrained by radar interferometry, *J. Appl. Geophys.*, *69*(1, Sp. Iss. SI), 1-15.

Lyard, F., F. Lefevre, T. Letellier, and O. Francis (2006), Modelling the global ocean tides: modern insights from FES2004, *Ocean Dynam.*, *56*(5-6), 394-415, doi: 10.1007/s10236-006-0086-x.

Martin, S. S., and D. M. Kakar (2012), The 19 January 2011 M-w 7.2 Dalbandin Earthquake, Balochistan, *B. Seismol. Soc. Am.*, *102*(4), 1810-1819, doi: 10.1785/0120110221.

Masson, F., M. Anvari, Y. Djamour, A. Walpersdorf, F. Tavakoli, M. Daignières, H. Nankali, and S. Van Gorp (2007), Large-scale velocity field and strain tensor in Iran inferred from GPS measurements: new insight for the present-day deformation pattern within NE Iran, *Geophys. J. Int.*, *170*(1), 436-440, doi: 10.1111/j.1365-246X.2007.03477.x.

Matsu'ura, T., and Y. Kase (2010), Late Quaternary and coseismic crustal deformation across the focal area of the 2008 Iwate-Miyagi Nairiku earthquake, *Tectonophysics*, *487*(1-4), 13-21, doi: 10.1016/j.tecto.2010.03.003.

Matsu'ura, T., A. Furusawa, and H. Saomoto (2008), Late Quaternary uplift rate of the northeastern Japan arc inferred from fluvial terraces, *Geomorphology*, *95*(3-4), 384-397, doi: 10.1016/j.geomorph.2007.06.011.

McClusky, S., R. Reilinger, S. Mahmoud, D. Ben Sari, and A. Tealeb (2003), GPS constraints on Africa (Nubia) and Arabia plate motions, *Geophys. J. Int.*, *155*(1), 126-138, doi: 10.1046/j.1365-246X.2003.02023.x.

McClusky, S., et al. (2000), Global Positioning System constraints on plate kinematics and dynamics in the eastern Mediterranean and Caucasus, *J. Geophys. Res.*, *105*(B3), 5695-5719, doi: 10.1029/1999jb900351.

Miyazaki, S., and K. M. Larson (2008), Coseismic and early postseismic slip for the 2003 Tokachi-oki earthquake sequence inferred from GPS data, *Geophys. Res. Lett.*, 35(4), doi: 10.1029/2007gl032309.

Mokhtari, M., I. A. Fard, and K. Hessami (2008), Structural elements of the Makran region, Oman sea and their potential relevance to tsunamigenisis, *Nat. Hazards*, *47*(2), 185-199, doi: 10.1007/s11069-007-9208-0.

Moreno, M., et al. (2011), Heterogeneous plate locking in the South-central Chile subduction zone: Building up the next great earthquake, *Earth Planet. Sci. Lett.*, *305*(3-4), 413-424.

Musson, R. M. W. (2009), Subduction in the Western Makran: the historian's contribution, *J. Geol. Soc.*, *166*(3), 387-391, doi: 10.1144/0016-76492008-119.

Nilforoushan, F., et al. (2003), GPS network monitors the Arabia-Eurasia collision deformation in Iran, *J. Geodesy*, *77*(7-8), 411-422, doi: 10.1007/s00190-003-0326-5.

Nowroosi, A. A. (1972), Focal mechanismo f earthquakesa nd plate tectonics of Middle East, *Bull. Seismol. Soc. Am.*, *62*, 823-850.

Okada, Y. (1985), Surface deformation due to shear and tensile faults in a half-space, *Bull. Seismol. Soc. Am.*, *75*(4), 1135-1154.

Onn, F., and H. A. Zebker (2006), Correction for interferometric synthetic aperture radar atmospheric phase artifacts using time series of zenith wet delay observations from a GPS network, *J. Geophys. Res.*, *111*, B09102.

Ozawa, S., T. Nishimura, H. Munekane, H. Suito, T. Kobayashi, M. Tobita, and T. Imakiire (2012), Preceding, coseismic, and postseismic slips of the 2011 Tohoku earthquake, Japan, *J. Geophys. Res.*, 117(B7), B07404, doi: 10.1029/2011JB009120.

Page, W. D., J. N. Alt, L. S. Cluff, and G. Plafker (1979), Evidence for the recurrence of large-magnitude earthquakes along the Makran coast of Iran and Pakistan, *Tectonophysics*, *52*(1-4), 533-547, doi: 10.1016/0040-1951(79)90269-5.

Perfettini, H., et al. (2010), Seismic and aseismic slip on the Central Peru megathrust, *Nature*, *465*(7294), 78-81, doi: 10.1038/nature09062.

Pinel, V., A. Hooper, S. De la Cruz-Reyna, G. Reyes-Davila, M. P. Doin, and P. Bascou (2011), The challenging retrieval of the displacement field from InSAR data for andesitic stratovolcanoes: Case study of Popocatepetl and Colima Volcano, Mexico, *J. Volcanol. Geotherm. Res.*, *200*(1-2), 49-61, doi: 10.1016/j.jvolgeores.2010.12.002.

Prawirodirdjo, L., and Y. Bock (2004), Instantaneous global plate motion model from 12 years of continuous GPS observations, *J. Geophys. Res.*, *109*(B8), doi: 10.1029/2003jb002944.

Pritchard, M. E., and M. Simons (2006), An aseismic slip pulse in northern Chile and along-strike variations in seismogenic behavior, *J. Geophys. Res.*, *111*(B8), B08405, doi: 10.1029/2006JB004258.

Pugh, D. T. (1987), *Tides, surges and mean sea-level*, John Wiley & Sons, Ltd.

Puysségur, B., R. Michel, and J.-P. Avouac (2007), Tropospheric phase delay in interferometric synthetic aperture radar estimated from meteorological model and multispectral imagery, *J. Geophys. Res.*, *112*, B05419.

Quittmeyer, R. C., and A. L. Kafka (1984), Constraints on plate motions in southern Pakistan and the northern Arabian Sea from the focal mechanisms of small earthquakes, *J. Geophys. Res.*, *89*(B4), 2444-2458, doi: 10.1029/JB089iB04p02444.

Rani, V. S., K. Srivastava, D. Srinagesh, and V. P. Dimri (2011), Spatial and Temporal Variations of b-Value and Fractal Analysis for the Makran Region, *Mar. Geol.*, *34*(1), 77-82, doi: 10.1080/01490419.2011.547804.

Rasul, G., Q. U. Z. Chaudhry, S. X. Zhao, Q. C. Zeng, L. L. Qi, and G. Y. Zhang (2005), A diagnostic study of heavy rainfall in Karachi due to merging of a mesoscale low and a diffused tropical depression during South Asian summer monsoon, *Adv. Atmos. Sci.*, *22*(3), 375-391, doi: 10.1007/bf02918751.

Reilinger, R., et al. (2006), GPS constraints on continental deformation in the Africa-Arabia-Eurasia continental collision zone and implications for the dynamics of plate interactions, *J. Geophys. Res.*, *111*(B5), doi: 10.1029/2005jb004051.

Rosen, P. A., S. Hensley, G. Peltzer, and M. Simons (2004), Updated repeat orbit interferometry package released, *Eos Trans. AGU*, *85*(5).

Ruegg, J. C., A. Rudloff, C. Vigny, R. Madariaga, J. B. de Chabalier, J. Campos, E. Kausel, S. Barrientos, and D. Dimitrov (2009), Interseismic strain accumulation measured by GPS in the seismic gap between Constitución and Concepción in Chile, *Phys. Earth Planet. Inter.*, *175*(1-2), 78-85, doi: 10.1016/j.pepi.2008.02.015.

Savage, J. C. (1983), A dislocation model of strain accumulation and release at a subduction zone, *J. Geophys. Res.*, *88*(B6), 4984-4996, doi: 10.1029/JB088iB06p04984.

Schluter, H. U., A. Prexl, C. Gaedicke, H. Roeser, C. Reichert, H. Meyer, and C. von Daniels (2002), The Makran accretionary wedge: sediment thicknesses and ages and the origin of mud volcanoes, *Mar. Geol.*, *185*(3-4), 219-232, doi: 10.1016/s0025-3227(02)00192-5.

Scholz, C. H., and C. Small (1997), The effect of seamount subduction on seismic coupling, *Geology*, *25*(6), 487-490, doi: 10.1130/0091-7613(1997)025<0487:TEOSSO>2.3.CO;2.

Scholz, C. H., and J. Campos (2012), The seismic coupling of subduction zones revisited, *J. Geophys. Res.*, *117*, doi: 10.1029/2011jb009003.

Sella, G. F., T. H. Dixon, and A. L. Mao (2002), REVEL: A model for Recent plate velocities from space geodesy, *J. Geophys. Res.*, *107*(B4), doi: 10.1029/2000jb000033.

Smith, G., L. McNeill, T. J. Henstock, and J. Bull (2012), The structure and fault activity of the Makran accretionary prism, *J. Geophys. Res.*, *117*(B7), B07407.

Spiess, V., L. Baumann, M. Bruning, and G. Collins (2007), Gold seeps of the Makran subduction zone (continental margin of Pakistan), cruise no. 74, leg 2, *Meteor Rep.*, *10-3*.

Vargas, G., M. Farias, S. Carretier, A. Tassara, S. Baize, and D. Melnick (2011), Coastal uplift and tsunami effects associated to the 2010 M(w)8.8 Maule earthquake in Central Chile, *Andean Geology*, *38*(1), 219-238.

Vernant, P., et al. (2004), Present-day crustal deformation and plate kinematics in the Middle East constrained by GPS measurements in Iran and northern Oman, *Geophys. J. Int.*, *157*(1), 381-398.

Victor, P., M. Sobiesiak, J. Glodny, S. N. Nielsen, and O. Oncken (2011), Long-term persistence of subduction earthquake segment boundaries: Evidence from Mejillones Peninsula, northern Chile, *J. Geophys. Res.*, *116*(B2), B02402, doi: 10.1029/2010JB007771.

Webley, P. W., R. M. Bingley, A. H. Dodson, G. Wadge, S. J. Waugh, and I. N. James (2002), Atmospheric water vapour correction to InSAR surface motion measurements on mountains: results from a dense GPS network on Mount Etna, *Phys. Chem. Earth*, *27*(4-5), 363-370, doi: 10.1016/s1474-7065(02)00013-x.

Zebker, H. A., P. A. Rosen, and S. Hensley (1997), Atmospheric effects in interferometric synthetic aperture radar surface deformation and topographic maps, *J. Geophys. Res.*, *102*, 7547-7563.

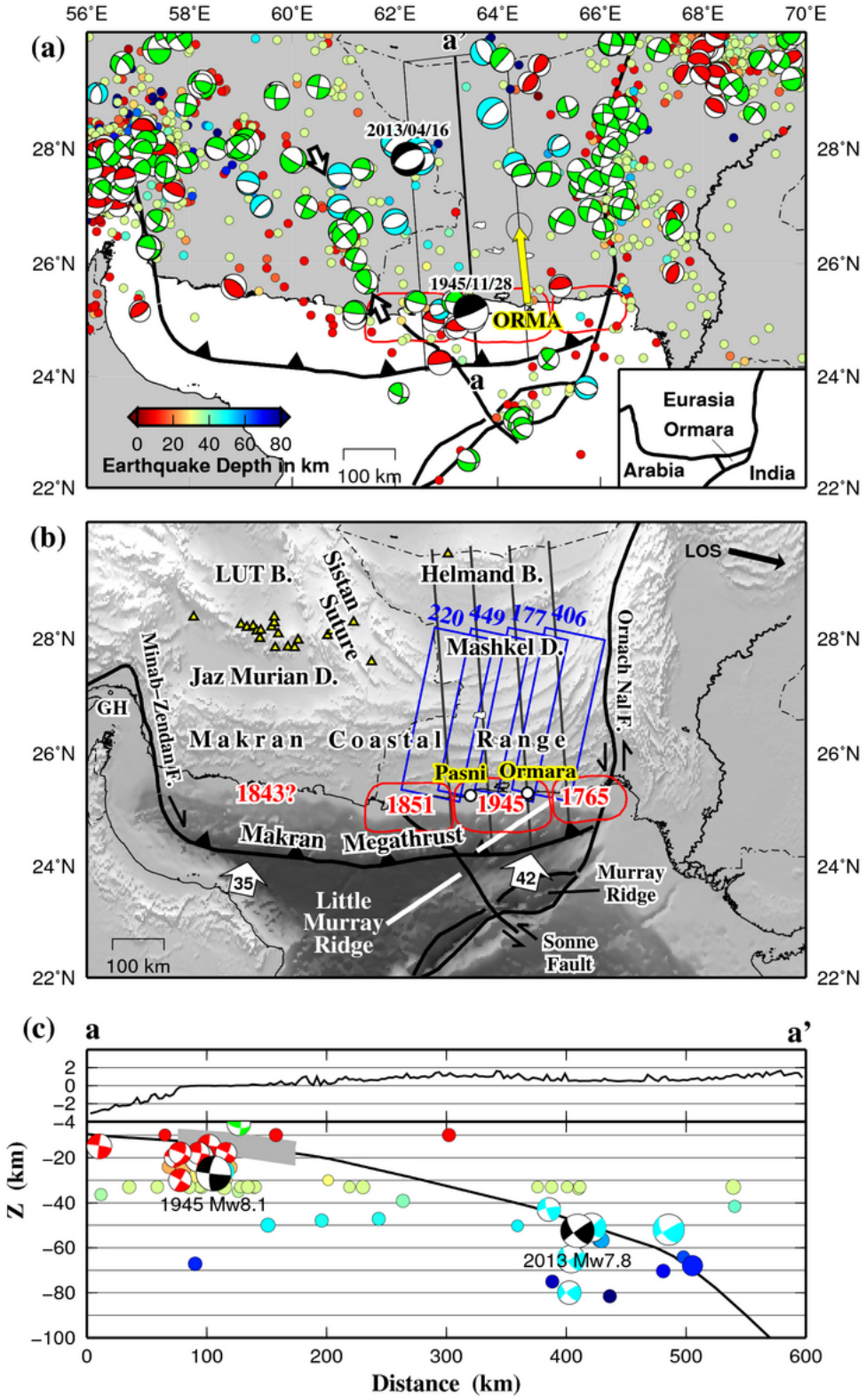
(a)
56°E
58°E
60°E
62°E
64°E
66°E
68°E
70°E
28°N
26°N
24°N
22°N
a
a'
2013/04/16
1945/11/28
ORMA
0 20 40 60 80
Earthquake Depth in km
100 km
Eurasia
Ormara
Arabia
India
(b)
LUT B.
Sistan Suture
Helmand B.
LOS
220 449 177 406
Mashkel D.
Ornach Nal F.
Minab-Zendan F.
Jaz Murian D.
GH
Makran Coastal Range
Pasni Ormara
1843?
1851
1945
1765
Makran Megathrust
35
42
Murray Ridge
Little Murray Ridge
Sonne Fault
100 km
(c)
a
a'
2
0
−2
−4
−20
−40
−60
−80
−100
Z (km)
1945 Mw8.1
2013 Mw7.8
0
100
200
300
400
500
600
Distance (km)

Figure 4.1. (a) Background seismicity and focal mechanisms in the Makran subduction zone. Small circles color-coded with depth are the M>3 events from the NEIC catalog between January 1973 and April 2013. Focal mechanisms are from Global Centroid Moment Tensor (GCMT) solutions between 1977 and 2013 [*Dziewonski et al.*, 1981; *Ekström et al.*, 2010] and from the work of *Byrne et al.* [1992], with the red color in compressional quadrants for thrusting events, green for strike-slip events, light blue for normal events, and black for the 1945 Mw=8.1 earthquake and the April 16, 2013 Mw=7.8 earthquake. Red lines circle the seismogenic patches associated with the 1851, 1945 and 1765 earthquakes from west to east [*Byrne et al.*, 1992] (also shown in Figure 4.1b). Yellow vector at Ormara (ORMA) is the only GPS measurement in east Makran relative to stable Eurasia [*Bilham et al.*, 2009]. White arrows highlight the alignment of a series of strike-slip events. Profile a-a' and the bounding box indicate the range of data projected onto the 2D profile in Figure 4.1c. Inset: outlines of different plates associated with the Makran subduction zone. (b) Physiographic features and geologic structures in Makran. B. = Block; D. = Depression; F. = Fault. GH = Gulf of Hormuz. Yellow triangles are Quaternary cal-alkaline andesitic volcanoes [*White*, 1984; *Dykstra and Birnie*, 1979; *Afāghi and Sālek*, 1977]. Blue rectangles are the footprints for ENVISAT ASAR images, with the line-of-sight (LOS) direction marked at the top-right corner of the map. Four black lines extending from the trench to the Helmand Block are the projection profiles associated with each ASAR track (used in the modeling of interseismic coupling). Thick white arrows are the relative plate motion (in mm/yr) of the Arabian plate with respect to the Eurasian plate based on NUVEL-1A plate model [*DeMets et al.*, 1994]. (c) Cross section showing the average topography and plate interface geometry along profile a-a'. Color codes for seismic data are the same as (a). The thick gray line represents the coseismic region proposed by *Byrne et al.* [1992].

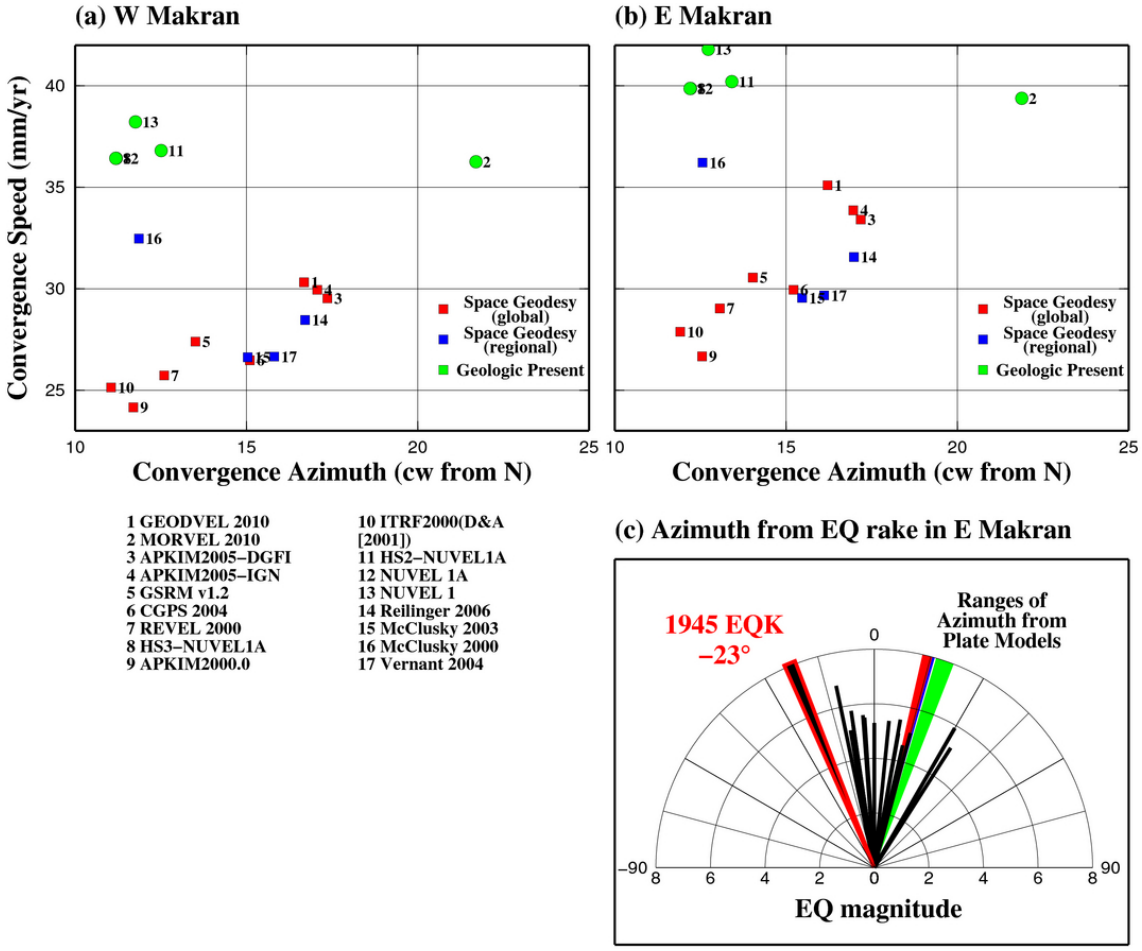

Figure 4.2. Relative plate motion of the Arabian plate with respect to the Eurasian plate predicted from different plate models at (a) west Makran and (b) east Makran. The convergent speeds obtained from geologic observations are in general higher than those from geodetic observations. All plate models predict convergence azimuth in the northeast direction, whereas (c) the trend of rakes from the thrusting events in the focal mechanisms (shown in Figure 4.1a) indicates an average of due north motion. The 1945 Mw8.1 earthquake even suggests the relative motion of the downgoing plate in the NW direction [*Byrne et al.*, 1992]. See text for the detailed references.

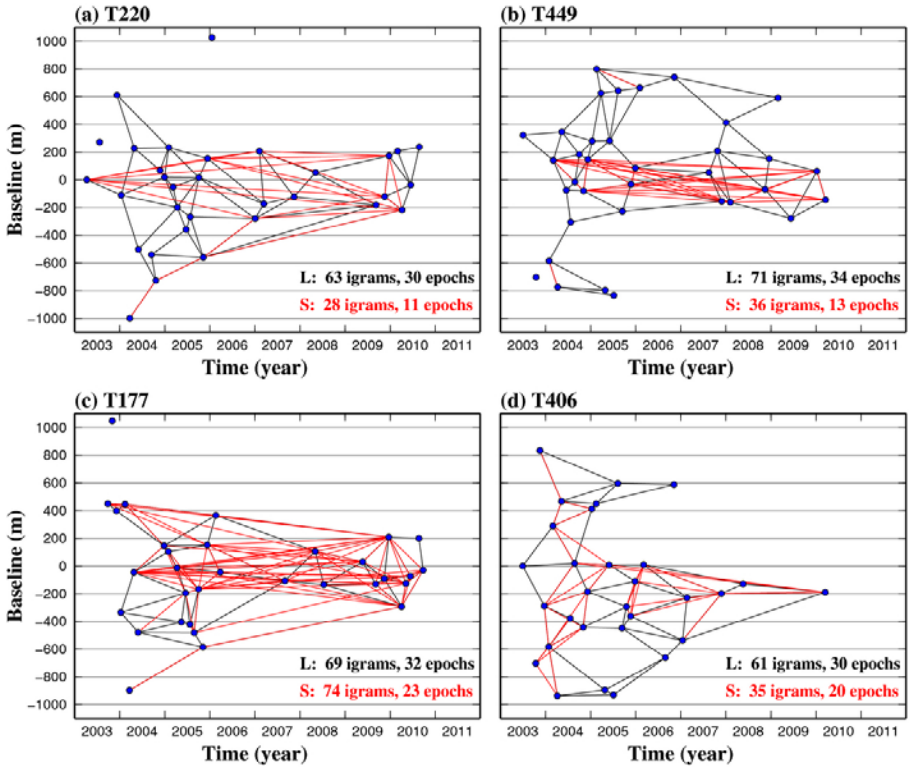

Figure. 4.3. The baseline plots for the interferograms used in the large ensemble (L, black lines) and small ensemble (S, red lines). Blue dot is for each acquisition. Some epochs are not included in the network due to bad qualities of the interferograms (decorrelation, unwrapping errors and so on). We use the Delaunay triangle to minimize the number of interferograms in the large ensemble while keeping the same amount of information in the network. The interferograms in the small ensemble are made from a subset of SAR acquisitions whose atmospheric noises are better predicted by MERIS corrections.

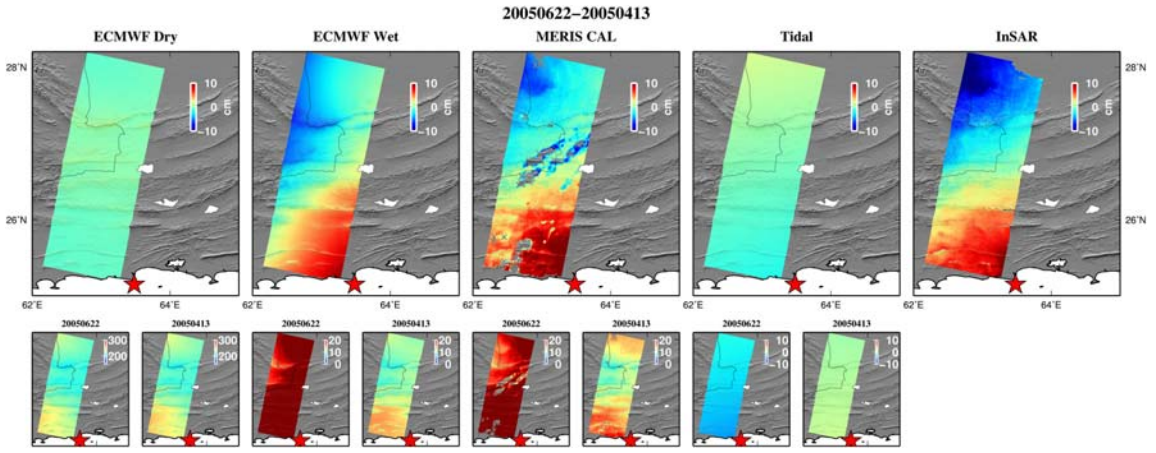

Figure 4.4. An example of the comparison plot between the ECMWF delays, MERIS wet delays calibrated with ECMWF data, ocean tidal load corrections, and the interferograms. All plots are in units of cm. This example demonstrates a case where both ECMWF and MERIS corrections capture the APS patterns in the interferogram. In some examples, both corrections may fail to predict the right pattern. Comparing plots like this over multiple interferograms with a common scene can help us determine the epochs with better correction results. Red star is for the 1945 Mw=8.1 earthquake. White polygons indicate lakes. Gray-scale image in the background shows the shaded–relief topography.

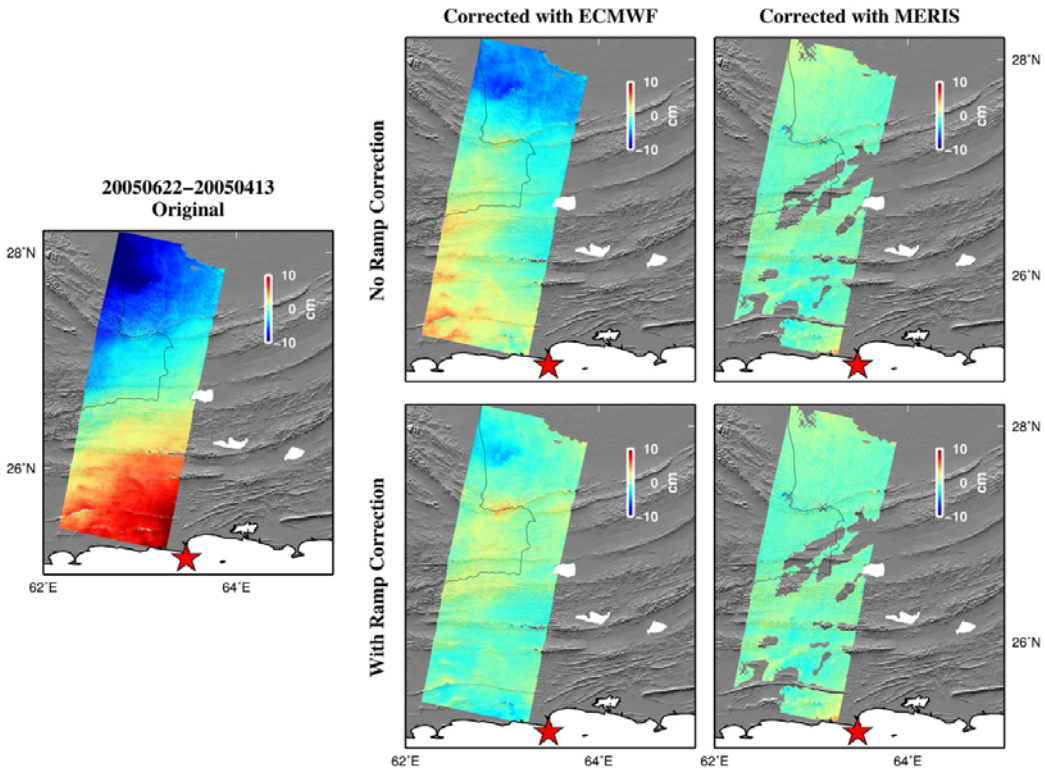

Figure. 4.5. Post-correction images of the same interferogram as Figure 4.4. The direct correction result (no ramp correction) shows residual APS noises in the ECMWF-corrected image, both in short and long spatial wavelengths, whereas the MERIS correction provides a cleaner result. After removing a bilinear ramp, there are still more structured noises in the ECMWF-corrected image. Symbology is the same as Figure 4.4.

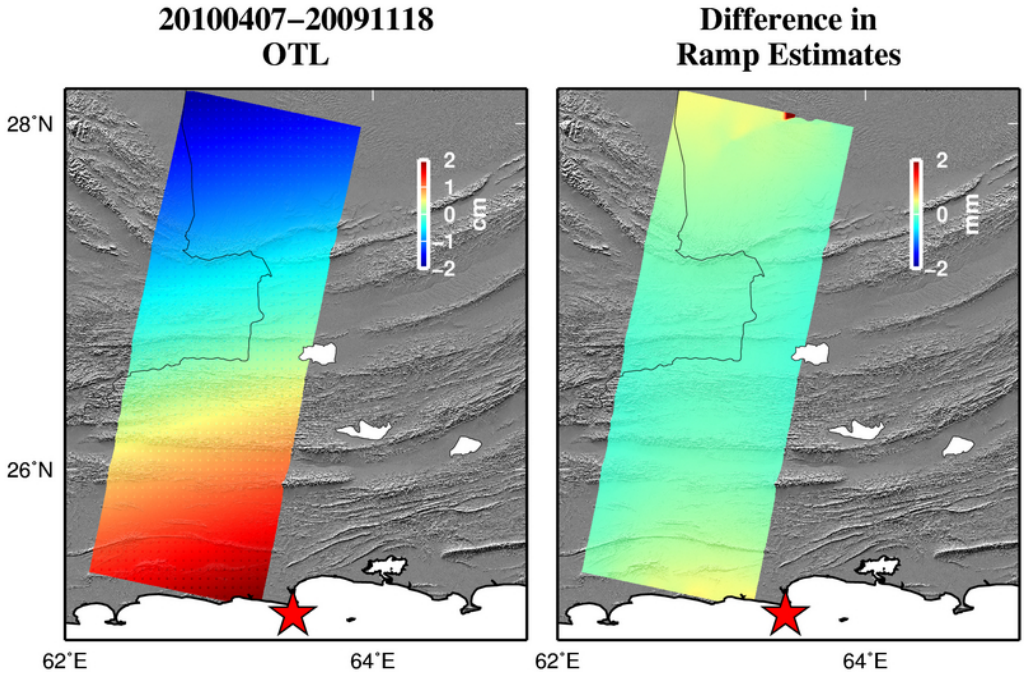

Figure 4.6. One example of the LOS displacement from ocean tidal loads (OTL), and its influence in the ramp estimation. The amplitude of relative displacement across the length of the swath is about 4 cm, close to the maximum value among all OTL responses at different epochs in this region. The difference in ramp estimation is calculated by taking the difference between an MERIS+ramp corrected image and an MERIS+OTL+ramp corrected image. This difference is minor (±1 mm), but if the target tectonic signal is of the same amplitude and wavelength, this difference may become an issue. Symbology is the same as Figure 4.4.

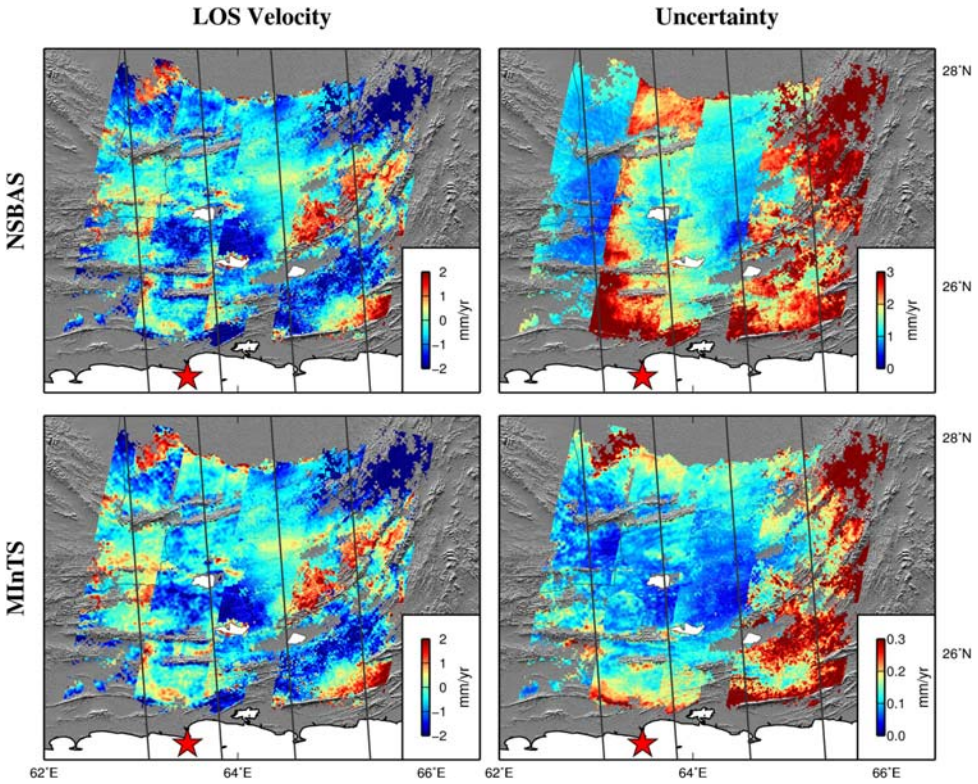

Figure 4.7. The LOS velocities and uncertainties obtained from the large ensemble of interferograms via NSBAS and MInTS. The LOS velocity maps are identical between different time-series methods, showing noisy short-wavelength patterns possibly on top of some vague long-wavelength signals. The four black lines mark the projection profiles associated with each track, same as those in Figure 4.1b. Red star is for the 1945 Mw=8.1 earthquake. Notice the change of color scale for the MInTS uncertainties. See the text for more discussion. Symbology is the same as Figure 4.4.

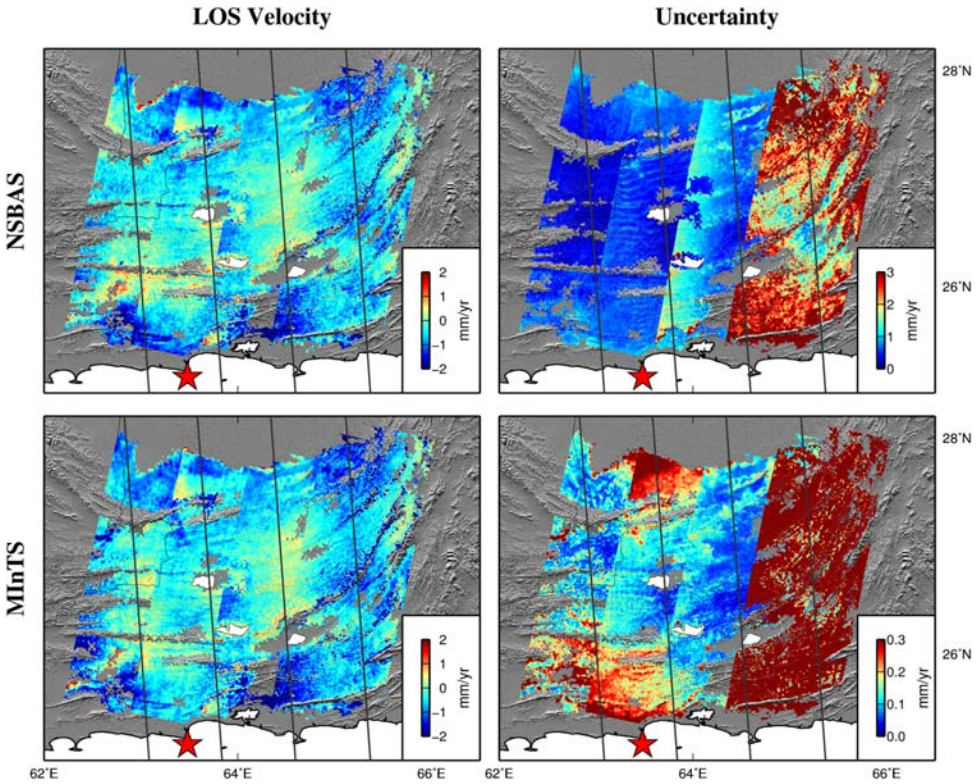

Figure. 4.8. Same with Figure 4.7 but obtained from the small ensemble of interferograms. The LOS velocity maps look cleaner and reveal long-wavelength signals continuous across different tracks. The uncertainties for the NSBAS results generally decrease except for T406 (the easternmost track), whereas the uncertainties for the MInTS results generally increase. The latter may be related to the decrease of support in the MInTS weight matrix due to a smaller number of interferograms in this ensemble. Symbology is the same as Figure 4.4.

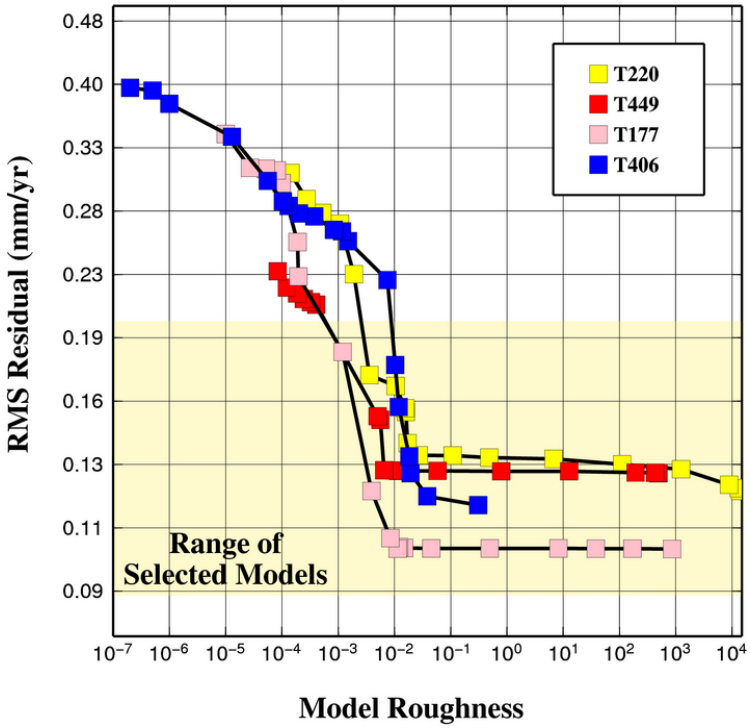

Figure 4.9. An example plot of RMS residuals versus model roughness (the "L-curve" plot) associated with each stacked profile (profile lines are shown in Figures 4.1 & 4.8) for the models with N8°W convergence azimuth. Each small square represents a λ value within a common set of λs for all four tracks. We use a common cut-off RMS residual, 0.2 mm/yr according to the approximate average of MInTS uncertainties for all tracks, as the criterion for model selections. The selected models are shown in Figure 4.10-3.

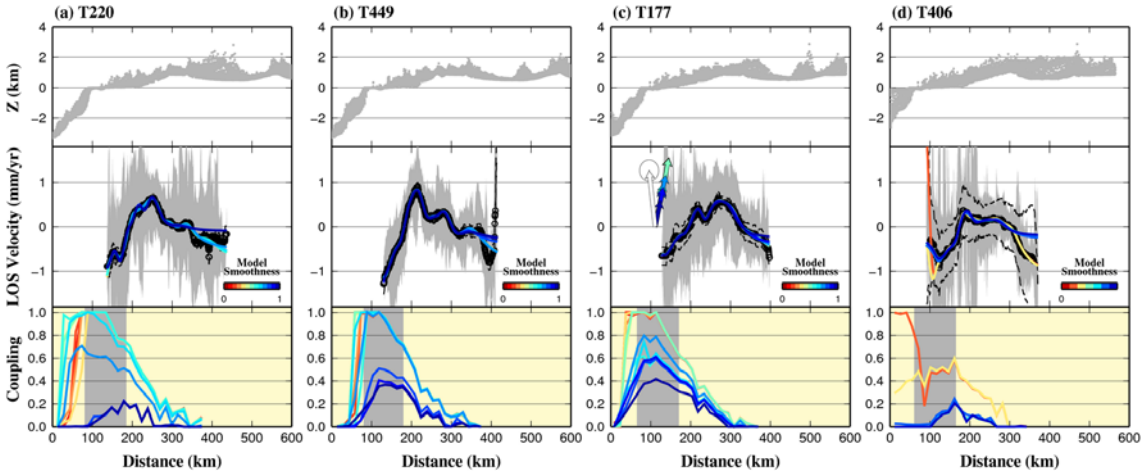

Figure 4.10-1. 2D interseismic coupling models with N10°E convergence azimuth. Figure show the average topography (upper panel), stacked LOS velocity profiles along with model predictions color-coded with different smoothness constraints (middle panel), and the coupling model as a function of distance, with the same color code as the middle panel (lower panel). The dash line in the middle panel indicates the 1σ LOS velocity uncertainty from MInTS time series analysis. The gray zone in the lower panel represents the coseismic region proposed by *Byrne et al.* [1992]. In the middle panel of (c), the horizontal component of the ORMA GPS measurement is plotted as a white vector with the map view convention (up for north, and right for east) at the projected distance. The predicted displacements at ORMA from different models are also shown at the same location with the same color code as the model smoothness.

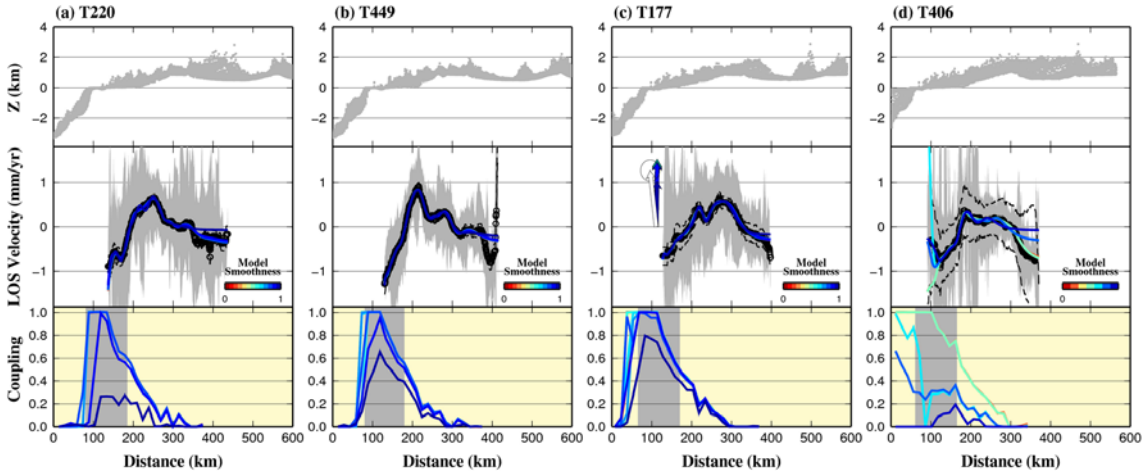

Figure 4.10-2. Same as Figure 4.10-1 but for the models with due north convergence azimuth.

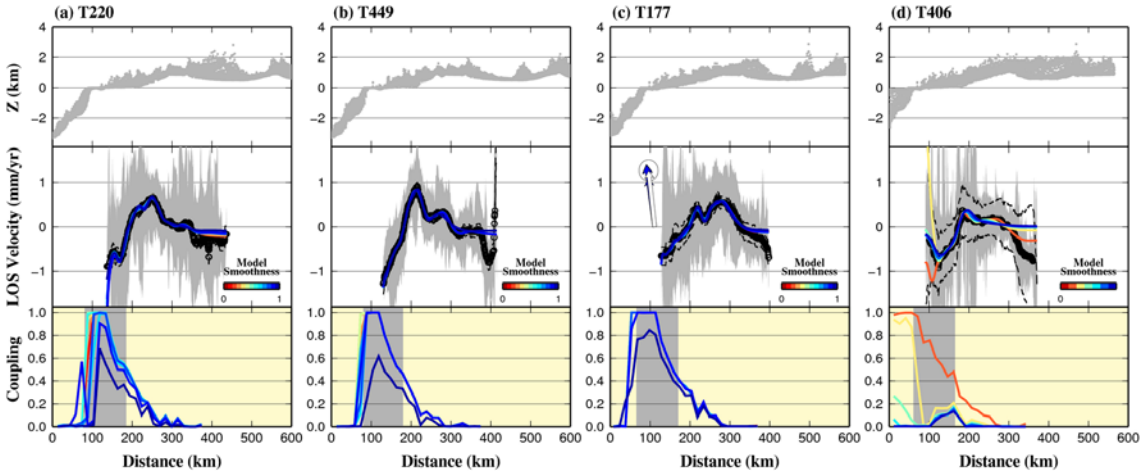

Figure 4.10-3. Same as Figure 4.10-1 but for the models with N8°W convergence azimuth.

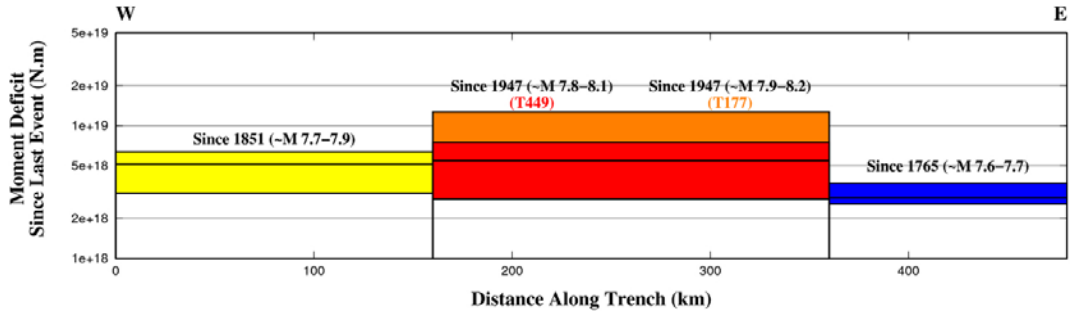

Figure 4.11. Cumulative moment deficit since last event as a function of distance along trench. The estimates are based on the proposed rupture area associated with the 1851, 1945-47 and 1765 earthquakes [*Byrne et al.*, 1992] (Figure 4.1b). These moment deficit estimates are taken from the smoothest coupling models within the selected of three different convergence azimuths.

Concluding Thoughts

This thesis provides tools for better understanding the distribution and behavior of asperities and barriers on the subduction interface. Exploiting recent technical advances in InSAR image processing and analysis allows us to expand their use beyond the more common targets of coseismic displacement, magmatic inflation, glacier flows, landslides, ground water/oil extraction or interseismic displacement on smaller length scales. Now it is the right time to dive back into the existing gigantic SAR catalogs, and address more challenging geophysical topics that were deemed impossible in the past. Future missions should consider concurrent atmospheric measurements as a necessity for the sake of broader applications of SAR observations.

Discriminating the spatial extent and temporal evolution of asperities and barriers is a long-term task. Any advance in data processing or model development will help achieve this goal. In the long run, after more asperities and barriers are identified with high precision and accuracy, the disputes between the influence of effective normal stress and frictional properties on subduction coupling patterns should be better addressed, or eventually, solved.

Appendix A

SUPPLEMENTARY MATERIAL OF CHAPTER II

A. 1 Comparison of Simultaneous and Iterative Decompositions

In principle it is necessary to solve for all components simultaneously to obtain the optimal rank-*k* approximation of the data matrix (note that this is not true for standard or weighted singular value decomposition). However, we ran into the complication of different components almost exclusively explaining separate datasets (Figure A1), annihilating the advantages of a joint inversion. The temporal functions for most components are discontinuous precisely at the epochs corresponding to the SAR images (Figure A1). To overcome that problem we solve for each component iteratively. This approach does not yield an optimal rank-*k* approximation of the data matrix, but it helps force each component to explain a significant fraction of all datasets. The procedure runs as follows:

1. Set X equal to the original data matrix.

2. Set $X_1 = X$.

3. Calculate the best rank-1 (1-component) model $\hat{X}_i$ of the data matrix X_i

4. Set $X_{i+1} = X_i - \hat{X}_i$

5. Return to step 3 unless termination condition has been reached.

The matrices $\hat{X}_i$ are the outer product of our spatial and temporal functions for the *i*th component. Due to the variation of optimal value of components with the total number of components (unlike in SVD, where the best *i*th component is independent of how that rank-*k* approximation is sought), the resultant principal components are close to but not exactly orthogonal. The PCAIM approach is valid for any linear combination of components regardless of orthogonality, even though mathematically it may not be optimal in terms of matrix approximation.

A. 2 Comparison of InSAR-only, EDM-only and InSAR + EDM Joint Inversions

We demonstrate here the benefit of the joint inversion of InSAR and EDM data, as compared to InSAR-only and EDM-only inversions. After the PCA decomposition, both the joint and the InSAR-only decomposition yield similar spatial functions for the 1st and 2nd components (Figure A2). By contrast the spatial functions of the 3rd and higher order components are quite different. Since the EDM data can be mostly reconstructed with only 2 components (notice how small the principal vectors are in the 3rd component of the joint decomposition), in the joint decomposition most of the InSAR signal that is not spatially coherent with the EDM data is taken account by the 3rd and higher order components. This leaves basically noise to higher components (in particular the tropospheric effects and the tectonic signals not visible in the EDM data). In the InSAR-only decomposition, without the guidance of EDM data, the spatial function can be any signal with coherent time history, and therefore what is extracted can be the coherent portion of atmospheric noises.

With regard to the time function, the joint and EDM-only decompositions yield very similar results for the first 3 components, whereas the joint and InSAR-only decompositions yield quite different results from the 2nd component and on. Again, since we assume that EDM data is better corrected for tropospheric noises and sampled in time, the incorporation of EDM data becomes a necessity because InSAR by itself cannot offer a reliable time evolution history.

At the decomposition stage it is clear that with our iterative approach the time functions are mostly constrained by the EDM data while the spatial functions are mostly controlled by the InSAR data. When it comes to source modeling, the benefit of using InSAR data becomes explicit in that it provides much better spatial constraints than the EDM data. If we consider only the EDM data, the inversion problem is highly underdetermined given the chosen gridded source of magmatic inflation (more than 6000 point sources as compared with 8 observations from the spatial function of each component). The inversion works but the resulting model depends heavily on the regularization. In this relatively simple magmatic inflation example, one can certainly use a source model defined with fewer adjustable parameters, such as the traditional single point source of inflation [Mogi, 1958] or the prolate ellipsoid model of inflation [*Yang et al.*, 1988], so that including InSAR data does not make huge difference. In a more complicated example such as the slip model on a fault plane, involving InSAR data greatly helps improve the resolution of the slip pattern on different fault patches.

The joint and InSAR-only inversions give similar source model. The best-fit results yield reduced Chi-square (χ_r^2) of 0.96 and 0.90 for the 1st and 1st+2nd component joint inversion respectively, and 1.07 and 0.89 for the 1st and 1st+2nd component InSAR-only inversion. However, as seen in the *F*-test (Table 2.1), with InSAR data only it is difficult to

determine the cut-off component to be used in inversion, and we lose the temporal resolution inherent in the EDM data. The time evolution obtained from the InSAR-only inversion is coarser and partly biased by atmospheric effects which are present in all the components rather than being rejected in the higher order components as happens in the joint inversion.

Reference

Mogi, K. (1958), Relations between the eruption of various volcanoes and the deformation of the ground surface around them, *Bull. Earthquake Res. Inst.*, 36, 99–143.

Yang, X.-M., P. M. Davis, and J. H. Dieterich (1988), Deformation from inflation of a dipping finite prolate spheroid in an elastic half-space as a model for volcanic stressing, *J. Geophys. Res.*, 93(B5), 4249–4257.

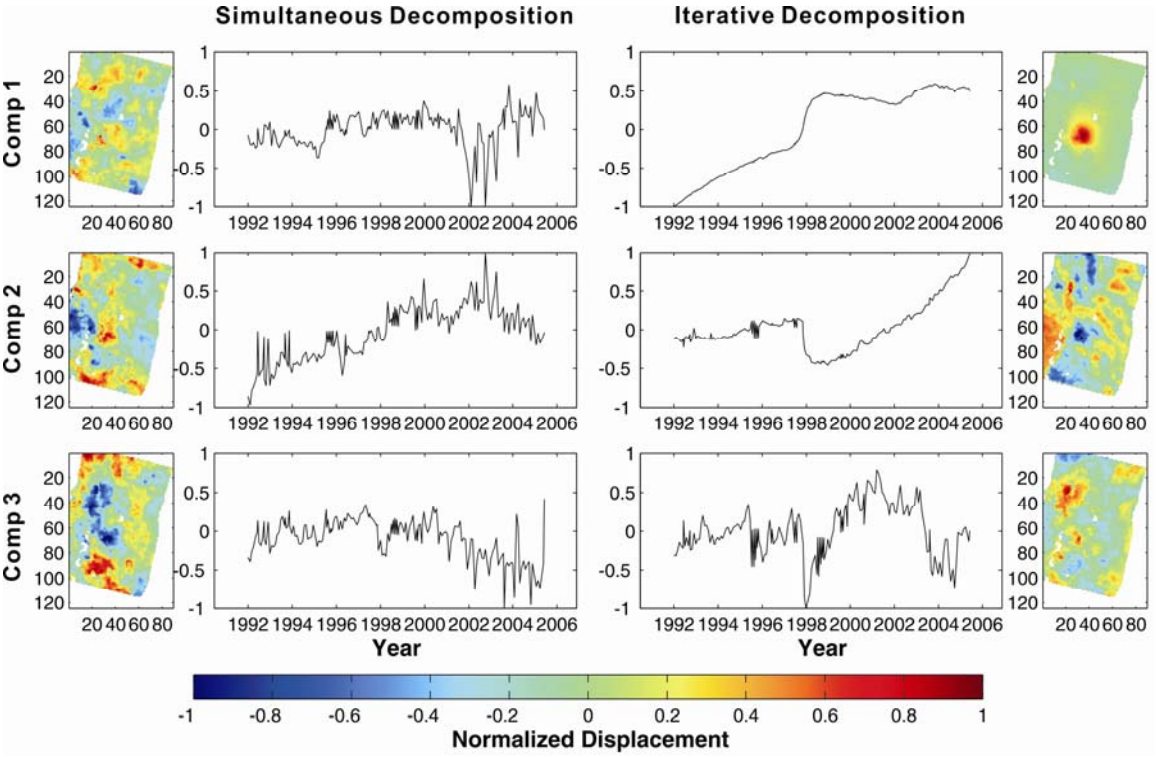

Figure A1. Comparison of simultaneous and iterative decompositions. The time functions of the simultaneous decomposition (left panel) are noisy and discontinuous at the epochs with SAR images, whereas the time functions of the iterative decomposition (right panel) are much smoother.

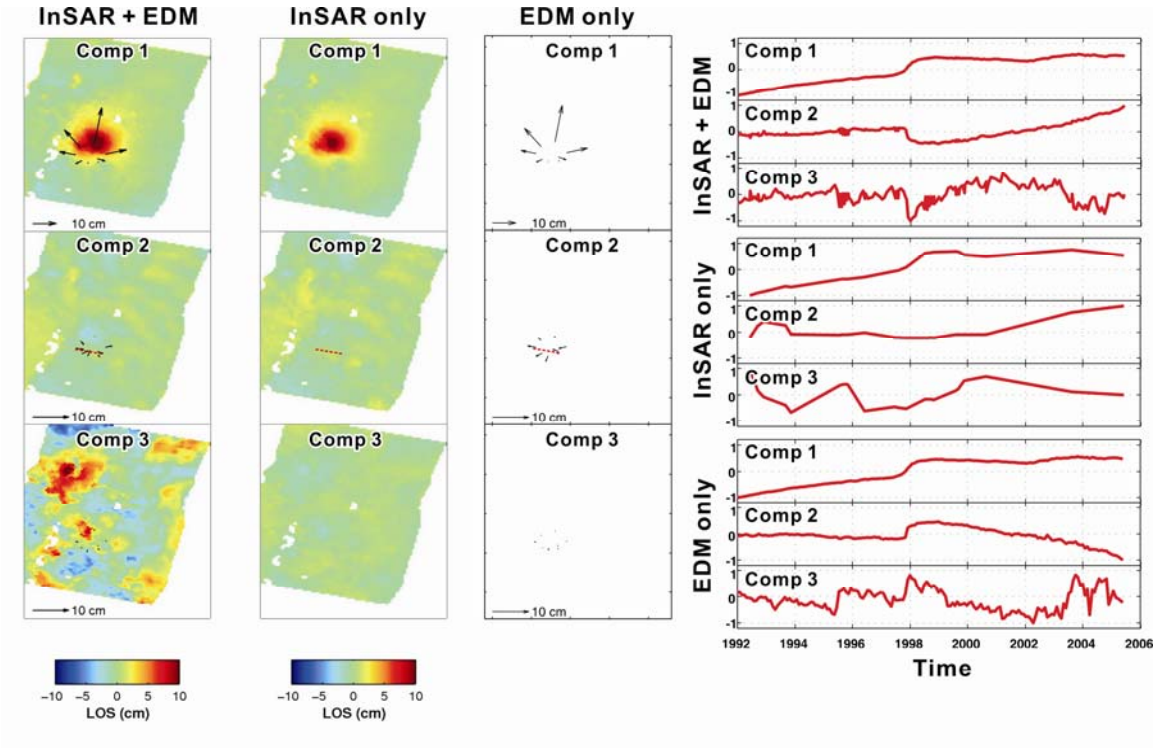

Figure A2. Comparison of the first 3 components from the joint (InSAR + EDM), InSAR-only and EDM-only principal component decomposition. The spatial functions of the first 2 components for InSAR + EDM and InSAR-only look identical, whereas the 3rd and higher components look quite different. The time function of the 3rd component for the InSAR-only decomposition still shows some pattern, whereas for the joint decomposition the 3rd and higher component is more noise-like. This difference results from the guiding EDM data in the joint decomposition, which leads to a clean cut between the 2nd and 3rd component. The time and spatial functions of the first 3 components for joint and EDM-only decomposition look identical, reflecting our assumption that EDM data is relatively clean of tropospheric noise and well sampled in time.

Appendix B

SUPPLEMENTARY MATERIAL OF CHAPTER III

B. 1 Data Selection and Processing

B.1.1 GPS Observations

Our general field, processing, and velocity analysis methods in South America have been described previously [*Bevis et al.*, 1997; *Brooks et al.*, 2003; *Brooks et al.*, 2011; *Kendrick et al.*, 2003]. We estimate velocities by stacking daily network solutions obtained using GAMIT [*King and Bock*, 2000] and GLOBK [*Herring*, 2000] software. All publicly available cGPS data in South America from 1 Jan 2007 through 10 June 2011 were processed using GAMIT with additional IGS sites included to provide reference frame stability. All data were processed using MIT precise orbits. Orbits were held tightly constrained and standard EOP and earth and ocean tides were applied. Due to the number of stations, two separate subnets were formed with common fiducial sites. The subnets were merged and combined with MIT's global solution using GLOBK. We express our solutions in a reference frame nominally attached to the stable South American craton that has horizontal RMS velocity of 0.92 mm/yr and vertical RMS velocity of 1.6mm/yr. We estimate positions and velocities in inner coordinates, treating the reference frame as a computational convenience and allowing it to rotate and translate freely (at constant rates) while focusing on the rate of change of the polyhedron's shape and size. One six parameter Helmert transformation is applied to each daily polyhedron solution so as to align the daily

polyhedra as closely as possible to a suite of constant velocity trajectories. No position or velocity constraints are imposed during this iterative stacking process: the only constraint is that the individual (daily) polyhedra are not allowed to change their size or shape.

We combined GPS data from multiple networks, resulting in a total of 127 3-component continuous records. To determine coseismic offsets, we use all stations that cover the time span around the mainshock, resulting in a total of 79 stations each with 3 components. This data set includes an augmentation of 27 stations to the existing dataset of 61 cGPS and 33 campaign-mode GPS stations from *Vigny et al.* [2011]. Compared to the GPS network used in *Moreno et al.* [2012], our dataset contains 21 more stations to the north near Valparaíso and Santiago, but has relatively sparse spatial coverage to the south near the Arauco region, and therefore our model results in this area depend heavily on InSAR observations.

For the postseismic GPS time series, we selected stations between 32°S and 40°S with at least 180 epochs recorded between the mainshock on February 27 2010 and June 30 2011. We omitted GPS sites south of 39.5°S which may still contain signatures of prolonged regional postseismic relaxation following the 1960 Valdivia earthquake [*Hu et al.*, 2004; *Moreno et al.*, 2008]. These criteria resulted in 66 stations, with 30 of them installed after the 2010 earthquake.

For each time series we use a conventional least squares approach to separate postseismic deformation from other signals, including secular rates, coseismic jumps (e.g., the Maule main shock, Pichilemu aftershock as well as other events) and seasonal variations (Figure 3.2). The RMS of the residuals is 3-5 mm in the horizontal and 10-15 mm in the vertical.

Of the 127 GPS stations, 81 stations have at least one and half year of observations before the Maule earthquake. We use the secular rates from these 81 stations plus those from two published studies (Figure 3.2A) [*Moreno et al.*, 2008; *Ruegg et al.*, 2009] to interpolate and correct for the 66 stations we use in our model. This correction is done for horizontal components only, because the uncertainties for the vertical components are larger than the secular rates in many stations (Figure 3.2B) [*Ruegg et al.*, 2009]. To avoid introducing errors into our model through improper corrections, we choose to use only the vertical component of the time series that have at least 1.5 years of pre-quake records with more than 365 epochs to allow estimates of their vertical secular rates (Figure B1). We did not interpolate the seasonal variations for the short time series, as these values tend to vary more rapidly in space due to the specific geological and hydrological setting of each station. We estimate seasonal variations based on the longest available records for each time series, and therefore the error for shorter time series is larger and the correction is less reliable. As a sanity check, we ensure that each of the corrected time series shows signals of similar order of magnitudes with other surrounding stations. In the end, 66 cGPS stations are used in the postseismic model and among them 22 vertical records were considered reliable.

The March 11 Mw=6.9 Pichilemu earthquake in 2010 and the January 2 Mw=7.1 Araucania earthquake in 2011 produced notable displacements in a few of the time series. These coseismic jumps and corresponding postseismic deformation, if significant, are also removed from the postseismic time series.

B.1.2 InSAR

The coseismic signal has sufficiently large amplitude (up to 3-4 m in the line of sight direction, Figure 3.4) that we did not attempt to correct for any atmospheric delays. However, given the small amplitude and long wavelength of the postseismic deformation, it is challenging to image the tectonic signal with InSAR. We correct for the topographically-correlated phase delay by using a multi-scale approach [*Lin et al.*, 2010a]. Given that the postseismic ascending SAR images were acquired much later than the descending track 422 (Figure 3.3), resulting in a smaller signal-to-noise ratio (as postseismic deformation rates generally decay approximately exponentially with time), and that each track covers a different temporal period and cannot form a continuous snapshot image, we choose to arbitrarily down weight these tracks 10 to 100 times more than the descending tracks. We adjust the weighting of the wide-swath descending track based on the relative number of resampled InSAR observations and total GPS acquisition epochs so that both datasets contribute equally to the model, i.e. each dataset contributes equally to the reduced Chi-square of the residuals.

We also correct for the deformation associated with the March 11, 2010 Pichilemu earthquake. This composite earthquake is presumably triggered by the stress transfer due to the slip on the subduction interface and is therefore considered as the aftershock of the Maule earthquake [*Ryder et al.*, 2012]. We run a simple 1-plane finite fault model by using the source parameters from GCMT (strike = 144°, dip = 55°, rake = -90°, depth = 12.9 km, Mw = 6.9). Only InSAR data track 114 and teleseismic data are used in this model, since the main purpose is to remove the deformation associated with the Pichilemu events from the interferogram. The corrected track 114 is then used in our postseismic slip model.

In order to reduce the computational cost associated with inverting all the InSAR data, we adopt the spatially variable data resampling/averaging approach based on the estimate of the inherent data resolution for a given source model [*Lohman and Simons*, 2005]. This approach efficiently reduces the total number of data to ~3000 points for the combination of all 32 tracks to be used in the inversion, while preserving the information contained in the original interferograms at all relevant scales.

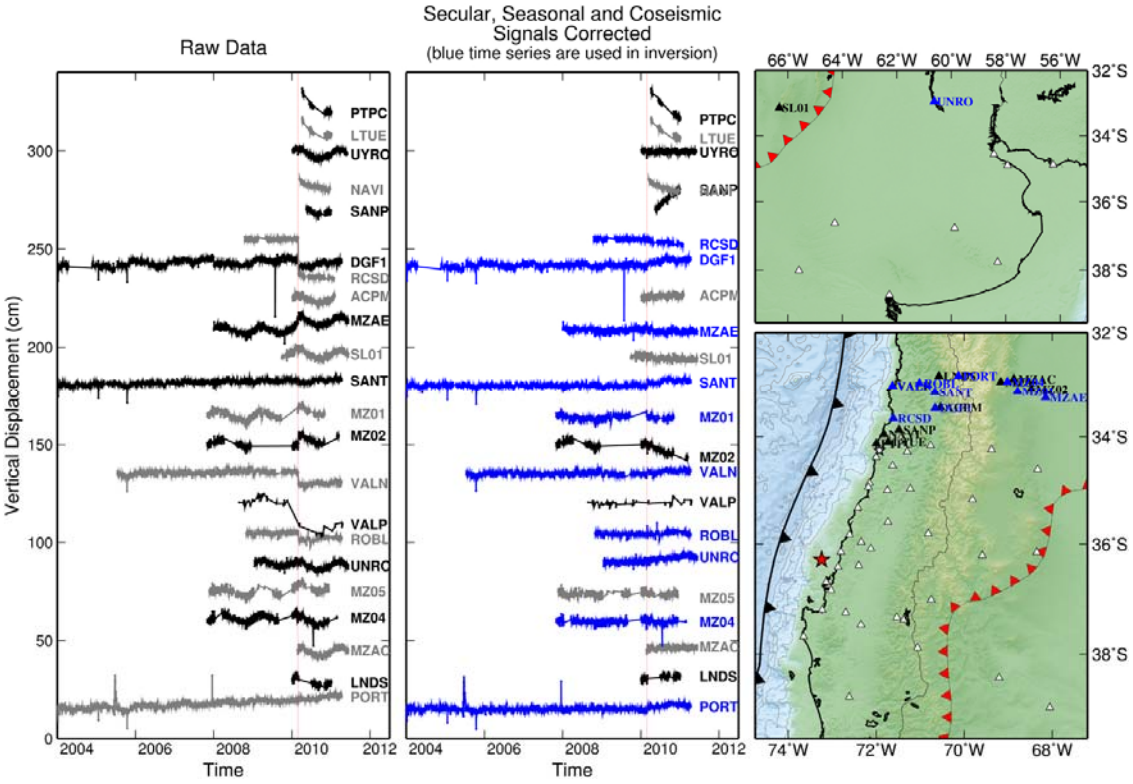

Figure B1-1. The vertical components of the cGPS time series, northern section. [Left] Raw time series. [Middle] The secular rates are estimated only with the long time series (with more than 1.5 years of records before the Maule earthquake). The seasonal variations are estimated with every time series. The coseismic jump is estimated whenever the time series span through the earthquake. [Right] The location of the stations. Blue stations are the ones picked for the postseismic slip inversion.

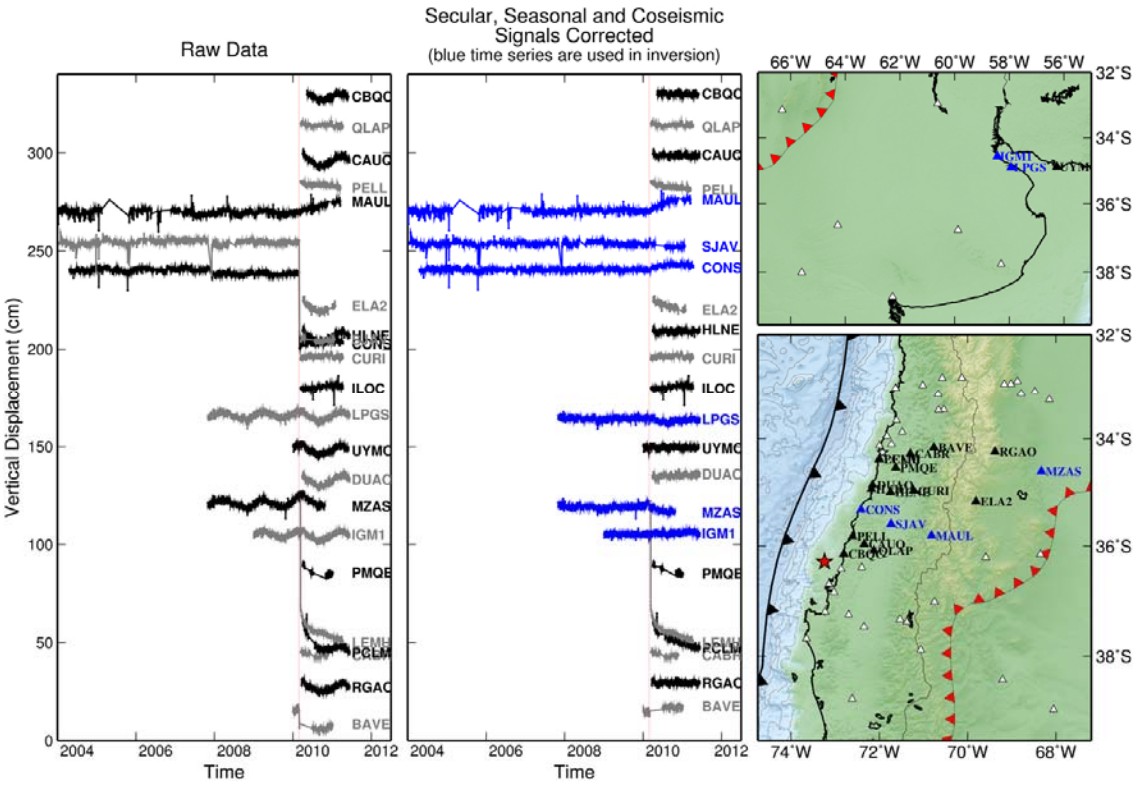

Figure B1-2. The vertical components of the cGPS time series, central section. [Left] Raw time series. [Middle] The secular rates are estimated only with the long time series (with more than 1.5 years of records before the Maule earthquake). The seasonal variations are estimated with every time series. The coseismic jump is estimated whenever the time series span through the earthquake. [Right] The location of the stations. Blue stations are the ones picked for the postseismic slip inversion.

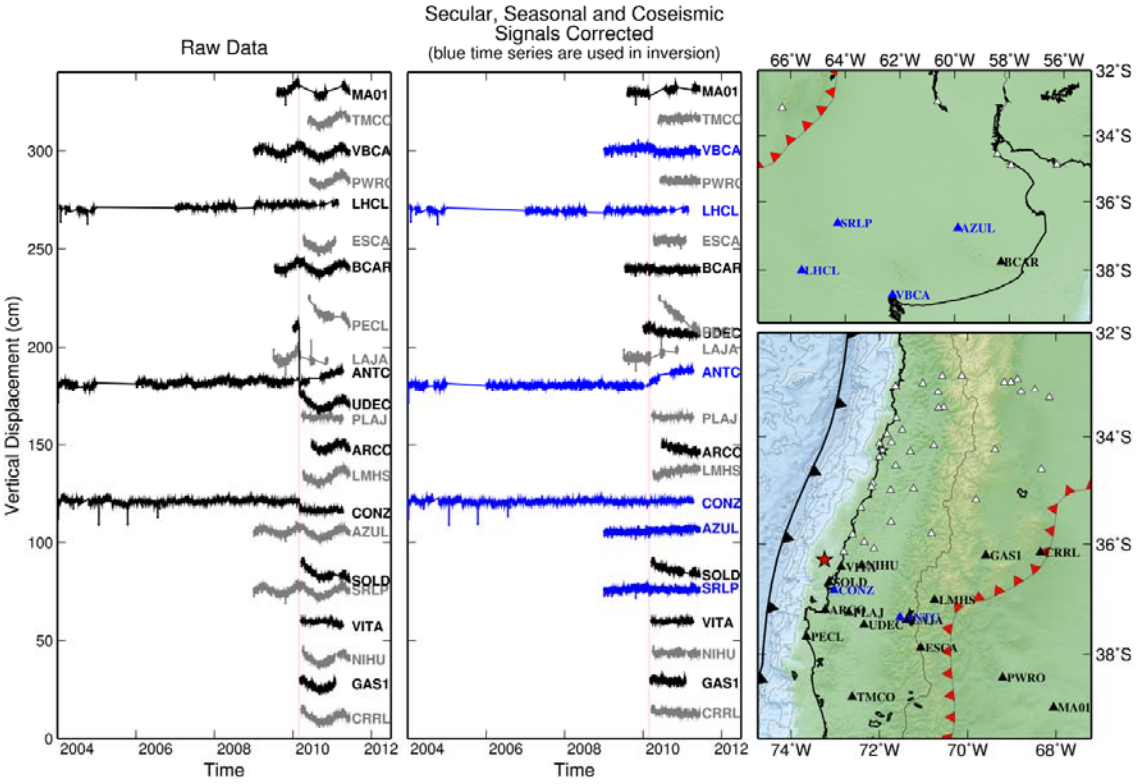

Figure B1-3. The vertical components of the cGPS time series, southern section. [Left] Raw time series. [Middle] The secular rates are estimated only with the long time series (with more than 1.5 years of records before the Maule earthquake). The seasonal variations are estimated with every time series. The coseismic jump is estimated whenever the time series span through the earthquake. [Right] The location of the stations. Blue stations are the ones picked for the postseismic slip inversion.

B. 2 Inversion Models

B.2.1 Coseismic Model

To solve for the distribution of coseismic slip of the Maule earthquake, we perform a joint inversion of all the static data previously described (i.e. InSAR and GPS) as well as teleseismic body waves. We use a simulated-annealing algorithm [*Ji et al.*, 2002] to solve this non-linear optimization problem. We use a fault geometry consisting of two fault segments aligned along strike to accommodate the curvature of the trench. Those segments also have variable dip angles to better approximate the shallower dip angle of the slab south of the Arauco peninsula. This geometry shows a very good agreement (Figure B2) with the USGS 3D slab model [*Hayes et al.*, 2009]. The fault geometry is discretized into 292 elements of 30 km x 15 km. For each fault element, we solve for 4 parameters: the slip amplitude and rake, as well as rupture initiation time and duration. The time evolution of each fault element is constructed using half-cosine functions with a minimum rise-time of 1 s. To limit the size of the parameter space as well as to account for uncertainties in the data and model (292x4 unknowns), we include Laplacian regularization term in the cost function that is minimized during the inversion procedure. We use the epicenter location estimate of *Vigny et al.* [2011]: 36.41°S and 73.18°W. Any given segment of the fault is only allowed to rupture once and its velocity is bounded in the 2.5 to 3 km/s range [*Delouis et al.*, 2010; *Vigny et al.*, 2011].

We selected 24 P waveforms from the GSN global broadband network. To avoid triplication in the crust and upper mantle, or diffraction at the core-mantle boundary, we selected stations in the 30-90° distance range (teleseismic range; Figure 3.5A). In that distance range, stations are selected to provide a good azimuthal coverage thereby

maximizing the resolution on the slip history. We use a 2.5 second to 200 second bandpass (0.005-0.4 Hz) on the seismograms (Figure 3.5B) and both the teleseismic and geodetic Green's functions are computed in a 1D layered elastic half-space. The velocity and density model is derived from the global 3D CRUST2.0 model [*Bassin et al.*, 2000] for a point on the coast at the latitude of the epicenter.

In the inversion, InSAR and GPS datasets are given equal weight. Because of the strong trade-offs in the rupture-process estimation [e.g. *Lay et al.*, 2010] and the lower resolution [e.g. *Delouis et al.*, 2010] while using only the teleseismic data, we double the weight of the geodetic data in the cost function relative to the teleseismic data. The contribution of the moment and smoothing regularization in the cost function follows *Ji et al.* [2002].

B.2.2 Postseismic Model

To derive the time-dependent finite source kinematic models, we use the Principle Component Analysis-based Inversion Method (PCAIM) developed by *Kositsky and Avouac* [2010]. This approach allows the joint inversion of multiple geodetic datasets with various spatiotemporal resolutions [*Lin et al.*, 2010b]. The two datasets we use in our model, GPS and InSAR data, provide complementary constraints on the temporal and spatial evolution of slip and therefore a joint inversion is crucial for understanding the detailed evolution of the postseismic creep. In our modified version of PCAIM, we only use the GPS data for the PCA. During the inversion stage, we apply InSAR data as extra constraints that bridge through different components. This adaptation from the method described in *Lin et al.* [2010b] is due to the temporal sparsity of the InSAR data in this

study (only 1-4 epochs for most of the ALOS tracks), making the joint decomposition not necessarily beneficial. With this adaptation, sparse InSAR data still provides a significant constraint.

Since afterslip may occur on significantly deeper portions of the fault, the model fault extends deeper and further along strike than that used in the coseismic model (Figure B2). For the post-seismic model, we reduce our spatial resolution to limit the computational cost of the inversion, and take into account the curved geometry of the fault plane. Our fault geometry is constrained by: (1) reflection seismic profiles [*Contreras-Reyes et al.*, 2008a; *Contreras-Reyes et al.*, 2008b], (2) background seismicity before the mainshock [*Campos et al.*, 2002; *Rietbrock et al.*, 2005; *Haberland et al.*, 2009], and (3) the distribution of aftershocks [*Rietbrock et al.*, 2012]. The shallow part of the geometry (0~25 km) is primarily constrained by reflection seismic profiles, whereas the deeper part between 25 and 150 km are primarily constrained by seismicity. The resulting fault plane is slightly deeper than SLAB 1.0 [*Hayes et al.*, 2009] for depths greater than 40 km, but agrees well with the relocated earthquakes from the NEIC and ISC catalog for the time period between February to September 2010 (Figure B5) [*Pesicek et al.*, 2012]. We tessellate the fault plane into a 30 km x 30 km "magic carpet" of square patches that respect the original curvature of the megathrust geometry. The elastic Green's functions are computed by using the same 1D layered structure as used for the coseismic slip model.

We use an F-test to determine the number of principle components used in the inversion, a procedure described in *Kositsky and Avouac* [2010]. Then we define our objective function $\Phi(\lambda) = ||C(Gm-d)||_2 + \lambda||WDm||_2$, where C is the Cholesky decomposition of the data covariance matrix, m is the slip on each fault patch, D is the Laplacian operator, W is a shape function that controls the differential Laplacian applied on each part of the fault

model, and λ is the weighting over the regularization term [*Lohman*, 2004]. W is defined as the reciprocal of the fault slip sensitivity $S = [1/\text{diag}(G^T G)]^{1/2}$ [*Ortega-Culaciati et al.*, 2013]. Each element in the vector S represents the summation of the displacements over all GPS stations and/or InSAR pixels due to unit slip on each individual patch, and corresponds to a measure of the resolution power of the observational constraints [*Loveless and Meade*, 2011] or equivalently a relative measure of the capacity of the fault slip for each path to be constrained by the available observations [*Ortega-Culaciati et al.*, 2013]. Figure B6 shows that the highest sensitivity occurs for regions of the fault model between 10 and 80 km at depth in the north, and can extend close to the trench near the Arauco Peninsula. W, defined in terms of the reciprocal of this sensitivity vector, will assign more smoothing to regions with smaller sensitivity and less smoothing to those with higher sensitivity. Using W as defined here limits the introduction of smearing of resolved slip variability into regions that are less constrained, improves the stability of the slip distribution and enables us to infer overall rougher slip models while imposing a stronger smoothing in regions that are less constrained by the observables [*Ortega-Culaciati et al.*, 2013]. In regions of low sensitivity, such as the shallowest and the deepest parts of the megathrust, while the resolved slip is close to an average low resolution value of the region with limited observational constraints – slip is not pushed to a zero value (Figure B7).

In addition to the aforementioned regularization terms, we enforce positivity in the up-dip slip direction. Under the assumption that the strike-slip components tend to vary more gradually in space than the dip-slip components, we choose by trial and error the relative damping of the strike-slip components to be a 1000 times larger than for the dip-slip components. We use a conventional L-curve method to determine the best λ.

To partially account for the fact that the Green's functions used will always be approximate, we incorporate an additional "prediction error" term in the error model. *Minson et al.* [2013] address this issue by assigning prediction errors that scale with the magnitude of data, under the assumption that the larger the observational response, the larger the prediction error in the response. Here, we assume that the Green's functions are good to about 5%. The final error model, E, is thus $E = E_{obs} + E_{pred}*0.05$. This is a crude approach to accounting for the prediction error, one that ignores covariances that are also induced by errors in our assumed Green's functions. Our data fits are shown in Figure 3.4 & 3.8.

For the postseismic InSAR data, we adopted a more sophisticated approach to deal with the systematic error associated with inaccurate orbit information. All the sub-swaths of descending track 422 share the same orbit, and therefore a single large ramp should be estimated jointly, whereas the ramp for each ascending track is estimated separately. The approach better avoids mixing the postseismic deformation signals with the bilinear ramp. The mean RMS residual is 2.5 cm for the InSAR data (Figure 3.4), a value consistent with the range of atmospheric delays observed elsewhere [*Mockler* 1995; *Li et al.*, 2003].

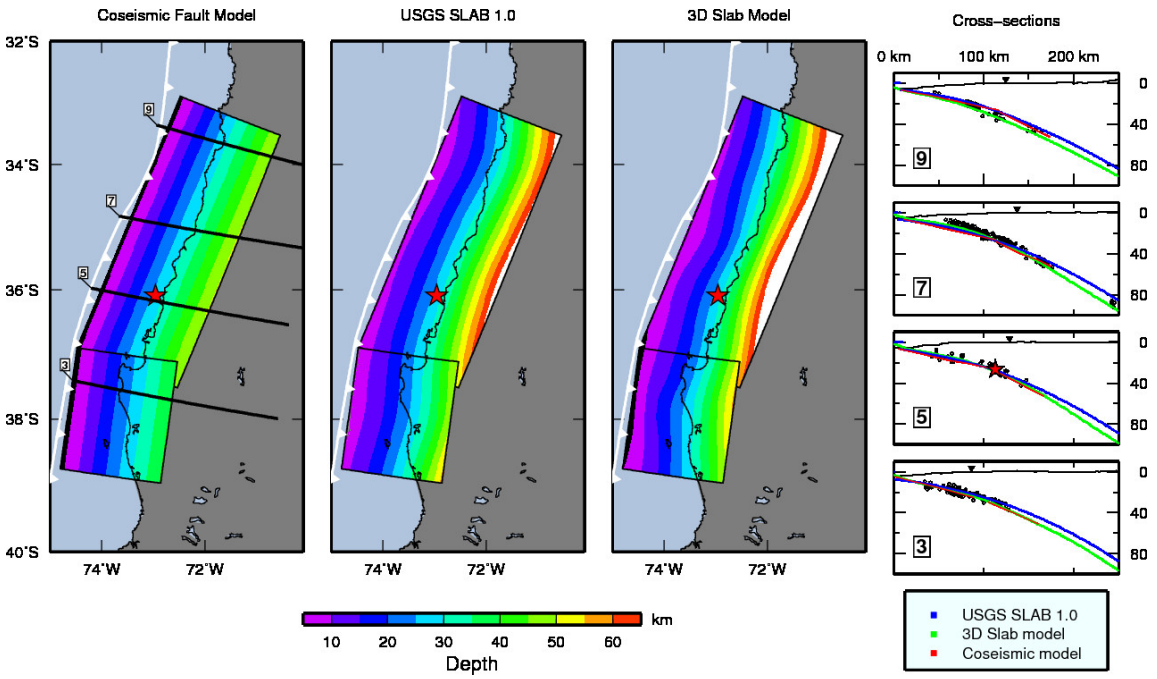

Figure B2. Comparisons between the coseismic fault geometry, USGS SLAB 1.0 [*Hayes et al.*, 2009] and the 3D slab model used in the postseismic slip model. The coseismic model is composed of two fault planes to describe the changes of dip angles from north to south. The postseismic model is meshed by using constraints from seismicity [*Campos et al.*, 2002; *Rietbrock e tal.*, 2005; *Haberland et al.*, 2009; *Rietbrock et al.*, 2012] and reflection seismic profiles [*Contreras-Reyes et al.*, 2008a; *Contreras-Reyes et al.*, 2008b].

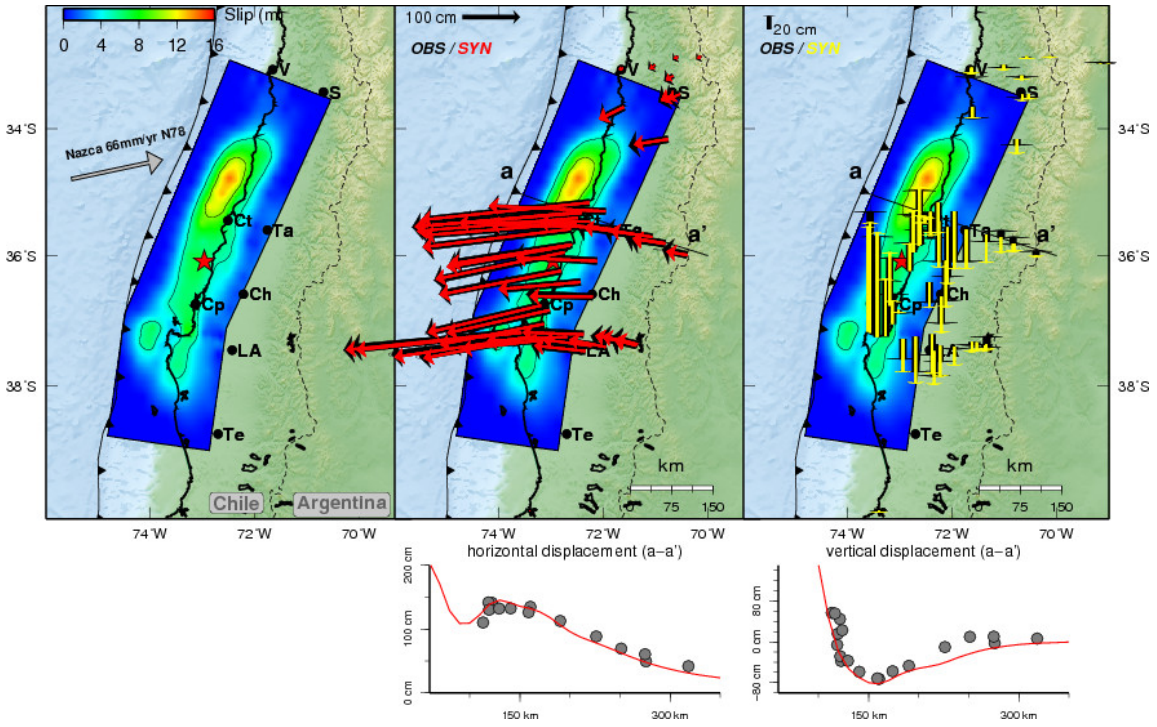

Figure B3. Results from geodetic-only inversion. (Left) Coseismic slip with 5-m contour intervals. (Center and Right) Black vectors indicate the observed GPS data; red and yellow vectors indicate modeled results in the horizontal and vertical components, respectively. The profile (aa') shows the predicted (red line) and observed (grey solid dots) surface displacements at the latitude of the main asperity, around latitude 36°S. Notice that for the vertical components (right), the slip model predicts a displacement field of longer wavelength than the observed data, a result similar to the kinematic source model shown in Figure 3.6. STF: Source time function. Ch: Chillán; Ct: Constitución; Cp: Concepción; LA: Los Angeles; Ta: Talca; Te: Temuco; S: Santiago; V: Valparaiso.

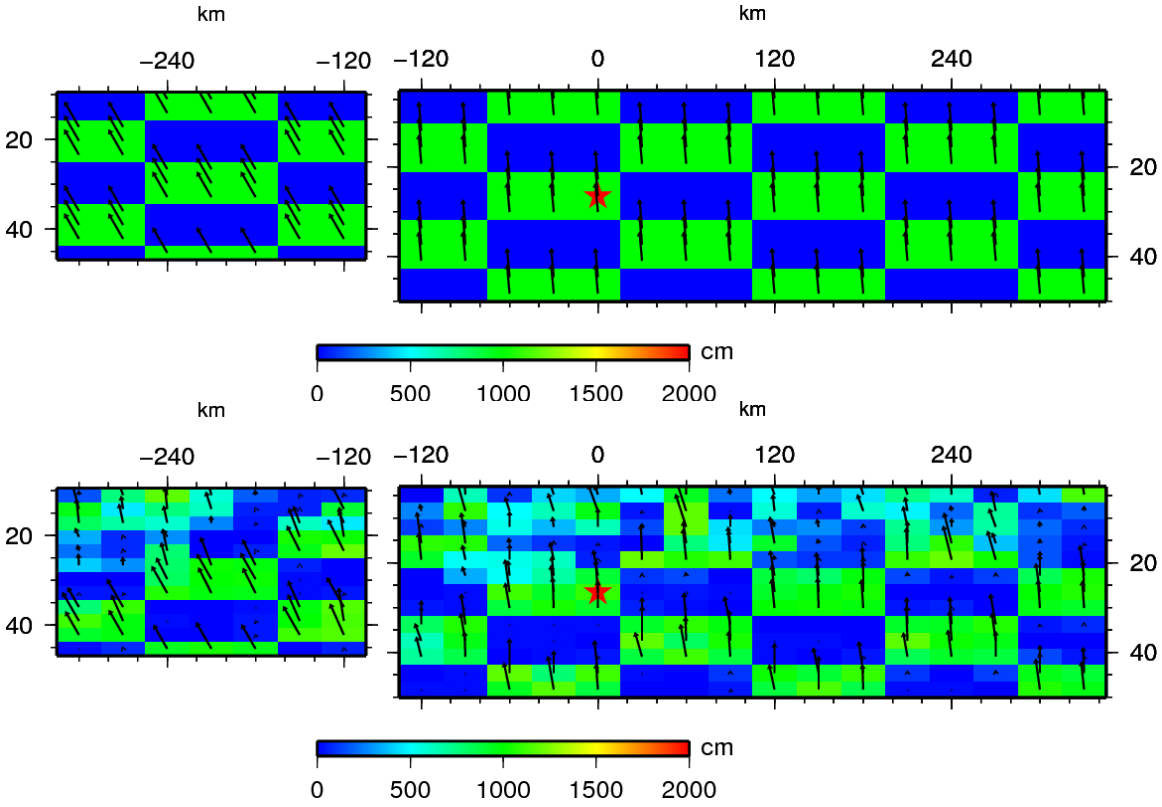

Figure B4. Checkerboard test for the geodetic-only inversion (InSAR+GPS). (Top) Pattern of the checkerboard slip distribution. (Bottom) Pattern recovered from the inversion of the synthetic data allowing the rake to vary on each cell. The model obtained from inversion clearly shows the decrease in resolution for the patches less than 15 km depth.

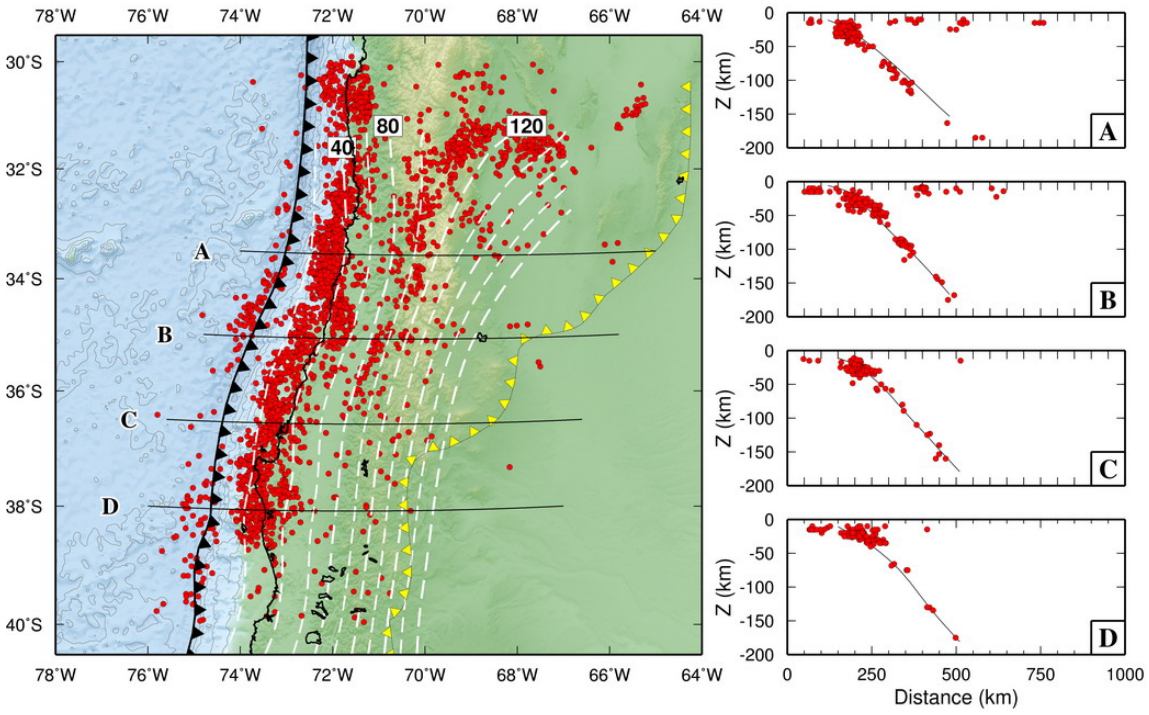

Figure B5. We compare the fault geometry for our postseismic model (white dashed lines for the contours) with the relocated earthquakes from the NEIC and ISC catalog for the time period between February to September 2010 (*Pesicek et al.* [2012], red circles). These earthquakes were not used in estimating the slab geometry. (A)-(D) The geometry agrees well with the location of earthquakes on the subduction zone interface to depths of at least 200 km, thereby validating the reconstruction of the fault plane.

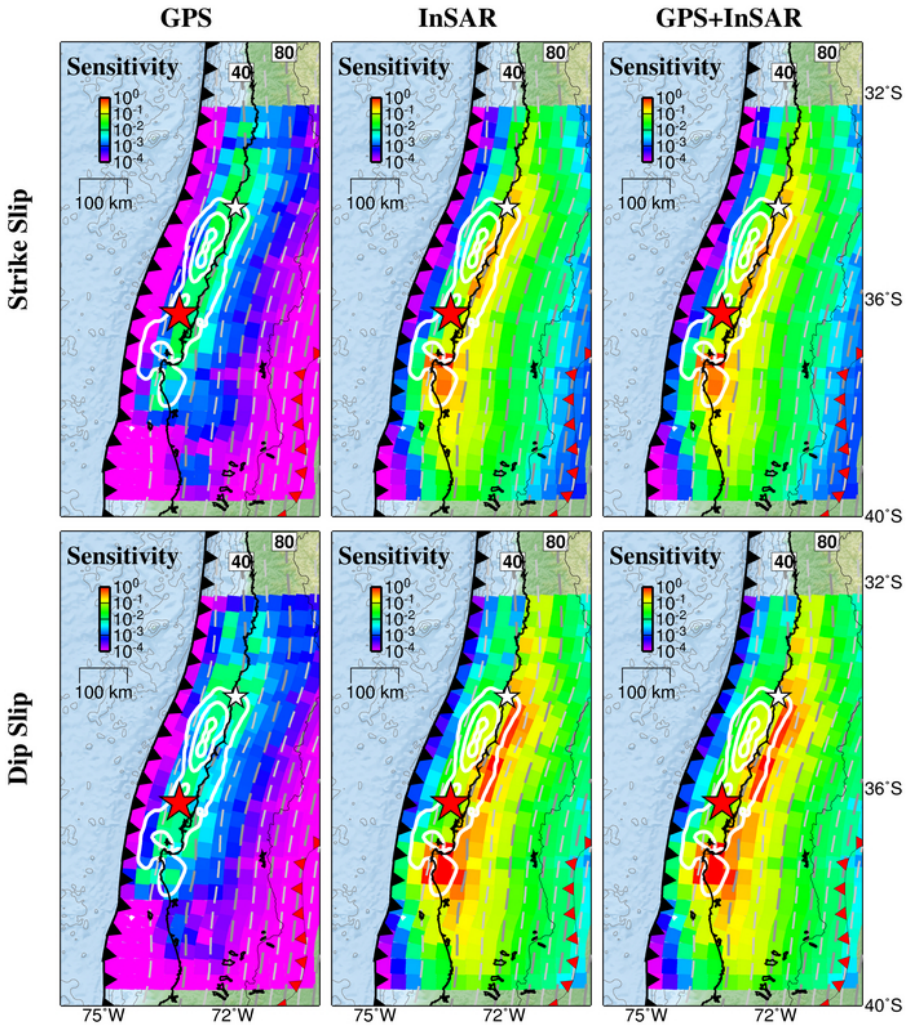

Figure B6. Postseismic model sensitivity for the strike-slip and dip-slip component when using GPS only (left), InSAR only (middle) and the GPS+InSAR joint dataset (right). Use of the joint dataset constrained maximizes the fraction of the model that is well constrained.

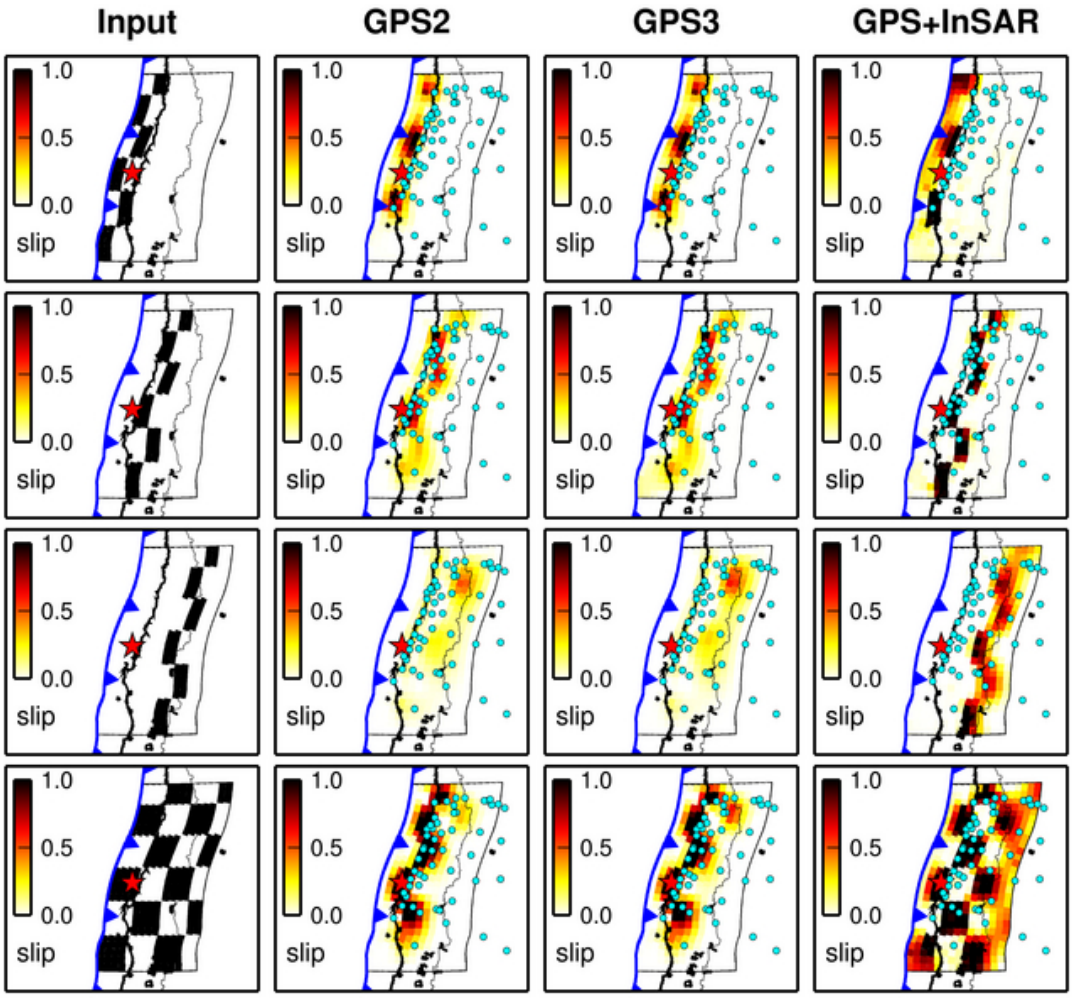

Figure B7. Checkerboard tests used for the postseismic inversion modeling. These tests assume observation errors of 5 mm in the GPS horizontal components and 15 mm in the GPS vertical components. Systematic bilinear ramps in the InSAR data and observation errors are derived following *Lohman and Simons* [2005]. This test shows that the lack of model sensitivity at shallowest and deepest depths (Figure B5) leads to more smeared and averaged slip patterns (last column).

B.3 Effects of Approximate Green's Function

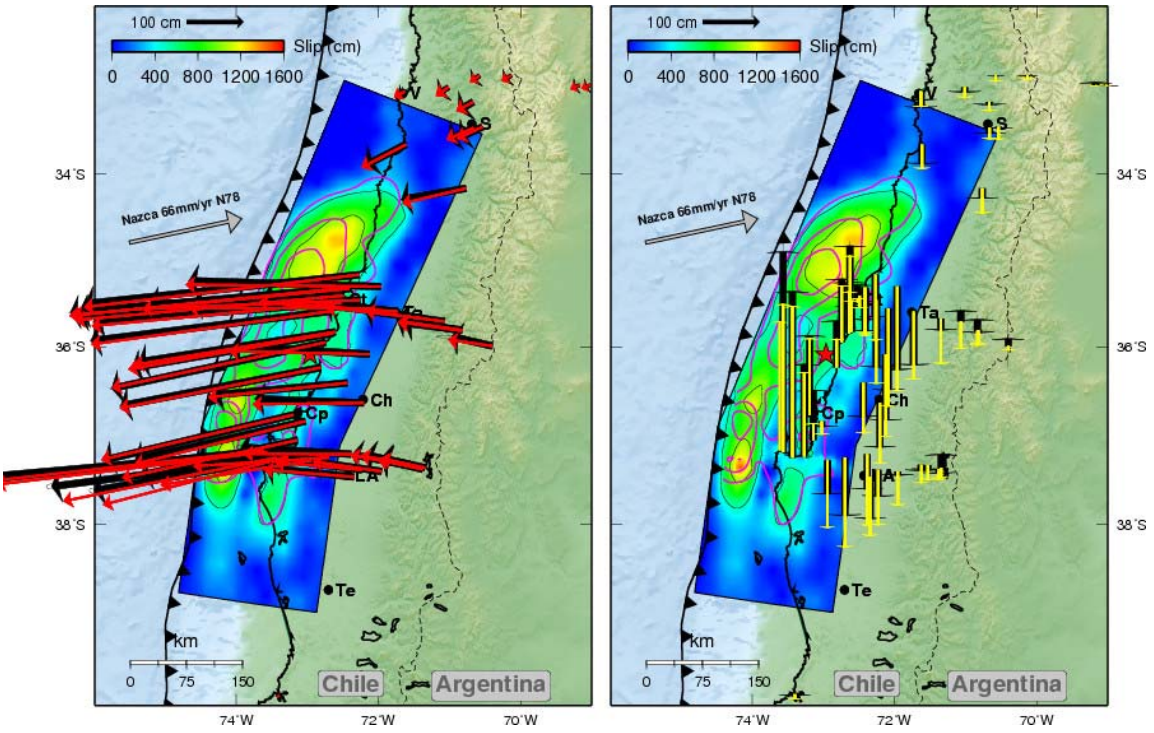

Figure. B8. Coseismic slip distribution, with 5-m contour intervals, obtained using the semi-inifite elastic half-space approximation instead of the layered elastic half-space approximation used for our preferred slip model (Figure 3.6). This model is overlain with the contours of Vigny et al. [2011] slip model (pink) which also uses the semi-infinite elastic half-space approximation. Black vectors are for observed GPS data; red and yellow vectors are for modeled results in the horizontal and vertical components. Both models shown here have a similar spatial extent and suggest a slip distribution shifted much closer to the trench than our prefered slip model using a layered elastic half-space (Figure 3.6). This comparison illustrates the influence of the physical model approximations on the solution.

B.4 Resolution of Updip Slip Extent from Tsunami Data

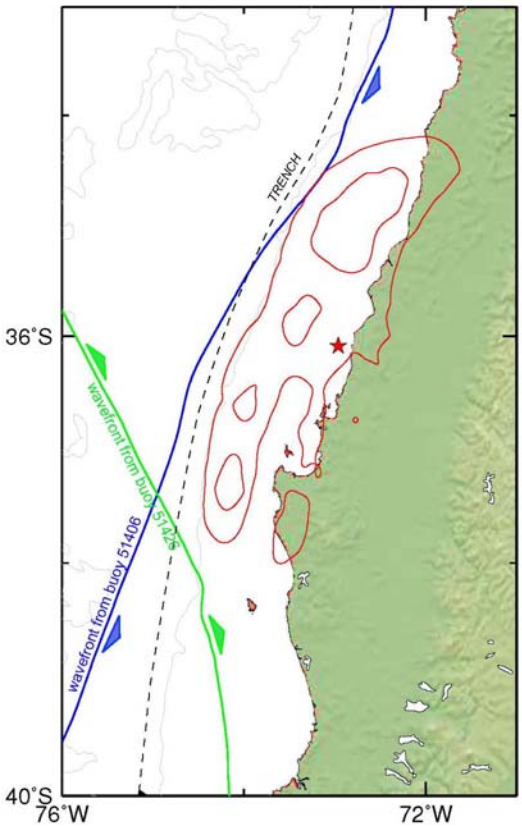

Figure. B9. Tsunami wavefronts propagated from the deep-ocean buoys 51406 (blue wave front) and 51426 (greenwave front) (see Figure 3.8 for the location map). The wavefront from buoy 51426 is representative of the group of buoys in the same distance range and azimuth —51425, 51426, 54401— of the southwest Pacific. Red contours correspond to 5-m slip contours of our preferred slip model. The red star is the mainshock epicenter. The tsunami wavefronts indicate that only station 51406 is a good discriminant of the updip extent of the source; for station 51426 and others nearby, the tsunami signal from the updip part of the source will be mixed with waves coming from the southern part of the fault.

B.5 Slip Potency Test for Shallow Slip

To test what is the likelihood of slip in the shallow part of the megathrust, we modify our objective function to

$$\Phi(\lambda_1,\lambda_2) = \|\mathbf{C(Gm-d)}\|_2 + \lambda_1\|\mathbf{WDm}\|_2 + \lambda_2\|\mathbf{mA}\text{-}P_o\|_2 \quad \text{(B1)}$$

where P_o is the slip potency equivalent to that of the mainshock, and λ_2 is the strength of this extra term of regularization. We apply this regularization term only to patches above 80 m deep. The assumption here is that the creeping energy on the megathrust from 0-80 km at depth within the first 488 days of the postseismic period does not exceed the energy released by the mainshock.

Figure B10 shows the plot of model roughness (in terms of moment magnitude) versus model bias (in terms of mean RMS for time series) for different values of the slip potency constraint (λ_2). Here instead of choosing the corner of the L-curve, we determine the reliable range by choosing the λ_2 values within an identical level of RMS (i.e., between 0 and 100). Figure B11 shows the postseismic slip models with selected values of λ_2. Right column shows the residual vectors of various time spans, reflecting the actual data length of each station. For the largest λ_2 value within the reliable range (λ_2=100), there is some shallow slip near the trench, but the values are quite small. We therefore conclude if there were any shallow slip during the postseismic period, the amount needs to be small.

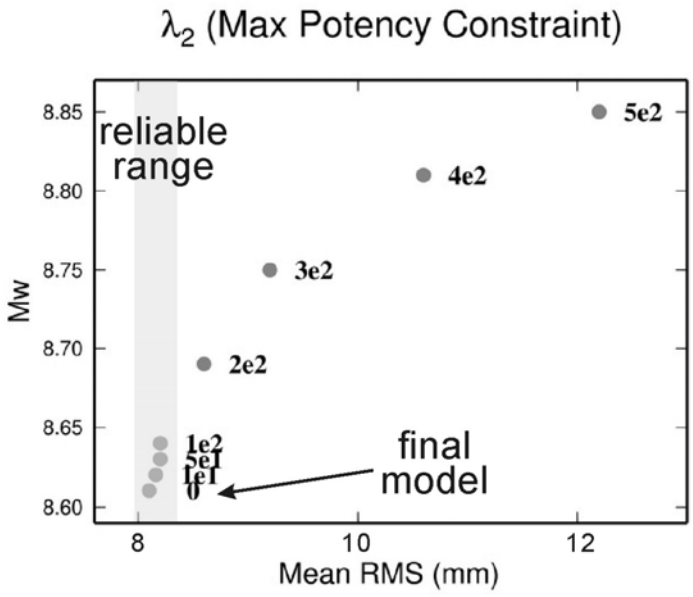

Figure B10. The L-curve test of λ_2 for slip potency test at the shallowest part of the megathrust. The grey band shows the region where the RMS values clusters and therefore is considered as a reliable range of λ_2.

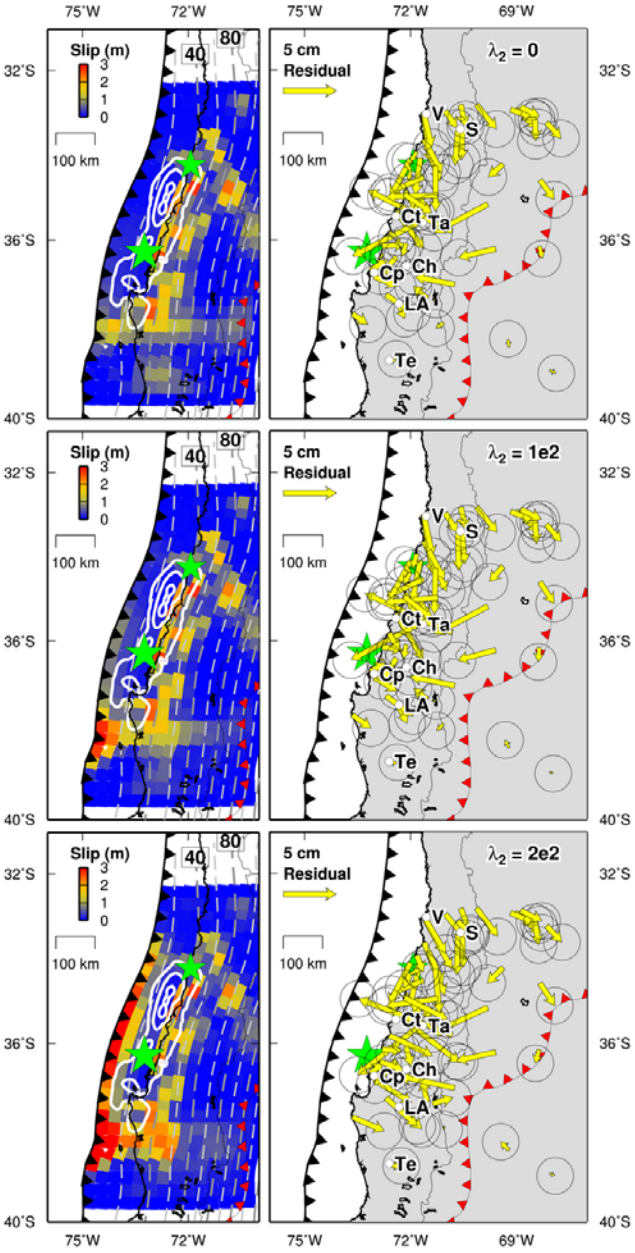

Figure B11. The slip models (left panel) and the corresponding residuals in the GPS horizontal components (right panel) for the λ_2 value of 0, 100 and 200. For the largest λ_2 value within the reliable range (λ_2=100), the shallow slip is still small compared to other part of the megathrust.

B.6 Comparison between Slip Models and Aftershock Focal Mechanisms

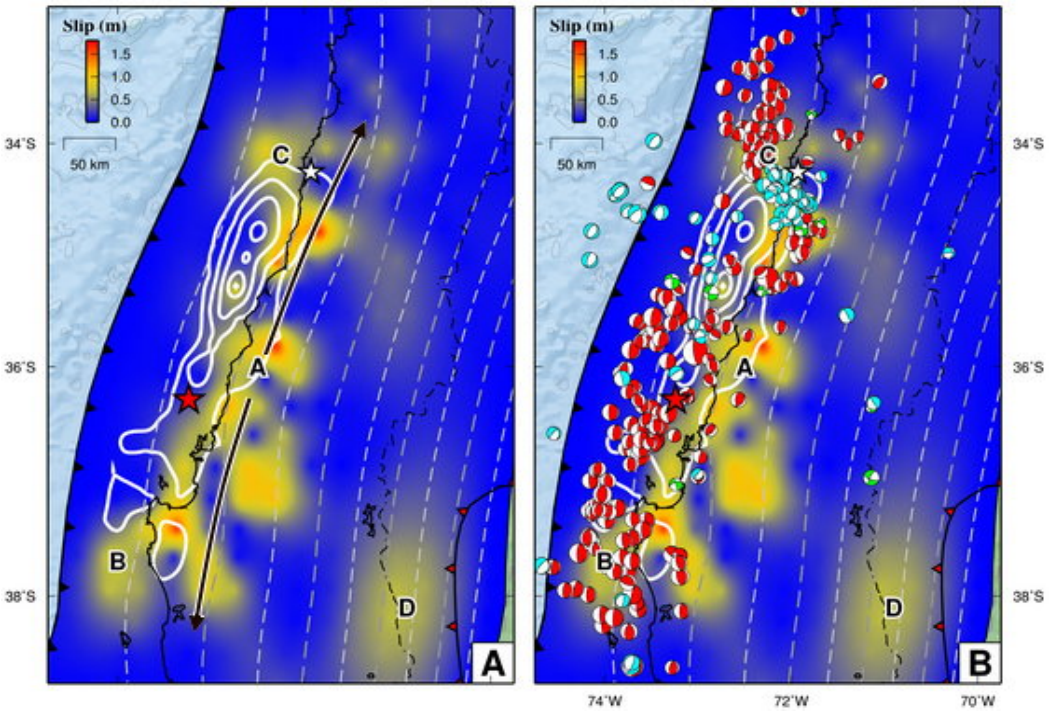

Figure B12. Comparison between the postseismic slip models derived from this study and the focal mechanisms for Maule aftershocks [*Agurto et al.*, 2012]. (A) Color maps are the postseismic slip model, overlain with white contours of the coseismic slip model. (B) Focal mechanisms of M>4 aftershocks. Red: thrust event; cyan: normal event; green: strike-slip event. There are many M>4 events along the up-dip side of the coseismic slip patch between 35.5 and 38.5° S, suggesting seismically-related afterslip along the shallow section of the megathrust, whereas along the down-dip side of the coseismic patch it is mostly the geodetic data that allows us to resolve afterslip.

References of Appendix B

Agurto, H., A. Rietbrock, I. Ryder, and M. Miller (2012), Seismic-afterslip characterization of the 2010 MW 8.8 Maule, Chile, earthquake based on moment tensor inversion, *Geophys. Res. Lett.*, 39, L20303, doi: doi:10.1029/2012GL053434.

Bassin, C., G. Laske, and G. Masters (2000), The current limits of resolution for surface wave tomography in North America, paper presented at Fall. Meet. Suppl., Abstract S12A-03, 2001.

Bevis, M., Y. Bock, P. Fang, R. Reilinger, T. Herring, J. Stowell, and R. Smalley (1997), Blending old and new approaches to regional GPS geodesy, *Eos, Transactions American Geophysical Union*, 78(6), 61-66, doi: 10.1029/97e000040.

Brooks, B. A., M. Bevis, R. Smalley, Jr., E. Kendrick, R. Manceda, E. Lauría, R. Maturana, and M. Araujo (2003), Crustal motion in the Southern Andes (26°-36°S): Do the Andes behave like a microplate?, *Geochem. Geophys. Geosyst.*, 4(10), 1085, doi: 10.1029/2003gc000505.

Brooks, B. A., et al. (2011), Orogenic-wedge deformation and potential for great earthquakes in the central Andean backarc, *Nat. Geosci.*, 4(6), 380-383, doi: 10.1038/ngeo1143.

Campos, J., D. Hatzfeld, R. Madariaga, G. Lopez, E. Kausel, A. Zollo, G. Iannacone, R. Fromm, S. Barrientos, and H. Lyon-Caen (2002), A seismological study of the 1835 seismic gap in south-central Chile, *Phys. Earth Planet. In.*, 132(1-3), 177-195, doi: 10.1016/S0031-9201(02)00051-1.

Contreras-Reyes, E., I. Grevemeyer, E. R. Flueh, and C. Reichert (2008), Upper lithospheric structure of the subduction zone offshore of southern Arauco peninsula, Chile, at ~38°S, *J. Geophys. Res.*, 113(B7), B07303, doi: 10.1029/2007JB005569.

Contreras-Reyes, E., I. Grevemeyer, E. R. Flueh, M. Scherwath, and J. Bialas (2008), Effect of trench-outer rise bending-related faulting on seismic Poisson's ratio and mantle anisotropy: a case study offshore of Southern Central Chile, *Geophys. J. Int.*, 173(1), 142-156, doi: 10.1111/j.1365-246X.2008.03716.x.

Delouis, B., J.-M. Nocquet, and M. Vallee (2010), Slip distribution of the February 27, 2010 Mw=8.8 Maule Earthquake, central Chile, from static and high-rate GPS, InSAR, and broadband teleseismic data, *Geophys. Res. Lett.*, 37, L17305, doi: 10.1029/2010GL043899.

Haberland, C., A. Rietbrock, D. Lange, K. Bataille, and T. Dahm (2009), Structure of the seismogenic zone of the southcentral Chilean margin revealed by local earthquake traveltime tomography, *J. Geophys. Res.*, 114, B01317, doi: 10.1029/2008JB005802.

Hayes, G. P., D. J. Wald, and K. Keranen (2009), Advancing techniques to constrain the geometry of the seismic rupture plane on subduction interfaces a priori: Higher-order functional fits, *Geochem. Geophys. Geosyst.*, 10(9), Q09006, doi: 10.1029/2009GC002633.

Herring, T. A. (2000), *Documentation for GLOBK: Global Kalman filter VLBI and GPS analysis program*, MIT.

Hu, Y., K. Wang, J. He, J. Klotz, and G. Khazaradze (2004), Three-dimensional viscoelastic finite element model for postseismic deformation of the great 1960 Chile earthquake, *J. Geophys. Res.*, 109(B12), B12403, doi: 10.1029/2004JB003163.

Ji, C., D. J. Wald, and D. V. Helmberger (2002), Source description of the 1999 Hector Mine, California, earthquake, part I: Wavelet domain inversion theory and resolution analysis, *B. Seismol. Soc. Am.*, 92(4), 1192-1207, doi: 10.1785/0120000916.

Kendrick, E., M. Bevis, R. Smalley, B. Brooks, R. B. Vargas, E. Lauriia, and L. P. S. Fortes (2003), The Nazca South America Euler vector and its rate of change, *J. S. Am. Earth Sci.*, 16(2), 125-131, doi: 10.1016/S0895-9811(03)00028-2.

King, R. W., and Y. Bock (2000), *Documentation for the GAMIT GPS Analysis Software Version 10.0*, 206 pp., Massachusetts Institute of Technology.

Kositsky, A., and J. P. Avouac (2010), Inverting geodetic time-series with a principal component analysis-based inverison method (PCAIM), *J. Geophys. Res.*, 115, B03401, doi: 10.1029/2009JB006535.

Lay, T., C. J. Ammon, H. Kanamori, K. D. Koper, O. Sufri, and A. R. Hutko (2010), Teleseismic inversion for rupture process of the 27 February 2010 Chile (M-w 8.8) earthquake, *Geophys. Res. Lett.*, 37, L13301, doi: 10.1029/2010GL043379.

Li, Z., J.-P. Muller, and P. Cross (2003), Comparison of precipitable water vapor derived from radiosonde, GPS, and Moderate-Resolution Imaging Spectroradiometer measurements, *J. Geophys. Res.*, 108(D20), 4651, doi: 10.1029/2003jd003372.

Lin, Y.-N. N., M. Simons, E. A. Hetland, P. Muse, and C. DiCaprio (2010a), A multiscale approach to estimating topographically correlated propagation delays in radar interferograms, *Geochem. Geophys. Geosyst.*, 11(9), Q09002, doi: 10.1029/2010GC003228.

Lin, Y.-N. N., A. P. Kositsky, and J.-P. Avouac (2010b), PCAIM joint inversion of InSAR and ground-based geodetic time series: Application to monitoring magmatic inflation beneath the Long Valley Caldera, *Geophys. Res. Lett.*, 37(23), L23301, doi: 10.1029/2010GL045769.

Lohman, R. B. (2004), *The inversion of geodetic data for earthquake parameters*, California Institute of Technology.

Lohman, R. B., and M. Simons (2005), Some thoughts on the use of InSAR data to constrain models of surface deformation: Noise structure and data downsampling, *Geochem. Geophys. Geosyst.*, 6, Q01007, doi: 10.1029/2004GC000841.

Loveless, J. P., and B. J. Meade (2011), Spatial correlation of interseismic coupling and coseismic rupture extent of the 2011 MW = 9.0 Tohoku-oki earthquake, *Geophys. Res. Lett.*, 38(17), L17306, doi: 10.1029/2011GL048561.

Minson, S., M. Simons, and J. L. Beck (2013), Bayesian inversion for finite fault earthquake source models I — Theory and algorithm, in preparation.

Mockler, S. B. (1995), *Water vapor in the climate system*, AGU, Washington, D. C.

Moreno, M. S., J. Klotz, D. Melnick, H. Echtler, and K. Bataille (2008), Active faulting and heterogeneous deformation across a megathrust segment boundary from GPS data, south central Chile (36-39°S), *Geochem. Geophys. Geosyst.*, 9, Q12024, doi: 10.1029/2008GC002198.

Moreno, M., et al. (2012), Toward understanding tectonic control on the Mw 8.8 2010 Maule Chile earthquake, *Earth Planet. Sci. Lett.*, 321-322(0), 152-165, doi: 10.1016/j.epsl.2012.01.006.

Ortega-Culaciati, F. et al., (2013), Post-seismic deformation of the great 11 March 2011 Tohoku-Oki (Mw 9.0) earthquake, in preparation.

Pesicek, J. D., E. R. Engdahl, C. H. Thurber, H. R. DeShon, and D. Lange (2012), Mantle subducting slab structure in the region of the 2010 M8.8 Maule earthquake (30–40°S), Chile, *Geophys. J. Int.*, 191(1), 317-324, doi: 10.1111/j.1365-246X.2012.05624.x.

Rietbrock, A., C. Haberland, K. Bataille, T. Dahm, and O. Oncken (2005), Studying the seismogenic coupling zone with a passive seismic array, *Eos Trans. AGU*, 86, 293-300, doi: 10.1029/2005EO320001.

Rietbrock, A., I. Ryder, G. Hayes, C. Haberland, D. Comte, S. Roecker, and H. Lyon-Caen (2012), Aftershock seismicity of the 2010 Maule Mw=8.8, Chile, earthquake: Correlation between co-seismic slip models and aftershock distribution?, *Geophys. Res. Lett.*, 39(8), L08310, doi: 10.1029/2012GL051308.

Ruegg, J. C., A. Rudloff, C. Vigny, R. Madariaga, J. B. de Chabalier, J. Campos, E. Kausel, S. Barrientos, and D. Dimitrov (2009), Interseismic strain accumulation measured by GPS in the seismic gap between Constitución and Concepción in Chile, *Phys. Earth Planet. Inter.*, 175(1-2), 78-85, doi: 10.1016/j.pepi.2008.02.015.

Ryder, I., A. Rietbrock, K. Kelson, R. Bürgmann, M. Floyd, A. Socquet, C. Vigny, and D. Carrizo (2012), Large extensional aftershocks in the continental forearc triggered by the 2010 Maule earthquake, Chile, *Geophys. J. Int.*, 188(3), 879-890, doi: 10.1111/j.1365-246X.2011.05321.x.

Vigny, C., et al. (2011), The 2010 Mw 8.8 Maule megathrust earthquake of central Chile, monitored by GPS, *Science*, 332(6036), 1417-1421, doi: 10.1126/science.1204132.

Appendix C

SUPPLEMENTARY MATERIAL OF CHAPTER IV

C. 1 Large Ensemble Interferograms

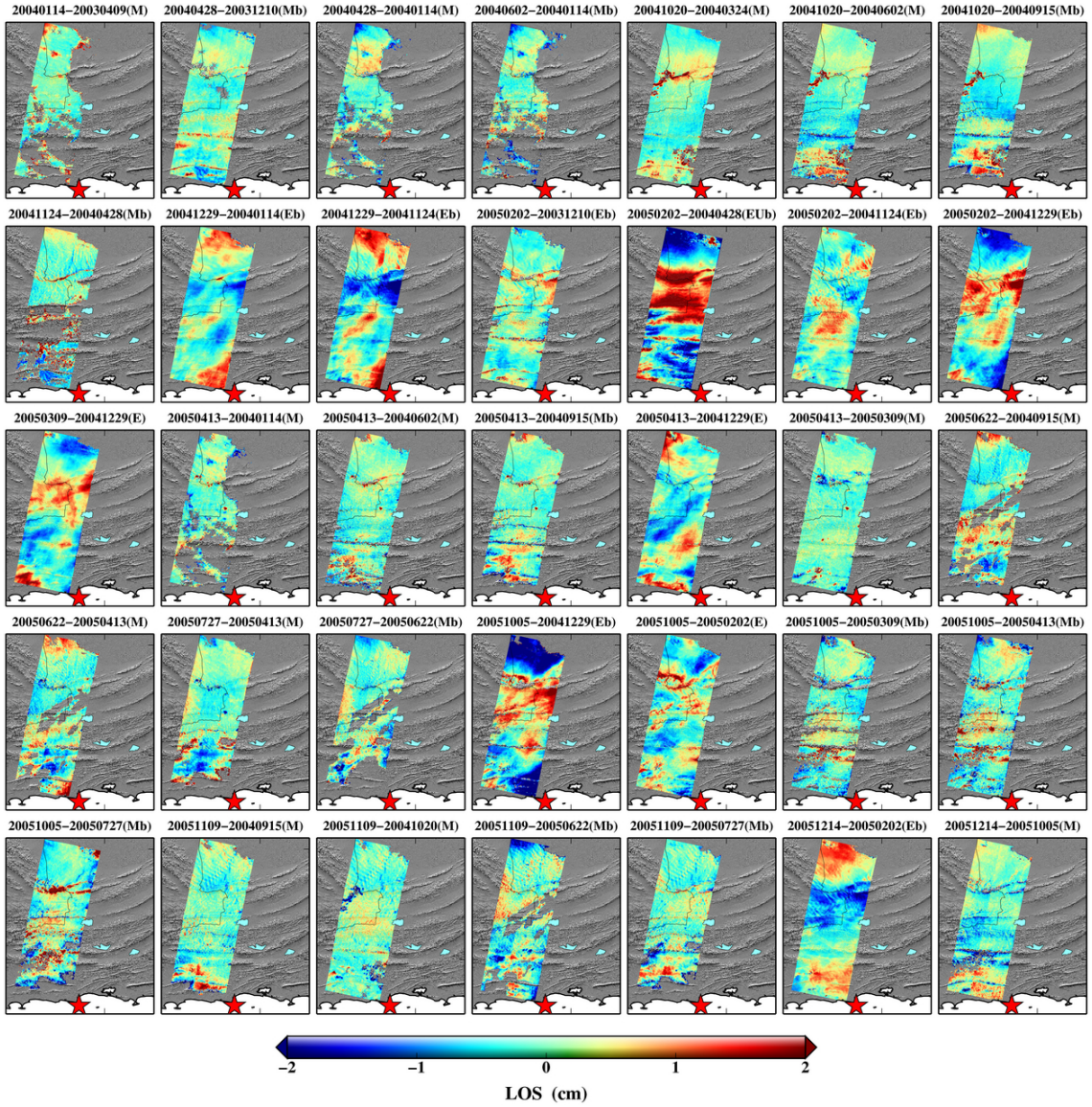

Figure C1-1. T220 large ensemble interferograms. All images are APS and OTL corrected, with bilinear ramps removed individually. M: MERIS APS correction applied; E: ECMWF APS correction applied; b: bridging applied during unwrapping.

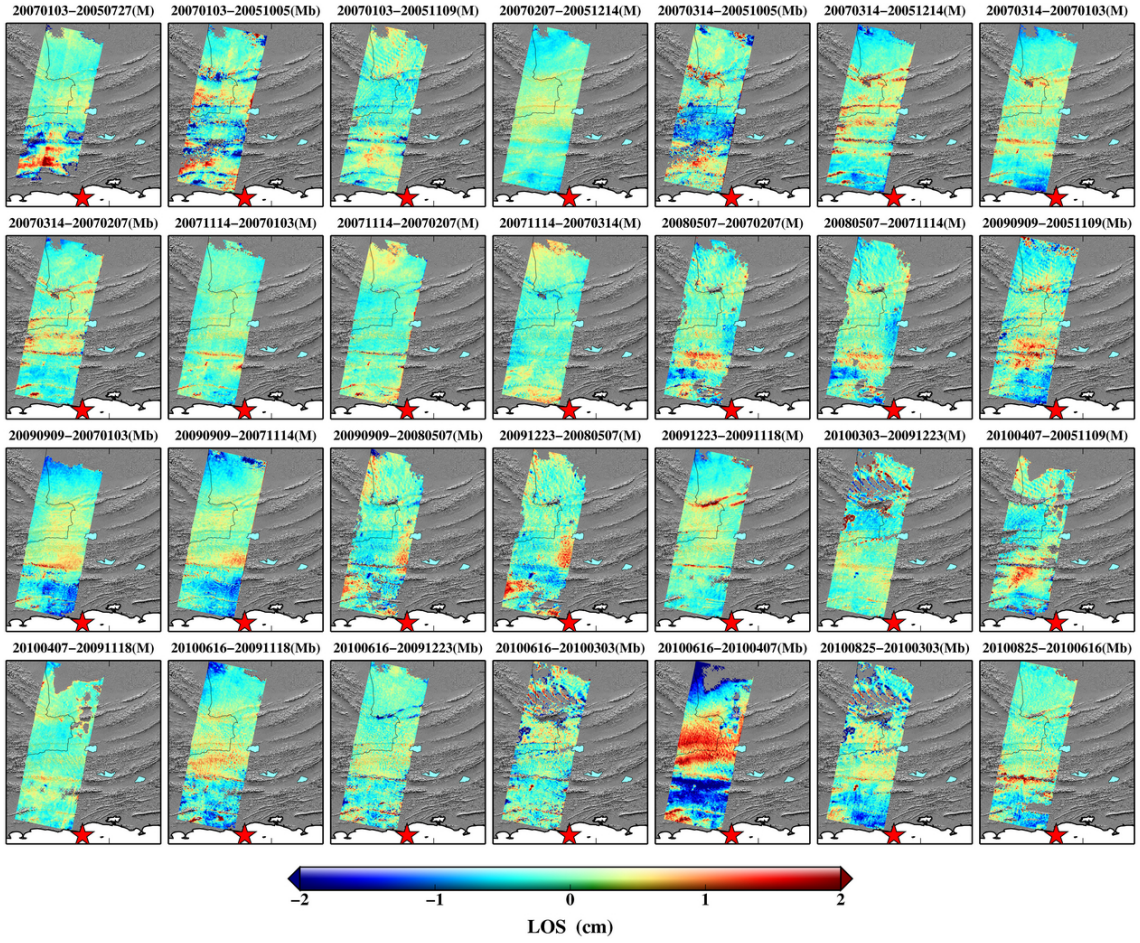

Figure C1-2. T220 large ensemble interferograms. All images are APS and OTL corrected, with bilinear ramps removed individually. M: MERIS APS correction applied; E: ECMWF APS correction applied; b: bridging applied during unwrapping.

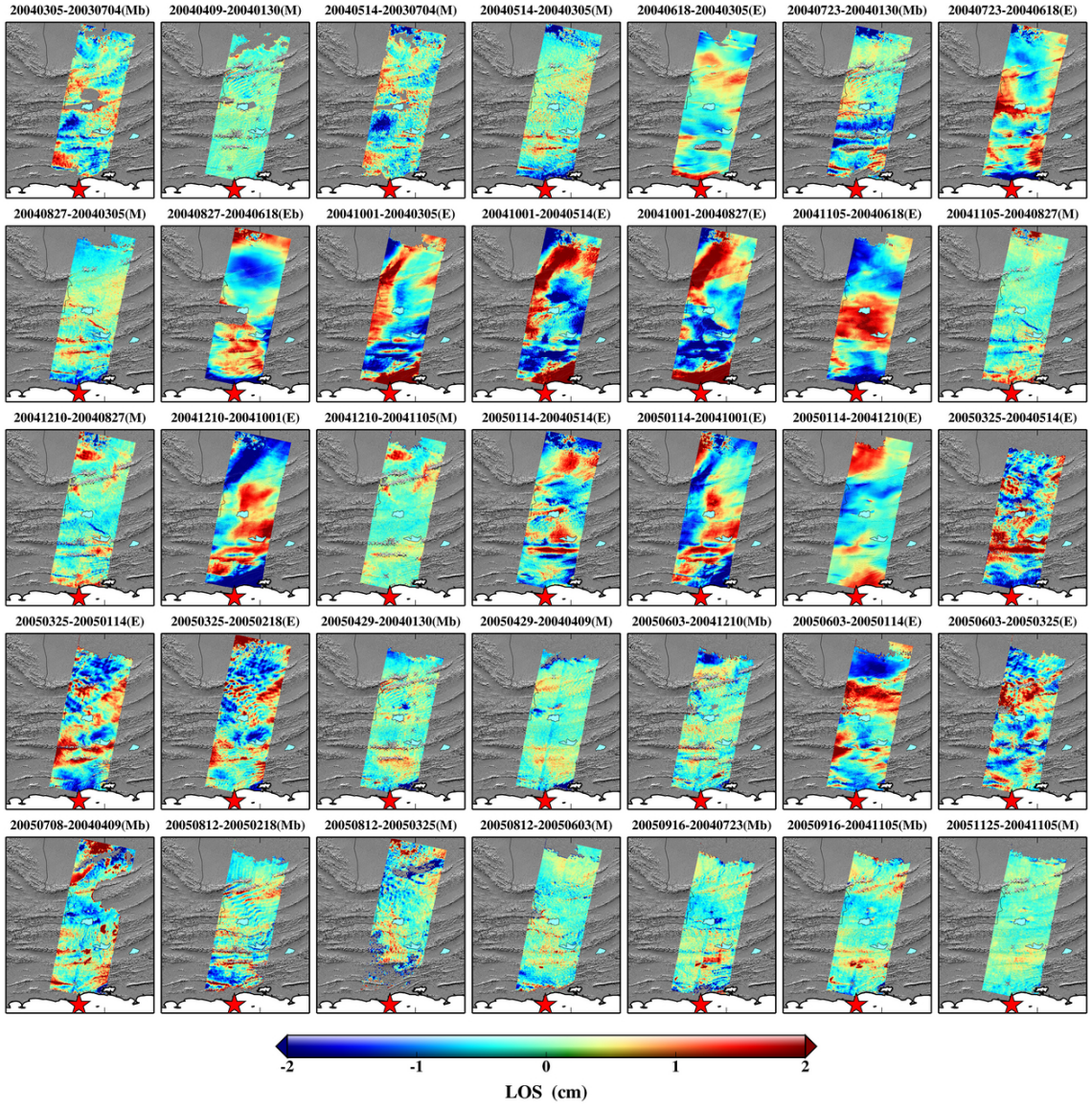

Figure C2-1. T449 large ensemble interferograms. All images are APS and OTL corrected, with bilinear ramps removed individually. M: MERIS APS correction applied; E: ECMWF APS correction applied; b: bridging applied during unwrapping.

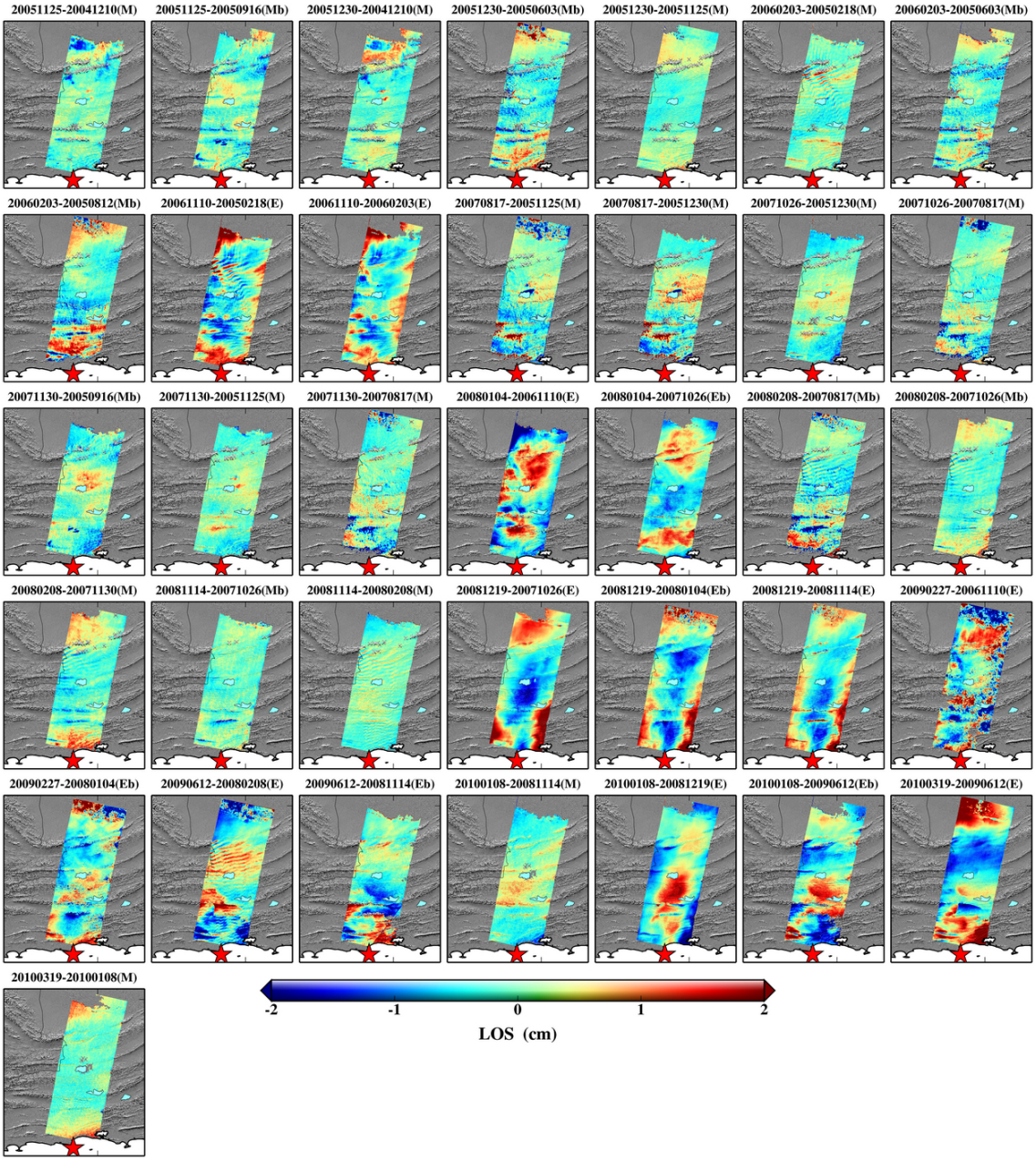

Figure C2-2. T449 large ensemble interferograms. All images are APS and OTL corrected, with bilinear ramps removed individually. M: MERIS APS correction applied; E: ECMWF APS correction applied; b: bridging applied during unwrapping.

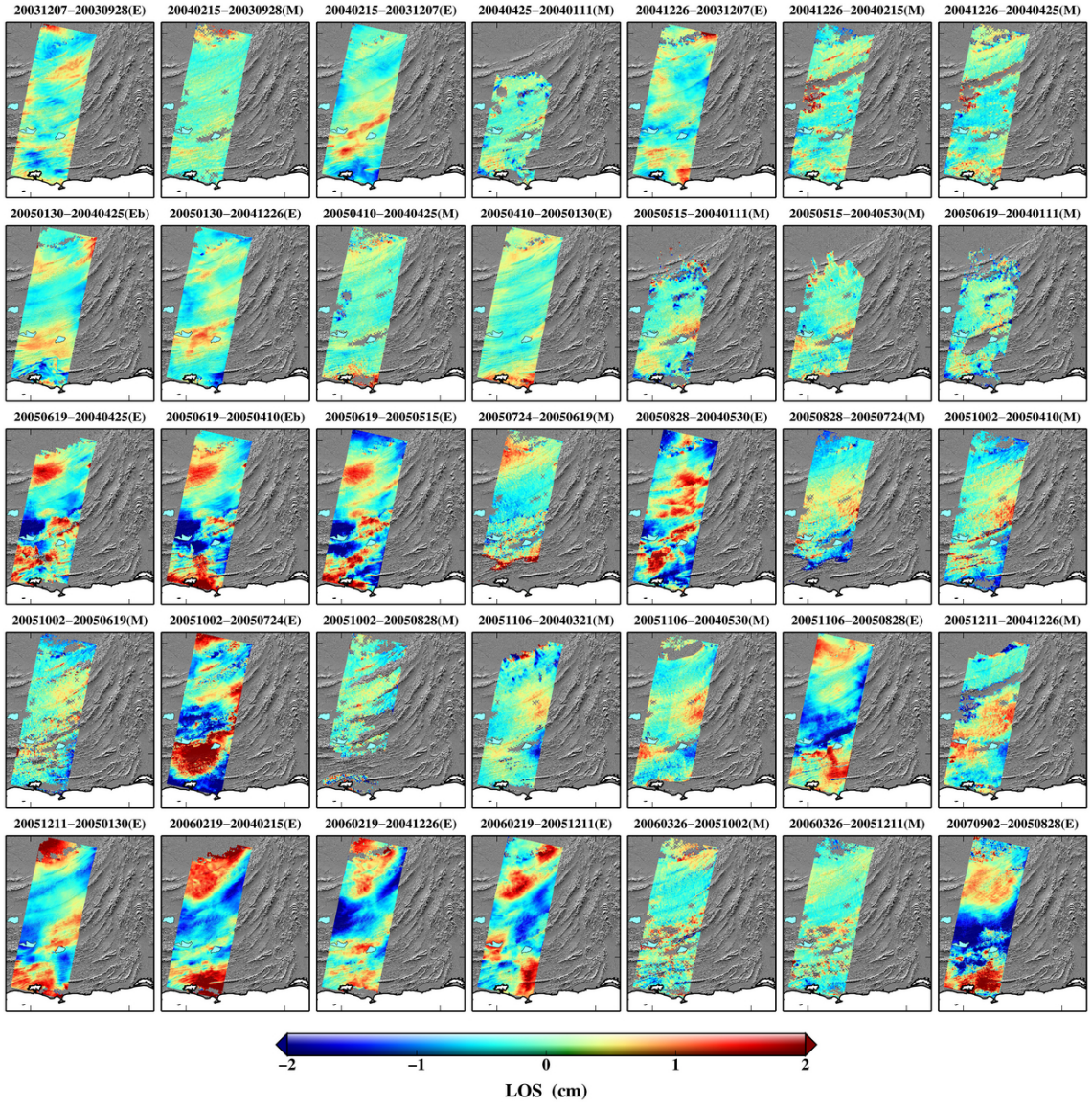

Figure C3-1. T177 large ensemble interferograms. All images are APS and OTL corrected, with bilinear ramps removed individually. M: MERIS APS correction applied; E: ECMWF APS correction applied; b: bridging applied during unwrapping.

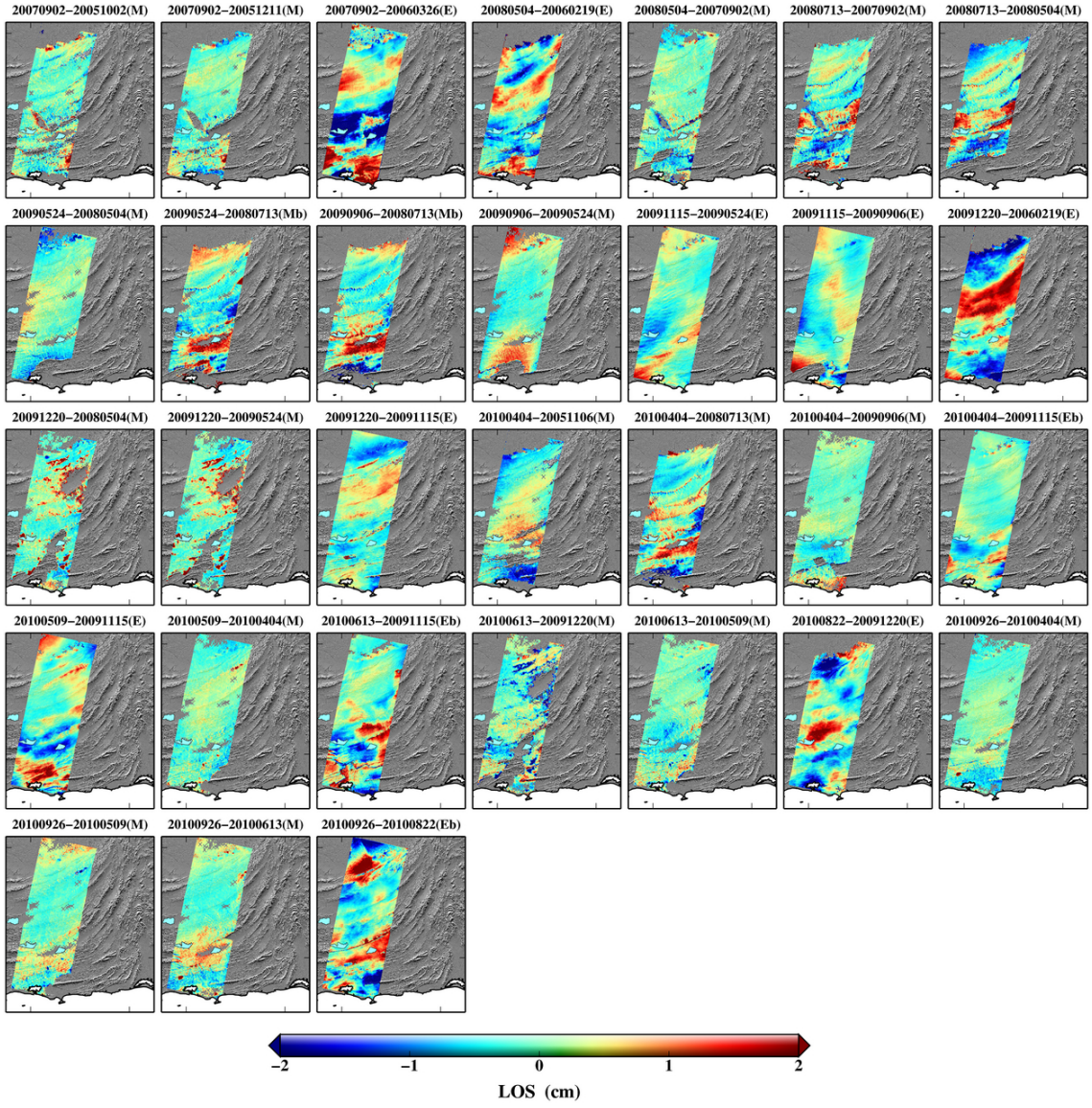

Figure C3-2. T177 large ensemble interferograms. All images are APS and OTL corrected, with bilinear ramps removed individually. M: MERIS APS correction applied; E: ECMWF APS correction applied; b: bridging applied during unwrapping.

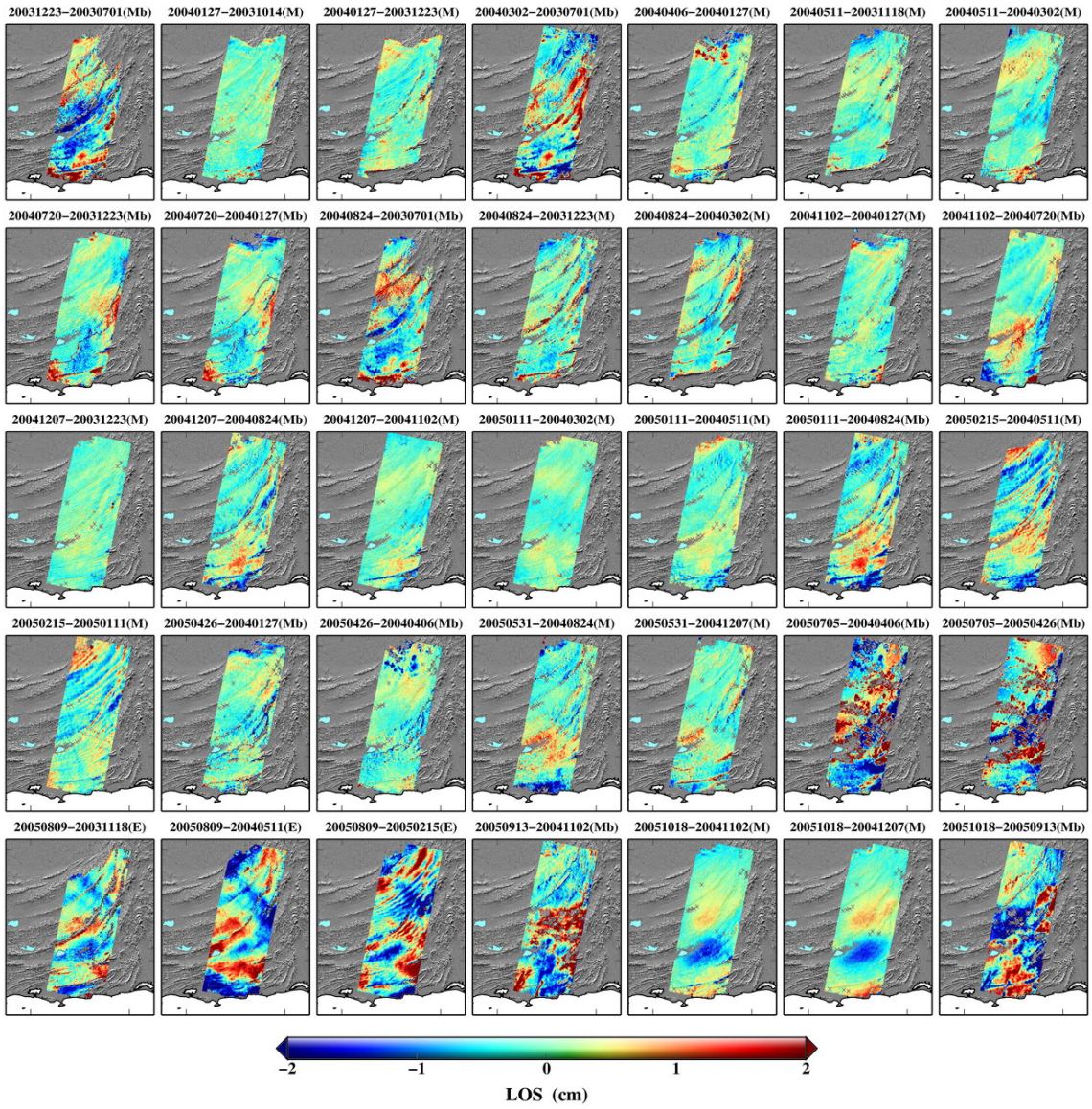

Figure C4-1. T406 large ensemble interferograms. All images are APS and OTL corrected, with bilinear ramps removed individually. M: MERIS APS correction applied; E: ECMWF APS correction applied; b: bridging applied during unwrapping.

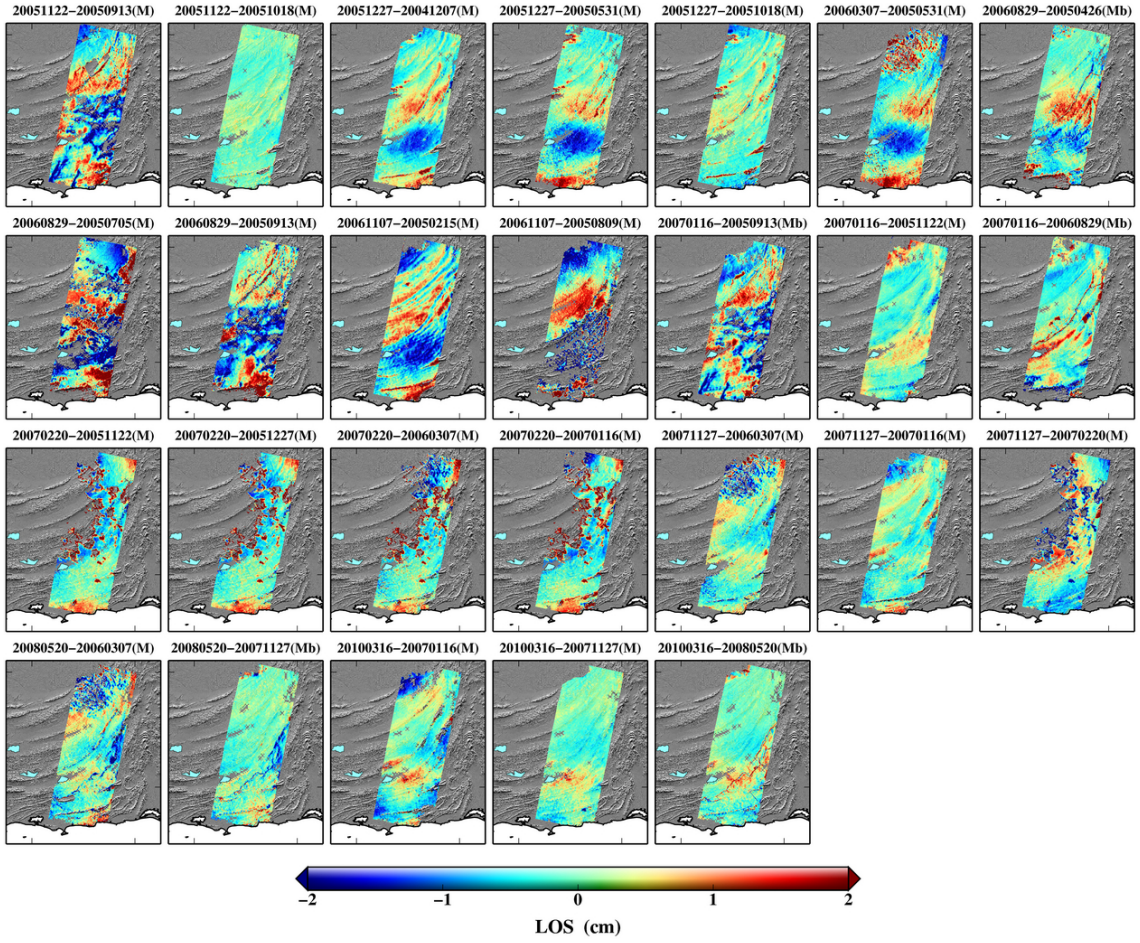

Figure C4-2. T406 large ensemble interferograms. All images are APS and OTL corrected, with bilinear ramps removed individually. M: MERIS APS correction applied; E: ECMWF APS correction applied; b: bridging applied during unwrapping.

C. 2 Small Ensemble Interferograms

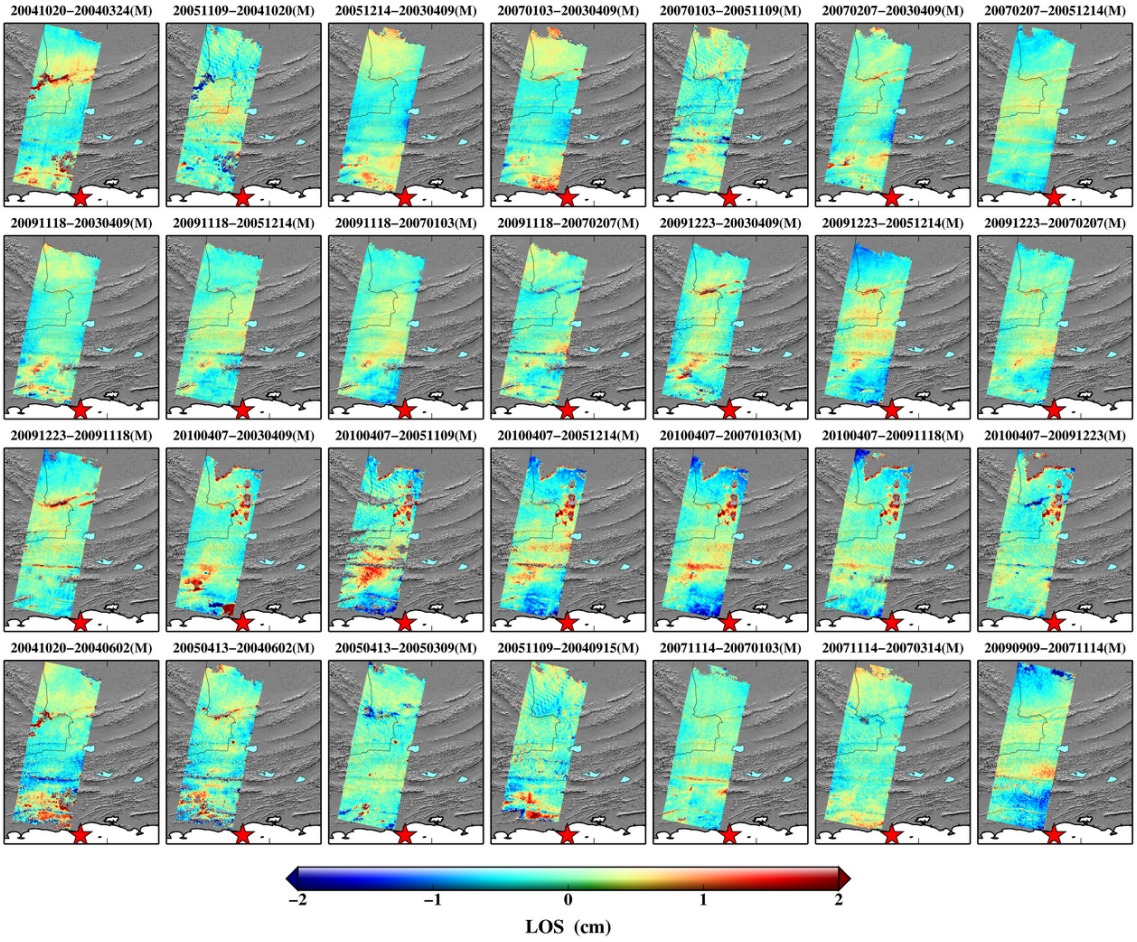

Figure C5. T220 small ensemble interferograms. All images are APS and OTL corrected, with bilinear ramps removed individually. M: MERIS APS correction applied.

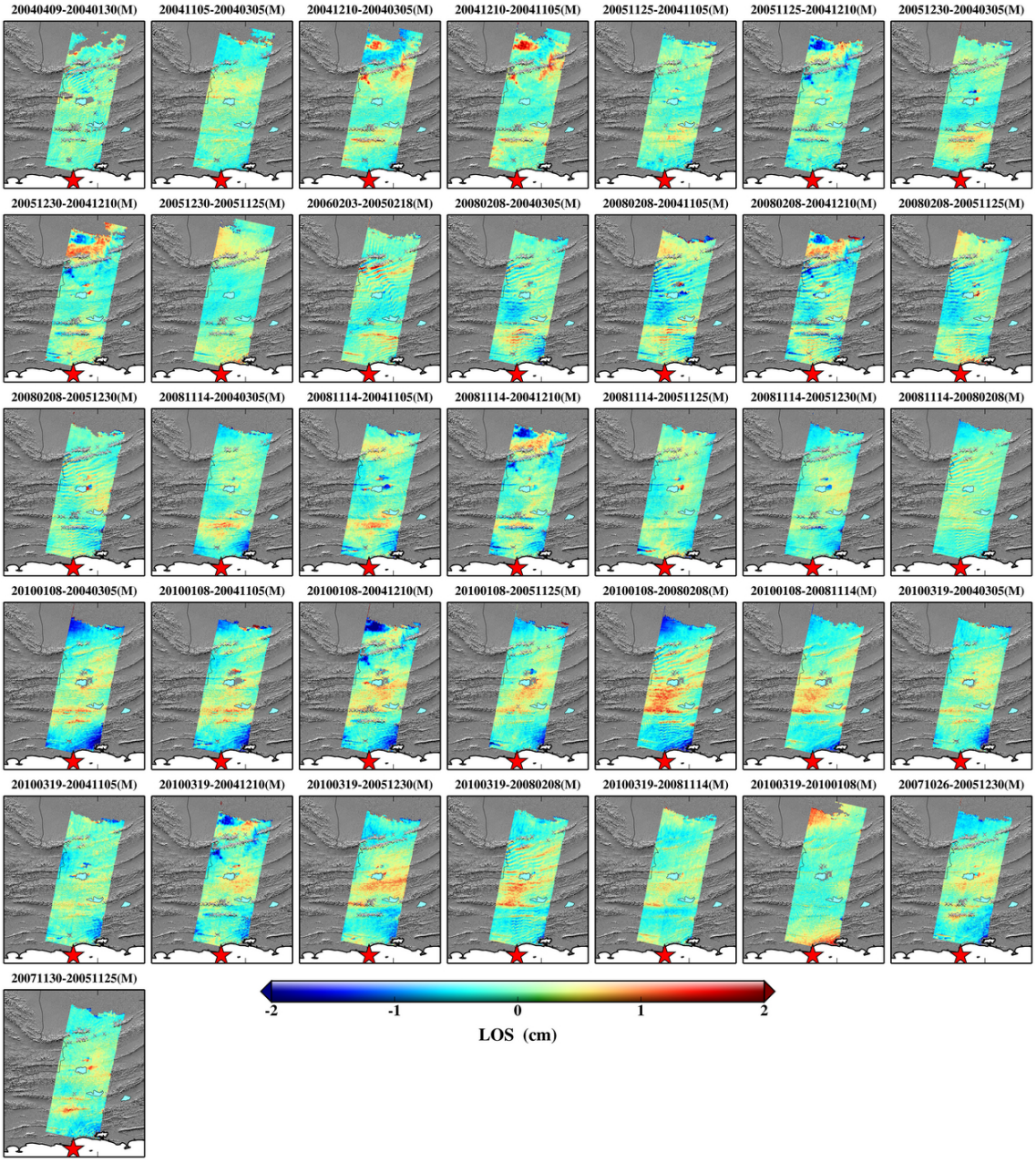

Figure C6. T449 small ensemble interferograms. All images are APS and OTL corrected, with bilinear ramps removed individually. M: MERIS APS correction applied.

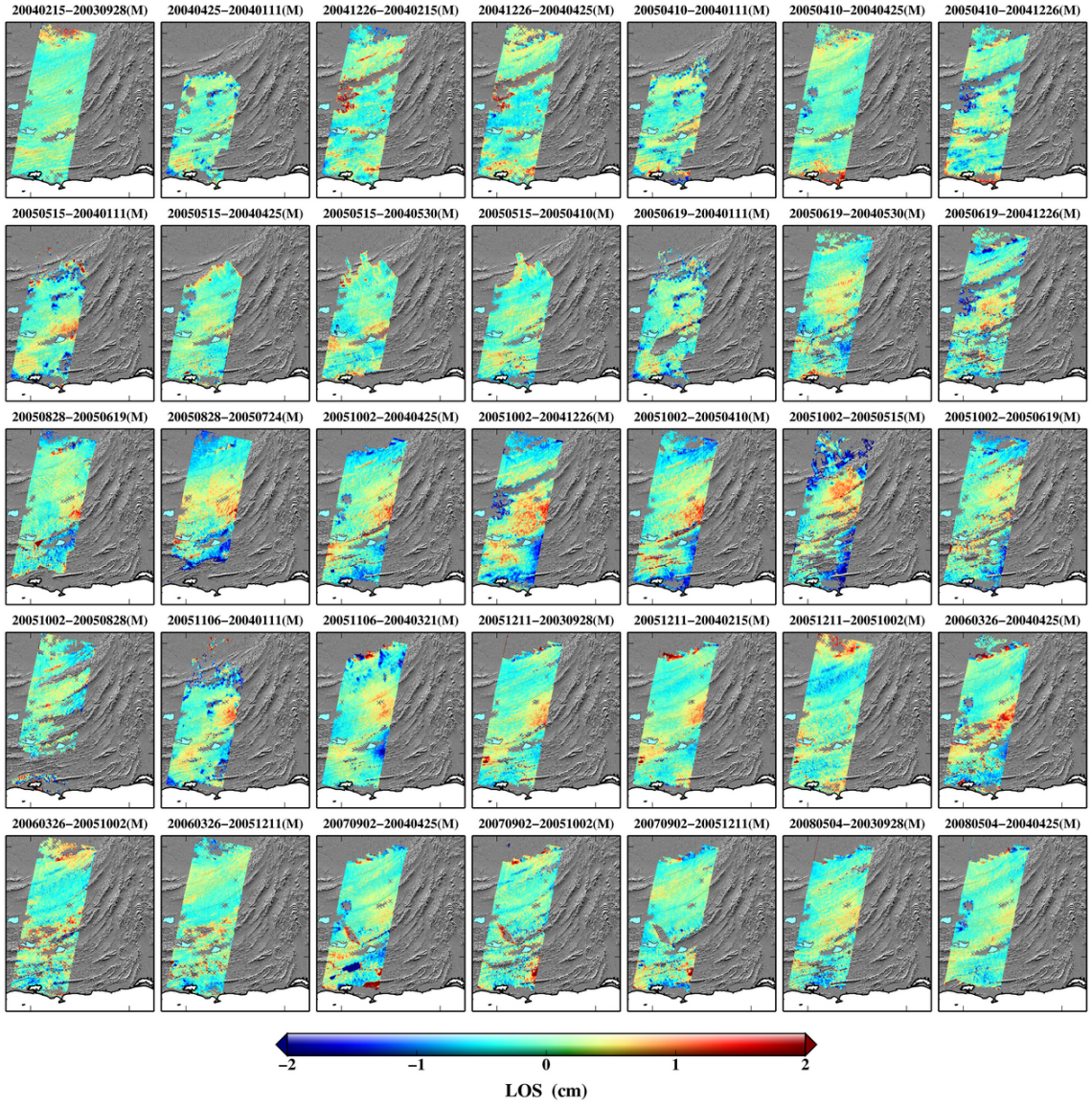

Figure C7-1. T177 small ensemble interferograms. All images are APS and OTL corrected, with bilinear ramps removed individually. M: MERIS APS correction applied.

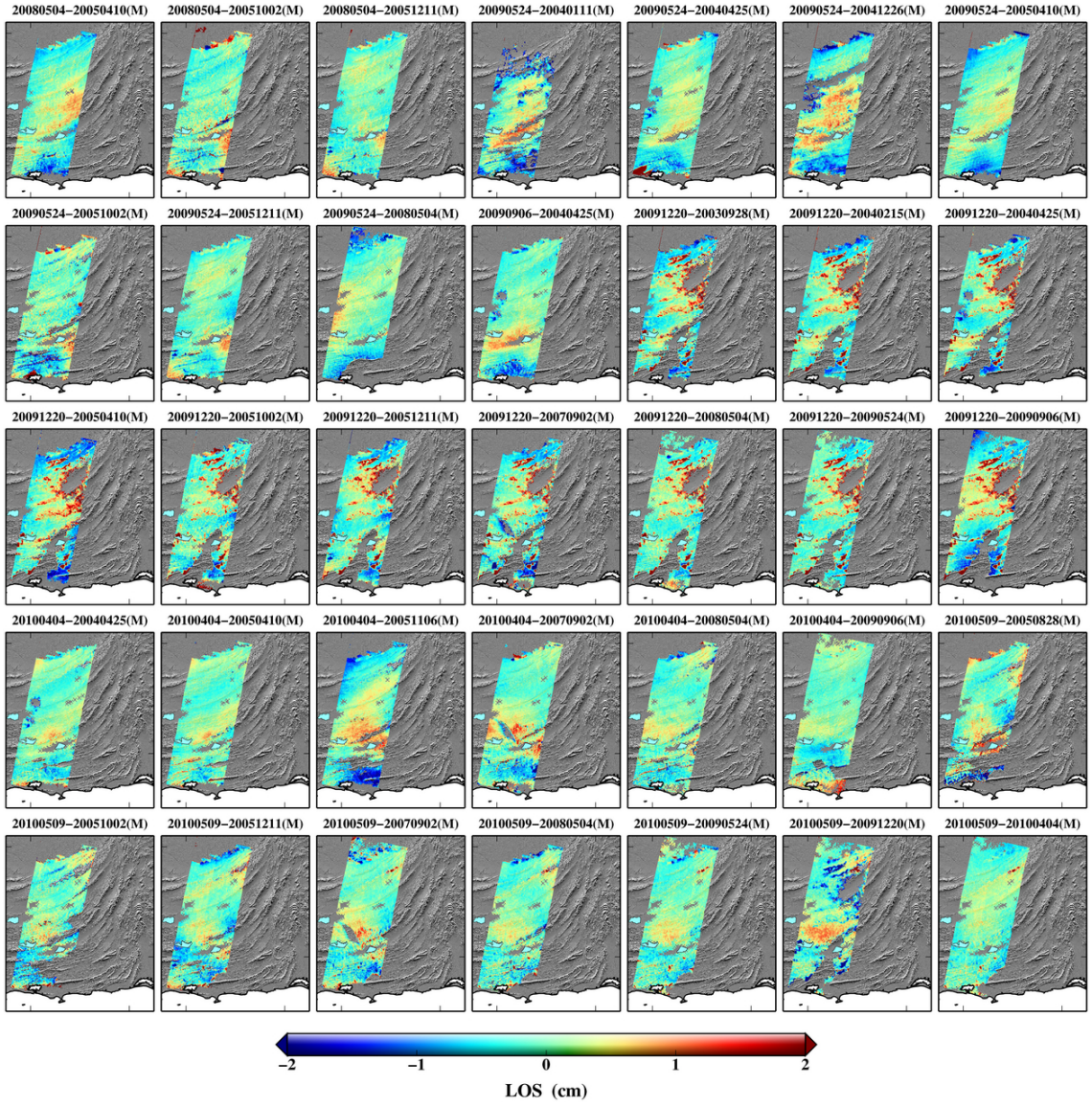

Figure C7-2. T177 small ensemble interferograms. All images are APS and OTL corrected, with bilinear ramps removed individually. M: MERIS APS correction applied.

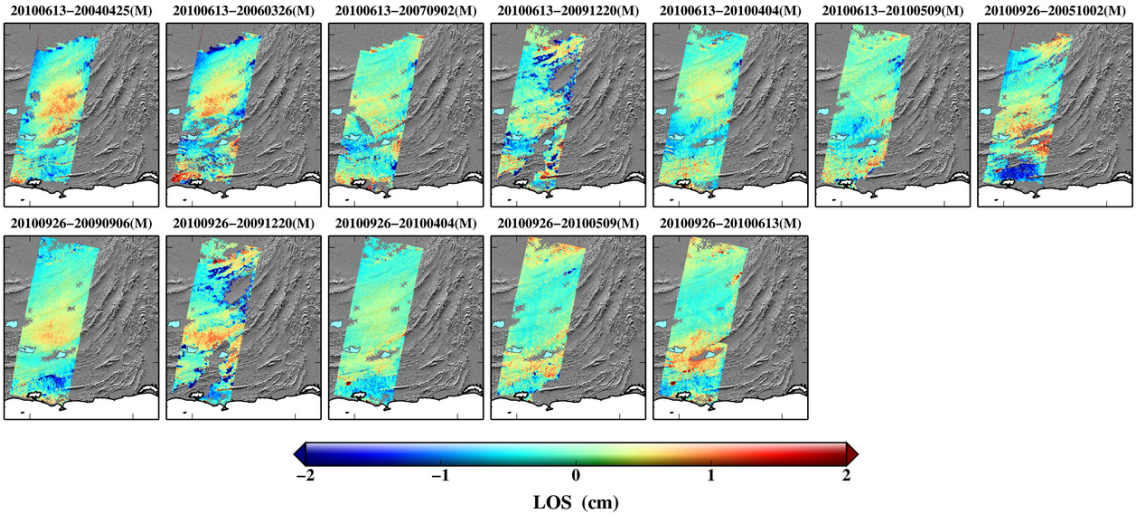

Figure C7-3. T177 small ensemble interferograms. All images are APS and OTL corrected, with bilinear ramps removed individually. M: MERIS APS correction applied.

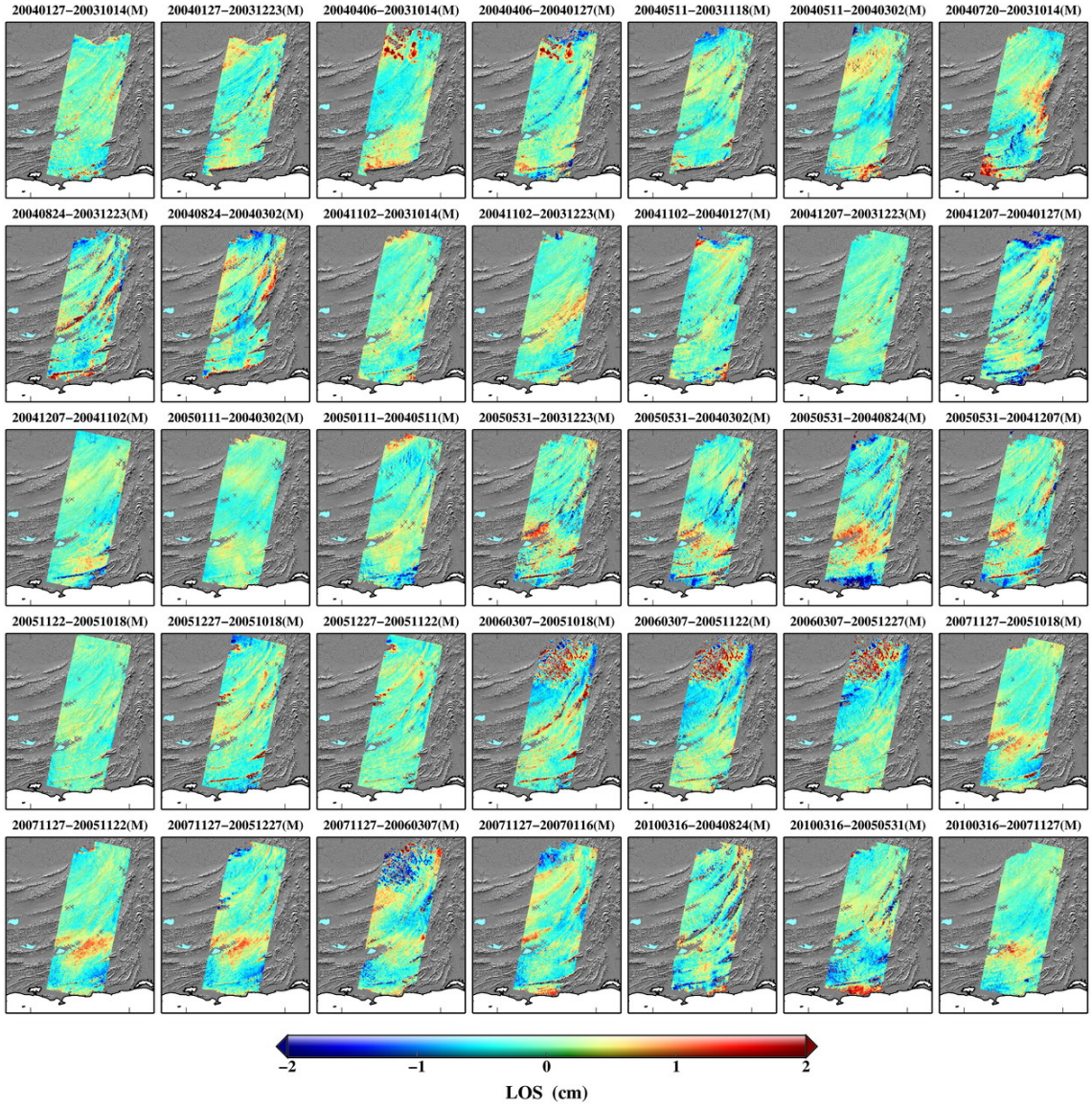

Figure C8. T200 small ensemble interferograms. All images are APS and OTL corrected, with bilinear ramps removed individually. M: MERIS APS correction applied.